Sub-Terahertz Integrated Metalens and its Applications

by Jiexin Lai

Thesis submitted in fulfilment of the requirements for the degree of Doctor of Philosophy

under the supervision of
Principal Supervisor: Prof. Yang Yang
Co-Supervisor: Prof. David McGloin
Co-Supervisor: Dr. Xiaojing Lv

University of Technology Sydney
Faculty of Engineering and Information Technology

Feb. 2026

CERTIFICATE OF ORIGINAL AUTHORSHIP

I, Jiexin Lai, declare that this thesis is submitted in fulfilment of the requirements for the award of Doctoral Degree, in the Faculty of Engineering and Information Technology at the University of Technology Sydney.

This thesis is wholly my own work unless otherwise referenced or acknowledged. In addition, I certify that all information sources and literature used are indicated in the thesis.

This document has not been submitted for qualifications at any other academic institution.

This research was supported by an Australian Government Research Training Program (RTP) Scholarship doi.org/10.82133/C42F-K220.

Production Note:
Signature: Signature removed prior to publication.

Date: 11/02/2026

Acknowledgement

I have had a colourful and fulfilling learning experience at the University of Technology Sydney, where I received tremendous support and assistance throughout my studies. During this journey, I have learned a great deal and met many wonderful people whose guidance and companionship will remain a valuable treasure and fond memory for the rest of my life.

First and foremost, I would like to express my sincere gratitude to my supervisor, Prof. Yang Yang, for his continuous guidance, patience, and encouragement during my PhD. His insightful advice and generous support have provided me with a nurturing environment in which to explore research and broaden my vision of the world.

I would also like to convey my heartfelt thanks to my co-supervisors for their invaluable guidance and expertise. I am particularly grateful to Prof. David McGloin for his guidance and valuable advice, and to Dr. Xiaojing Lv for his insights and inspiration, which have greatly influenced my work on metasurfaces. Special thanks are also extended to A/Prof. Jianfeng Zhu for their technical support and assistance with experiments.

My sincere appreciation goes to my group members, A/Prof. Jingyu Lin, Dr Mengze Li, Zhiwei Yin, Dr Xuyi Zhu, Dr Jiaqi Cai, Zhenxi Liang, Zhenlin Dai, Dr Zhichao Sun, Fuyou Yong, Dr Madiha Farasat, Shaghayegh Chamani and Meisam Esfandiari, for their insightful discussions, encouragement, and friendship, which have made this journey both academically rewarding and personally enjoyable.

I am also deeply thankful to Dr Shuvashis Dey, Md Ashif Islam Oni and Md Mirazur Rahman at North Dakota State University for their kind help in sample fabrication. Special thanks are extended to Joseph Samuya and Bobby Chan from Nano Dimension for their valuable assistance in fabricating the samples used in this work.

Finally, I would like to express my heartfelt gratitude to my family and friends for their unwavering encouragement and emotional support throughout this journey. Their belief in me has been a constant source of motivation and strength.

Published and Under Review Papers

[1] **J. Lai** and Y. Yang, "3D terahertz antenna measurement: A comparison between solid-state electronics and photomixing approaches," in *IEEE Antennas and Propagation Magazine*, vol. 66, no. 4, pp. 37-50, Aug. 2024. **[Chapter I, Section 1.4]**

[2] **J. Lai**, X. Lv and Y. Yang, "A 3-D printed 140 GHz multifocal dielectric transmitarray antenna for 2-D mechanical beam scanning," in *IEEE Antennas and Wireless Propagation Letters*, vol. 23, no. 4, pp. 1366-1370, Apr. 2024. **[Chapter III, Section 3.2]**

[3] **J. Lai** and Y. Yang, "A 3D printing 120 GHz lens antenna for terahertz 1D beam-scanning applications," *2022 International Symposium on Antennas and Propagation (ISAP)*, Sydney, Australia, 2022, pp. 75-76. **[Chapter III, Section 3.3]**

[4] **J. Lai**, X. Lv, M. M. Rahman, M. A. I. Oni, S. Dey and Y. Yang, "An angle-multiplexed multifocal method for D-band 2-D beam-scanning transmitarray leveraging 3-D transmission line component," in *IEEE Antennas and Wireless Propagation Letters*, vol. 24, no. 3, pp. 731-735, Mar. 2025. **[Chapter IV, Section 4.2]**

[5] **J. Lai** and Y. Yang, "A 3D printed terahertz metamaterial lens for beam-steering applications," *2023 IEEE/MTT-S International Microwave Symposium - IMS 2023*, San Diego, CA, USA, 2023, pp. 692-695. **[Chapter IV, Section 4.3]**

[6] **J. Lai** and Y. Yang, "Sub-THz metasurface sensor for real-time skin condition monitoring," in submission. **[Chapter V]**

[7] **J. Lai**, X. Guo and Y. Yang, "Dual polarised metasurface with dual OAM modes using curved broadside-coupled striplines," in *IEEE Transactions on Microwave Theory and Techniques*, under review.

[8] J. Zhu, Y. Yang, **J. Lai**, J. Nulman, "Additively manufactured polarization insensitive broadband transmissive metasurfaces for arbitrary polarization conversion and wavefront shaping," in *Advanced Optical Materials*, vol. 10, no. 21, pp. 2200928-

2200921, Nov. 2022.

[9] J. Zhu, Y. Yang, F. Wang, **J. Lai**, M. Li, "3D printed spin‐decoupled transmissive metasurfaces based on versatile broadband cross‐polarization rotation meta‐atom," in *Advanced Optical Materials*, vol. 11, no. 4, pp. 2202416, Feb. 2023.

[10] J. Zhu, M. Li, **J. Lai**, Y. Yang, "Multimaterial additively manufactured transmissive spin‐decoupled polarization‐maintaining metasurfaces," in *Laser & Photonics Reviews*, vol. 17, no. 12, pp. 2300433, Dec. 2023.

[11] J. Zhu, Y. Yang, **J. Lai** and M. Li, "3-D printed noninterleaved reflective metasurfaces supporting dual-band spin-decoupled quadruplex channel independent beam-shaping with controllable energy distribution," in *IEEE Transactions on Microwave Theory and Techniques*, vol. 72, no. 2, pp. 1196-1205, Feb. 2024

[12] L. -Z. Song, T. Zhang, **J. Lai**, Y. Yang and J. Du, "A 180-GHz to 220-GHz wideband transmitarray with wide-angle beam steering for intersatellite communications," in *IEEE Transactions on Antennas and Propagation*, vol. 72, no. 1, pp. 950-955, Jan. 2024

[13] Z. Yin, H. Zhu, X. Lv, **J. Lai** and Y. Yang, "3-D-printed ultracompact butler matrix for wideband millimeter-wave beamforming," in *IEEE Transactions on Microwave Theory and Techniques*, vol. 73, no. 9, pp. 5953-5965, Sep. 2025

Abstract

This research aims to explore the feasibility of integrating sub-terahertz (THz) technology with metalenses for applications, such as next-generation communications and biomedical detection. The sub-THz band, ranging from 100 GHz to 1 THz, offers unique features, including abundant spectral resources, shorter wavelengths, non-ionising radiation, and high sensitivity to water. Its broadband capabilities make it a promising candidate for sixth-generation (6G) wireless communication systems, such as inter-satellite communications. The shorter wavelengths enable high-accuracy imaging, while the non-ionising radiation ensures safety for humans. Additionally, the high sensitivity to water makes it particularly suitable for biomedical detection. For 6G communication applications, metalenses for two-dimensional (2D) beam scanning have been developed, offering advantages such as low cost, high gain enhancement, and reduced scanning losses. Beam-scanning antennas, which are key components of 5G systems, hold significant potential for 6G applications. In the field of biomedical imaging, a real-time skin detection system utilising metalenses, metasurface sensors, and a sub-THz camera has been proposed. This proposed system shows potential for further development into a portable device for skin cancer detection. These findings highlight the potential for sub-THz-based systems to advance both wireless communications and real-time biomedical applications.

Chapter I: Introduction

This chapter overviews the THz frequency band and its applications in communication and biomedical fields. Methods for generating and detecting THz waves are also introduced as background.

Chapter II: Literature Review

This chapter provides an overview of various metasurfaces and skin cancer detection methods, serving as a foundation for the subsequent chapters.

Chapter III: All-Dielectric Metalens Design

This chapter presents three 3D-printed metalenses with distinct functions: a one-dimensional lens, a two-dimensional lens, and a real-time reflection imaging lens—the latter of which will be applied in Chapter V.

Chapter IV: Conductive and Dielectric Multimaterial Metasurface Lens

This chapter presents various metasurface lenses fabricated using additive manufacturing technology.

Chapter V: Sub-THz Metasurface Sensor for Real-Time Skin Condition Monitoring

This chapter provides a metasurface sensor and its corresponding skin condition monitoring system. The experiments on pork skin verify the concept of using the metasurface sensor for skin detection, which has valuable potential to be developed into skin cancer detection systems.

Keywords: Sub-THz, 3D printing, metasurface, lens, transmitarray, beam scanning, sensor, skin cancer detection.

CONTENTS

Chapter I Introduction

1.1 Research Background

The terahertz (THz) spectrum (0.1 - 10 THz) lies between the microwave and infrared regimes and is often referred to as the “Terahertz Gap.” As illustrated in Fig. 1.1, the THz band bridges the domains of electronics and photonics. Compared with the microwave and millimetre-wave regions, THz waves offer abundant spectral bandwidth that can support higher-capacity and low-latency communication [1], while their shorter wavelengths enable high-resolution imaging, because the image is related to the diffraction limit, which is a function of wavelength [2]. THz waves exhibit excellent scattering characteristics. Compared with near-infrared imaging, THz waves can penetrate common clothing materials [3] and effectively avoid interference from particle scattering effects [4]. Moreover, THz spectroscopy enables the identification of resonant spectral fingerprints of low-absorption materials [5], allows the detection of vibrational, rotational, and wagging modes of biomolecules [6], and facilitates the measurement of water molecule absorption [7]. In contrast to the infrared and optical regions, THz waves are partially transparent to a variety of non-conductive materials [8] such as clothing, paper products, plastics, and ceramics. Moreover, as a form of non-ionising radiation [9], THz waves are inherently safer than X-rays [10]. Owing to these advantages, THz technology is regarded as a promising candidate for future sixth-generation (6G) mobile communications, biomedical applications, security screening, and advanced automotive systems. This thesis primarily focuses on the study of THz metasurfaces and their applications in communication and biomedical fields.

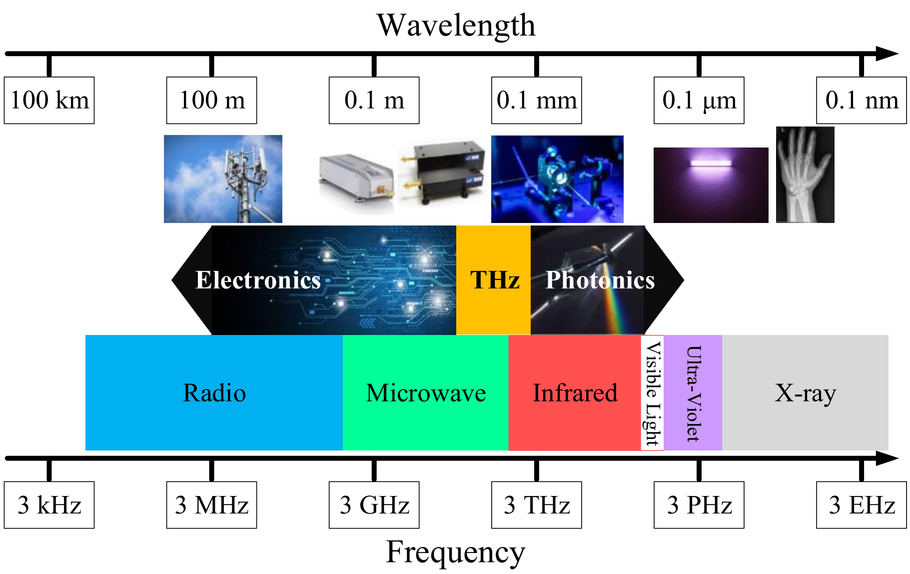

Fig. 1.1. The electromagnetic spectrum and the position of the THz band.

1.2 Terahertz Communications Application

In March 2019, the Federal Communications Commission (FCC) proposed allocating the frequency range from 95 GHz to 3 THz for sixth-generation (6G) wireless communication experiments [11]. At present, the fifth-generation (5G) mobile network has been deployed, offering transmission speeds of up to 10 Gbps. The International Telecommunication Union (ITU) forecasts that the number of wireless communication devices could reach 50 billion in the near future [12]. However, the millimetre-wave spectrum might not be sufficient to meet the projected bandwidth demands of the coming decade [13]. The underutilised THz spectrum, with hundreds of gigahertz of available bandwidth, has the potential to deliver data rates up to ten times higher than those of 5G. With ongoing technological advancements, frequency bands that are currently unsuitable for wireless communications may become viable. Consequently, research on THz antennas has become increasingly critical, as they serve as a key enabling component of future wireless communication systems.

1.2.1 Terahertz Antenna

There are various candidates for the THz communication antenna [14], [15], [16], including the series-fed patch antenna [17], the leaky wave antenna [18], the horn antenna [19], the integrated lens antenna [20] and the photoconductive antenna [21]. Metasurface lens antennas (MLAs) [22] or transmitarray antennas (TAAs) [23] are promising candidates for THz wireless communication applications.

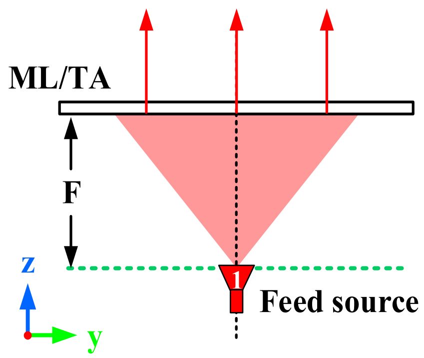

Fig. 1.2. Schematics of the MLA or TAA.

As shown in Fig. 1.2, the MLA is composed of a metasurface lens (ML), also known as a transmitarray (TA), and a feed source. The feed source illuminates the upper ML, which transforms the incident wavefront into a plane wave, thereby enhancing the antenna's directivity and gain. The main advantages of the MLA are as follows:

1) They can achieve high-gain performance;

Electromagnetic (EM) waves can be absorbed in the atmosphere due to the polar molecule H_2O (water vapour) in the air [24]. The EM waves' attenuation aggravates with the increase in their frequency [25]. The attenuation peak lies at 60 GHz with an attenuation of 15 dB/km, and atmospheric transmission windows still exist in the lower THz frequency band, with about 0.4 ~ 2 dB/km attenuation in the D-band (frequency range from 110 GHz to 170 GHz) [26]. Thus, the high-gain antenna is necessary to tackle this problem. Traditional array antennas are not able to realise high-gain performance in the THz band due to the significant insertion loss introduced by the feeding network [27], while the spatial feed of the MLAs can avoid insertion loss at the cost of increasing the antenna profile. The aperture size of the MLAs can be enlarged according to the requirements for gain.

2) They can realise beam-scanning performance;

The increase in the antenna's gain and directivity reduces the EM wave radiation coverage, while the beam-scanning antenna can increase the signal coverage. The communication system using the beam-scanning antenna can track and serve multiple users sequentially [28].

3) They are easy to manufacture;

It is well-known that the size of the EM structure correlates with its operating frequency wavelength. The half wavelength in the D-band is from 0.8 mm to 1.3 mm. Printed circuit board (PCB), dielectric 3D printing, and additive manufacturing technology can fabricate the MLAs in the D-band because the MLAs can be simple in structure [29], [30], [31].

As previously mentioned, this thesis mainly focuses on studying the MLAs and TAAs.

1.3 Terahertz Biomedical Applications

THz waves possess several advantageous characteristics, including non-ionising radiation and strong sensitivity to water content [32], making them suitable for biomedical applications. In particular, THz technology has attracted significant interest in skin cancer detection. This is primarily because THz waves can effectively distinguish between cancerous and normal tissues, owing to their sensitivity to variations in tissue water content and dielectric properties. The tissue dielectric properties correlate with their water contents and other biochemistry [33], [34], [35]. As the permittivity changes, cancerous tissue can be detected in the breast, lungs and skin [36], [37], [38], [39] using electromagnetic waves. The THz waves from 0.4 to 0.6 THz have a maximum penetration depth of about 0.3 mm into the skin [40], and the THz skin cancer detection system operates in the frequency range of 0.1–3 THz [41], enabling the detection of skin features within a depth of 1 mm. Therefore, it is suitable for in vivo measurement since the THz wave detection results may not be affected by the fat layer, and its penetration depth covers most of the skin. In [42], a THz pulse imaging system with a frequency range of 0.1 – 2.7 THz was employed to image ex vivo skin cancer tissue.

According to the Skin Cancer Foundation [43], more than 5 million cases of skin cancer are diagnosed each year. They also estimate that nearly 1.9 million new cases will occur in 2021, excluding the most common types such as basal cell carcinoma (BCC) and squamous cell carcinoma (SCC). Timely detection plays a critical role in improving the cure rate of skin cancer patients. In this context, THz technology demonstrates significant practical value for skin cancer diagnosis.

1.3.1 Skin

The skin is the largest organ of the body, covering approximately 95% of its surface and serving as a protective barrier against the environment. From an EM perspective, the skin can be modelled as a multilayer structure with distinct dielectric constants and loss tangents [44]. It consists of three primary layers—epidermis, dermis, and subcutaneous fat layer—as illustrated in Fig. 1.3.

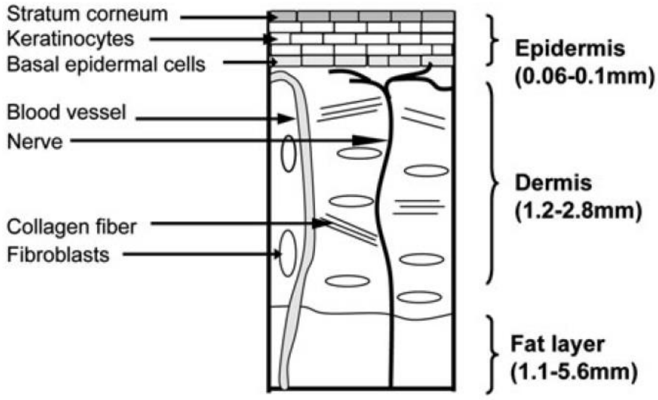

Fig. 1.3. Skin structure diagram [44].

The stratum corneum (SC) has a thickness of $10 - 30\ \mu m$, which is the outermost layer of the epidermis. The total thickness of the epidermis is about $60 - 100\ \mu m$. The medium layer, dermis, has a thickness of $1.2 - 2.8\ mm$. The bottom layer is the hypodermis or subcutaneous fat. The SC, the outer layer of flattened, keratinised cells of the epidermis, contains a larger amount of the protein keratin [45]. Its main function is to provide a protective barrier against water evaporation, microorganisms and harmful materials.

According to [46], the SC has the lowest water content, ranging from 10 - 15%, whereas the epidermis and dermis contain 45 - 55% and 70 - 80% water, respectively.

Water in biological tissues exists in two forms: bulk (free) water and bound water. Bulk water is the primary factor influencing the skin's dielectric constant and loss tangent, and tumours generally contain more water than normal skin tissue [47]. Specifically, the water content of tumours is approximately 81.7%, compared to 60.9% in healthy skin [48]. In addition, malignant tumours exhibit higher sodium content, enabling greater water retention and resulting in elevated relative permittivity and conductivity [49]. Therefore, variations in skin water content lead to differences in complex dielectric permittivity, which can be detected using microwave measurements.

Skin cancer is prevalent in regions such as North America, Europe, and Australia, and can be classified into two main types: melanoma (MM) and non-melanoma skin cancer [50]. Among non-melanoma cancers, BCC [51] and SCC [52] are the most common. MM is the most dangerous skin tumour, characterised by low incidence but high malignancy, and its etiology remains unclear. SCC primarily affects the head and neck, followed by the trunk, with typical lesions ranging from 0.5 to 1.2 cm in diameter and a cure rate of approximately 97.3%. In the early stages, skin cancer thickness is around 1 mm [53]; at this stage, tumour cells may metastasise, and the prognosis worsens. Therefore, timely detection is crucial for effective treatment and improving patient outcomes.

1.3.2 Skin Parameterisation

When applying an electric magnetic field, the dielectric property of biological tissue cells generates a polarisation reaction, which includes the variation of permittivity, dielectric constant, loss tangent and conductivity. Permittivity and dielectric constant represent the insulating properties of cells, and conductivity represents the conductive properties of cells. When the frequency of an electromagnetic field changes, the dielectric properties of biological tissue also change, which is referred to as dispersive properties. It includes α, β and γ dispersions [54].

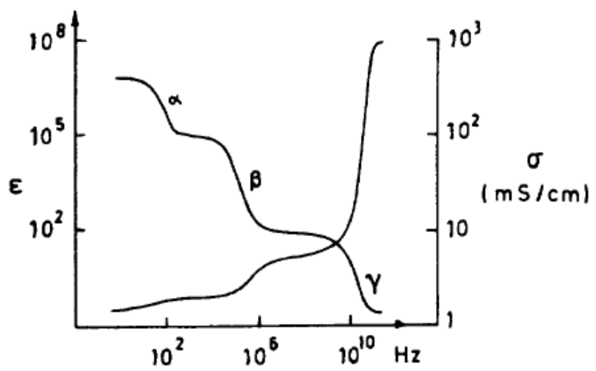

Fig. 1.4. Dielectric constant and conductivity [54].

The α-dispersion is related to ionic diffusion of the cell membrane. There are three established mechanism: 1) Studies of colloidal solutions have shown that the presence of frequency dependent surface conductance and surface capacitance is mainly due to the response of counter-ionic atmosphere near the cell surface; 2) Channel proteins in cell membranes will change in conductance with the vary of the frequency; and 3) the presence of sarcoplasmic reticulum seems to be the main cause of strong dispersion.

The polarisation of cell membranes, proteins, and other macromolecules gives rise to β-dispersion in biological tissues, which typically occurs in the frequency range of 0.1 - 10 MHz. As first proposed by K. S. Cole [55], this phenomenon is attributed to the poor conductivity of the cell membrane separating the cytoplasm from the extracellular space, resulting in a finite charging time for the membrane. At the tail end of β-dispersion, proteins contribute to relaxation effects. In contrast, γ-dispersion occurs at frequencies above 1 GHz and is primarily caused by the polarisation of water molecules. A weaker δ-dispersion is also observed, arising from protein-bound water. The dielectric properties of biological tissues have been investigated for many decades. Gabriel et al. [56] characterised the permittivity of skin in the microwave band by establishing a Cole–Cole model and extrapolating the results. Subsequent studies by Alabaster [57], Hwang et al. [58], and Alekseev et al. [59] measured the permittivity of human skin directly at various frequencies, providing more accurate experimental data across different frequency ranges. The permittivity of biological tissue is constant in an electrostatic field but dynamic in an alternating electric field. When the field shifts from dynamic to static, a finite recovery period is required, known as the relaxation time.

The dielectric properties of different biological tissues depend on their biological composition as well as ambient temperature. To describe these frequency-dependent behaviours, the Debye model [60] and the Cole–Cole model [61] have been widely employed to calculate the permittivity and conductivity of biological tissues across different frequency ranges.

1) Debye model

It is a well-known fact that the dielectric constant of many liquids and solids depends significantly on the frequency of measurement. In general, the correlation decreases from a static value $\varepsilon_r(0)$ at low frequencies to a smaller limit value $\varepsilon_r(\infty)$ at high frequencies. The complex permittivity can be described by $\varepsilon_r^* = \varepsilon_r' - i\,\varepsilon_r''$. The real part and imaginary part of the complex permittivity can be given by the Debye model:

$$\varepsilon_r'(\omega) = \varepsilon_r(\infty) + \frac{\varepsilon_r(0) - \varepsilon_r(\infty)}{1 + (\omega\tau_0)^2} \tag{1.1}$$

$$\varepsilon_r''(\omega) = \frac{\varepsilon_r(0) - \varepsilon_r(\infty)}{1 + (\omega\tau_0)^2}\,\omega\tau_0 \tag{1.2}$$

Where $\varepsilon_r(0)$ is the static permittivity, $\varepsilon_r(\infty)$ is the permittivity as the frequency approaches infinity, τ_0 is a characteristic constant called the relaxation time, ω is the angular frequency and equals 2π ·frequency.

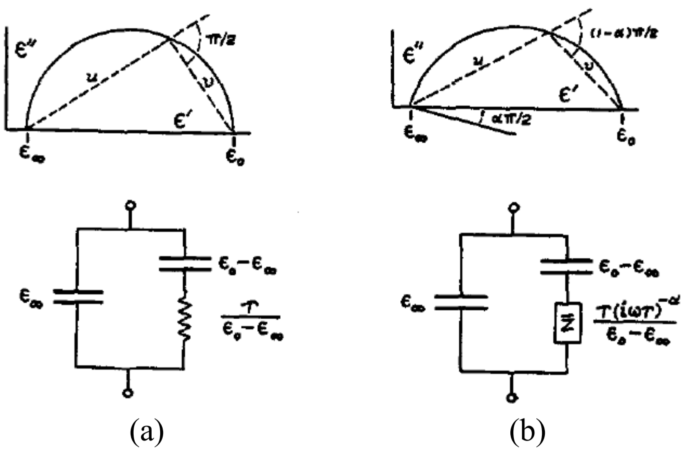

Fig. 1.5. The complex dielectric constant in the complex plane and the corresponding equivalent circuits; (a) Debye model. (b) Cole-Cole model [61].

It can be seen that Equations (1.1) and (1.2) can be given in the form $u + v = \varepsilon_r(0) - \varepsilon_r(\infty)$, Where $u = \varepsilon_r^*(\omega) - \varepsilon_r(\infty)$, $v = i\omega\tau_0(\varepsilon_r^*(\omega) - \varepsilon_r(\infty))$ and $\varepsilon_r(0) - \varepsilon_r(\infty)$ remains constant. Therefore, the curve of the dielectric constant of the Debye model is a semicircle, and its intersection with the axis is $\varepsilon_r(0)$ and $\varepsilon_r(\infty)$, as shown in Fig. 1.5 (a).

2) Cole-Cole model

Some materials, such as ethyl alcohol and chlorinated biphenyl, do not conform to the theoretical semicircle predicted by the Debye model [61]. To address this limitation, K. S. Cole and R. H. Cole introduced a modification by incorporating an additional empirical constant, α, which ranges from 0 to 1. This parameter accounts for deviations from ideal Debye behaviour and allows for a more accurate calculation of dielectric properties across a wide frequency band.

$$\varepsilon_r^*(\omega) - \varepsilon_r(\infty) = \frac{\varepsilon_r(0) - \varepsilon_r(\infty)}{1 + (i\omega\tau_0)^{1-\alpha}} \tag{1.3}$$

In Fig. 1.5 (a), the resistance can be replaced by a complex impedance (Z), as illustrated in Fig. 1.5 (b). The angle between the vertical line of the semicircular locus and the real axis is given by $\alpha\pi/2$. Since this is an empirical formulation, a series of known dielectric constants at different frequencies must be used to determine the parameter α. In Fig. 1.5 (b), the vectors (u) and (v) satisfy the following relations:

$$u + v = u(1 + (\omega\tau_0)^{1-\alpha}) = \varepsilon_r(0) - \varepsilon_r(\infty) \tag{1.4}$$

The real and imaginary parts can be given by the Cole-Cole model:

$$\varepsilon_r'(\omega) = \frac{1}{2}[\varepsilon_r(0) - \varepsilon_r(\infty)] \cdot [1 - \frac{\sinh[(1-\alpha)\,x]}{\cosh[(1-\alpha)\,x] + \cos(\alpha\pi/2)}] \tag{1.5}$$

$$\varepsilon_r''(\omega) = \frac{1}{2}[\varepsilon_r(0) - \varepsilon_r(\infty)]\ \frac{\cos(\alpha\pi/2)}{\cosh[(1-\alpha)\,x] + \sin(\alpha\pi/2)}] \tag{1.6}$$

where $x = \ln(\omega\tau_0)$. Equations (1.5) and (1.6) can be turned into the Debye expression if $\alpha = 0$.

3) Quasi-optical model

C.M. Alabaster proposed a quasi-optical model for calculating skin dielectric constants at frequencies ranging from 60 GHz to 100 GHz [57]. When a plane wave illuminates a dielectric plate of thickness t_s, reflection, transmission and absorption occur on the dielectric plate. After many reflections and transmissions, the reflected and transmitted signals contain many patterns. The total reflected signal (r) and transmitted signal (t) are:

$$r = \frac{r_1 - r_1 \exp(-2k_s t_s)}{1 - r_1^2 \exp(-2k_s t_s)} \tag{1.7}$$

$$t = \frac{(1 - r_1^2)\exp(-k_s t_s)}{1 - r_1^2 \exp(-2k_s t_s)} \tag{1.8}$$

Where k_s is the propagation constant inside the skin, r_1 is the reflection coefficient on the skin surface, and r_1 and k_s are expressed by the dielectric constant of the skin:

$$r_1 = -\frac{\sqrt{\varepsilon_r} - \sqrt{\varepsilon_0}}{\sqrt{\varepsilon_r} + \sqrt{\varepsilon_0}} \tag{1.9}$$

$$k_s = k_0\sqrt{\varepsilon_r} \tag{1.10}$$

where k_0 is the propagation constant, and ε_0 is permittivity in free space.

1.3.3 THz Safety

Extensive studies have investigated the biological effects of THz radiation by exposing biomolecules, living cells, and various tissues or organs (primarily skin) to THz waves. In [62], the reported effects of THz radiation on different living cells were summarised. For example, human blood leukocytes exposed to pulsed THz waves in the 0.1 - 6.5 THz range, with a power intensity of approximately $200\ \mu W/cm^2$ for 20 minutes, showed no evidence of DNA damage. Human skin fibroblasts showed no observable effects after continuous exposure to 0.14 THz continuous-wave radiation at an intensity of $20-200\ mW/cm^2$ for 20 minutes, while exposure to 2.52 THz radiation at an intensity of $84.8\ mW/cm^2$ for 40 minutes led to a 10% reduction in the number of viable human skin fibroblasts. Overall, THz radiation can have a multitude of effects on animal cells, but low-power and low-frequency THz radiation has no detectable effect on cells. A literature review [63] highlights the potential of THz radiation for diagnosing skin cancer and treating various diseases. Research on the biological impact of THz waves typically distinguishes between thermal and non-thermal effects. The thermal effect refers to heating caused by the absorption of electromagnetic waves and is directly related to the power density of continuous-wave sources. However, THz waves generally exhibit limited heating capability [64]. For instance, exposure to a high-power 2.52 THz laser at a power density of $84.8\ mW/cm^2$ resulted in only a 3 ℃ temperature increase in cells, with virtually no additional temperature rise even after 80 minutes of exposure [65]. The non-thermal effects of THz radiation are linked to interactions with biomolecules through linear or nonlinear resonance. For instance, THz waves have been shown to affect deoxyribonucleic acid (DNA) by locally disrupting hydrogen bonds at the molecular level [66]. However, many such experiments are performed in solution and neglect intermolecular vibrational relaxation as well as solvent effects [67], since the THz resonance spectra of a given material differ significantly between crystalline and non-crystalline (solution) states. According to recent literature reviews [68], the influence of THz exposure on gene expression remains inconclusive: some studies suggest that it may enhance immune cells, while others report potential impairment of cellular components.

According to the most recent IEEE Standard for Safety Levels [69], on page 50, the local exposure dosimetric reference limits (DRLs) for the body surface at frequencies between 6 GHz and 300 GHz are specified as not exceeding an epithelial power density of $20\ W/m^2$ ($2\ mW/cm^2$) for individuals in unrestricted environments. Similarly, the whole-body exposure reference levels (ERLs) are limited to $10\ W/m^2$

($1\, mW/cm^2$) for frequencies between 2 GHz and 300 GHz in unrestricted environments.

Experimental studies in the frequency range of 100–300 GHz primarily rely on vector network analysers (VNAs) in conjunction with frequency extension modules. The output power levels of these frequency extension modules [70] for various waveguide bands are summarised in Table 1.1.

Table 1.1. VNAX Module Product Specifications [70]

Waveguide Band	Frequency (GHz)	Test Port Power (dBm, typ.)
WR 6.5	110-170	13
WR 5.1	140-220	6
WR 4.3	170-260	4
WR 3.4	220-330	1

The output power of the frequency extension modules is adjustable. The 1, 4, 6 and 13 dBm typical port power is approximately $1.3\, mW$, $2.5\, mW$, $4\, mW$, and $20\, mW$. Therefore, it is important to pay attention to the power density when using the WR 6.5 frequency extension modules. In [71], artificial human skin tissues are exposed to the $0.1\, \mu J$ THz and $0.024\, \mu J$ ultraviolet-A (UVA) pulses for comparison for 10 minutes, resulting in the changes in the expression of 397 and 290 genes, respectively. The THz beam focuses on a spot with a diameter of 1.5 mm. Roughly, the duration of the THz pulse is $1ps$. The repetition rate of THz pulses is 1 kHz. The average power is $0.1\mu J \times 1kHz = 0.1mW$, and the peak power is $0.1\mu J/1ps = 100kW$. The power density can be given:

$$\mathrm{S} = \frac{P}{A} \tag{1.11}$$

where P, A and S represent the power of the pulse, the illumination area and the power density of the THz pulse. The average power density and the peak power density are $1.4\, mW/cm^2$ and $1.4 \times 10^9\, mW/cm^2$. The peak power density of the THz pulses in this experiment is extremely high, and the calculation illustrates the significant role of power density in determining the impact of THz radiation on skin. Similarly, ultraviolet radiation can also alter cellular gene expression under high-power conditions [72]. Therefore, when evaluating the biological effects of THz waves on human tissue, power density is a critical factor. By contrast, low-power THz waves are considered safe and do not produce adverse biological effects.

1.4 THz Measurement System

Research methods for THz waves can broadly be classified into two categories: those analogous to electronic techniques and those analogous to photonic techniques. THz wave generation can be achieved through two primary approaches: solid-state electronics-based measurement systems and photonics-based measurement systems.

1.4.1 Solid-State Electronics-Based Measurement

The first is solid-state electronics–based generation, which extends microwave technology into the terahertz regime by employing frequency-multiplying techniques. This method typically involves a vector network analyser (VNA) architecture integrated with frequency extenders, signal generators, and signal analysers. The conventional configuration of a solid-state electronics-based measurement (SSEBM) system for antenna characterisation is shown in Fig. 1.6. The setup consists of a transmitting (Tx) and a receiving (Rx) unit, which can be arranged in several measurement configurations: direct far-field (DFF), indirect far-field (IFF), near-field (NF), or midfield (MF) setups [73]. These configurations differ according to the separation distance between the Tx and Rx antennas. The antenna under test (AUT) is connected to the Tx module on the transmitting side. The Tx/Rx modules enable both transmission and reception for vector network analyser (VNA)-based measurements. The main parameters of interest for the AUT include the return loss $|S_{11}|$, gain, half-power beamwidth (HPBW), sidelobe level (SLL), and cross-polarisation level (X-pol). Due to the complexity of THz beam measurement platforms—for example, the configuration of the frequency extender—the front-to-back ratio (FBR) of THz antennas is rarely measured. The VNA directly measures the return loss $|S_{11}|$, while the antenna gain is typically obtained by comparing the measured data with that of a standard horn antenna. However, measurement setups based on a generator–analyser approach are unable to measure $|S_{11}|$.

Due to the high atmospheric absorption of THz waves, antenna main-beam measurements in the THz range do not always require an anechoic chamber. However, for high-precision measurements, the use of an anechoic chamber, precise positioning systems, and advanced data-processing algorithms remains essential.

A variety of measurements require the use of frequency extenders, including antenna characterisation, on-wafer testing, material property evaluation, and wireless communication experiments. At present, THz measurement systems can be categorised into four main configurations: direct far-field (DFF) [74], indirect far-field (IFF) [75], [76], near-field (NF) [77], and on-wafer setups [78] as illustrated in Fig. 1.7.

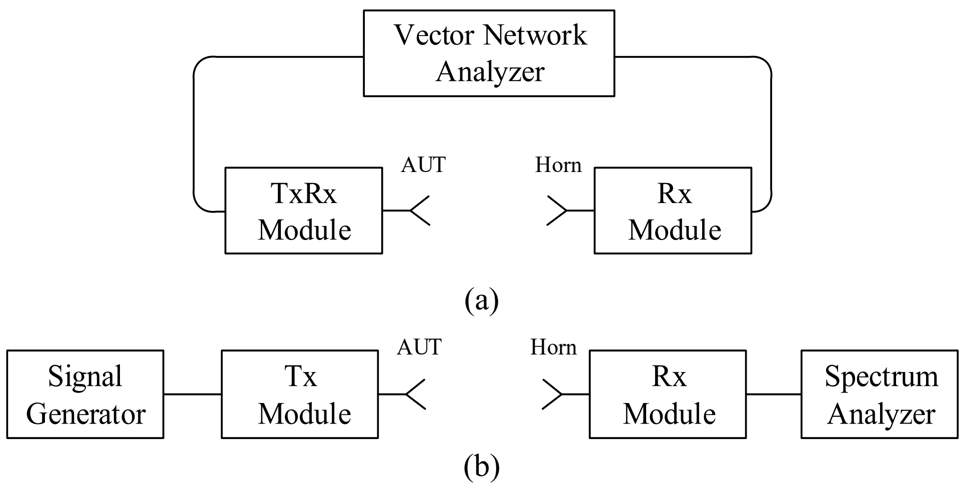

Fig. 1.6. The basic schematic diagram of the SSEBM systems: (a) VNA measurement, (b) Spectrum analyser measurement.

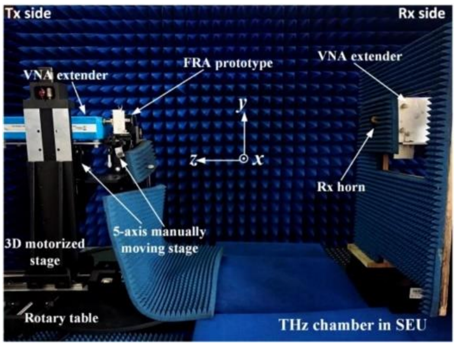

(a)

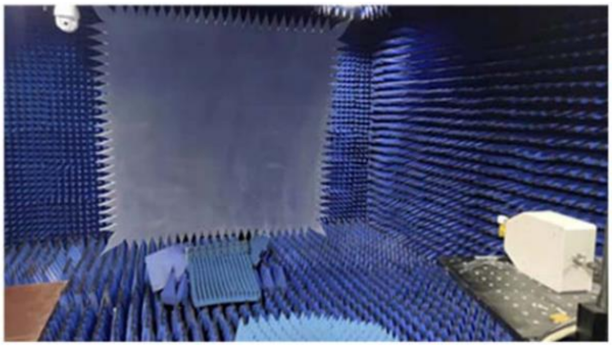

(b)

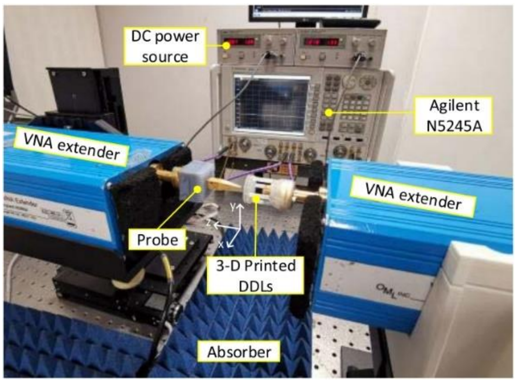

(c)

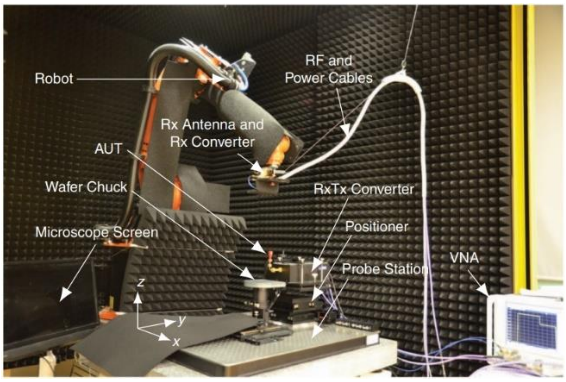

(d)

Fig. 1.7. Photos of the THz measurement systems: (a) Terahertz antenna measurement setup in the anechoic chamber [74]; (b) Serrated edge reflector CATR measurement system [76]; Terahertz near-field measurement setup [77]. On-wafer measurement by using a robotic arm [78].

The Tx and Rx frequency extension modules are typically frequency extenders. Each extender consists of several key components, including isolators, amplifiers, frequency doublers or multipliers, and harmonic mixers. The frequency mixer [79] plays a crucial role in both frequency upconversion and downconversion, featuring two input ports and one output port. In the upconversion process, the two input ports correspond to the intermediate-frequency (IF) and local-oscillator (LO) signals, while the output port corresponds to the radio-frequency (RF) signal. Ideally, the RF output contains the sum and difference frequencies of the IF and LO signals. For downconversion, the RF signal is mixed with the LO signal, producing an IF output whose frequency equals the difference between the RF and LO frequencies, as illustrated in Fig. 1.8. In principle, a mixer or a frequency multiplier can function as a frequency extender; however, modern electromagnetic measurement systems require high-performance extenders with key parameters such as output power, frequency stability, and dynamic range.

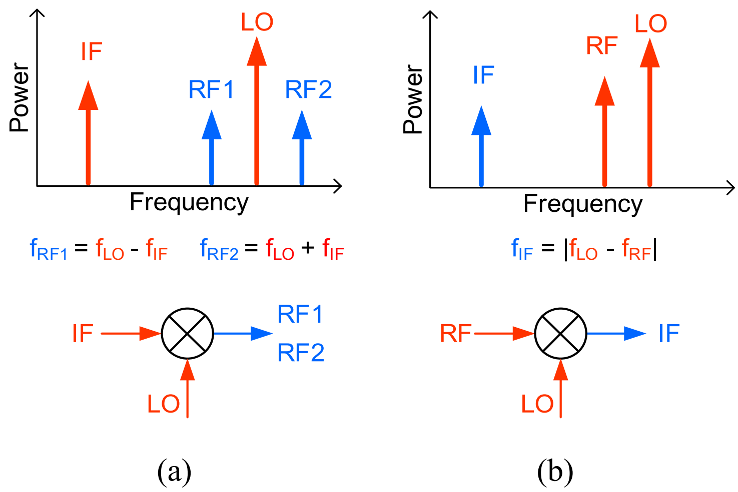

Fig. 1.8. Principles of (a) Frequency upconversion, (b) Frequency downconversion [80].

1.4.2 Photonic-Based Measurement

The second is photonic-based generation, which relies on the photomixing technique, where laser beams are down-converted using an electro-optic (EO) crystal. Representative devices employing this approach include terahertz time-domain spectroscopy (THz-TDS) systems, photomixers, and photoconductive antennas (PCAs). The basic configuration of a photonic-based measurement (PBM) system for THz waves is shown in Fig. 1.9. The setup consists of laser sources, a power divider (PD), two optical paths, an emitter, and a detector. PBM systems can detect either THz pulses or continuous waves (CW), depending on the type of laser used. In this arrangement, the optical path directed toward the emitter generates THz radiation using PCAs or optical-to-electrical (O/E) converters, while the path leading to the detector provides synchronisation between the optical and THz signals. However, due to the nature of the laser excitation and detection scheme, PBM systems are generally unable to measure the reflected power from the sample under test.

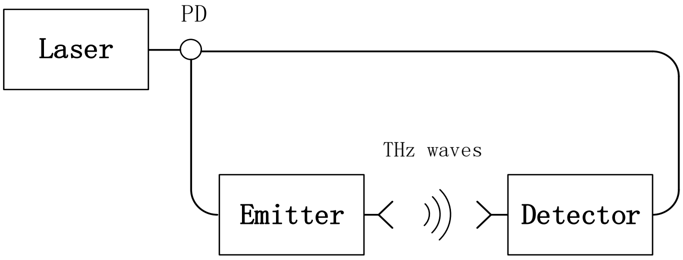

Fig. 1.9. The basic schematic diagram of the PBM systems

THz-TDS system [81] has become an important technique in fields such as chemistry, materials science, and imaging. As illustrated in Fig. 1.10, a PCA biased with a DC voltage converts laser pulses into THz pulses. By employing pump-probe technology [82], the waveform of the THz pulse can be measured. Applying the Fourier transform to this waveform converts it into the frequency domain, thereby obtaining the THz spectrum over the range of approximately 0.1 - 3 THz. The overall configuration of a THz-TDS system [83] is shown in Fig. 1.10. The system contains two optical paths that must remain synchronised in time, which constrains the distance between the emitter and the detector. Consequently, THz-TDS is seldom used for radio-frequency (RF) antenna measurements, where larger spatial separations are typically required.

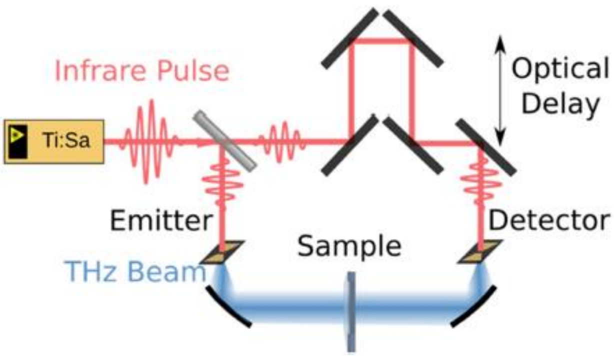

Fig. 1.10. Schematic of a THz-TDS setup [83]. Ti:Sa means a femtosecond Ti:Sa laser.

PCAs are widely used in THz-TDS systems as key components for THz emission. However, they cannot be directly connected to antennas under test (AUTs) for CW measurements. To achieve O/E conversion suitable for CW generation, a uni-travelling-carrier photodiode (UTC-PD) [84], [85] is typically employed. As shown in Fig. 1.11, two laser beams with different frequencies (f_1 and f_2) are combined by an optical coupler and directed into the photodiode. The photodiode then generates a radio-frequency (RF) signal at the difference frequency $f_1 - f_2$, a process known as optical heterodyning [86]. This technique provides a simple and cost-effective means to achieve wide frequency tunability, covering a range from gigahertz to terahertz. However, a notable drawback is the relatively poor frequency stability of the generated RF signals compared with electronic sources.

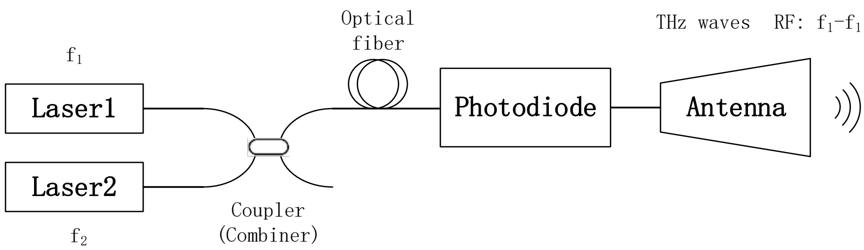

Fig. 1.11. THz wave generation by optical heterodyning.

Early THz systems detected THz waves using photoconductive switches for THz pulse measurement. As shown in Fig. 1.12, a PCA combined with an external circuit functions as a photomixer for THz wave detection [87].

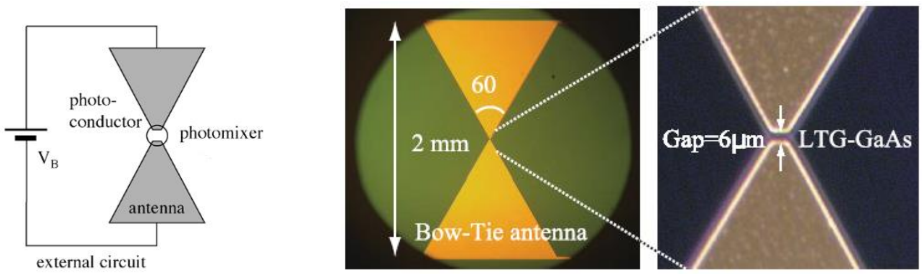

Fig. 1.12. (a) Schematic of a photomixer for CW-THz wave generation [87], (b) Photos of an LTG-GaAs-based photoconductive antenna [88]. LTG: low-temperature-grown

In Fig. 1.13, the EO probe consists of a high-reflection (HR) mirror, EO crystal, and gradient-index (GRIN) lens connected to the polarisation-maintaining fibre (PMF). The EO probe can be divided into five types [89]. The HR mirror has a high reflection coefficient for the optical beam. It can reflect all the optical beams, but cannot reflect the EM waves. The EM waves interact with the LO optical beams in the EO crystal so that the EO modulation occurs. The E-fields' amplitude and phase information are transferred to the LO optical beams because the refractive index of the EO crystal changes with the applied E-field. When measuring the E-field, the polarisation of the E-field needs to be parallel to the optic axis of the EO crystal.

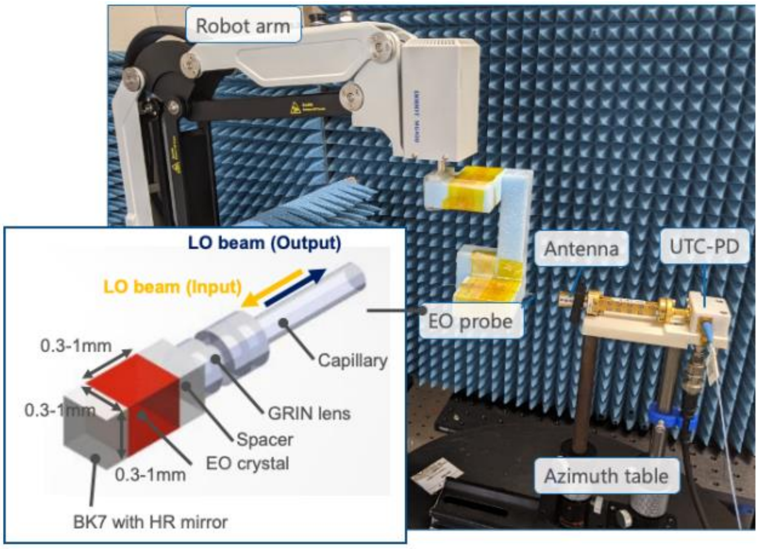

Fig. 1.13. EO probe with a robot arm. A WR-3.4 rectangular horn antenna is being tested. GRIN lens: graded index lens, HR mirror: high reflection mirror, BK7: BK-7 glass, an optical borosilicate crown glass [90].

In 2022, photonic technology was introduced into antenna measurement systems, as illustrated in Fig. 1.13. A planar and cylindrical scanning THz NF measurement setup was developed at Gifu University [90], employing a robotic arm. The system operates over a frequency range from 1 GHz to 600 GHz. The photonic techniques used include EO sensing [91], non-polarimetric frequency down-conversion [92], and self-heterodyne detection [88]. Compared with conventional metallic probe antennas, the EO probe head is extremely compact, with a realisable aperture size of $0.2\ mm \times 0.2\ mm$. As the probe is fabricated from crystalline materials such as GaAs or $LiTaO_3$, its influence on the measured field is negligible in near-field measurements, ensuring low invasiveness. Additionally, the EO probe is very lightweight, avoiding mechanical deflection when scanned by a robotic arm. The detected signal is transmitted through low-loss, flexible optical fibres, allowing flexible and precise probe scanning. Finally, the system achieves a much wider operational bandwidth without the need to replace the EO probe.

1.4.3 Comparison Between the Solid-State Electronics-Based and Photonic-Based Measurement

The main difference between the two methods lies in how THz waves are generated and detected. Although further improvements in operating frequency are still needed, solid-state electronics-based measurement (SSEBM) systems represent relatively mature technology. They are well established and can be customised to meet specific experimental requirements. In contrast, photonic-based measurement (PBM) systems are more recently developed and remain an emerging technology, offering greater potential for future advancements in measurement bandwidth and precision. Table 1.2 summarises the parameters and capabilities of SSEBM and PBM setups for comparison. In SSEBM systems, the operating frequency is determined by the frequency extenders, with detailed specifications available from the manufacturer. For SSEBM systems, nearly all frequency extenders use waveguide interfaces as their feed ports. In contrast, PBM systems employ a UTC-PD to feed a waveguide antenna directly. In the THz band, a ground–signal–ground (GSG) probe can also be connected to a waveguide through a converter; therefore, this configuration is likewise considered a waveguide-fed system. The UTC-PD has the output power of -14 dBm at 286 GHz [93], and the radiated power of the THz wave in [94] was 650 μW (about -1.87 dBm) at 125 GHz, which contains the gain of a horn antenna. By comparison, according to data from the VDI Mini extension modules, the typical test port output power was 18 dBm in the frequency band of 110 - 170 GHz, while output power in the frequency range from 220 to 330 GHz was 6 dBm. Regarding the radiated power, the PBM system has the potential to realise the DFF and IFF tests. The PBM systems utilise fibres to transmit signals, which have more advantages than RF cables, including lower loss, flexibility, and line length. Dynamic range is the ratio between the largest and smallest values that a certain power can be detected, which is an essential performance for antenna measurement systems.

As for the SSEBMs, a probe-based millimetre-wave antenna measurement system [95] has a dynamic range of more than 60 dB at 50 to 110 GHz. The dynamic ranges for return and insertion losses are better than 20 and 35 dB at 325 to 508 GHz [96], and the dynamic ranges of the frequency extender [97] reach 60 to 80 dB from 1.1 THz to 1.5 THz. On the other hand, the EO probe in [89] is expected to have a 120 dB dynamic range, while the PBM system in [92] has a dynamic range of approximately 40 dB.

TABLE 1.2. A COMPARISON BETWEEN SSEBM AND PBM

Performance	SSE-based Measurement	Photonic-based Measurement
Frequency (GHz)	110-170 170-260 260-400 330-500 500-750 750-1100	1-600
Feed Interfaces	Waveguide fed	Waveguide fed
DFF Test	√	×
IFF Test	√	×
NF Test	√	√
3D Radiation Pattern	√	√
Gain Measurement	√	√
Return Loss Measurement	√	×
Amplitude Measurement	√	√
Phase Measurement	√	√
D-band Output Power	13 dBm	-
J-band Output Power	6 dBm	-14 dBm
Scanning Range	±90°	±50°
Transmission Line	RF cables	Fibres
Cost	High	Moderate
Reference	[70], [74]-[78]	[88],[90], [93], [94]

1.5 Conclusion

In summary, this chapter first introduced the background and fundamental properties of THz waves. Owing to these properties, THz technology shows strong potential across various application areas. The two major fields discussed in detail are wireless communications and biomedical sensing. Based on a review of recent academic studies, metasurface lens antennas (MLAs) or transmitarray antennas (TAAs) were identified as promising candidates for future wireless communication applications; a detailed literature review of these antenna types is presented in the next chapter. For biomedical applications, the focus was placed on THz-based skin cancer detection, with supporting discussions on skin structure and THz safety considerations. Finally, THz measurement systems were introduced. As THz waves can be generated using two main methods, solid-state electronics-based measurement (SSEBM) and photonic-based measurement (PBM), both systems were compared in terms of structure and capability. Unlike conventional low-frequency measurements conducted in anechoic chambers, THz measurement systems remain less mature, and a comprehensive understanding of their operating principles is essential for conducting accurate THz experiments.

Chapter II Literature Review

2.1 Introduction

This chapter introduces the various metasurfaces and skin cancer detection methods because the content of this thesis mainly focuses on the design of these two aspects. Metasurface lenses and sensors can be used in the skin imaging system.

Metasurfaces have emerged as an innovative platform for manipulating electromagnetic waves. They are artificially engineered flat structures composed of subwavelength unit cells (UCs), typically arranged in a periodic pattern resembling a checkerboard, as illustrated in Fig. 2.1. The UCs can realise multiple functions, such as phase shifting [98], magnitude changing [99], polarisation conversion [100] and frequency selecting [101]. The UCs can be arranged using several formulas, and the arrangement of the UCs is referred to as “phase distribution” because the amount of phase shifting of each UC is different in the metasurface. Metasurface is a broad concept that includes transmitarray [102], [103], lens[104], [105], reflectarray [106], [107], absorber [108], [109], frequency selective surface [110], [111], and sensor [112],[113]. Some functions of the MS depend on the function of the UC, and others rely on the phase distribution (PD). According to the formulas of the PD, the metasurface can achieve various functions, including gain enhancement [114], multibeam [115], beam-steering [116], abnormal reflection and refraction [117], focusing [118], orbital angular momentum (OAM) [119] and holography [120].

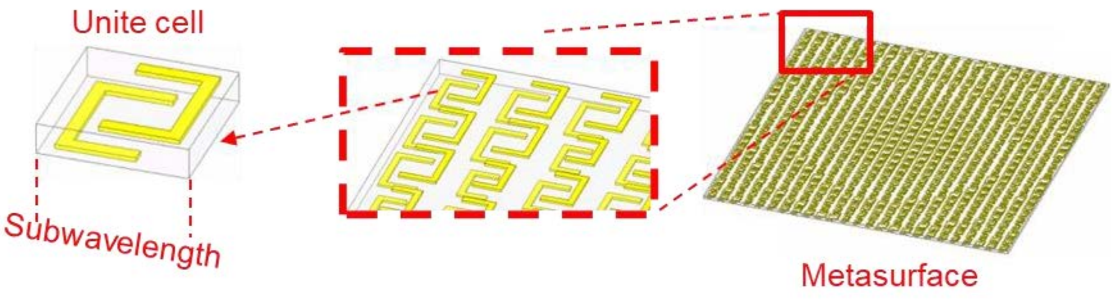

Fig. 2.1 Schematic of the metasurface.

There are various types of UCs operating in the terahertz (THz) band. The main limitation of THz metasurfaces lies in their fabrication process. The size of a metasurface UC is typically less than half the wavelength of its operating frequency. In the THz band, this small feature size poses significant challenges for manufacturing precision. The lowest frequency range of the THz band is the D-band, spanning 110 - 170 GHz, corresponding to half-wavelengths between $1.36\,mm$ and $0.88\,mm$. By comparison, standard printed circuit board (PCB) technology [121] can achieve a minimum metal line width of approximately $0.1\,mm$ and a minimum via-hole diameter of about $0.2\,mm$. Therefore, the design of THz metasurface UCs must remain relatively simple to ensure manufacturability and minimise fabrication errors.

Skin cancer detection is based on the difference between the cancerous and normal tissue. Water content in cells can provide the most obvious discrepancy under electromagnetic (EM) waves [122]. As for EW waves, the detection methods can be categorised into two groups based on the EM wave generation approach: vector network analyser (VNA) and THz time-domain spectroscopy (THz-TDS). VNA-based methods primarily utilise detection probes, as VNAs typically generate low-frequency waves with long wavelengths. More details will be introduced later. The probe tips effectively concentrate these waves into a small area, enabling the detection of small cancerous tissues. TDS-based methods rely on the spectral analysis of cancerous tissues, as THz-TDS systems operate over a broad frequency range, providing rich information for identifying cancerous tissues. THz-TDS systems operate at a higher frequency with higher resolution, making them suitable for imaging.

2.2 Metasurface Lens

2.2.1 All-Dielectric Unit Cell

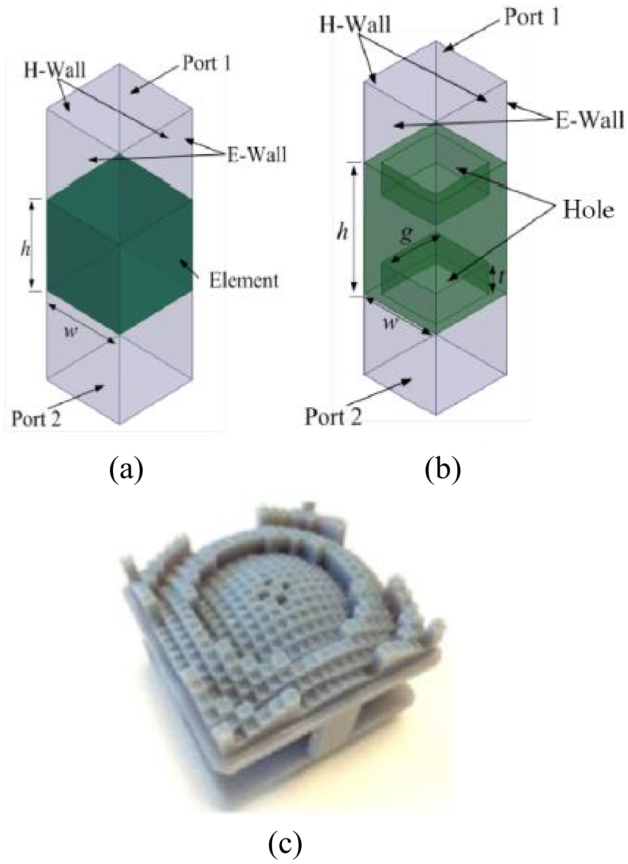

Fig. 2.2 Simulation model of the all-dielectric UC [123]. (a) Normal dielectric UC. (b) Dielectric UC with antireflection (AR) structures. (c) Discrete dielectric lens using the dielectric UC with AR.

The all-dielectric UC can constitute a discrete dielectric lens (DDL), as shown in Fig. 2.2 (a). Different from the traditional glass or dielectric thick lens, which is based on the ray-tracing formula, DDL is based on Fermat's principle and is easy to design. In the simulation, primary and secondary boundary conditions are used to mimic an infinite array. The phase-shifting performance relies on the shorter wavelength in the dielectric medium than in the air. The dielectric post consists of a part of air and a part of dielectric material, which can increase the transmission phase delay by increasing the dielectric material and reducing the air. The transmission phase of the UC can realise a 360° phase cycle. Therefore, the DDL is thin compared to the traditional thick lens, but the operating frequency bandwidth is narrower. In [123], an antireflection (AR) structure is used to alleviate the reflection of the UC, as shown in Fig. 2.2 (b). The difference in dielectric constant between medium and air is relatively large, and a dielectric material with an air hole, the AR structure, can be equivalent to a dielectric material with a smaller dielectric constant. The AR structure can work as a transition layer because the difference in the dielectric constant between the air and the transition layer becomes smaller.

The AR structure can be a pyramid shape [124]. By adding a circularly polarised (CP) polariser [125] or an elliptical cylinder dielectric resonator [126], the DDL can realise the linear polarisation to CP conversion. In [127], a dielectric UC with a multilayer structure can be used to design a dual-band reflectarray. Using a dielectric UC with an air through-hole can be a DDL operating at the millimetre wave band [128]. The all-dielectric UC can be used to design a THz metasurface lens [129]. In [130], by using a fused deposition modelling (FDM) 3D printer, the all-dielectric UC is used to design a 0.14 THz polarising beam splitter, with the UC period of $1\ mm$. In [131], a 0.3 THz DDL is fabricated using a stereo lithography appearance (SLA) 3D printer, with the UC period of $0.5\ mm$.

2.2.2 Fabry-Perot Unit Cell

The Fabry-Perot (FP) UC [132] is shown in Fig. 2.3, which consists of the upper and lower orthogonal gratings and a $45°$-tilted intermediate metal layer. The FP UC can realise the linear polarisation conversion from X to Y polarised wave in Fig. 2.3 (a). The X-polarised wave can pass through the lower grating. The $45°$-tilted intermediate metal layer can divide the incident wave into X and Y components. The Y component then passes through the upper grating, while the upper grating reflects the X component. The reflective X component is divided into two components by the intermediate layer. After the multiple reflections between two gratings, the incident X-polarised wave converts into a Y-polarised wave [133]. The intermediate layer can determine the transmission phase and the operating frequency bandwidth of the FPUC. The intermediate layer can be of various shapes: split-ring resonator [134], cross-bar [135], rectangle [136], and so on. Due to its excellent phase-shifting performance, simple structure and ease of fabrication, the FPUC can be used to design the THz metasurface for various applications. In [137], the FPUC performs broadband from 80 GHz to 220 GHz. In [138], the operating frequency of the FPUC is up to H-band, ranging from 225 GHz to 325 GHz.

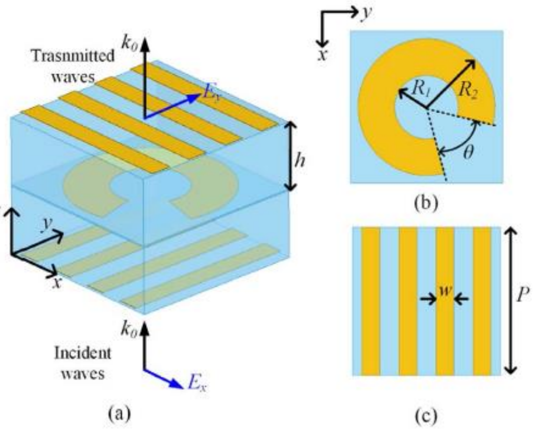

Fig. 2.3 Simulation model of the FPUC [132]. (a) Oblique view. (b) Intermediate metal layer. (c) Upper and lower grating.

2.2.3 Frequency Selective Surface Unit Cell

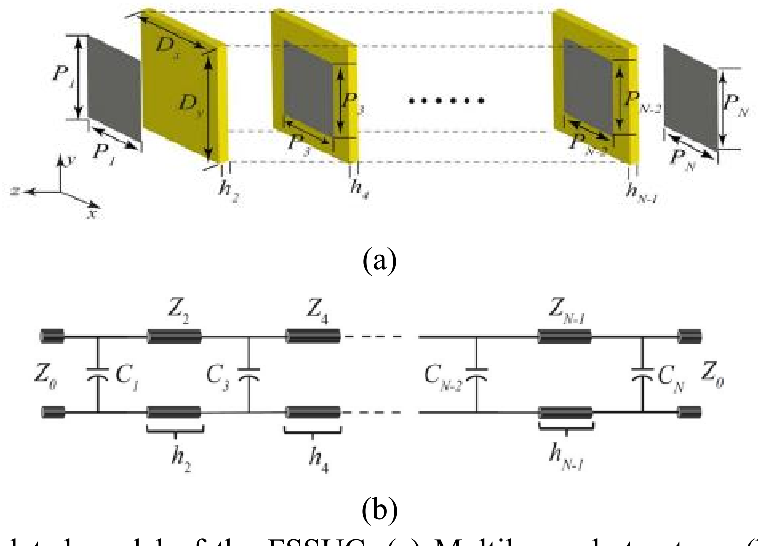

Fig. 2.4 Simulated model of the FSSUC. (a) Multilayered structure. (b) Equivalent circuits [139].

The frequency selective surface unit cell (FSSUC) [139] is illustrated in Fig. 2.4.

Its multilayered configuration is well suited to conventional printed circuit board (PCB) fabrication. The fundamental principle of the FSSUC is based on impedance matching with free space, which has an impedance of approximately $377\ \Omega$. The multilayered structure can be represented by an equivalent circuit model, where adjacent metal patches act as capacitors and the dielectric substrates between them function as transmission lines. By optimising the geometry of the metal patches, the FSSUC can be designed to match the free-space impedance and control the transmission phase of electromagnetic waves passing through it. The phase-shifting capability of the FSSUC depends on the frequency-dependent response of its layers, and as a result, its overall bandwidth is limited [140]. In [141], a three-layer FSSUC composed of concentric circular rings operates at 5.5 GHz. A conformal three-metal-layer FSSUC reported in [142] achieves a structural height of only $0.04\ \lambda_0$ at 25 GHz. In [143], an FSSUC with one dielectric layer and two metal layers utilising cross-shaped patches demonstrated gain enhancement. Variations of FSSUC metal patterns include the Jerusalem cross [144], Malta cross with vias [145], and hexagonal shapes [146]. Due to its simple and manufacturable design, the FSSUC can be effectively implemented in the D-band, covering frequencies from 110 GHz to 170 GHz [147].

2.2.4 Huygens Unit Cell

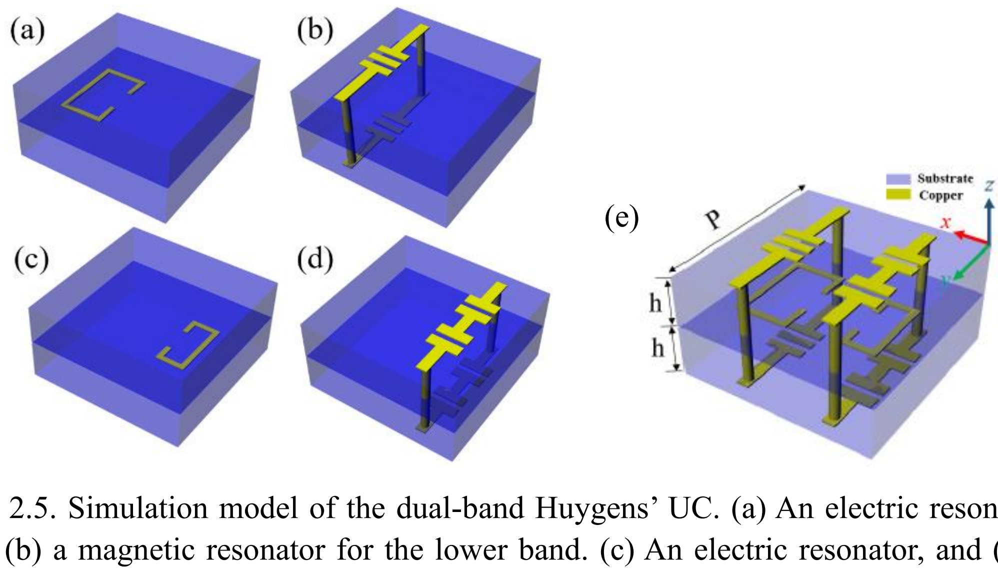

Fig. 2.5. Simulation model of the dual-band Huygens' UC. (a) An electric resonator, and (b) a magnetic resonator for the lower band. (c) An electric resonator, and (d) a magnetic resonator for the lower band. (e) Oblique view of the HUC [148].

The basic structure of a Huygens' unit cell (HUC) consists of an electric resonator and a magnetic resonator [148], as shown in Fig. 2.5. These resonators generate orthogonal induced electric and magnetic currents [149]. The resulting currents can be characterised by the electric surface admittance and magnetic surface impedance. Consequently, the HUC can be designed to match the free-space impedance and, in theory, achieve a reflectionless surface [150]. There are two fundamental types of HUCs, as illustrated in Fig. 2.6: the wire-loop unit cell and the multilayered shunt-admittance unit cell [151].

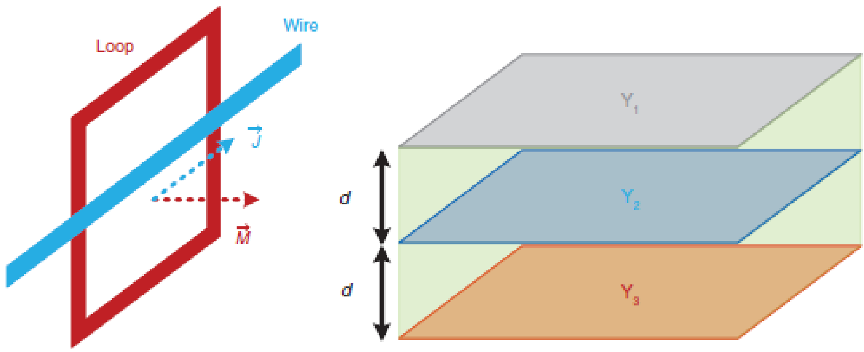

(a) (b)

Fig. 2.6. Schematics of the Huygens' UC. (a) the wire-loop UC. (b) the multilayered shunt-admittance UC [151].

The major advantage of the HUC is easy-to-fabricate. They can be fabricated using a single layer of dielectric substrate with two metal layers [152], [153]. Therefore, it can be used to design a THz frequency band metasurface [154]. However, its phase-shifting performance is based on the resonance shift, and the transmission phase is nonlinear [155] over the frequency band, and thus, the bandwidth of the HUC tends to be narrow.

2.2.5 Transmitting and Receiving Unit Cell

The basic structure of a transmitting–receiving unit cell (Tx–Rx UC) [156] is shown in Fig. 2.7. It consists of a receiving (Rx) antenna, phase-delay lines, and a transmitting (Tx) antenna. The Rx antenna captures incident EM waves and converts them into electrical signals, which then propagate through the phase-delay line. This line provides the required phase-shifting functionality before the Tx antenna re-radiates the EM waves.

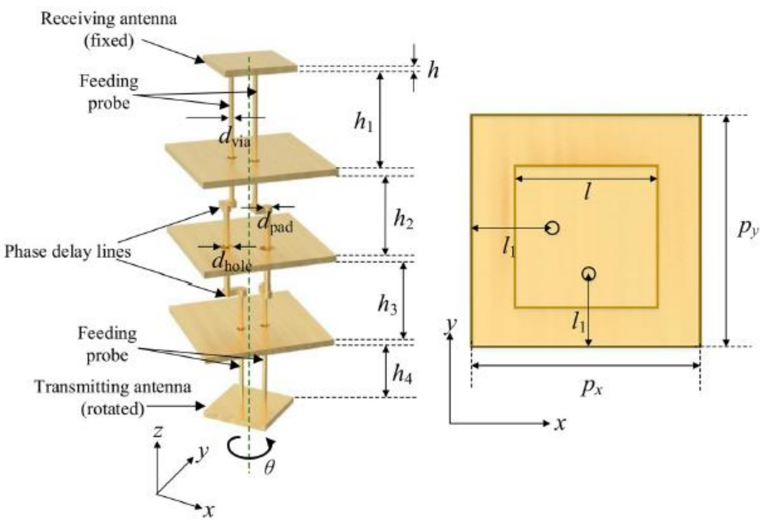

Fig. 2.7. Simulated model of the Tx-Rx UC using two phase delay lines [156].

The Tx–Rx UC exists in many configurations, as it can be inspired by different antenna types and microwave circuit concepts. Its phase-shifting mechanism is straightforward and intuitive, making it relatively easy to achieve a full 360° phase coverage. By varying the antenna design, the Tx–Rx UC can realise diverse functions, such as arbitrary polarisation conversion [156]. The Tx and Rx antennas can take various forms, including dipole antennas [157], magnetoelectric (ME) dipole antennas [158], dual-polarised patch antennas [159], and circularly polarised antennas [160]. In [161], dual-band performance was achieved by interlacing high-frequency and low-frequency UCs. In [162], a substrate-integrated waveguide (SIW) was used as the phase-delay line, operating at 140 GHz. Reconfigurability can be introduced by incorporating p-i-n diodes and a control circuit [163]. However, using a large number of p-i-n diodes increases cost, and few diodes operate effectively at higher frequencies; thus, reconfigurable UCs are currently unsuitable for sub-THz applications. The key limitations in designing Tx–Rx UCs stem from fabrication constraints, including dielectric material losses, machining precision, design complexity, and electromagnetic coupling between adjacent UCs.

2.3 Metasurface Sensor

2.3.1 Refractive Index Sensor

The refractive index metasurface sensor is composed of multiple resonators, each of which can be modelled using an equivalent circuit model (ECM) [164]. ECM has been widely employed in the analysis of microwave and terahertz metasurfaces to interpret their amplitude and phase responses. Because the EM response of the metasurface can be measured and observed using a vector network analyser (VNA), any change in the measured response indicates a corresponding change in the capacitance value of the equivalent circuit. Since capacitance is strongly correlated with the dielectric constant of the surrounding material, variations in the dielectric constant can thus be detected. This establishes a relationship between the dielectric properties of a material (microscale) and the measurable EM response of the metasurface sensor (macroscale). Fig. 2.8 (a) shows a representative metasurface resonator [165], the split-ring resonator (SRR). When EM waves are incident on the metasurface, the induced current oscillates within the ring, as illustrated in Fig. 2.8 (b). A strong electric field is concentrated in the gap of the ring, as shown in Fig. 2.8 (c), making the structure highly sensitive to the dielectric constant of any material present in that gap.

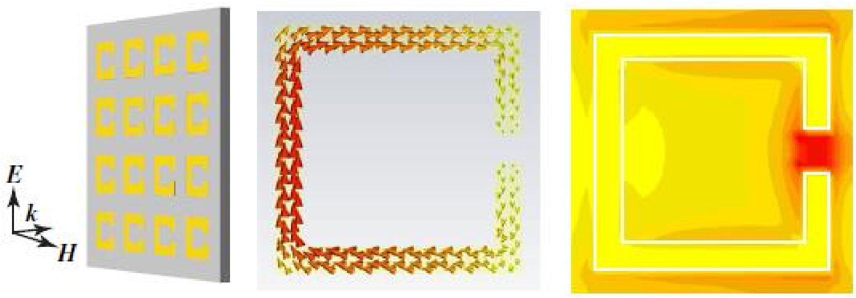

(a) (b) (c)

Fig. 2.8. Metasurface of split-ring resonators (SRRs). (a) An array of SRRs with an incident electromagnetic wave (EM-wave). (b) Induced surface current on SRR. Induced electric field distribution around the SRR [165].

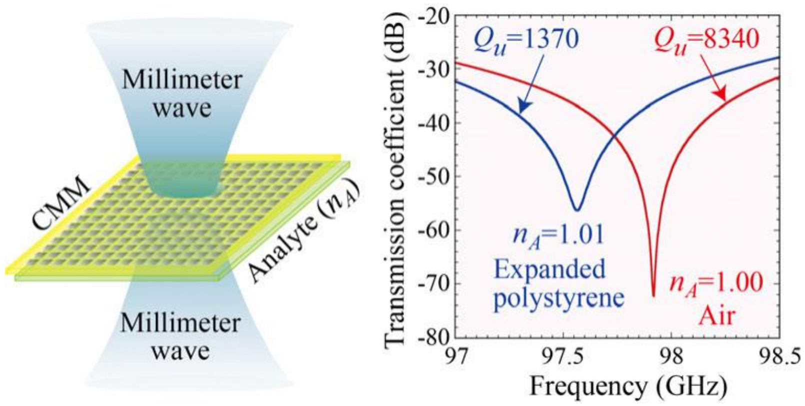

(a) (b)

Fig. 2.9. Metasurface sensing for the refractive index of the analyte. (a) Schematic of the sensing process. (b) Detected transmission coefficients with various refractive indexes [167]. CMM: capacitive metal mesh (CMM).

Sensitivity and figure of merit (FOM) are important parameters to evaluate the performance of the metasurface sensor [166]. In order to explain these parameters, Fig. 2.9 (a) shows the experiment environment of a metasurface sensor [167]. The analyte is a layer of the dielectric plate, referring to the material under test. When the refractive index of the analyte changes, the transmission coefficient changes accordingly, as shown in Fig. 2.9 (b). The resonance frequency point shifts from 97.5 GHz to about 98 GHz. The sensitivity (S) and the FOM of the metasurface can be given as [168]:

$$\mathrm{S} = \Delta f / \Delta n \tag{2.1}$$

$$\mathrm{Q} = f / \mathrm{FWHM} \tag{2.2}$$

$$\mathrm{FOM} = \mathrm{S} \times \mathrm{Q} \tag{2.3}$$

where Δf and Δn are the variation in the resonance frequency and refractive index, f and FWHM represent the resonance frequency and the full width at half maximum, Q refers to the quality factor, the units of the S and Q are GHz/RIU and RIU^{-1}. There are various types of metasurface sensors. Some are based on RLC resonance and fabricated using PCB technology [169], while others rely on surface plasmon resonance using plasmonic materials such as $LiTaO_3$ [170], graphene [171]. In addition, all-dielectric metasurface sensors employing high-refractive-index materials have been developed to minimise losses associated with plasmonic materials [172], [173]. In [174], it was reported that applying an electrical voltage to an ion gel covering a graphene metasurface enhances both its sensitivity and tunability. Owing to their ease of fabrication, metasurface sensors can effectively operate in the THz frequency band [175], as shown in Fig. 2.10.

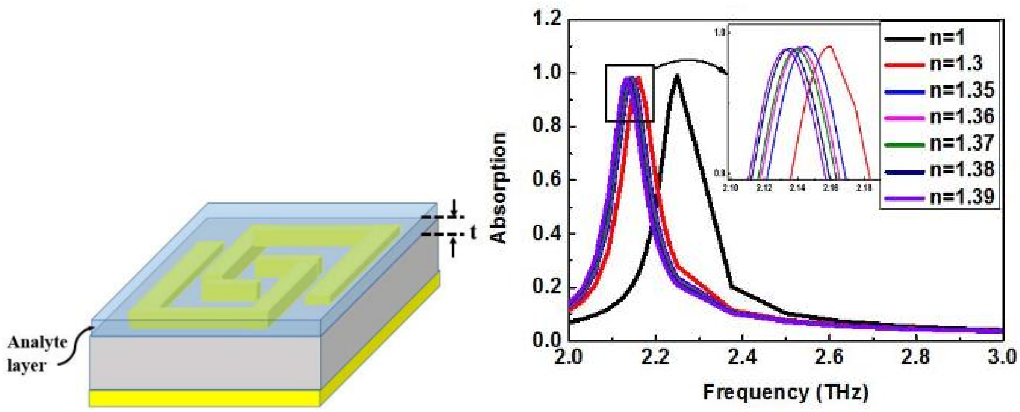

(a) (b)

Fig. 2.10. Terahertz metasurface sensor. (a) Simulation model of the unit cell. (b) Simulated absorption with various refractive indexes [175].

In [176], a cross-shaped absorber is presented, as shown in Fig. 2.11. It is composed of a silicon substrate and two aluminium layers. Induced charges accumulate at both ends of the conductive patch, forming an electric field that interacts with the analyte layer. This interaction causes a frequency shift, attributed to the shorter effective wavelength within the medium. The dual conductive-layer configuration enables the design of a narrowband, near-perfect metamaterial absorber with a high quality (Q) factor. A higher Q-factor corresponds to a sharper absorption spectrum, meaning that even small frequency shifts in the absorption peak can be more easily detected.

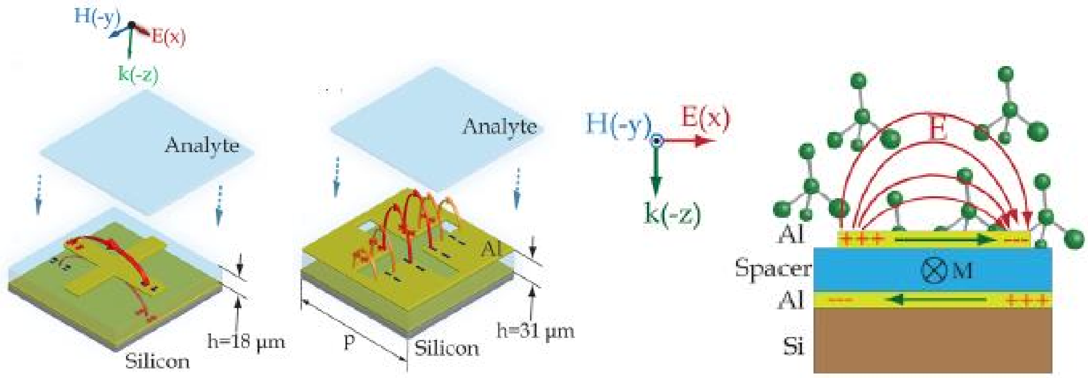

(a) (b) (c)

Fig. 2.11. (a) Cross-shaped absorber and (b) Complementary cross-shaped absorber. (c) Schematic of the electric field across the analyte layer [176].

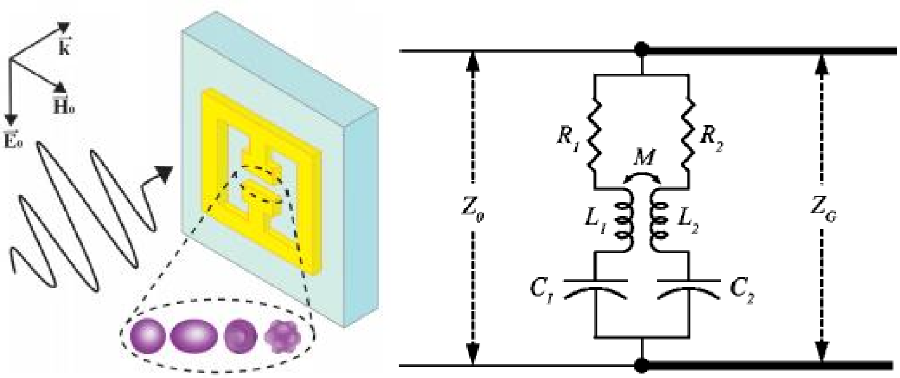

(a) (b)

Fig. 2.12. (a) Modified split-ring resonator (MSRR) for the sensing application [177]. (b) Corresponding equivalent RLC circuit [178].

As shown in Fig. 2.12 (a), the material under test [177] is placed in contact with the capacitor located at the centre of the structure. The metasurface comprises a single conductive layer and a dielectric substrate, and its transmission coefficient is measured. The electric field of the incident wave is oriented perpendicular to the gap of the central capacitor, which enhances the electric field concentration within the gap and thereby increases the sensor’s sensitivity. The corresponding equivalent circuit [178] is shown in Fig. 2.12 (b). The impedance of free space, Z_0, is approximately 377 Ω, and the metasurface resonator can be represented as a transmission-line junction. The Q-factor can be improved by narrowing the linewidth without altering the resonance frequency. However, when the edges of the metallic ring approach too close to the central capacitor, the assumptions of the equivalent circuit model no longer hold, leading to deviations between simulation and theoretical prediction.

Attenuated total reflection (ATR) using a metasurface sensor [179] is implemented with a silicon prism positioned beneath the structure, as shown in Fig. 2.13. The prism is incorporated to achieve total internal reflection (TIR), which enhances the sensitivity of the metasurface sensor. The reflection coefficients are measured and exhibit a reduction within a certain frequency range due to the presence of evanescent fields. At an incident angle of 55°, evanescent fields generated by TIR re-radiate along the boundary of the split-ring resonator (SRR) [180], as illustrated in Fig. 2.14. Under normal circumstances, very little electromagnetic energy penetrates through the metasurface into the air during total internal reflection, resulting in low background noise and improved signal-to-noise ratio in such measurement configurations.

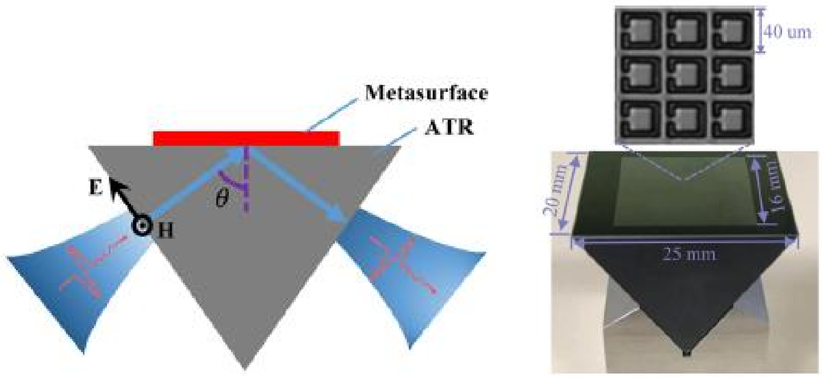

(a) (b)

Fig. 2.13. (a) Schematic of the ATR measurement process. (b) Structure of the metasurface with a prism [179].

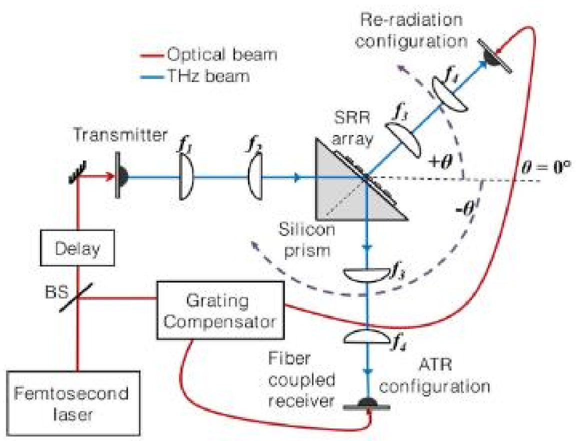

Fig. 2.14. Measurement setup for the evanescent field re-radiation [180].

Fano resonance, first proposed in 1961 [181], gives rise to a phenomenon known as electromagnetically induced transparency (EIT), which is often studied in quantum mechanics. EIT describes a narrow transmission window where an otherwise opaque medium becomes transparent to light due to quantum interference effects [182]. The narrow transmission band corresponds to a high Q-factor, and the resonance behaviour provides strong sensitivity to environmental changes, making EIT highly suitable for sensing applications [183].

In the context of electromagnetic waves, the EIT-like effect is achieved through the coupling of “bright” and “dark” mode resonators [184], as shown in Fig. 2.15(a). The “bright” mode resonator interacts directly with the incident electromagnetic wave from free space, exhibiting a broadband response with a relatively low Q-factor. In contrast, the “dark” mode resonator does not directly couple to the incident wave but interacts strongly with the “bright” mode within a certain frequency range, producing a narrowband, high Q-factor response. As illustrated in Fig. 2.15 (b), when an X-polarised wave is incident on the metasurface, currents are primarily concentrated along the vertical segments of the square ring, indicating that the ring resonator is excited and exhibits self-resonance, resulting in a transmission dip. As the frequency increases to the higher transmission dip, the currents in split-ring resonators (SRRs) 1 and 4 flow anticlockwise, while those in SRRs 2 and 3 flow in the opposite direction, as shown in Fig. 2.15 (c). The currents in the square ring also flow opposite to those in the SRRs, leading to mutual cancellation and another transmission dip. In Fig. 2.15 (d), the currents in the four SRRs become stronger, and the opposing currents in the square ring are insufficient to counterbalance them. Consequently, the incident wave can pass through the metasurface, producing a transmission peak.

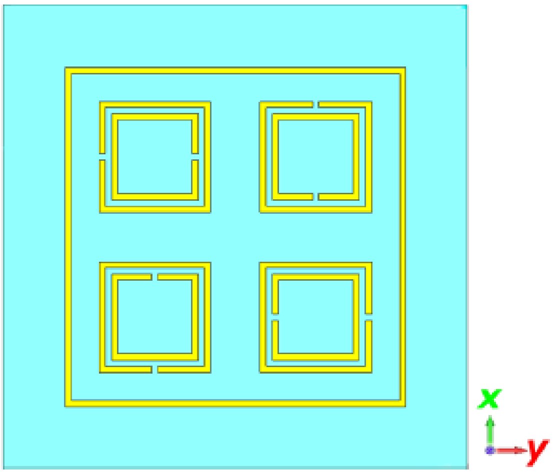

(a)

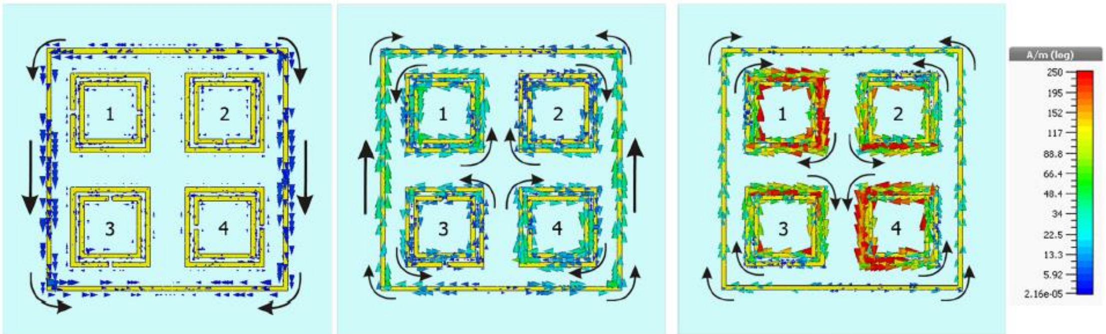

(b) (c) (d)

Fig. 2.15. (a) Simulation model of the EIT-like metasurface unit cell [184]. Surface current distributions at the (b) low-frequency transmission dip, (c) high-frequency transmission dip, and (d) transmission peak.

2.3.2 Biosensor

Biosensors based on metasurfaces play an important role in detecting biomolecules, cancer cells, and microorganisms. They enable direct measurement of biomolecular interactions in their native state without requiring fluorescent or other external labels. The sensing mechanism is fundamentally based on variations in the refractive index. When biomolecules such as proteins, DNA, or antibodies bind to the sensor surface [185], [186], the local refractive index changes, causing a shift in the resonance wavelength or frequency. However, biological tissues typically contain a high water content, leading to greater losses and absorption compared with ordinary dielectric materials. This characteristic significantly affects the performance of metasurface-based sensing. The experimental procedure [187] is illustrated in Fig. 2.16.

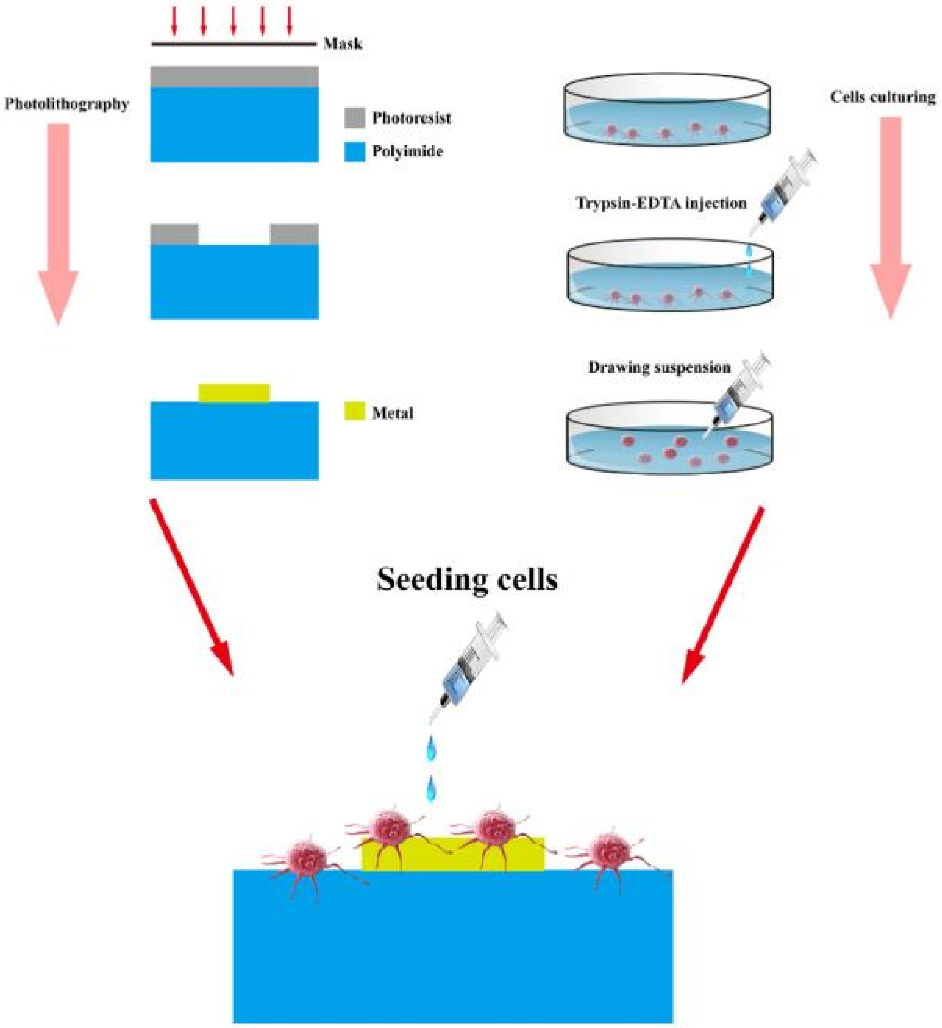

Fig. 2.16. Experimental process of the metasurface biosensor by culturing cells on the surface of the sensor [187].

A metasurface sensor [188] can function as a gas sensor, chemical sensor, or biosensor; however, its figure of merit (FOM) and Q-factor decrease significantly during biosensing due to the higher loss associated with biological tissues. In [189], a biosensor based on toroidal dipole resonance was proposed for detecting chlorothalonil in water, achieving a detection limit as low as 0.001 mg/L. The study also provided an equivalent RLC circuit model of the metasurface, demonstrating how variations in the refractive index of the analyte layer alter the transmission characteristics of the structure.

A metasurface absorber [190] can also be utilised as a biosensor, using a SiO_2 substrate with a gold disk array. Various metasurface biosensors have been designed for cell detection, including those targeting lung cancer cells [191], colon cancer cells [192], and malignant glioma cells [193]. The biosensor for early cancer detection [194] operates on a similar principle to the refractive index sensor, as illustrated in Fig. 2.17, where the analyte layer is placed in direct contact with the resonator. In this configuration, the analyte layer is typically very thin, ranging from 1 μm to 5 μm, which helps to minimise the effects of material losses while maintaining high detection sensitivity.

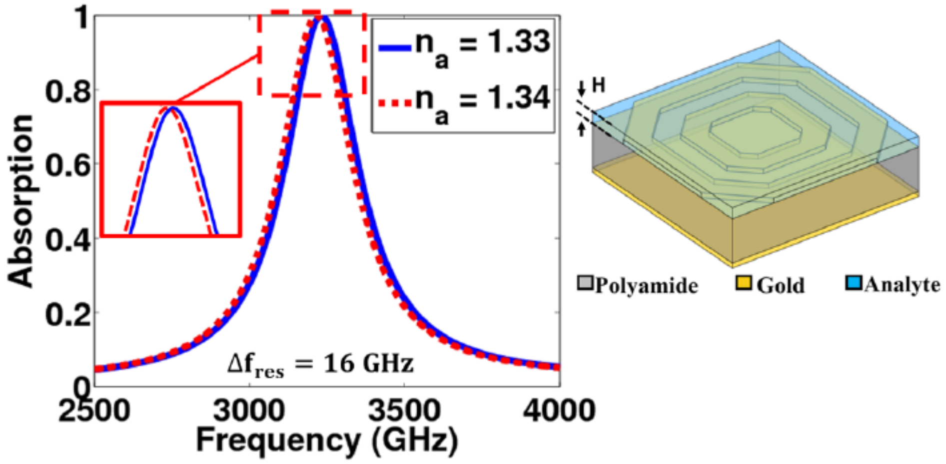

(a) (b)

Fig. 2.17. Metasurface sensor for cancer detection. (a) Absorption with various refractive indexes of the analyte. (b) Simulation model [194].

In [195], an EIT-like metasurface sensor, shown in Fig. 2.18 (a), was proposed for lung cancer cell detection. The structure consists of cut wires (CWs) and SRRs fabricated using PCB technology. In this design, the SRRs act as "dark" mode resonators, while the CWs serve as "bright" mode resonators. The polarisation of the incident wave is aligned parallel to the CWs, as the CW functions as an electric dipole antenna, whereas the SRR operates as a magnetic dipole antenna [196]. The spacing between the CW and the SRR determines the coupling coefficient of the EIT metasurface, representing the interaction between the "bright" and "dark" modes. The distances between the CW and the left and right SRRs are made equal to ensure that the SRRs exhibit a 180° phase difference when excited by the CW resonator. As illustrated in Fig. 2.18 (b), the CW resonator alone produces a single resonance at 1.18 THz, with opposite electric field intensities at its two ends. In Fig. 2.18 (c), the SRR exhibits opposing electric fields on either side, and the current distribution shown in Fig. 2.18 (d) confirms this behaviour, demonstrating the excitation of the “dark” mode magnetic dipole. Because the induced electric fields in the CW and SRR have comparable magnitudes but opposite phases, they cancel each other, resulting in a narrow transmission passband characteristic of the EIT-like effect.

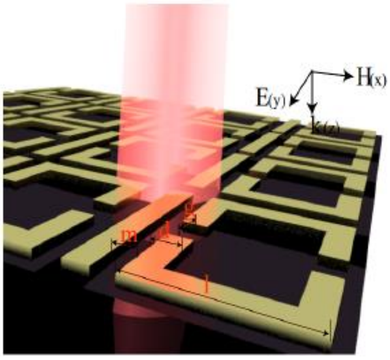

(a)

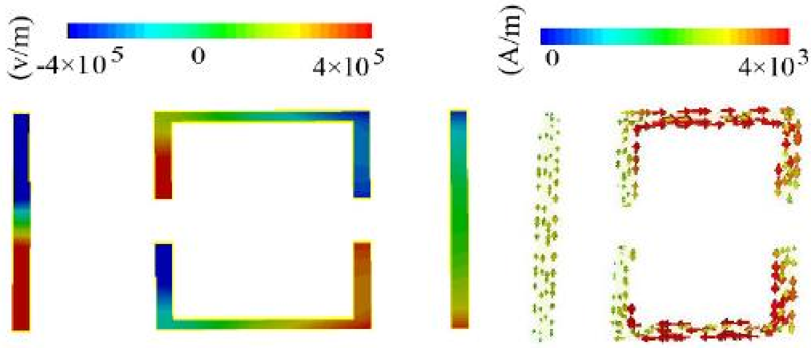

(b) (c) (d)

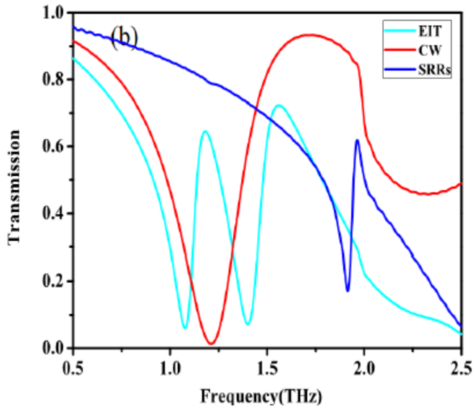

(e)

Fig. 2.18. (a) Schematic of the EIT metasurface [195]. Simulated electric field of the (b) CW at the transmission dip and (c) EIT metasurface unit cell at the transmission peak. (d) Simulated current distribution of the EIT metasurface unit cell. (e) Transmission coefficients of the EIT, CW and SRR.

Metasurface sensors have been used in skin cancer cell detection [197] using EIT-like resonance. The metasurface sensor has a thickness of 5 μm with a single layer of gold pattern, as shown in Fig. 2.19. The asymmetric split ring resonator (ASRR) is already capable of realising the EIT-like resonance [198]. The material under test is placed in direct contact with the resonators of the metasurface. As the loss tangent of the material increases, the Q-factor of the sensor decreases significantly. Therefore, this type of metasurface sensor is suitable only for ex vivo skin cancer cell detection, where the typical thickness of tumour cells is approximately 13 μm.

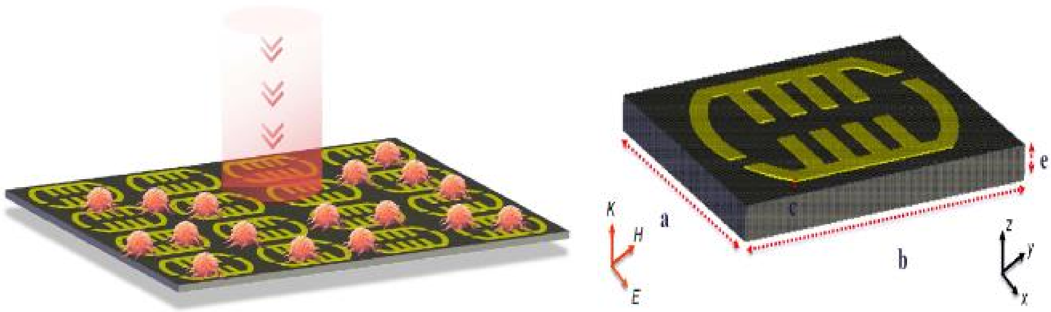

(a) (b)

Fig. 2.19 (a) Schematic of the metasurface biosensing for skin cancer cell detection application. (b) Side view of the EIT-like resonance unit cell with the X-polarised incident wave [197].

Metasurface sensors are typically employed for ex vivo biological sample sensing by measuring their transmission and absorption coefficients. However, their application in in vivo skin detection remains uncommon. In [199], a water-based metasurface sensor was proposed, consisting of two water bars with a width of 40 μm and a thickness of 7 μm, as shown in Fig. 2.20 (a). Simulation results, illustrated in Fig. 2.20 (b), demonstrate that the design can achieve measurable resonance frequency shifts. Despite this promising behaviour, the fabrication process is challenging, which limits its practicality for real-world biomedical use. Nevertheless, the study provides valuable insight into the potential of using metasurfaces for skin cancer detection, suggesting that future fabrication advancements may enable them in vivo implementation.

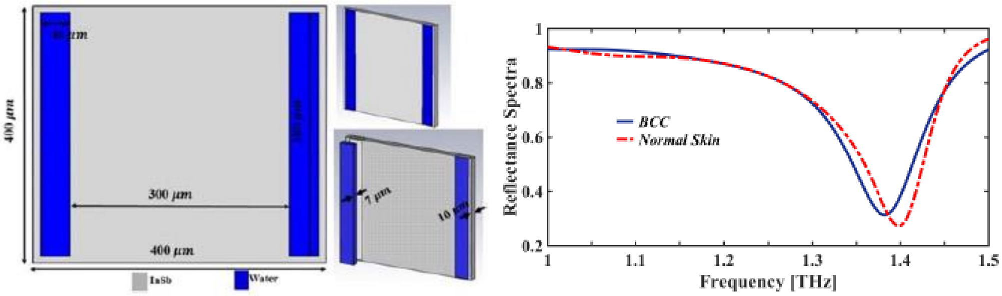

(a) (b)

Fig. 2.20. (a) Simulation model of the water-based metasurface sensor. (b) Simulated results of normal skin and BCC [199].

2.4 Skin Cancer Detection Methods

2.4.1 Common Detection Methods

1) Dermoscopy

Clinical skin cancer detection primarily relies on analysing the visual and structural features of skin lesions, following certain diagnostic frameworks such as the ABCD-E rule and the 7-point checklist.

The ABCD-E rule is an empirical method used for identifying potential melanomas: A refers to asymmetry, B to border irregularity, C to colour variation (typically brown or black), and D to diameter greater than 6 mm (recently revised to 4 mm). E stands for evolution, indicating that the lesion changes in size, shape, or colour over time. Abbasi et al. [200], [201] recommended adding the “E” criterion in 2004. Although not all melanomas display all these characteristics, any evolving lesion or dark spot on the skin should be carefully monitored and investigated.

The 7-point checklist is another well-established method for diagnosing malignant melanoma (MM). It classifies seven key clinical features associated with MM: sensory changes, lesion diameter greater than 1 cm, lesion growth, irregular edges, irregular pigmentation, inflammation, and surface changes such as crusting, oozing, or bleeding [202]. Compared with the ABCD-E rule, the 7-point checklist can achieve a higher diagnostic accuracy. However, in some cases, MM lesions can be smaller than 6 mm in diameter, making accurate diagnosis challenging. Moreover, early-stage MM and benign lesions often share similar visual features, which can lead to diagnostic uncertainty [203].

The detection methods described above are direct-viewing and easy to operate, but their diagnostic accuracy is not highly reliable. The sensitivity of dermoscopy-based detection remains limited and largely depends on the clinician's experience. Tumours smaller than 6 mm in diameter are particularly difficult to identify, leading to a relatively high rate of misdiagnosis. Dermatologists demonstrated significantly higher diagnostic accuracy for both neoplastic and inflammatory skin diseases compared with nondermatologists, correctly diagnosing 75% vs. 40% of neoplastic lesions and 71% vs. 34% of inflammatory cases, respectively [204]. Automated decision support systems based on the ABCD rule are less computationally demanding and offer more consistent reliability. However, they still present a risk of false positives, as benign nevi may occasionally be misclassified as melanomas [205].

2) Laser-based diagnosis

Confocal laser scanning microscopy (CLSM) can be used to analyse the moisture content of nails, producing image-based results [206] using an 830 nm near-infrared laser with a power level of $20\ mW$. The low power level ensures safety for human tissue. CLSM provides high lateral and axial resolutions of $1-2\ \mu m$ and $3-5\ \mu m$, respectively; however, its penetration depth is limited to approximately $200-500\ \mu m$. Therefore, it is suitable for detecting the epidermis and dermis layers. Using classification tree analysis of CLSM images, melanoma and benign nevi were correctly classified with accuracies of 97.55% and 96.32% [207].

3) Optical coherence tomography (OCT)

OCT is a low-coherence interferometric technique used as an optical analogue to ultrasound. This technique enables skin imaging with high axial and lateral resolutions of $10-20\ \mu m$ and a maximum penetration depth of about 1.5 mm [208], [209], [210]. The axial resolution is based on the ultra-broad bandwidth of the light source. It cannot distinguish malignant lesions from benign lesions due to limited resolution because there is a strong scattering in skin tissues [205].

4) Ultrasound imaging

Ultrasound imaging is based on the interaction between high-frequency acoustic waves (typically 1–20 MHz) and biological tissues. Because soft tissues contain a large proportion of water, the propagation of ultrasound in the human body is similar to that in water, making it particularly suitable for medical diagnostics. As ultrasound pulses travel through the body, they encounter interfaces between tissues of differing acoustic impedance, producing reflected waves (echoes) that are detected and reconstructed into images. Ultrasound imaging is safe, involves no ionising radiation, and offers short examination times with relatively low equipment cost. It is especially effective for visualising soft tissues and internal organs. The axial and lateral resolution of the detector is $100\,\mu m$ and $300\,\mu m$, respectively [211]. The sensitivity of ultrasound (ultrasonography, B-ultrasound, ultrasonography) is more than 25% higher than that of clinical palpation, especially for post-operative examination of regional lymph nodes [212]. However, to ensure high diagnostic accuracy, well-trained users and clearly defined regional lymph node areas associated with the primary site are required.

5) Magnetic resonance (MR)

In [213], the MR image is used to obtain longitudinal sections of the tumour extending toward the surface skin. This progression was caused by the spread of metastatic lesions through regional lymph nodes. In [214], a high-field MR microscopy study demonstrated that MRI can be effectively applied for differentiating skin tumours when sufficient spatial resolution is achieved. Normal skin, nevocellular nevi, basal cell carcinomas, melanomas, and seborrhoeic keratoses were examined ex vivo. However, the resolution of the MR image is generally limited, and it is typically sufficient only for detecting secondary metastatic tumours.

2.4.2 Microwave Detection Methods

Detection of tumour location based on the dielectric properties of biological tissue forms the fundamental principle of millimetre-wave sensing. The dielectric constant and loss tangent of skin are primarily determined by its moisture, protein content, nucleic acid, and glucose concentrations, all of which differ between healthy and cancerous tissues [215]. Malignant BCC skin tissues exhibited about 15% higher free (bulk) water content than normal skin tissues [216].

In [217], a narrow-band microstrip line-fed probe is proposed for near-field microwave microscopy. The prototype device operating at 13.5 GHz is presented in Fig. 2.21 (a). Due to a lower operating frequency, the microwave signal has a strong penetrating force; hence, the microstrip probe is capable of detecting hidden "lipoma" (fat layer). According to the authors' further experiment, the detection of skin cancer is achievable. By observing the magnitude of S_{11} at 13.5 GHz, the cancerous region can be detected. The triangle microstrip line tip focuses the microwave electromagnetic field and increases the lateral resolution by reducing the aperture size, but the lower operating frequency limits its highest resolution. When it comes to a millimetre wave, the microstrip line naturally has higher radiation loss, which may deteriorate the resolution. In addition, narrow-band performance potentially causes a similar magnitude of S_{11} corresponding to different frequencies; the better curve of S_{11} is a steep slope, but the operating frequency and resolution are lower; this effect is negligible and can cause obvious responsivity. On the other hand, due to non-contact measurement, as shown in Fig. 2.21 (b), the microstrip probe can scan fast without the influence of friction. However, it requires ex vivo measurement for skin cancer detection. Also, the microstrip probe is easy to fabricate and low-cost.

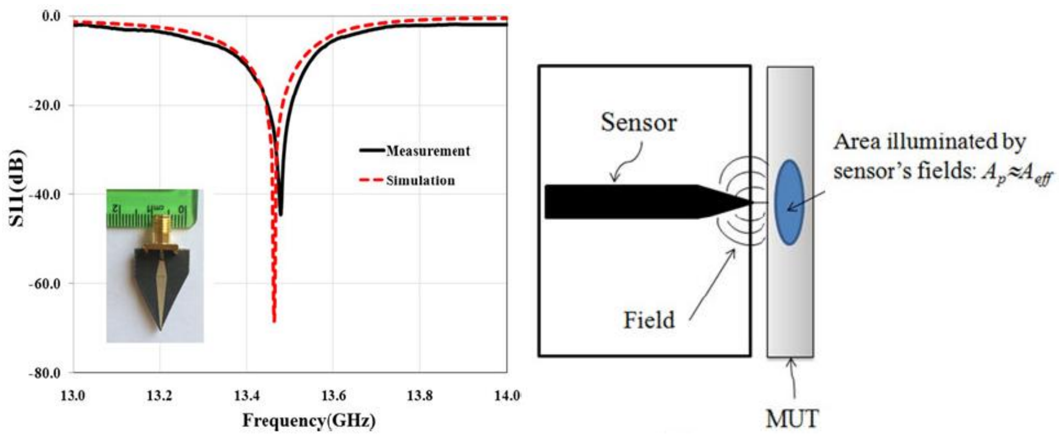

(a) (b)

Fig. 2.21. (a) Reflection coefficient of the probe and the fabricated prototype. (b) Measurement scenario [217].

In [218], Taeb et al. developed a detection system based on a rectangular waveguide to measure the reflected voltage from BCC tissues. The reflected voltages obtained from BCC and normal skin differed significantly, enabling the detection of skin cancer. The proposed reflectometer was constructed using a waveguide-based configuration comprising a Gunn diode, a ferrite Y-circulator, an open-ended rectangular waveguide, and a zero-bias Schottky diode, operating at 42 GHz and 70 GHz. As illustrated in Fig. 2.22, the Gunn diode source provides a stable millimetre-wave signal, which passes through the Y-circulator to the waveguide and is then reflected by the skin sample back to the Y-circulator. The reflected signal is subsequently directed to the detector (Schottky diode), which generates a DC voltage for measurement. When testing healthy skin, the reflectometer recorded voltages ranging from 12 to 12.8 mV, whereas for BCC tissue, the values ranged from 6.8 to 7.7 mV, indicating a clear distinction between the two tissue types. The advantages of the proposed reflectometer include its low cost, rapid detection, and non-invasive operation, eliminating the need for a vector network analyser (VNA). However, its spatial resolution is largely determined by the aperture size of the open-ended waveguide, which is relatively large. Furthermore, tight contact between the waveguide and the skin surface must be maintained to avoid air gaps, which could otherwise degrade measurement accuracy.

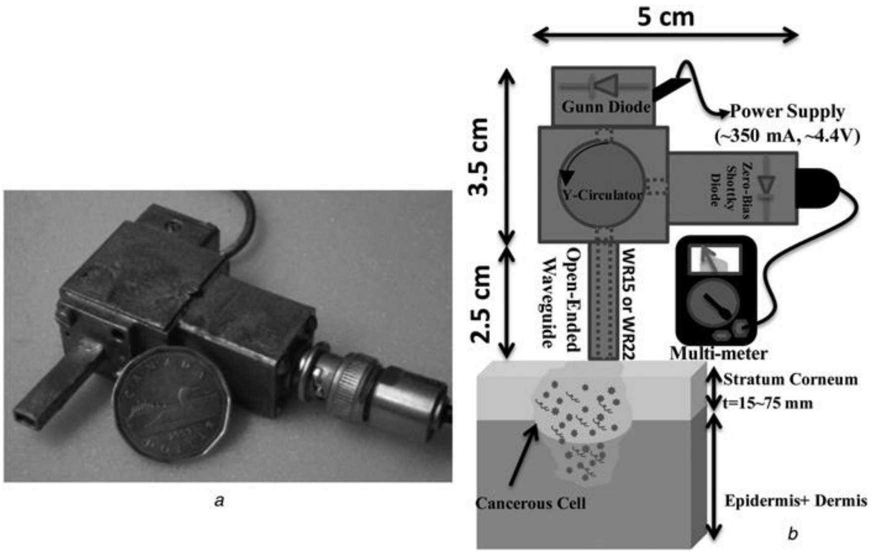

(a) (b)

Fig. 2.22. (a) Proposed reflectometer device (b) Equivalent model [218].

In [219], a broadband near-field probe is presented by inserting the tapered dielectric-rod waveguide (DRW) into the WR-10 waveguide, as shown in Fig. 2.23 (a). Its operating frequency band covers 90 to 104 GHz. The probe prototype is made from a high-resistivity silicon substrate (HRSS) wafer ($> 4000\Omega \cdot cm, \epsilon_r = 11.6$, $\tan\delta$ of 6×10^4 measured at 100GHz), and the four sidewalls are covered by gold, and its tip is non-metalised. By adding the DRW probe, the aperture size of the waveguide decreases significantly, to only 5.6% of the aperture size of the WR-10 waveguide; hence, the lateral resolution increases to $200\ \mu m$, and the sensing depth is $300 - 400\mu m$. Fig. 2.23 (b) presents the setup for probe-based reflection coefficient measurements. The proposed detection probe is connected to a VNA and fixed on an XYZ scan stage to control the position with $10\mu m$ precision. When the probe contacts different materials, the measured S_{11} at 96 GHz changes clearly. The proposed detection probe realises high resolution and high responsivity at 96 GHz. Due to the small size of the probe tip and the elasticity of the skin, the air gap between the probe tip and the skin can be removed. On the other hand, the fabrication process is complex, and the size of the probe tip is only $0.6mm \times 0.3mm$, it has the risk of puncturing the skin, and it is too sharp to scan the skin fast.

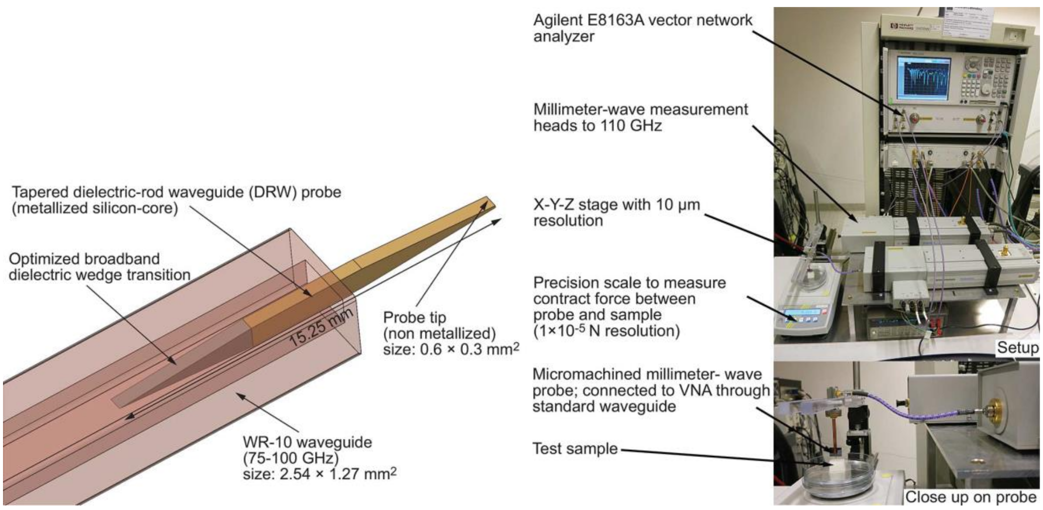

(a) (b)

Fig. 2.23. Probe design. (a) Schematic drawing (b) Setup for measurements [219].

In [220], A coaxial probe has been investigated for the detection of skin cancer. The probe's isolation layer is made of Teflon, with an outer conductor diameter of $3.62\ mm$ and an inner conductor diameter of $1.08\ mm$. It is connected to a VNA for measuring the reflection coefficient across a frequency range of 300 MHz to 3 GHz. The study also examined the effect of applied pressure on the probe's reflection coefficient, categorising the applied force into low, medium, and high pressure levels. The results showed that variations in the measured values were within 3% across different pressure conditions, indicating that pressure has a minimal effect provided that the air gap between the probe tip and the skin surface is eliminated. The magnitude of the reflection coefficients for moist and dry skin differed by approximately 0.06 within the 300 MHz – 3 GHz range, corresponding to about an 8% difference. Furthermore, the reflection coefficient of cancerous tissue was consistently lower than that of normal skin, although minor variations were observed among repeated measurements. These experimental results demonstrate that the coaxial probe is capable of effectively distinguishing lesion areas from healthy skin tissue.

The dimensions of the probe tip determine the measurement's spatial resolution and accuracy. When testing an unknown sample, the probe must make direct contact with the surface of the material. Rectangular waveguide probes are more prone to residual air gaps, whereas Teflon-filled coaxial probes — with a flange around their aperture — may also produce inaccuracies or unreliable results due to mechanical imperfections [221]. For instance, small positional shifts of the Teflon relative to the metal conductor can partially obscure the conductor or alter the spacing between the Teflon and the conductor. A bulging of the Teflon insulating layer by only 0.1 mm can cause up to a 30% variation in the measured reflection coefficient, and this deviation increases with frequency. In contrast, the influence of the gap between the Teflon and the conductor is relatively minor. Therefore, careful handling and precise alignment of coaxial probes are essential to ensure accurate and repeatable measurements.

In [222], a substrate integrated waveguide (SIW) structure was employed to develop a probe for skin cancer detection. The SIW can be fabricated using standard printed circuit board (PCB) technology, offering the advantages of low cost and ease of manufacture. The model of the probe is illustrated in Fig. 2.24 (a). The resonant frequency of the SIW probe is approximately 40 GHz, which provides sufficient sensing depth while ensuring that the microwave signal does not penetrate deeply enough to reach the fat layer. The narrow probe tip concentrates the electromagnetic field, achieving a lateral resolution of about 0.2 mm. When the probe tip contacts healthy skin, the resonance position — specifically the magnitude and corresponding frequency of the S_{11} — is recorded as a reference baseline, as shown in Fig. 2.24 (b). When measuring an unknown sample, a shift in the resonant frequency indicates a change in the dielectric properties of the tissue. The proposed imaging algorithm incorporates both the magnitude and frequency information of S_{11} to generate a pixel-based image. Regions where the calculated output exceeds a predefined threshold are identified as potentially cancerous. This SIW-based cancer detection system provides a low-cost and rapid measurement method, achieving safe operation without the risk of skin penetration, although at the expense of reduced lateral resolution.

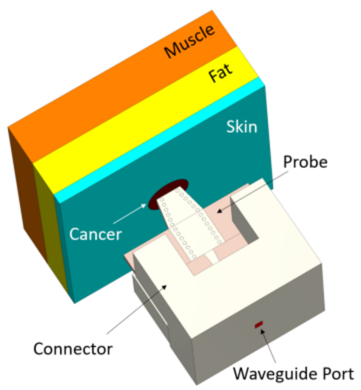

(a)

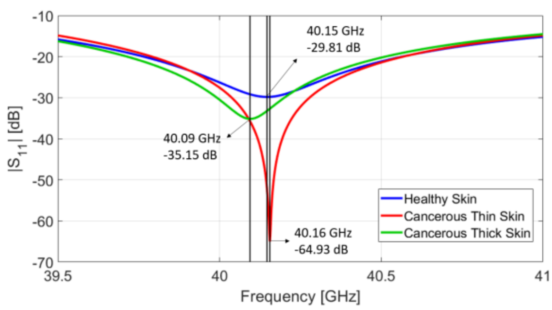

(b)

Fig. 2.24. (a) Model of the probe. (b) Measured S_{11} with different states of skin [222].

Several near-field probes have been presented in the previous section for skin cancer detection. However, antennas have also been used as sensing elements. A raster scanning imaging system achieving ultra-high resolution millimetre-wave imaging (MMWI) is presented in [223], [224]. The basic principle comes from the equation given by [225]. The lateral and axial resolution (δ) is determined by the bandwidth of the detector.

$$\delta \approx c/2B \tag{2.4}$$

where c refers to the speed of light in the medium, and B represents the bandwidth of the detector. Therefore, the bandwidth of the system needs to become ultra-wideband to realise ultra-high resolution. According to Equation (2.4), a lateral resolution of $200\ \mu m$ requires an ultra-wideband (UWB) of 100GHz. To achieve such performance, Mirbeik-Sabzevari et al. proposed a "synthetic" ultra-wide bandwidth of 98 GHz, covering frequencies from 12 GHz to 110 GHz. Their design employed four sub-antennas, each operating over a distinct frequency range. These sub-bands were then synthesised to form a virtual UWB antenna. A modulated Gaussian pulse in the time domain was used to excite this virtual antenna; the signal was transformed into the frequency domain to calculate the pulse response, then converted back into the time domain as the input for the imaging algorithm. As shown in Fig. 2.25, during the scanning process, four sub-band antennas are sequentially positioned in front of the sample, and the corresponding backscattered signals are recorded. The sample is mounted on an XY translation stage with an imaging area of $2\ cm \times 2.7\ cm$. In [223], a 3×3 scanning grid was used with a step size of $1.5\ mm$. Each sub-band antenna has a field of view (FOV) of at least $4\ mm \times 8\ mm$, resulting in a total illuminated area of approximately $7\ mm \times 11\ mm$. With this configuration, two adjacent tumours separated by $200\ \mu m$ can be clearly distinguished. In addition, by analysing the pulse responses, the system can measure the round-trip time delay and reconstruct images using the confocal delay-and-sum (DAS) algorithm [226]. This enables the generation of three-dimensional (3D) skin images, where each sub-band antenna functions as both transmitter and receiver. The key advantage of the proposed skin cancer detection system is its high lateral and axial resolution of $200\ \mu m$. In [227], imaging an area of $15\ mm \times 10\ mm$ required approximately 10 minutes; however, this acquisition time can be reduced to about one minute if all four sub-band antennas operate synchronously.

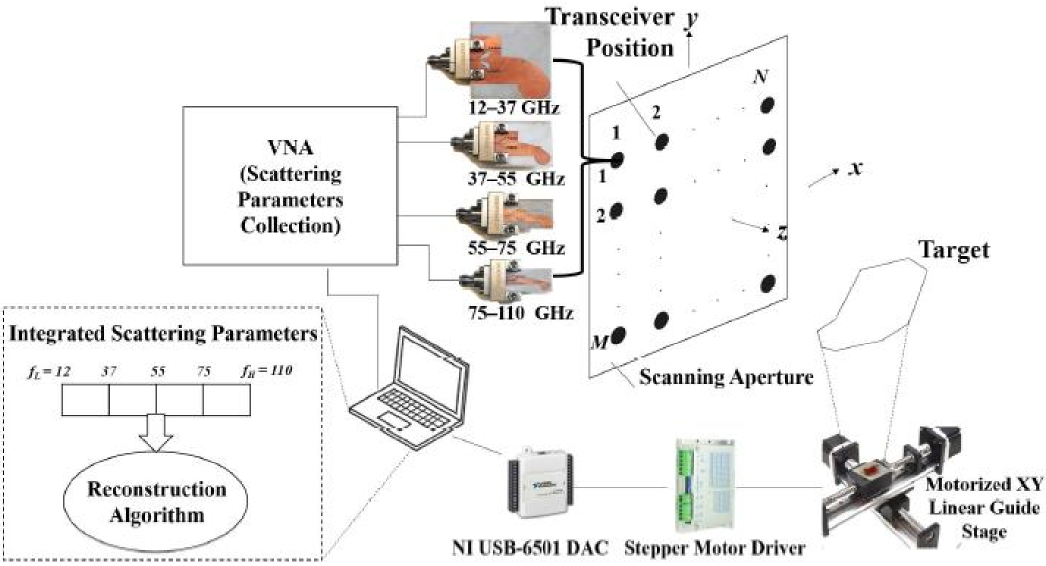

Fig. 2.25. Diagram of the ultra-high resolution millimetre-wave imaging system [224].

2.4.3 Terahertz Detection Methods

According to the detection method, THz technology can be classified into two main categories: terahertz spectroscopy and terahertz imaging [227]. THz spectroscopy is employed to investigate intra- and intermolecular vibrations in molecular and biomolecular systems, offering valuable insights for biosafety assessment and biological applications [228]. Real-time, dynamic observation of these macromolecular interactions helps elucidate the cellular pathophysiological mechanisms underlying disease progression. THz imaging, on the other hand, distinguishes cancerous tissues from normal tissues by comparing their absorption characteristics under THz radiation. Because different biological tissues exhibit distinct dielectric and absorption behaviours in the THz frequency range, THz imaging has already been applied in various biomedical areas, including skin burn assessment [229], gastric tissue analysis [230], breast cancer detection [231], diabetes monitoring [232], and skin cancer diagnosis [233].

In [234], Pickwell et al. conducted an in vivo study of the forearm and palm skin under THz radiation using Terahertz Pulsed Imaging (TPI) technology for biomedical applications. The main advantage of TPI lies in its broad operational frequency range -

from 0.1 THz to 3 THz - which is achieved by generating ultrashort pulses with a half-power width of approximately $0.3\ ps$, analysed using Fourier transform methods. The average power of the emitted THz pulse is around $100\ nW$, ensuring safe exposure for biological tissues. TPI provides both phase and amplitude information of the reflected signal, which can be used to determine the refractive index and absorption coefficient of the sample. When THz waves propagate from a medium with a lower refractive index to one with a higher refractive index, the reflected wave experiences a phase shift of π radians. In the frequency band of $0.1 - 3$THz, a 3D image can be obtained, the reflection depth resolution and the axial resolution can be $50\ \mu m$ and $100\ \mu m$.

The sample was positioned on a quartz imaging plate for measurement. The reflection response is illustrated in Fig. 2.26, where n_q, n_{sc} and ne represent the refractive indices of the quartz, stratum corneum and epidermis, respectively. In addition, n_{sc} is larger than n_q, n_e is lower than n_s, and n_q is equal to 2.1. Normal skin exhibits a relatively high refractive index due to its greater moisture content; therefore, when an incident wave enters the skin, the reflected wave undergoes a phase shift of π. By investigating the volar, dorsal, and palmar regions of the forearm, it was found that the pulse response obtained from the volar side was the most consistent among all subjects. In simulation studies, the volar forearm was modelled as a single-layer structure, whereas the palm was represented by a two-layer system. This FDTD model for in vivo measurement demonstrates strong potential for future THz biomedical applications, providing a reliable framework for studying the interaction between THz waves and human skin.

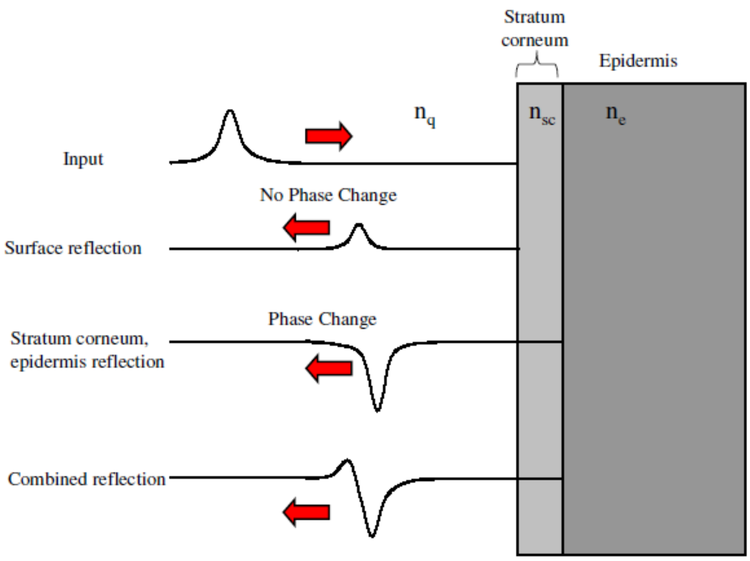

Fig. 2.26. Schematic of the TPI reflection [234].

In [235], a TPI technique was proposed for in vivo analysis of the hydration profile of the human stratum corneum (SC). By exciting a photoconductive antenna with an ultrafast laser pulse, the generated THz pulses cover a frequency range from 0.1 THz to 2 THz. The pump–probe TPI system is illustrated in Fig. 2.27. It employs the standard pump–probe configuration, where both the pump and probe beams are derived from a single laser source using a beamsplitter (BS). The pump beam excites the photoconductive antenna to generate the THz pulses, while the probe beam is used for THz-gated detection. A 1 mm-gap GaAs photoconductive antenna was employed to generate the THz wave, which was then directed onto the sample using two off-axis parabolic mirrors. A 2 mm-thick glass plate was placed over the skin sample to ensure a flat and uniform surface. The reflected THz signal was detected using the electro-optic sampling technique [236]. The incident pulse is influenced by the permittivity and absorption coefficient of the various skin layers, and the time-of-flight of the THz pulse through the skin can be determined from the delay of the reflected wave to extract skin thickness information. The TPI configuration is illustrated in Fig. 2.28. This system achieves a spatial resolution of approximately 350 μm, a temporal resolution of 0.5 ps, and a depth resolution of about 40 μm. The developed TPI setup is capable of quantitatively assessing the moisture content of the stratum corneum. A 1-cm line scan of the SC can be acquired in only 3 seconds, and a complete 3D dataset in under four minutes.

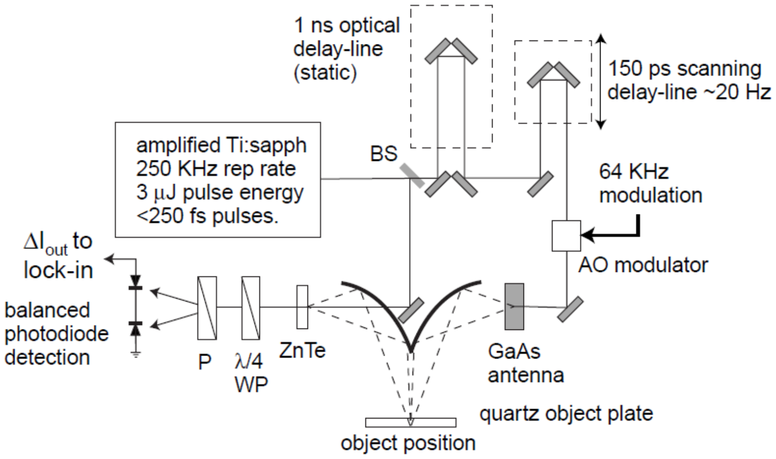

Fig. 2.27. TPI system: solid lines represent the NIR beam path, dotted lines represent the THz path. Shaded boxes represent mirrors. Abbreviations: BS - beamsplitter, P - polariser, WP – waveplate [235].

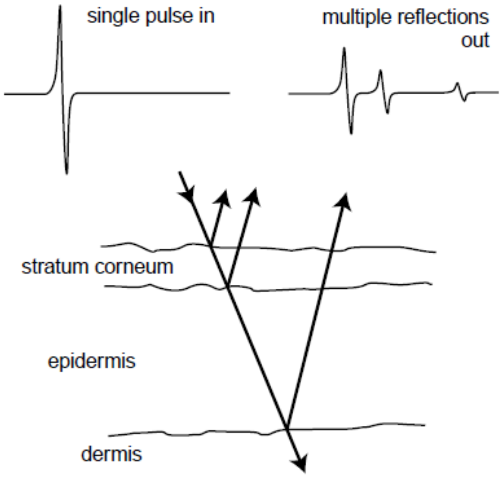

Fig. 2.28. THz pulse imaging approach [235].

In [237], TPI has been shown to study differences between basal cell carcinoma and normal skin tissue in the laboratory. The stratum corneum–epidermis interface is imaged, enabling the investigation of skin hydration levels. The paper further discussed the potential applications of this technique in the cosmetic industry and for treating inflammatory skin diseases such as psoriasis and eczema, underscoring the significance of skin hydration profile measurement.

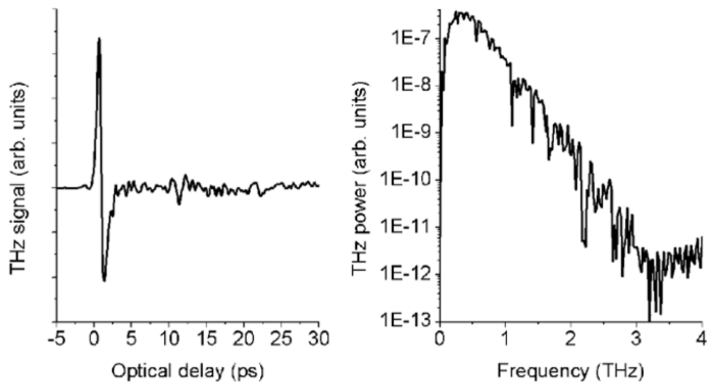

(a) (b)

Fig. 2.29. (a) A time domain THz pulse. (b) The THz spectrum from the Fourier transform [237].

A time domain THz pulse is shown in Fig. 2.29 (a). By using a Fourier transform, the spectrum is presented in Fig. 2.29 (b). The smaller vibrations are caused by atmospheric water-vapour absorption. A time domain algorithm is used to distinguish the BCC from the normal tissue. By normalising the impulse formula E(t) at time t, the "time post pulse (TPP)" algorithm is given by:

$$\mathrm{f(t)} = \frac{\mathrm{E(t)}}{\mathrm{E_{min}}} \tag{2.5}$$

Where t is the time of the maximum reflected pulse, the proposed TPP can detect BCC and normal skin tissue. The minimum value of BCC's TPP is larger than the maximum value of the normal skin tissue.

In [233], a portable TPI system was proposed for BCC measurement, utilising TPI technology to map the position of cancerous tissue. The device is illustrated in Fig. 2.30. The operating frequency band spans 0.1 - 3 THz. Scanning a $25 \times 25\ mm$ area takes less than 100 seconds, and the detector achieves a detection depth of approximately $1\ mm$. By measuring 18 BCC samples ex vivo and 5 BCC samples in vivo, a clear distinction between cancerous and normal tissues was observed, as the reflected pulse intensity from diseased tissue was significantly higher than that from normal tissue. Skin cancer and BCC have an obvious contrast with normal tissue, including absorption and refractive index [238].

Fig. 2.30. The proposed portable TPI system [233].

TPI has already been used to detect BCC. Continuous wave (CW) terahertz imaging can also offer simple, low-cost, and ex vivo skin cancer detection [239], as shown in Fig. 2.31. Two far-infrared lasers at the frequencies of 1.39 and 1.63 THz are used to illuminate the sample. The tissue absorption characteristics at 1.4 THz depend on both water and tryptophan content. At 1.6 THz, however, the absorption is primarily determined by the water content. The skin cancer sample on the XY scan stage is obtained from Mohs surgeries. A total of ten samples were exposed to the THz laser. When the light passes through the sample, the difference in the transmission coefficient between abnormal and normal tissue is about 60%.

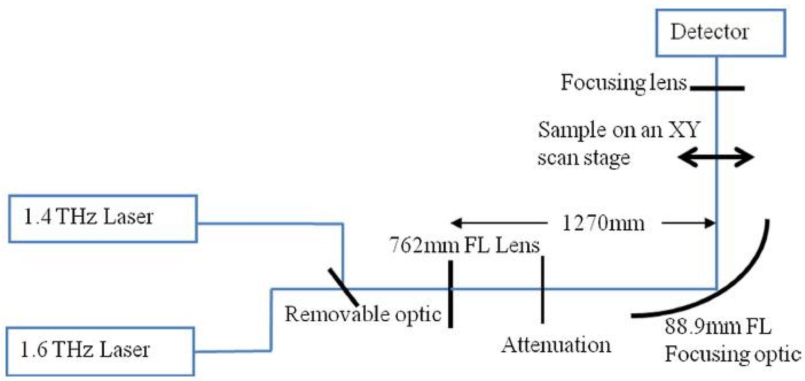

Fig. 2.31. CW imaging system [239].

In [240], a terahertz imaging and spectroscopy system was proposed for cancer detection. Terahertz pulsed spectroscopy (TPS) is also an important cancer detection technology. The proposed system is an ex vivo measurement. The tissue sample is about 0.1 mm thick and placed on the XY scan stage with a minimum step size of 50 μm. Hence, it is also feasible for skin cancer detection systems, as shown in Fig. 2.32. The interactions between the THz wave and the sample are obtained through spectroscopy measurements. According to the inversion algorithm, the amplitude and phase error are minimised, and the dielectric constant and loss tangent are extracted in the frequency band from 0.1 to 4 THz. Although it has a higher resolution of 200 μm, the proposed terahertz imaging and spectroscopy system takes about 35 minutes to measure the cancer sample with an area of 1 $cm \times 1\ cm$.

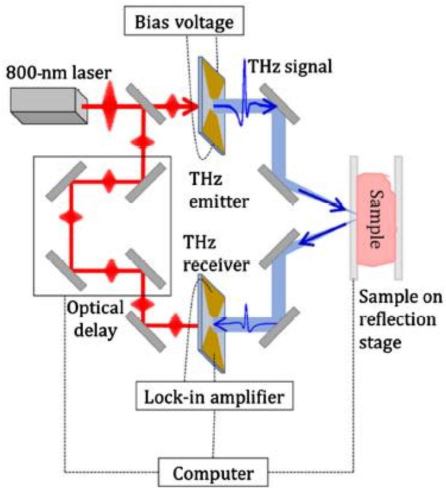

Fig. 2.32. Terahertz imaging and spectroscopy system [239].

2.5 Conclusion

In summary, metasurfaces offer a wide range of potential applications. Various metasurface unit cells for phase shifting and sensing have been introduced, corresponding to the metasurface lens and metasurface sensor. The metasurface lens can be utilised in future communication systems, providing low-cost, high-gain, and multifunctional transmitting front-end. The metasurface sensor can be applied to material detection and biomedical sensing, offering a label-free detection approach. Furthermore, the metasurface sensor shows strong potential for in-vivo skin cancer detection. To this end, existing skin cancer detection methods have been reviewed. However, these detection systems are generally bulky and time-consuming. Therefore, a rapid and compact detection approach for in vivo skin cancer diagnosis is of significant value.

Chapter III All-Dielectric Metalens Design

3.1 Introduction

All-dielectric lenses, as the name implies, are lenses composed entirely of dielectric materials. Traditional glass lenses are a typical example of this category. Conventional fabrication methods are based on subtractive manufacturing techniques, such as cutting, grinding, and polishing, to produce these lenses.

A metalens, derived from the combination of "metasurface" and "lens," utilises subwavelength microstructures to manipulate light and waves. Unlike traditional lenses, which rely on ray-tracing theory and control light through refraction and optical path length, metalenses achieve similar or enhanced functionalities by precisely engineering the phase, amplitude, and polarisation of light at the subwavelength scale. Metalens, lens and transmitarray are sometimes almost the same in terms of function and application.

3D printing, also known as additive manufacturing (AM), has the advantage of rapid prototyping, cost-effectiveness and a high degree of freedom, which enables complex lens designs that are difficult to achieve with traditional manufacturing. It has been widely used in designing various lenses, including the cylinder Luneburg lens [241], flat Luneburg lens [242], gradient-index (GRIN) lens [243], discrete dielectric lens (DDL) [244], transmitarray [245], beam splitter [130], reflectarray [246] and three-dimensional (3D) Luneburg lens [247]. The DDL can be designed into the circularly polarised transmitarray [248], the near-field beam-scanning lens [249] and the OAM generator [250]. By adding the truncated pyramid hole, the 3D-printed dielectric lens antenna [251] can achieve 21.5 % relative bandwidth at 1dB level. In [252], by considering the oblique incidences, the all-dielectric lens antenna realised a gain enhancement of 4.5 dB at 26 GHz with a lower focal-to-diameter ratio.

A metalens comprises two main components: subwavelength unit cells and a phase distribution. Various types of unit cells have been introduced in Chapter II. In the following section, the focus will be on phase distribution, which represents the primary source of innovation in this chapter.

3.1.1 Phase Distribution

The phase distribution (PD) plays a crucial role in determining the wavefront of the transmitted electromagnetic wave. By carefully designing the phase shift imparted by each unit cell, the transmitarray can precisely manipulate the direction, focus, or shape of the transmitted beam. The objective is to ensure that all rays arriving at the observation plane are in phase, thereby achieving constructive interference. This PD can be tailored to realise beam steering, beam focusing, or other advanced wavefront control functionalities. The coordinate system of the metalens antenna is illustrated in Fig. 3.1(a), where F denotes the focal length. The fabricated metalens is shown in Fig. 3.1(b). The PD of the metalens is derived based on Fermat's principle, and the phase distribution for each unit cell can be expressed as follows:

$$\varphi_{ij} = k_0(\sqrt{{x_{ij}}^2 + {y_{ij}}^2 + F^2} - \mathrm{F}) \tag{3.1}$$

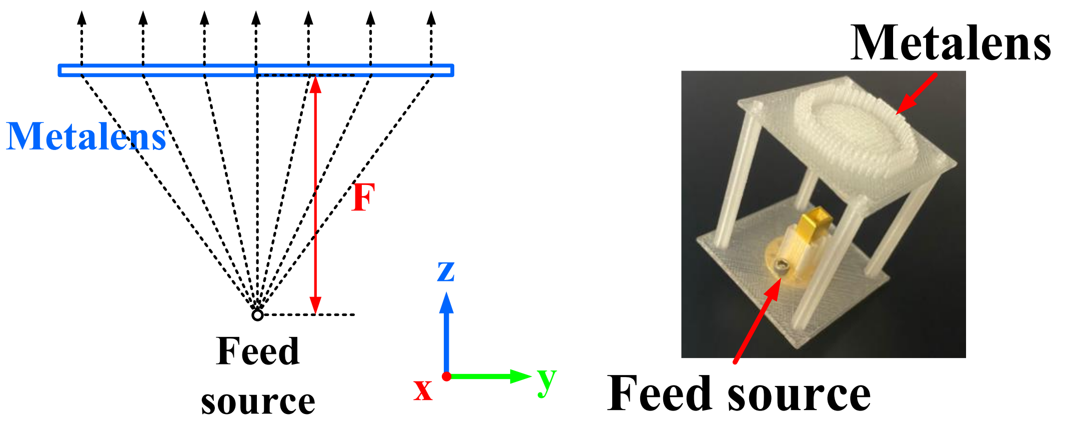

(a) (b)

Fig. 3.1. (a) Schematics of the metalens antenna. (b) Photo of a metalens antenna.

where k_0 is the wavenumber, $2\pi/\lambda$. (x_{ij}, y_{ij}) denotes the position of the unit cell in the i-th row and j-th column, and φ_{ij} is its phase delay. The function of the metalens is to compensate for the phase delay introduced by variations in propagation distance. However, to realise more advanced functionalities, the calculation of the phase distribution becomes increasingly complex.

3.1.2 Beam-Scanning Metalenses

Broad-range beam scanning is one of the most desirable features in emerging terahertz (THz) telecommunication systems. To achieve extensive coverage with high gain, metalenses, transmitarray antennas (TAAs), and lens antennas (LAs) have attracted considerable attention. Over the last decade, existing unifocal [253], bifocal [254], [255] and multifocal [256], [257], [258] beam-scanning TAAs and LAs have been designed based on geometric optics (GO) analysis and the Fresnel formula. Their performance is dependent on the degrees of freedom (DOFs), which include the positioning and tilt angles of the feeding sources, as well as the shape of the PD.

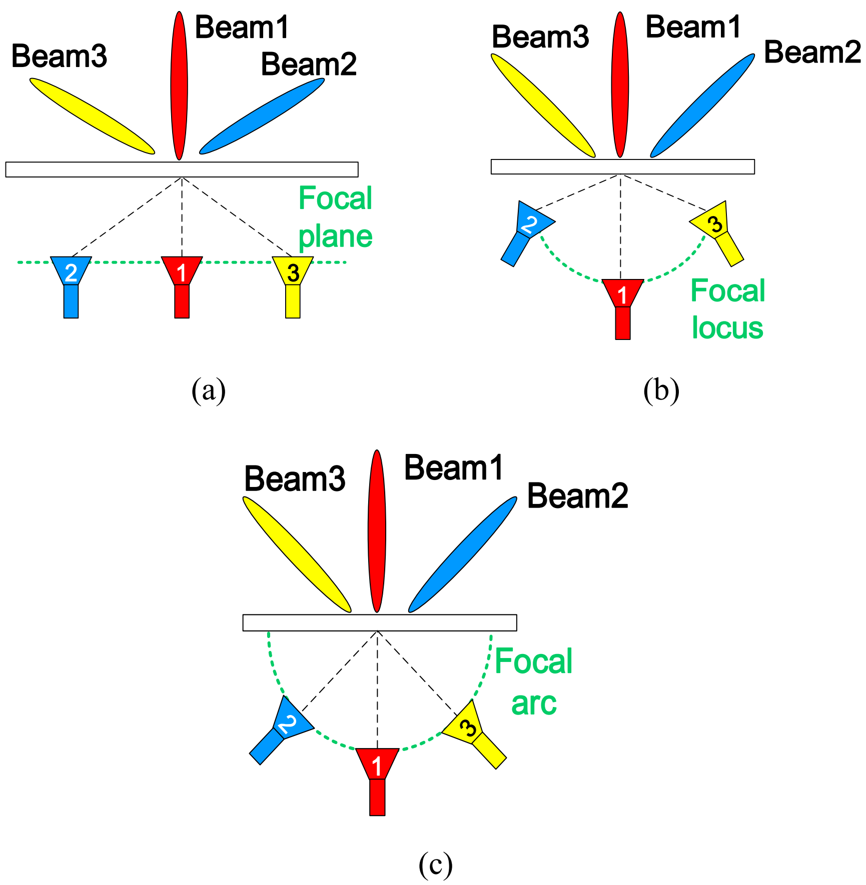

Fig. 3.2. Schematics of the beam-steering metalens. (a) Metalens with a focal plane; (b) Metalens with a focal locus; (c) Metalens with a focal arc.

Overall, there are three main types of mechanical beam-scanning or electronic scanning TAA or LA. Fig. 3.2 (a) illustrates an LA with a focal plane [253], which has the strength of a wide beam-scanning range. To cover the radiation of all the feeding sources, the aperture size of this LA tends to be large [254], [255]; therefore, the aperture efficiency (AE) and a lower focal-to-diameter ratio (F/D) are compromised. The shape of the phase distribution needs to be elliptical for a wider one-dimensional (1D) beam-scanning range. A two-dimensional (2D) gradient index (GRIN) lens [256] with limited DOFs of the PD can only realise the $-20°$ to $20°$ range. LAs [257] with a focal locus in Fig. 3.2 (b) fully utilise the DOF of the feeding sources, which can achieve a wide coverage. Recently, a 2D beam-scanning lens with a $\pm 45°$ coverage has been proposed [258], [259]. The focal length and direction angle of each feeding source differ from one another. Consequently, the analytical expression of the focal locus becomes complex, which limits its applicability to continuous 2D beam scanning. LAs with a focal arc [260], [261], as shown in Fig. 3.2 (c), can achieve high AE and wide coverage, where the beam deviation factor (BDF) equals 1. The BDF is defined as the ratio between the main beam direction and the tilt angle of the feeding source. Only a few studies have reported 2D beam-scanning LAs with a focal arc, since the PD must be circular, and the feeding source must be directed towards the centre of the LA, where the DOF is restricted.

3.1.3 Imaging Metalenses

There are various kinds of imaging lenses. In Fig. 3.3 (a), the lens is used to focus the output electromagnetic (EM) waves onto a single point [262], [263]: the focal point. The electromagnetic field is concentrated at this small spot, enabling high-resolution imaging through raster scanning [264]. The radius of the focal spot can be given by the following formula.

$$2\omega_0 = \frac{4 \cdot M^2 \cdot \lambda \cdot F}{\pi \cdot D} \approx 2\lambda \cdot F/D \tag{3.2}$$

where ω_0 represents the radius of the focal spot, λ is the wavelength, D is the diameter of the beam at the lens surface, F represents the focal length of the lens, M is the beam quality parameter. The formula can be simplified to a function of the wavelength and the focal-to-diameter ratio. Therefore, the focal length-to-diameter ratio is important, it can reduce the size of the focal spot and determine the resolution of imaging. This type of lens can achieve high-resolution imaging, but the imaging process relies on scanning, which makes it very time-consuming. In terms of application, it functions more like a probe that focuses electromagnetic waves. By rotating and adjusting two or three lenses, the focal point can be moved arbitrarily, which offers the potential for three-dimensional scanning [265], [266].

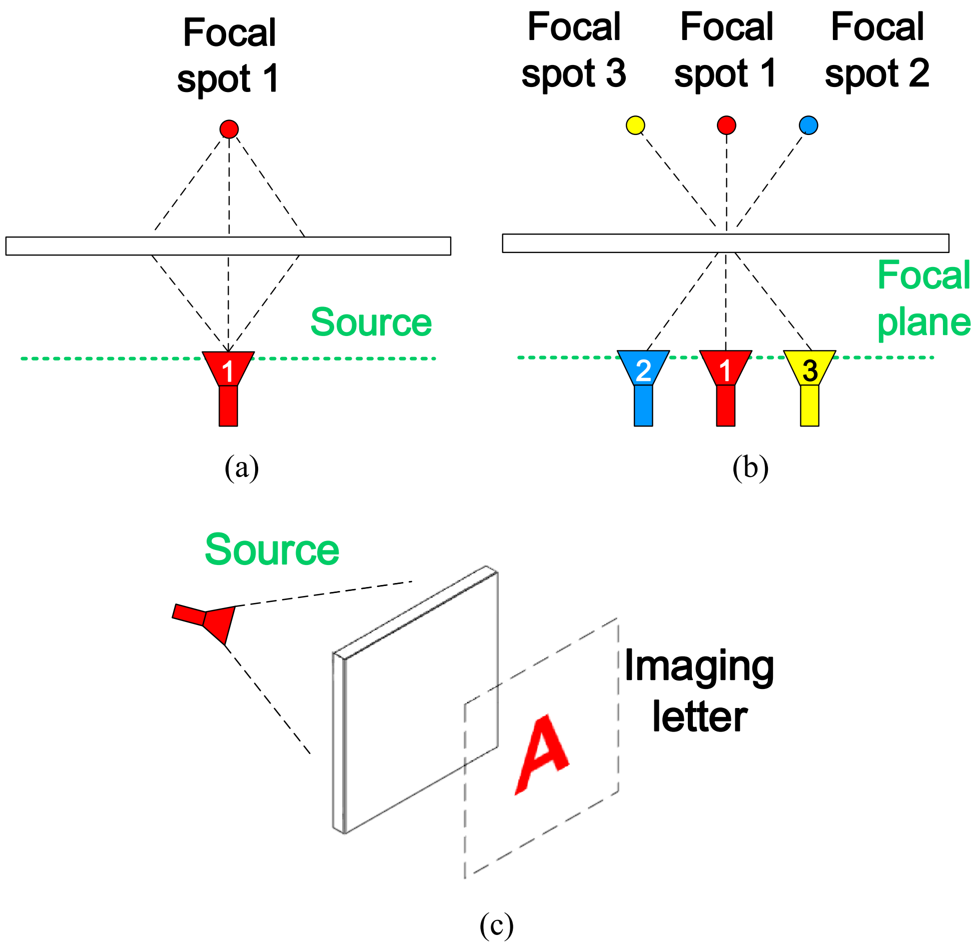

Fig. 3.3. Schematics of imaging metalens. (a) Single focal point. (b) Multiple focal points. (c) Holography imaging.

In Fig. 3.3 (b), multifocal lenses are theoretically challenging to implement, as a single-phase distribution typically produces only one focal point. Once a lens is designed, its phase profile is fixed, making it theoretically incapable of generating multiple focal spots. However, in practice, by compromising the focusing performance, it is possible to achieve multiple focal points. As a result, compared to single-focus lenses, multifocal lenses tend to have slightly inferior imaging quality, with aberrations such as coma appearing at the edges, which can be mitigated using optimisation algorithms [267]. The main advantage of multifocal lenses is their ability to perform real-time mirror imaging. Such lenses are commonly found in optical applications. In Fig. 3.3 (c), the last one is the holographic imaging metalens, which shapes the electromagnetic wavefront through carefully designed phase distributions. These surfaces focus the electric field within a specific region to form patterns or characters [268], [269], [270], [271]. In terms of application, they function more like static images or photographs.

3.2 3D-Printed Low-Cost Continuous Metalens for 1D Beam Scanning

Antennas capable of beam steering or beam scanning have been widely reported in the literature. Mechanically scanned metalens antennas suffer from low scanning speed [272], while frequency-dependent beam scanning cannot fully exploit the available spectrum resources [273]. Phased array antennas (PAAs) and digital beamforming (DBF) array antennas[274], [275] can overcome the above limitations; however, this advantage comes at the cost of increased fabrication complexity and expense.

In this section, a 3D-printed metalens is proposed for a 1D linear antenna array in multibeam applications. The metalens can be fabricated using 3D printing technology and has minimal impact on the beam-scanning performance of the 1D array, while simultaneously enhancing the array gain. The proposed metalens, fed by a WR-06 waveguide probe, is analysed through full-wave simulation.

3.2.1 Continuous Metalens Design

Fig. 3.4 (a) shows the proposed dielectric metalens and the WR-06 waveguide probe. The 3D-printed dielectric metalens and its support structures are fabricated from polylactic acid (PLA), which has a relative dielectric constant of 2.5 and a loss tangent of 0.02. The WR-06 waveguide probe operates in the D-band (110–170 GHz), with dimensions of $1.651\,mm \times 0.8255\,mm$. The basic geometry of the proposed metalens was simulated and optimised using ANSYS HFSS, with a central operating frequency of 120 GHz.

The dielectric metalens is designed to be a whole rather than a discrete structure [276]. This means the metalens structure can also be fabricated using moulds, which is very suitable for low-volume production and reduces the fabrication cost. The usage of a metalens is convenient. One can just put it above the antenna chip [277] or combine it with the product shell, which introduces little impact on the original systems.

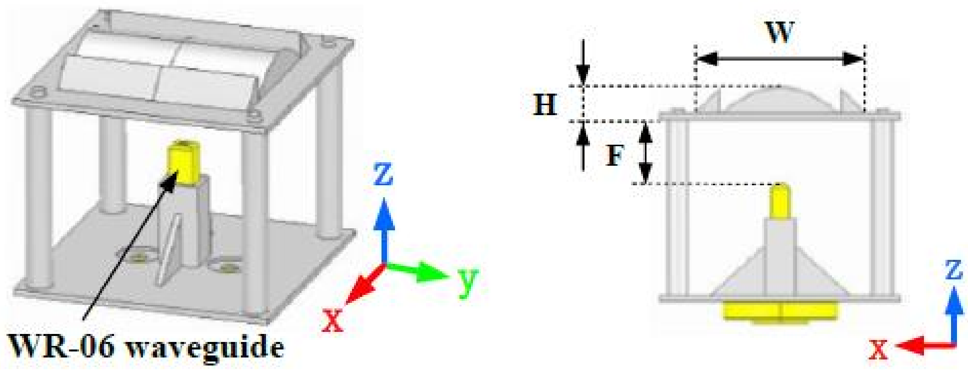

(a) (b)

Fig. 3.4. Proposed 1D dielectric metalens and WR-06 waveguide probe and support. (a) Oblique view. (b) Side view.

As shown in Fig. 3.4 (b), the focal length (F) is 12 mm, determined by the phase centre of the WR-06 waveguide. The total height (H) of the metalens is 5.8 mm, and its width (W) is 28.6 mm. The length of the metalens can be customised according to the size of the underlying 1D antenna array, if applicable. The arc profile of the proposed metalens is designed based on the input phase distribution, which can be derived from Fermat's principle:

$$\varphi(x) = \frac{2\pi}{\lambda}\left(\sqrt{x^2 + F^2} - F\right) + \varphi_0 \tag{3.3}$$

where F represents the focal length, λ represents wavelength at 120GHz, and φ_0 is the initial phase at the feed source. To realise 1D beam scanning along the Y-axis, the phase distribution is kept invariant in that direction. The gain enhancement is achieved by narrowing the beamwidth along the X-axis. Fig. 3.5 illustrates the linear relationship between the dielectric layer thickness and the transmission phase. The metalens unit cell is simulated using primary and secondary boundaries; the height of the air box is fixed at H_1 = 6 mm, while the height of the dielectric layer is varied. Owing to the continuous design of the metalens, no air gap exists between adjacent unit cells. Based on Equation (3.3), the phase distribution can be calculated, and the required height of the dielectric layer can then be determined from the linear relationship shown in Fig. 3.5. Consequently, the arc profile of the proposed metalens can be constructed and further optimised.

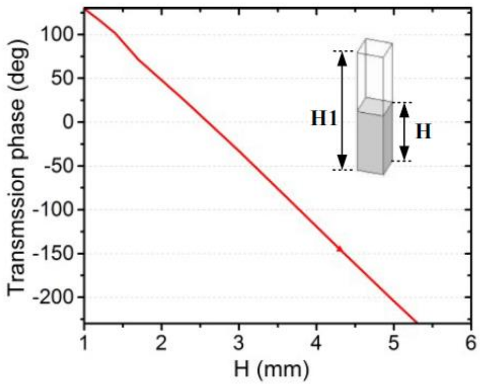

Fig. 3.5. Relationship between the height of the dielectric layer and its transmission phase.

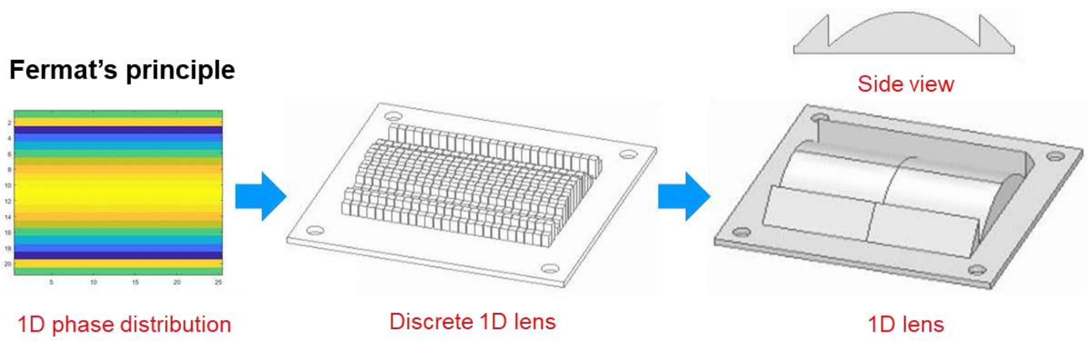

Fig. 3.6. One-dimensional (1D) metalens evolution.

By applying Fermat's principle with a central frequency of 120 GHz and a focal length of $20\,mm$, the resulting phase distribution is illustrated in Fig. 3.6. In a traditional design, a discrete 1D metalens can be constructed. Based on the height variation within this metalens, an equation-defined surface can be generated in ANSYS HFSS to obtain the proposed 1D metalens. The side view of the structure is also presented. In theory, both metalenses exhibit comparable performance; however, the metalens with a smooth surface is more suitable for mass production, as it can be fabricated using mould-based manufacturing techniques.

3.2.2 Metalens Performance

Fig. 3.7 (a) presents the radiation pattern comparison of the antenna with and without the proposed metalens. The simulated results come from the model in Fig. 3.4. It can be seen that the broadside gain of the waveguide can be increased from 6.2 dBi to 14.55 dBi. The 3-dB beamwidth of the waveguide is about 104.7° in the E-plane and 73.5° in the H-plane, while that of the metalens antenna is 6.7° and 72° in the E-plane and H-plane, respectively. The proposed metalens narrows the beamwidth in the E-plane and has little effect on the beamwidth in the H-plane. When a 1D linear antenna array is employed as the feed source to provide beam-scanning capability, the metalens antenna can realise 1D beam scanning without interference across the scanning range, achieving approximately 8 dB gain enhancement. During the simulation process, a 1D microstrip patch antenna array is used to validate the beam-scanning performance. As shown in Fig. 3.7 (b), a 4.3 dBi gain enhancement is achieved at different beam angles, with scan losses of 1.4 dB and 1.1 dB for the arrays with and without the metalens, respectively. Moreover, the metalens has a negligible impact on the main beam direction. The corresponding schematic of the 1D beam-scanning metalens antenna is shown in Fig. 3.7 (c). The comparison between the array antenna with and without the lens clearly demonstrates the gain enhancement achieved by the proposed metasurface lens. The lens effectively focuses the radiated energy, resulting in a noticeable increase in the overall antenna gain. Moreover, this improvement is obtained without affecting the beam-scanning capability of the array, indicating that the lens can enhance the radiation performance while maintaining the original scanning range.

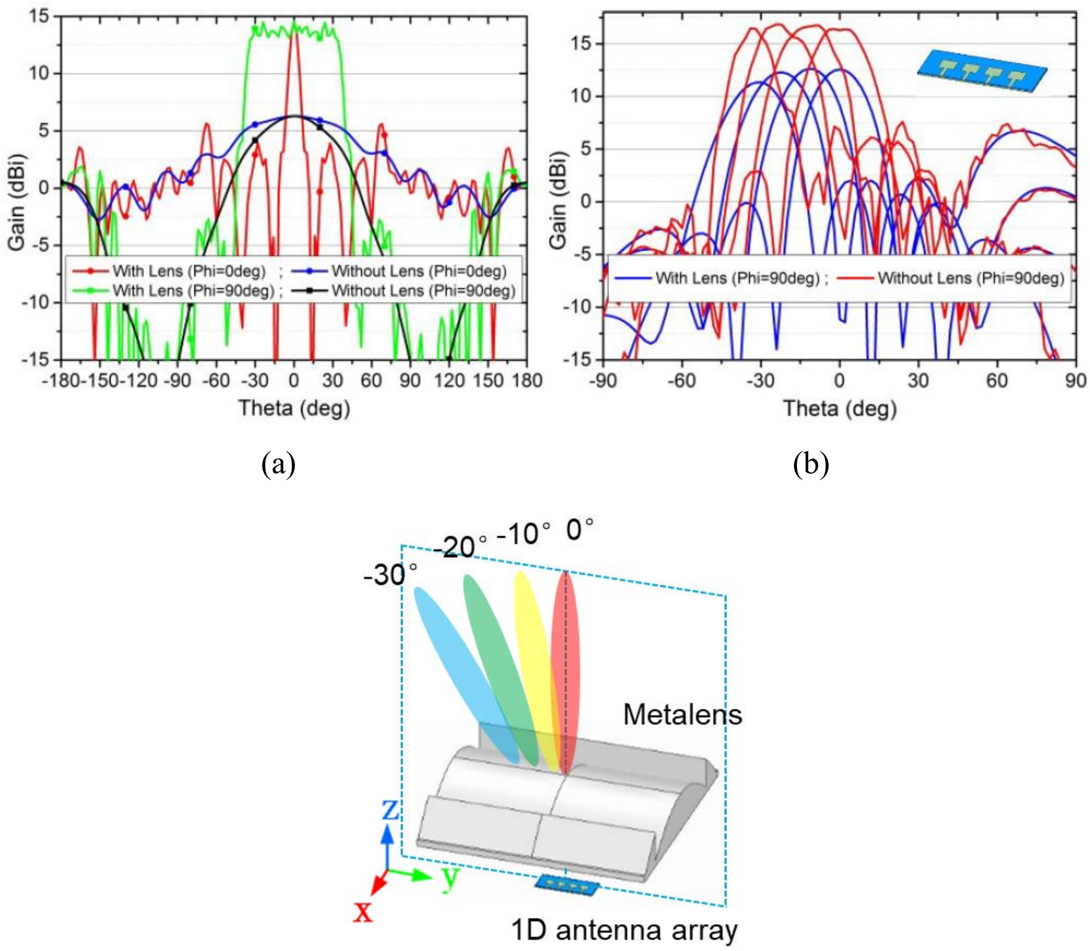

(a) (b)

(c)

Fig. 3.7. Radiation patterns at 120 GHz with and without the 3D printed metalens excited by: (a) Waveguide probe. (b) A 1D linear antenna array. (c) Schematic of the 1D beam-scanning metalens antenna.

This section proposes a 3D-printed dielectric metalens antenna for the THz application. The simulation results show that the proposed metalens can achieve high gain enhancement and 1D beam-scanning performance.

3.3 3D-Printed Discrete Multifocal Metalens for 2D Beam Scanning

This section presents a genetic algorithm (GA)-based optimisation method for designing 2D beam-steering dielectric metalenses. An additional degree of freedom

(DOF) is introduced for multifocal optimisation by adjusting the rotation centre of the feed sources. By utilising the phase-shifting characteristics of the metalens unit cells under varying incident angles, the proposed metalens satisfies the phase-compensation requirements for feed beams from multiple ports, thereby realising continuous 2D beam scanning from $-30°$ to $30°$ in E-plane, H-plane, and D-plane (Diagonal-plane, $\phi = 45°$). The circular phase distribution (PD) reduces the number of optimisation parameters and enables a quasi-Luneburg lens performance with 2D beam steering. The proposed metalens obtains a measured aperture efficiency of 29.3%. The broadband performance of the dielectric unit cells makes the metalens achieve the 24 % 3-dB gain bandwidth and 18.3% 1-dB gain bandwidth. The proposed metalens is ideal for broadband 2D beam-steering at the sub-THz band with low manufacturing cost and easy fabrication.

3.3.1 Dielectric Unit Cell

The all-dielectric unit cell shown in Fig. 3.8 (a) is simulated using ANSYS High-Frequency Structure Simulator (HFSS). A dielectric square post with width (W) and variable height (H) is fabricated from cyclic olefin copolymer (COC), a 3D-printable material with a relative permittivity of 2.34 and a loss tangent of 0.00017 at THz frequencies [278]. It should be noted that the H_1 is the total height of the unit cell, which contains both the air and dielectric parts, and the height of the base is H_2, and the H is the height of the dielectric pole. By changing the height H of the unit cell (ranging from H_1 to H_2), the unit cell can achieve a complete 2π phase shift [279]. There is a $0.1\ mm$ air gap between the pillars to prevent the modelling error in HFSS. In Fig. 3.8 (b), the transmission coefficient is better than -1 dB by varying the height H. In Fig. 3.8 (c), the phase response for different incident angles needs to be considered, as transmission phases against different incident angles θ_e are shown, with varying unit cell heights H.

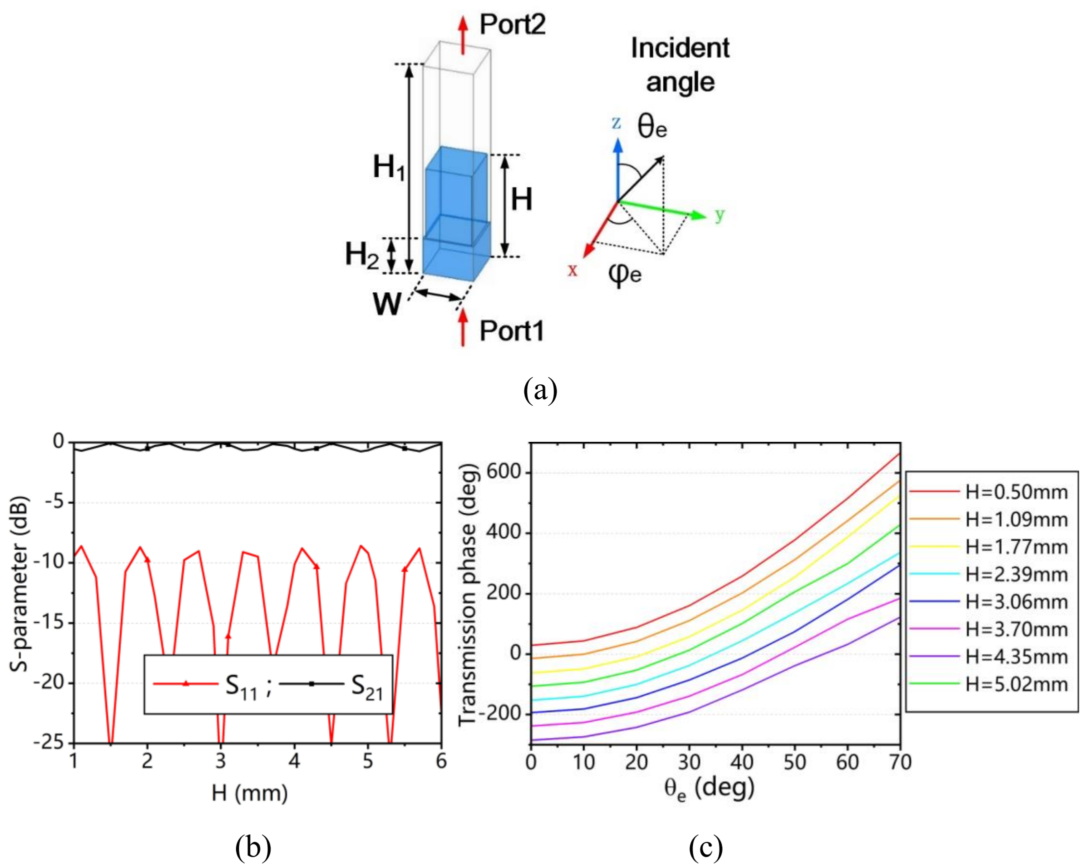

Fig. 3.8. Proposed method of TAA unit cell transmission phase shifting by varying incident angles: (a) Unit cell configuration. ($H1 = 6mm$, $H2 = 0.5mm$, $W = 1\ mm$, H is variable). (b) Transmission and reflection coefficients vary with height at 140 GHz. (c) Transmission phase varies with the incident angle (θ_e) at 140 GHz.

The incidence angle effect [280] has been considered in designing reflectarray antennas (RAAs). As for metalens, the influence of incident angle can be shown in Fig. 3.8 (c). To obtain the relationship between the transmission phase and the incident angle, eight curvilinear equations need to be extracted and utilised in PD calculation. By using the MATLAB basic fitting tool, the cubic curve fitting equation coefficients are obtained, and their corresponding coefficients are shown in Table 3.1, where φ_{trans} is the transmission phase and θ_e represents the incident angle, unit cell 1 corresponds to $H = 5.02\ mm$ in Fig. 3.8 (c), while unit cell 2 refers to $H = 4.35\ mm$ and so on. Additionally, the increase in φ_e (Fig. 3.8 (a)) has little effect on the transmission phase. Therefore, φ_e is equal to 0° in this case.

TABLE 3.1

TRANSMISSION PHASE (φ_{trans}) VS. INCIDENT ANGEL (θ_e) BY CUBIC CURVE FITTING EQUATION (φ_{trans}=A*$\theta_e{}^3$+B*$\theta_e{}^2$+C*θ_e+D)

Unit cell	1(H=5.02mm)	2(H=4.35mm)	3(H=3.7mm)	4(H=3.06mm)	5(H=2.39mm)	6(H=1.77mm)	7(H=1.09mm)	8(H=0.5mm)
A	-0.00083	-0.00117	-0.00034	-0.00089	-0.00075	-0.00042	-0.00063	-0.00054
B	0.148068	0.186158	0.119518	0.166241	0.164166	0.153432	0.169227	0.172056
C	-0.486	-1.22129	0.305155	-0.30907	-0.19753	-0.22715	-0.33878	-0.28517
D	-284.45	-235.344	-194.466	-152.824	-106.515	-62.1204	-13.8539	29.78446

3.3.2 Multifocal Principle and Genetic Algorithm Optimisation

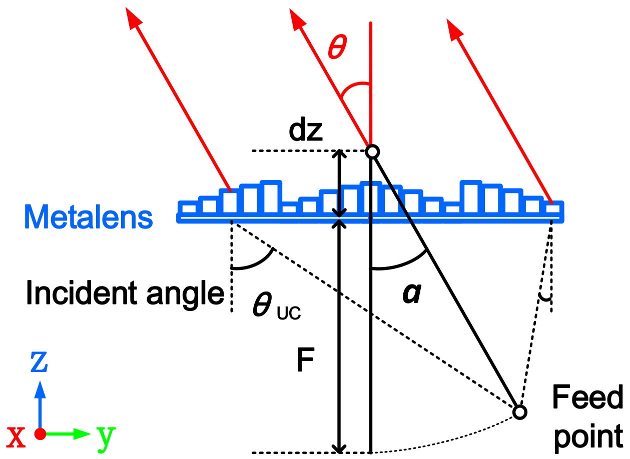

Fig. 3.9. Coordinate system of the proposed metalens.

A 25×25 metalens is employed to demonstrate the principle by using the coordinate system shown in Fig. 3.9, where the focal length is F, dz is the offset of the feeding source rotation centre, α is the rotation angle of the feeding source, and θ is the radiation beam direction. By default, the feeding source is coplanar with the beam. The PD of the metalens is based on Fermat's principle. The input PD for each unit cell can be given by:

$$\varphi_{ij} = k_0(\sqrt{\left(x_{ij} - x_F\right)^2 + \left(y_{ij} - y_F\right)^2 + F^2} - (F - z_F)) \tag{3.4}$$

where k_0 is the wave number in free space, and (x_F, y_F, z_F) represents the position of the feeding source, and (x_{ij}, y_{ij}) is the position of the unit cell. Regarding the metalens, the incident angle of the i, j th unit cell $\theta_{e\,ij}$ can be given by:

$$\theta_{e\,ij} = \left| \arctan\left(\frac{\sqrt{\left(x_{ij} - x_F\right)^2 + \left(y_{ij} - y_F\right)^2}}{F - z_F}\right) \right| \tag{3.5}$$

The transmission phase can be calculated using the equation from Table 3.1.

$$\varphi_{trans,ij} = f(\theta_{e\,ij}) \tag{3.6}$$

Thus, the calculated PD is given by:

$$\varphi_{cal,ij} = \varphi_{ij} - \varphi_{trans,ij} \tag{3.7}$$

To obtain a tilting beam angle, the i, j th ideal output PD can be given by:

$$\varphi_{ideal,ij} = k_0\, y_{ij}\, sin\theta \tag{3.8}$$

$$\varphi_{ideal,ij} = mod(\varphi_{ideal,ij} + \varphi_0, 360°) \tag{3.9}$$

where k_0 represents the wave number, (θ, φ) indicates the angle of the radiation beam, and φ_0 is the additional phase that does not affect the main beam direction. The ultimate purpose is to make φ_{cal} close to φ_{ideal}. In this case, there are four output PDs φ_{cal}, when $\alpha = 0°$, $\alpha = 10°$, $\alpha = 20°$,and $\alpha = 30°$. Their corresponding PDs φ_{ideal} are related to $\theta = 0°$, $\theta = 10°$, $\theta = 20°$, and $\theta = 30°$.

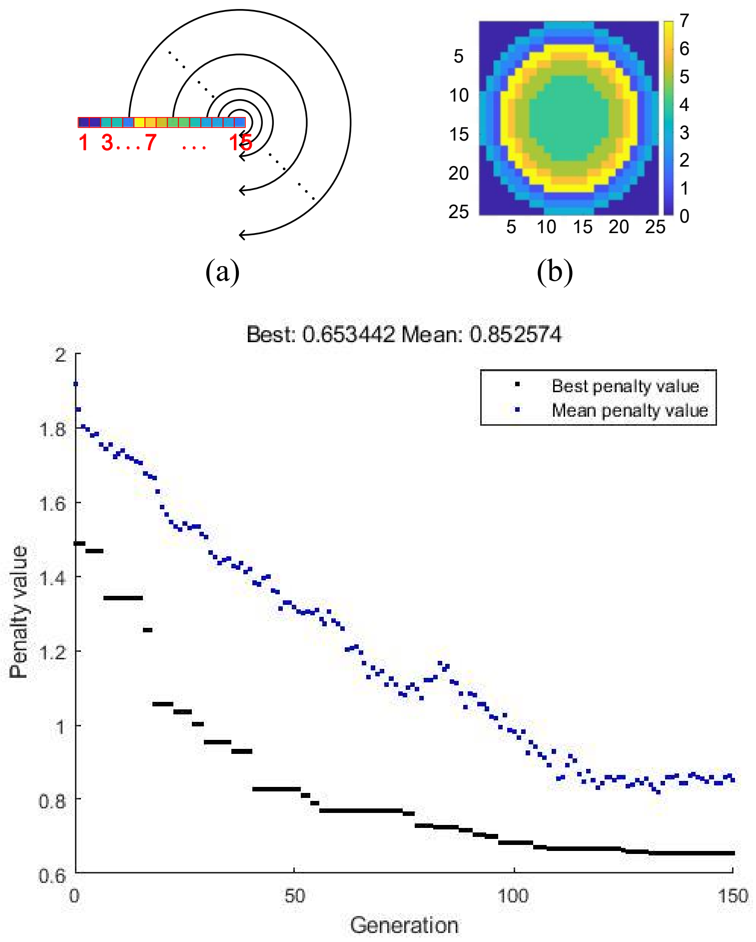

(c)

Fig. 3.10. GA-based 2D multifocal metalens. (a) Rotation of a row of unit cells. (b) Optimal PD. (c) GA convergence procedure.

Genetic algorithm (GA) [281], [282] has been used in designing an ultrawideband metalens or transmitarray. It can also be used to optimise the unit cells to fit the dielectric unit cell in a multifocal metalens. However, there are some restrictions to optimisation. As shown in Fig. 3.10 (a), to realise centrosymmetric PD, a row of unit cells rotates around the centre to generate a 2D PD in Fig. 3.10 (b), and the dark blue parts except the circle are set to 0. This process can reduce the number of optimisation parameters instead of optimising an entire matrix, which can reduce the computational load. The population size is 120, and the generation is 150 in the GA-based optimisation. These unit cells' series numbers are integer variables to be optimised. The parameters of 'dz' and 'F' are also included in the optimisation parameters. The cost function is set as an average difference between the calculated and ideal phase for all the unit cells.

There are four ideal PDs for $\theta = 0°$, $\theta = 10°$, $\theta = 20°$, and $\theta = 30°$. Thus, their corresponding initial phases φ_0 are also set as optimisation parameters. The GA convergence procedure is shown in Fig. 3.10 (c).

$$\sigma = \frac{1}{4 \times n \times n} \sqrt{\sum_{m=1}^{4} \sum_{i=1}^{n} \sum_{j=1}^{n} |\varphi_{cal,ij} - \varphi_{ideal,ij}|} \qquad (3.10)$$

where $n = 25$ is the dimension of the metalens, and m represents the four beam directions ($\theta = 0°$, $\theta = 10°$, $\theta = 20°$, and $\theta = 30°$). The optimised unit cell series is [3, 2, 1, 7, 6, 5, 5, 4, 4, 4, 4, 4, 4], which corresponds to the phase transmission in Fig. 3.10 (b). The optimal focal length 'F' and the centre offset 'dz' are 24.2 mm and 3.9 mm. The additional phases φ_0 for $\theta = 0°$, $\theta = 10°$, $\theta = 20°$, and $\theta = 30°$ are 221.9°, 243.6°, 91.9°, and 167.3°, respectively. The PD comparisons are shown in Fig. 3.11. The PDs in Fig. 3.11 (a) are obtained by calculating Equation (3.6), while the ideal PDs in Fig. 3.11 (b) are from Equation (3.8). The difference between the calculated PDs and the ideal PDs is shown in Fig. 3.11 (c), where the phase difference is lower than 65° when $\alpha = 0°$, which is enough for generating a plane wave. The other phase differences with different α are mostly lower than 45° (dark blue).

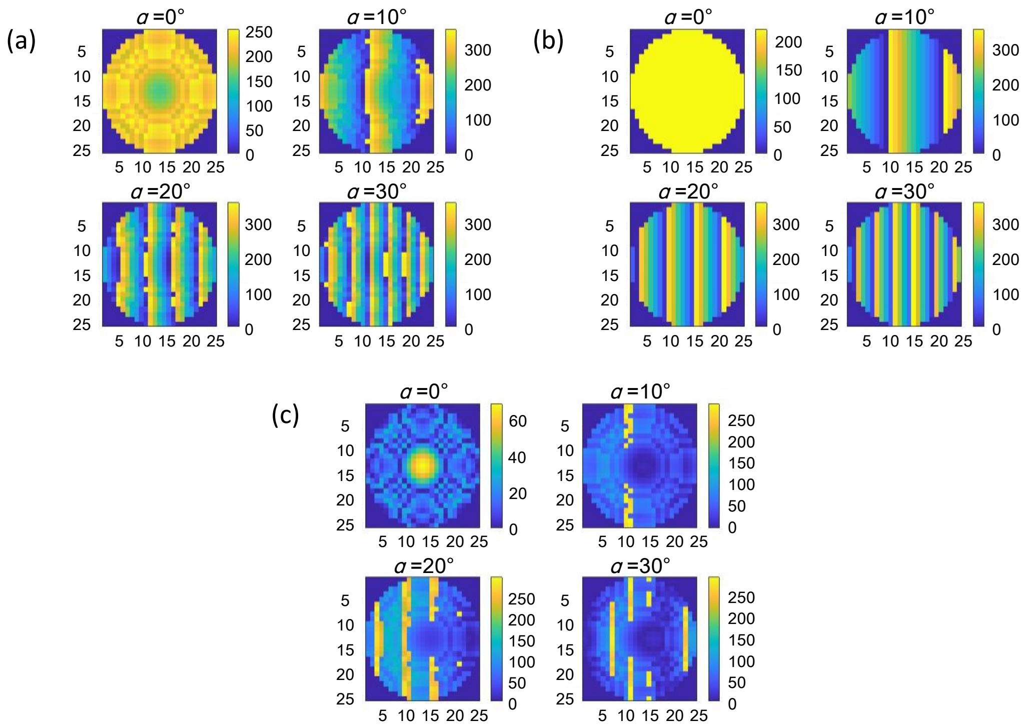

Fig. 3.11. GA-based multifocal metalens PDs. (a) Calculated output PDs of the proposed metalens, (b) Ideal output PDs, and (c) Difference between (a) and (b).

3.3.3 Influence of the Feed Source

In aperture-type antennas, like reflectarray and lens, aperture efficiency (η_{ap}) can be calculated as:

$$\eta_{ap} = \frac{G \cdot \lambda^2}{4\pi A} \tag{3.11}$$

where G represents the gain of the antenna without a logarithmic unit, λ is the wavelength, and A is the physical aperture size. However, Equation (3.11) cannot express the main factors that influence the overall aperture efficiency, and the dominant factors are spillover (η_s) and illumination (η_i) efficiencies[283].

$$\eta_{ap} = \eta_s \, \eta_i \tag{3.12}$$

These two factors are directly related to the aperture-type antenna's performance. The term "spillover" is defined in [284]. Spillover efficiency (η_s) is defined as the power from the feed that is not intercepted by the reflecting elements. The illumination efficiency (η_i) is defined as the power received by the reflectarray divided by the power radiated by the feed into a section of space limited by the reflectarray [285]. Although references [283] and [285] discussed reflectarrays, the basic principle of the reflectarray is similar to that of the lenses. Therefore, the same aperture efficiency definitions can be applied in the lens analysis. In this context, η_s represents the ratio of the total power radiated by the feed source to the power received by the lens, and η_i denotes the ratio of the output power to the input power of the lens. In other words, η_s and η_i correspond to the feed source and the lens, respectively. The purpose of this discussion is to emphasise that a certain level of feed directivity is essential to achieve high aperture efficiency in the metalens.

The gains of the waveguide probe and waveguide horn in Fig. 3.12 (a) and (b) are 6 dBi and 14 dBi, respectively. The proposed metalens is shown in Fig. 3.12 (c). Its aperture size is about $14.5^2\pi$ mm^2 for the tradeoff of aperture efficiency. The focal length (*f*) is 24.1 mm since the phase centre of the waveguide horn in Fig. 3.12 (d) is close to its front end. The tilting angles of the waveguide horn, *a*, and the focal arc are shown. By contrast between the waveguide probe-fed metalens and waveguide horn-fed metalens of the radiation pattern, the simulated value of the performances for different α is shown in Fig. 3.13. The metalens leads to the gain enhancement of about 16.5 dB and 13.8 dB for the waveguide probe and horn. The feed sources influence the aperture efficiency primarily through their spillover efficiency. The beamwidth of the waveguide probe is excessively large to be fully covered by the metalens. In such cases, increasing the metalens size leads to excessively large incident angles of the EM wave at the outermost ring, causing the unit cells of the metalens to operate improperly. Therefore, it is essential to limit the beamwidth of the feed source. The proposed metalens achieves high gain, high aperture efficiency, and a low side-lobe level (SLL) across different scanning angles.

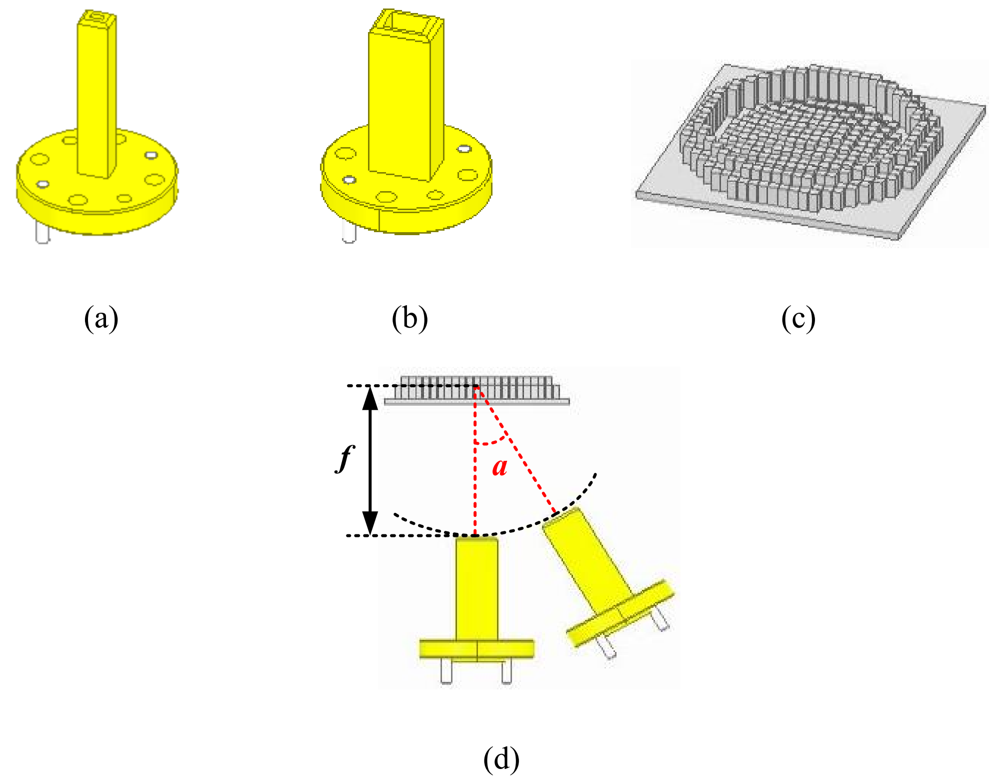

Fig. 3.12. GA-based metalens antenna comparison. (a) WR-06 waveguide probe. (b) WR-06 waveguide rectangular horn. (c) Metalens. (d) Metalens antenna.

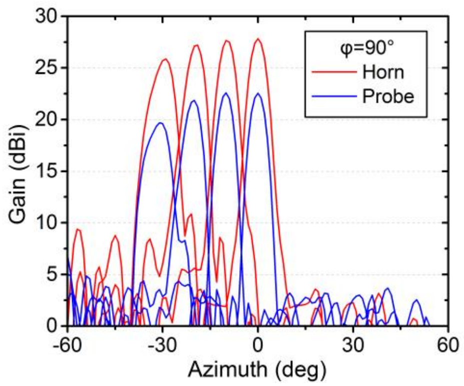

Fig. 3.13. Radiation pattern comparison of the GA-based metalens antenna.

The design and optimisation process of the proposed 2D beam-steering metalens can be summarised as follows:

1) Select the desired central operating frequency of the metalens.
2) Design eight metalens unit cells that cover a full phase cycle (2π). These can be metal–dielectric unit cells provided that their transmission phase varies with the incident angle, as illustrated in Fig. 3.8 (c).
3) Obtain the fitting curves of these metalens unit cells and ensure the relationship

between the transmission phase and incident angle.

4) Mark these eight unit cells and their corresponding fitting curves from 1 to 8. These integer numbers 1-8 are used as optimisation parameters.
5) Select a row of unit cells (unit cell range from 1 to 8) and rotate it to generate a phase distribution. Calculate the phase distribution's output phase distribution based on Equation (3.7).
6) Calculate the ideal output phase distribution of different radiation angles based on Equation (3.8). Each radiation angle corresponds to an initial phase φ_0. These initial phases are used as optimisation parameters.
7) Calculate the root-mean-square error (RMSE) between the output phase distribution in step 5 and the ideal output phase distribution.
8) Input the scanning centre offset 'dz' and focal length '*f*' as the optimisation parameters.
9) Use GA optimisation in MATLAB to minimise the RMSE.
10) Obtain the 2D phase distribution and simulate it using HFSS, and optimise the parameters 'dz' and '*f*'.

The dielectric metalens readily satisfy the requirements outlined in Step 2, although the possibility of metal–dielectric unit cells meeting the same criteria is not excluded. The output phase distribution calculation in Step 5 incorporates the positional information of the feed sources; therefore, the proposed method can realise both a common focal plane and various focal-arc configurations. If the result obtained in Step 10 is unsatisfactory, the process can revert to Step 9, where the random seed of the optimisation is modified to identify another minimum root-mean-square error (RMSE). Based on an analysis of its operating principle, a 2D multifocal metalens design procedure is established, resulting in a metalens with higher gain and a lower side-lobe level (SLL).

3.3.4 Measurement and Comparison

The far-field measurement setup consists of a Keysight PNA Network Analyser N5225B, a VDI WR 6.5 extension module transmitter (D-band, 110 – 170 GHz), and a

VDI WR 6.5 extension module receiver. The D-band transmitter is aligned with the receiver. The transmitter and the metalens are placed on the white plastic tray. The tray can be rotated along the track by controlling the motor through a computer. The gain of the feed horn is about 14 - 15 dBi. The aperture size is about $14.5^2\pi\ mm^2$, the focal length is $24.2\ mm$, and the offset of the centre is $3.9\ mm$ in HFSS, and the focal-to-diameter (F/D) ratio is 0.83.

Fig. 3.14 shows the simulated and measured beam-scanning radiation patterns at 130 GHz, 140 GHz, and 150 GHz in the E-plane ($\varphi = 0°$), D-plane ($\varphi = 45°$), and H-plane ($\varphi = 90°$). The simulated and measured cross-polarisation is 30-40 dB lower than the co-polarisation. Thus, they are omitted for brevity. The simulated gains of the metalens at 140 GHz are from 26.6 to 28.1 dBi with a scan loss of about 1.5 dB, while the measured ones are from 24.5 to 26.6 dBi with a scan loss of 2.1 dB. This means the proposed dielectric metalens realises a 2D beam-scanning performance within ±30° from the frequency of 130 GHz to 150 GHz. The simulated and measured peak gains at different scanning angles are given in Fig. 3.15. The peak gains with the same θ are almost equal. The simulated peak gains are 27.4–28.2 dBi at $\theta = 0°$ and $\theta = 10°$, 27.0–28.0 dBi at $\theta = 20°$, and 25.6–27.2 dBi at $\theta = 30°$. The measured peak gains are 26.5–28.0 dBi at $\theta = 0°$, 26.1–27.8 dBi at $\theta = 10°$, 26.3–28.0 dBi at $\theta = 20°$, and 24.7–26.2 dBi at $\theta = 30°$.

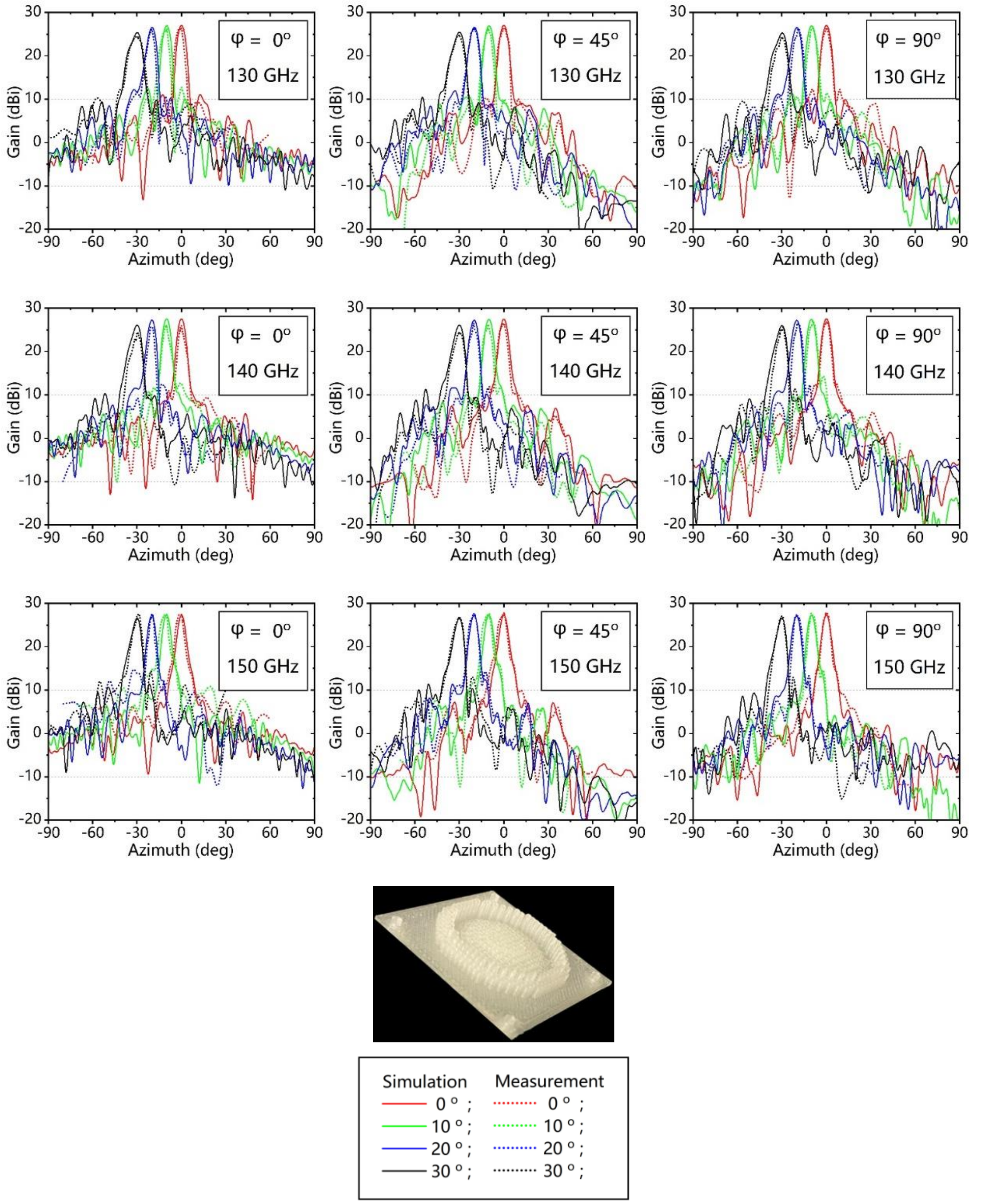

Fig. 3.14. Simulated and measured beam steering radiation patterns at 130 GHz, 140 GHz, and 150 GHz.

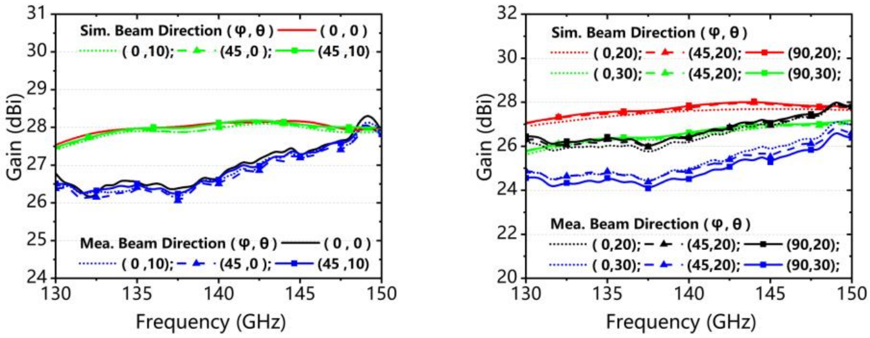

(a) (b)

Fig. 3.15. Simulated and measured peak gain for different scanning angles when (a) $\theta = 0°$, $\theta = 10°$, (b) $\theta = 20°$, and $\theta = 30°$.

The proposed metalens is compared with other relevant state-of-the-art designs in Table 3.2. Since measured results can be affected by fabrication tolerance and experimental setup, to be fair, we only compare the simulated results of our proposed design to simulations of those in the literature with experimental validation. Due to a lower focal length and a large F/D, lens antennas in [258], [259] realise high AE and wide scanning range, but the gain improvement compared to the feeding source is limited. In [261], by using a tapered matching structure, the transmission phase of the unit cells is not sensitive to the incident angles. Whereas the proposed design can realise high gain improvement (about 14.1 dB in simulation) and $\pm 30°$ 2D beam scanning performance. Nevertheless, the measured gain experiences a 1-2 dB reduction due to fabrication errors.

TABLE 3.2
COMPARISONS WITH OTHER MECHANICAL BEAM STEERING LENSES

Ref	Freq. (GHz)	Gain (dBi)	Source Gain (dBi)	Gain Impv. (dB)	AE (%)	D*(λ_0)	F*(λ_0)	F/D	Scan range	Scan loss (dB)
[258]	13	21.9	17.5	4.4	64.31	4.94	3.64	0.73	$\pm 45°$ (2D)	2.6
[259]	190	29.6	22	7.6	35.7	14.2	35.2	2.48	$\pm 48°$ (1D)	1.4~4
[261]	30	29.97	17	12.97	35.12	15	15	1	$\pm 30°$ (1D)	2.9
This work	140	28.1	14	14.1	48.06	11.67	11.25	0.96	$\pm 30°$ (2D)	1.5

D* : Diameter; F* : Focal length

In summary, a sub-THz multifocal dielectric metalens for 2D mechanical beam-scanning is presented. The proposed metalens can be simultaneously excited by multiple ports with different incident angles. By using a cubic curve fitting equation, the eight unit cells' relationships between the transmission phase and incident angle are obtained and incorporated into the GA optimisation. The circular PD of the metalens reduces the parameter to be optimised and achieves 2D beam-scanning performance. The beams are tilted at 0°, 10°, 20°, and 30° in the E-, D-, and H-planes. Owing to its 2D beam-scanning capability, high gain, high AE, and low fabrication cost, the proposed metalens represents a promising candidate for future THz communication applications.

3.4 3D-Printed Continuous Quasi-Fresnel Metalens for THz Tilted Imaging Application

Fresnel lenses (FLs) have a broad application in lighting, collimators, imaging, and concentrated solar energy [286], which has the advantage of being lightweight and having a better ability to focus light. Conventional optical FLs feature a concentric circular configuration and are primarily used to transform spherical waves into planar waves. In such lenses, portions of the straight optical path within the glass can be removed while retaining the refractive surface profile. Traditional FLs are mainly designed to perform the simple function of converting a plane wave into a spherical wave under normal incidence. However, the calculation of curved surfaces becomes increasingly complex when designing lenses for more advanced functionalities. Discrete dielectric lenses (DDLs) [287] are created by dividing the lens like a chessboard. Its phase distribution can be calculated using Fermat's principle [288], making it easier to design various types of lenses. 3D printing techniques [289] are well-suited for fabricating lenses with special structures. In this context, this section proposes a quasi-Fresnel lens (QFL) for near-field focusing, inspired by the principle of DDLs. The proposed configuration significantly reduces slicing and printing time, enabling the fabrication of larger-aperture lenses.

3.4.1 Quasi-Fresnel Metalens Design

The UC shown in Fig. 3.16 (a) is fabricated using cyclic olefin copolymer (COC), a 3D-printing material with 100% infill, a relative permittivity of 2.23, and a loss tangent of 0.001 at the D-band (110–170 GHz). The UC consists of an air box section and a uniform dielectric post, with a total height fixed at H_1 = 6 mm. As illustrated in Fig. 3.16(b), the transmission phase covers a full 360° phase cycle as the height of the dielectric post increases.

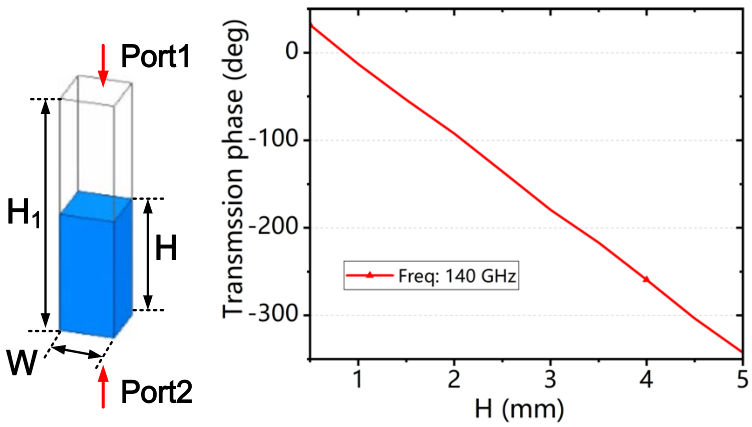

(a) (b)

Fig. 3.16. Discrete dielectric lens unit cell. (a) UC configuration (H1 = 6 mm, W = 1 mm, H is variable) ; (b) Transmission phase varies with the high (H) dielectric post.

To generate a focal spot on the other side, the phase distribution of DDL can be given:

$$\varphi_{in} = k_0(\sqrt{F^2 + x^2 + (y + d)^2} - F) \tag{3.13}$$

$$\varphi_{out} = k_0(\sqrt{F^2 + x^2 + (y - d)^2} - F) \tag{3.14}$$

$$\varphi = \varphi_{in} + \varphi_{out} \tag{3.15}$$

where k_0 and d represent the wave number and the offset of the feed source, (x, y) is the position of the UC. The calculated phase distribution of the DDL is shown in Fig. 3.17 (a). As for the DDL, the period of the UC is about half the wavelength. When modelling the DDL, there is a tiny air gap between the UC to prevent the modelling error in simulation [30]. Therefore, UCs need to be built one by one, and the model of the DDL is shown in Fig. 3.17 (b). Imaging lenses require a larger aperture to capture more light for higher-quality images. With the increase in the aperture size, the number of UCs in the array increases rapidly, growing by a factor of the square of the number of columns. The modelling and 3D printing of DDLs with a large aperture requires significant time. Therefore, a QFL is proposed to generate a larger imaging lens. With the same edge length *D*, the UC's period of the QFL is one-tenth that of the DDL. Based on the corresponding phase distribution shown in Fig. 3.17 (c), the lens surface is depicted using two-point Polylines in Ansys. Then, the lens connection can create the cross-section of the lens, and the surface connection creates the lens shown in Fig. 3.17 (d). According to the simulation in Fig. 3.18, the proposed QFL has a similar focusing performance to the corresponding DDL at 140 GHz, as shown in Fig. 3.19. The half-power beam width of the focal spot is 3.6 mm.

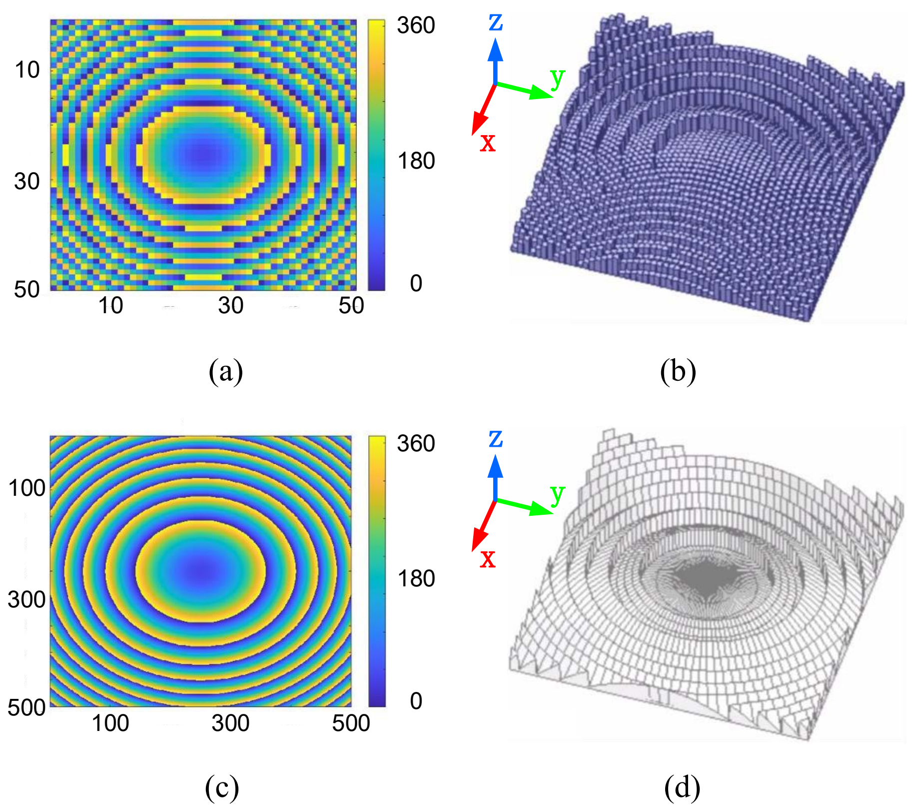

Fig. 3.17. Comparison between DDL and QFL (F = 40 mm, D = 50 mm, d = 23.1 mm, Incident angle is 30°). (a) Phase distribution of the DDL; (b) Model of DDL; (c) Phase distribution of the QFL. (d) Model of QFL.

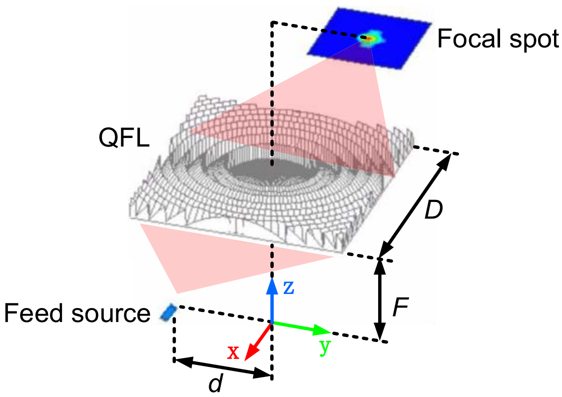

Fig. 3.18. Schematic of the QFL. (F = 40 mm, D = 50 mm, d = 23.1 mm, Incident angle is 30°).

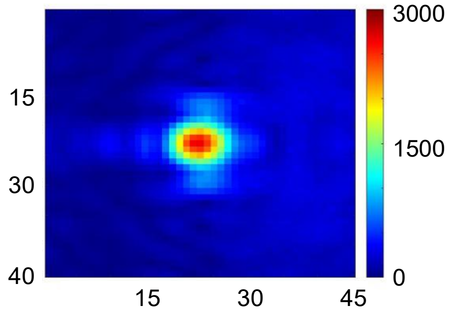

Fig. 3.19. Simulated electric field of the focus spot at 140 GHz.

3.4.2 Focusing Effect Measurement

Owing to the configuration of the QFL, both the slicing and printing times are significantly reduced when fabricated using a fused deposition modelling (FDM) 3D printer. The printing process requires approximately two and a half hours. The fabricated QFL is shown in Fig. 3.20 (a), with a focal length of 68 mm and a diameter of 80 mm. The measurement setup, illustrated in Fig. 3.20 (b), consists of a 140 GHz feed source and a THz camera (TeraSense). The camera outputs intensity values ranging from 0 to 255 and contains 1024 pixels arranged in a 32 × 32 array, with a pixel size of 1.5 mm. The focal spot diameter, shown in Fig. 3.21 (a) and (b), ranges from 4.5 mm to 6 mm when the feed source is a horn antenna. As illustrated in Fig. 3.21 (c), the focusing effect becomes more pronounced when the feed source is a waveguide probe, resulting in a focal spot diameter of approximately 3 - 4.5 mm, corresponding to 2–3 pixels, indicating an approximate imaging resolution of around 3 – 4.5 mm. The 3D-printed QFL successfully demonstrates near-field focusing capability, exhibiting a clear focusing effect. Furthermore, its compact and efficient configuration enables the fabrication of larger-aperture lenses, making it a promising candidate for sub-THz imaging system applications.

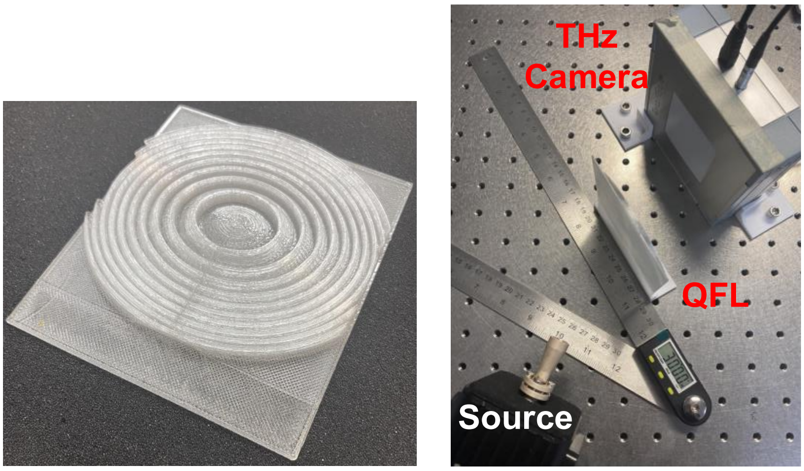

(a) (b)

Fig. 3.20. (a) Photo of the 3D printed QFL. (F = 68 mm, D = 80 mm, d = 39.2 mm, Incident angle is 30°. (b) Measurement setup.

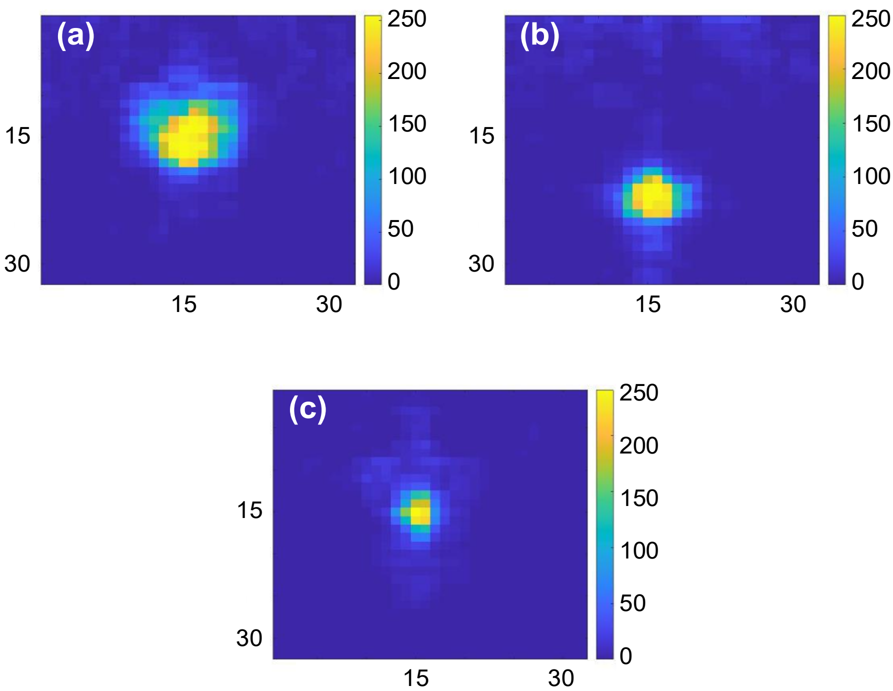

Fig. 3.21. The measured electric field of the focal spot at 140 GHz: (a) when the source is a horn antenna, (b) when the horn antenna source is moved, and (c) when the source is a waveguide probe.

The 3D-printed QFL has been demonstrated for near-field focusing. The focusing effect is obvious. The configuration of the QFL enables the fabrication of a larger lens, which can potentially be used in sub-THz imaging systems.

3.4.3 Fresnel Lens Imaging Experiment

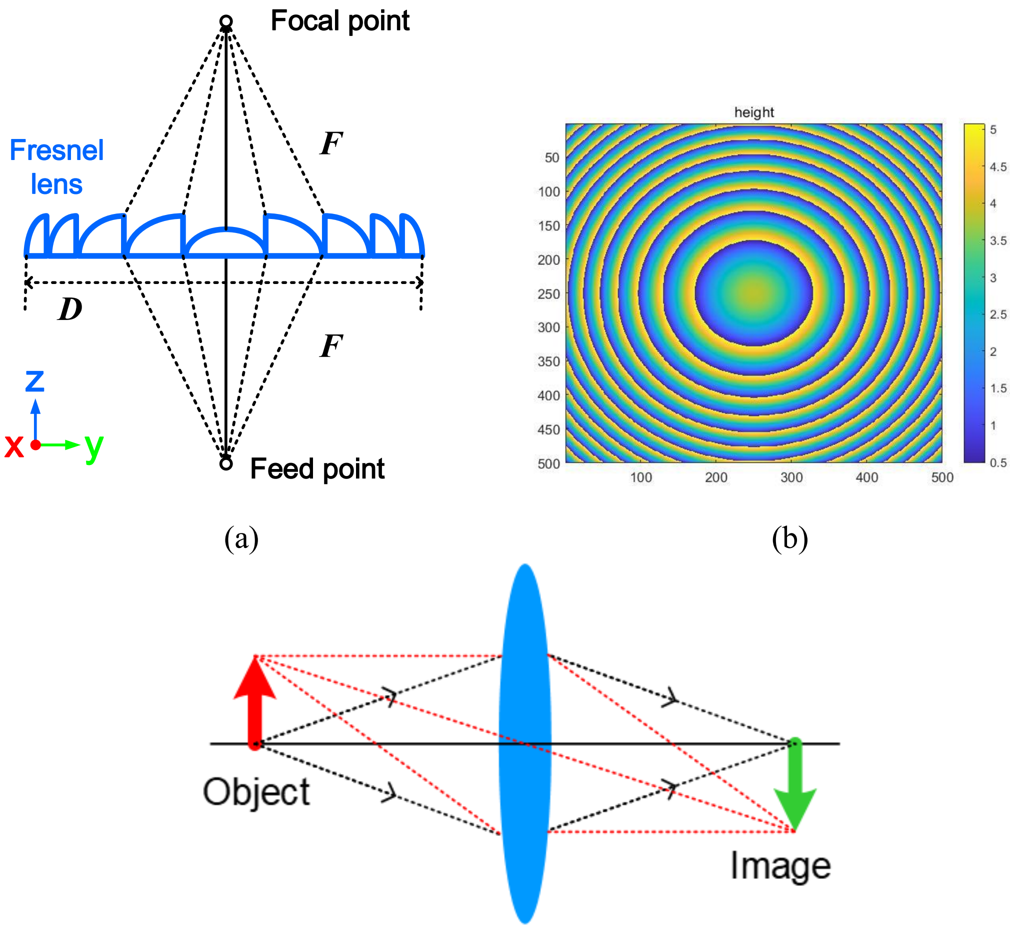

(c)

Fig. 3.22. (a) Schematic of the Fresnel lens ($F = 35\,mm, D = 50\,mm$). (b) Phase distribution of the Fresnel lens when $W = 0.1\,mm$. (c) Schematic of the ideal imaging condition.

Based on the aforementioned design method, another quasi-Fresnel lens is designed for normal incident real-time imaging. Based on Fermat's principle, which states that the circuit length of the incident electromagnetic wave is equal, the required phase compensation for each unit cell is obtained.

$$\varphi_{in} = k_0(\sqrt{F^2 + x^2 + y^2} - F) \tag{3.16}$$

$$\varphi_{out} = k_0(\sqrt{F^2 + x^2 + y^2} - F) \tag{3.17}$$

$$\varphi = \varphi_{in} + \varphi_{out} \tag{3.18}$$

where F is the focal length, k_0 represents the wave number, (x, y) is the position of the UC. The schematic of the Fresnel lens is shown in Fig. 3.22 (a), featuring a focal length of 35 mm and a diameter of 50 mm. As the aperture size increases, the number of UCs in the array rises rapidly, proportional to the square of the number of columns. In comparison, the continuous structure of the proposed Fresnel lens substantially reduces both modelling and printing time. Fig. 3.22 (b) illustrates the thickness distribution of the lens units, where the horizontal and vertical axes represent the unit indices in the array. The schematic of the ideal imaging condition is presented in Fig. 3.22 (c). Lens imaging can be understood as the refocusing of diverging waves emitted from an object. The object is regarded as an electromagnetic emitter composed of multiple point sources, while the lens operates to converge the waves from each point source onto their corresponding focal positions on the opposite side, thereby achieving real-time imaging in the THz band.

The simulation model is shown in Fig. 3.23 (a), with a WR06 waveguide probe feeding at the bottom of the lens. Due to the large size of the lens used for testing, the simulation requires an excessive amount of memory. Therefore, a smaller model is used for simulation. The electric field is displayed within a $22\ mm\ \times\ 22\ mm$ range, with a working frequency of 140 GHz. To reduce simulation time, the diameter was adjusted to 41.6 mm. The simulated electric field pattern is shown in Fig. 3.23 (b). When the waveguide is positioned at the points (0,0), (3.5,0), and (7,0), the energy radiated by the waveguide converges again to the corresponding locations in the electric field display area. This indicates that a mirrored image can be formed on the other side of the lens. The corresponding half-power beam widths (HPBWs) are 2.8 mm, 2.5 mm, and 2.9 mm, indicating an approximate imaging resolution of around 2.5 - 2.9 mm.

Fig. 3.24 (a) illustrates the structure of the real-time imaging system, which comprises a 140 GHz feed source, a convex lens, a plano-convex lens, a conductive sticker with a T-shaped notch, a Fresnel imaging lens, and a THz camera (TeraSense).

All lenses are 3D-printed using COC material. The focal points of the convex and plano-convex lenses overlap, and their large separation distance helps minimise the direct influence of the feed source on the imaging process. The plano-convex lens generates plane waves, while the conductive sticker blocks EM waves, with the T-shaped notch serving as the test object. As shown in Fig. 3.24 (b), a mirrored image of the T-shaped notch is formed on the camera sensor. The camera provides intensity values ranging from 0 to 255 and contains 1024 pixels arranged in a 32×32 array, with a pixel size of 1.5 mm. Since the focal lengths of the lenses are identical on both sides, the actual size of the T-shaped notch closely matches the image captured by the camera, measuring approximately 3 mm in width and 10 mm in length. The conductive sticker is mounted on a manually controlled XY motor stage to enable precise positional adjustment. Slight asymmetry and blurred edges in the image may result from measurement errors or fabrication inaccuracies; however, a clear mirrored image of the T-shaped notch was successfully obtained.

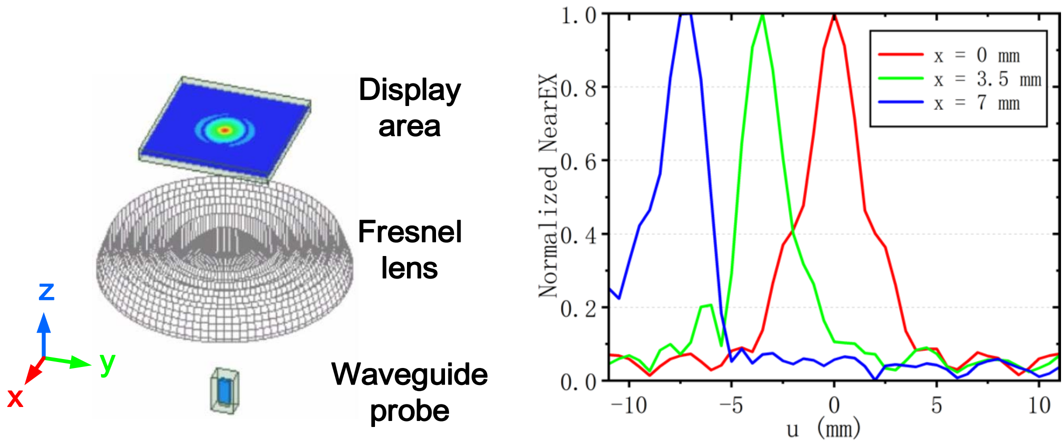

(a) (b)

Fig. 3.23. (a) Simulation model ($F = 35\,mm, D = 41.6\,mm$). (b) The normalised electric field amplitude varies with the position of the waveguide.

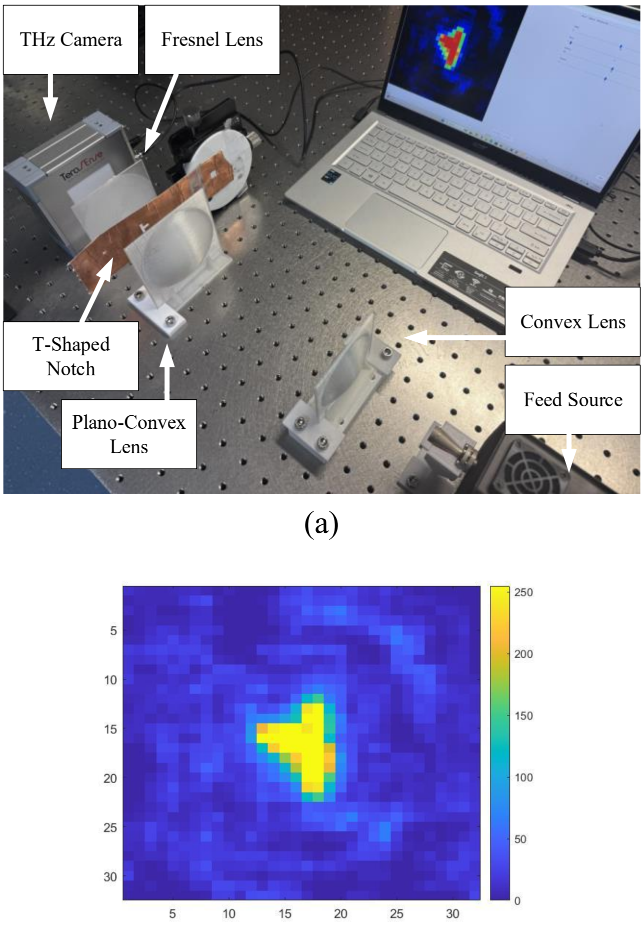

(a)

(b)

Fig. 3.24. (a) Real-time imaging setup. (b) Measured imaging result.

3.5 Conclusion

In this chapter, a series of 3D-printed metalenses for 2D beam scanning, 1D beam scanning, and tilted imaging applications has been presented, demonstrating the potential of low-cost 3D printing technology for THz systems. The discrete metalens facilitates the design of phase distributions for diverse applications; however, its modelling and fabrication processes are time-consuming. In contrast, the continuous metalens significantly reduces modelling time and enables the fabrication of larger apertures, which can collect more electromagnetic waves and thereby enhance imaging quality. Overall, 3D printing technology proves to be a promising and versatile approach for the realisation of all-dielectric metalenses in THz applications.

Chapter IV Conductive and Dielectric Multimaterial Metasurface Lens

4.1 Introduction

Conductive and dielectric metasurface lenses can be fabricated using printed circuit board (PCB) and additively manufactured electronics (AME) technology. Conductive structures can achieve stronger resonance than dielectric structures and can have more freedom in design. AME technology includes metal-only [290], [291], dielectric-only [292], [293] and mixed medium-conductor structures [294], [295], [296], [297]. At present, one of the industry-leading AME technologies originates from the DragonFly IV printer developed by Nano Dimension [298], which can fabricate various electronic components, including the filter [299], metasurface [300], [301], [302], antenna and circuit [303]. The DragonFly IV operates on a piezoelectric inkjet system equipped with two nozzles that simultaneously deposit liquid acrylate dielectric ink (DI) and conductive silver nanoparticle ink (CI). Each of the two print heads contains 512 nozzles dedicated to DI and CI, respectively. Following deposition, an ultraviolet (UV) lamp cures the DI droplets, while an infrared (IR) lamp sinters the CI droplets. Through this process, the prototype is fabricated layer by layer, as illustrated in Fig. 4.1 (where the DI and CI print heads are not shown). The printed prototype is formed on a Kapton film and subsequently peeled off once printing is complete. A solder mask is unnecessary when no lumped components are required for soldering. Moreover, step-shaped and conical structures with non-planar geometries can be readily realised using AME technology.

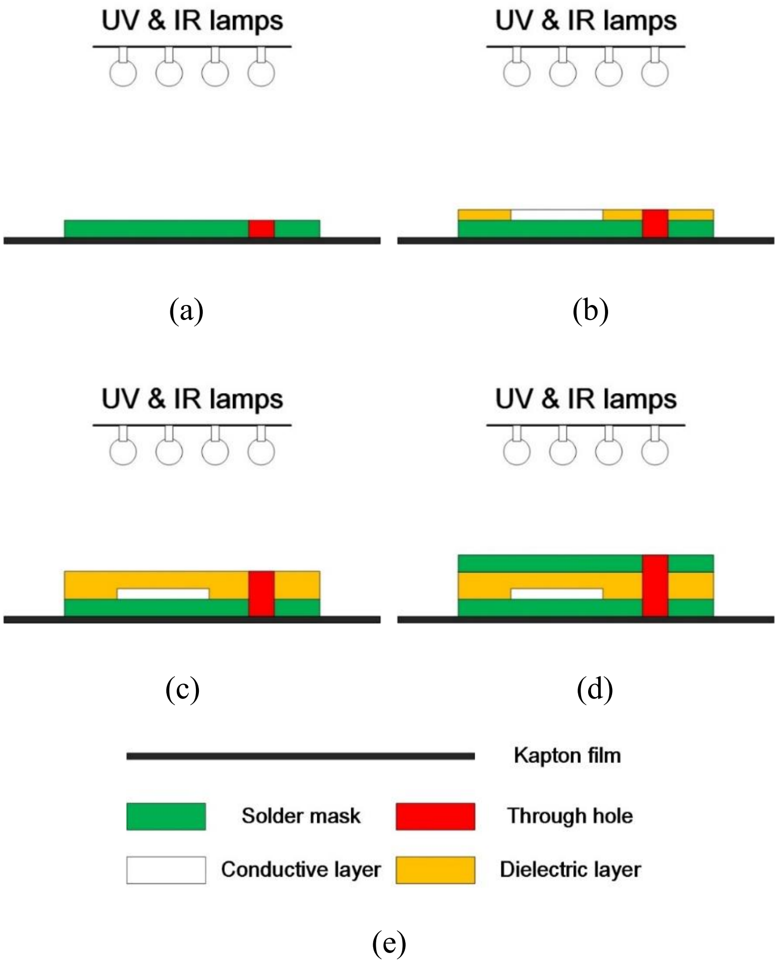

Fig. 4.1. Fabrication process of the applied multimaterial 3D printing. (a) Step 1 – Print the bottom solder mask layer. (b) Step 2 – Print dielectric, conductive patterns and through holes (if any). (c) Step 3 – Print 3D patterns. (d) Step 4 – Print the top solder mask layer for finishing. (e) Graphic symbol.

However, at terahertz (THz) frequencies, the fabrication of metasurfaces using PCB and AME technologies becomes highly challenging due to stringent precision requirements, which in turn restricts the design flexibility. The THz spectrum spans 0.1 - 10 THz, corresponding to wavelengths ranging from 3 mm to 0.03 mm. The typical size of a metasurface unit cell is less than half the wavelength, resulting in a maximum dimension of approximately $1.5\,mm \times 1.5\,mm$. In contrast, the fabrication precision achievable by PCB and AME processes is typically around 0.1 mm, making the design and realisation of THz metasurfaces particularly challenging. Circularly polarised and multi-polarised unit cells are among the key areas of focus in metasurface research. To realise phase modulation of circularly polarised waves, the following section provides a brief introduction to the Pancharatnam–Berry (PB) phase and the corresponding Jones matrix analysis.

4.1.1 Pancharatnam−Berry Phase

In the field of electromagnetic (EM) waves, the PB phase [304], [305] is a widely used mechanism for the phase control of circular polarisation, also referred to as the geometric phase [306], [307], [308]. This concept originates from optical metasurfaces employing nano-pillar structures [309], [310]. By rotating the orientation of the unit cell pattern, the transmission phase of the circularly polarised wave can be effectively modulated [311]. In this manner, ultrathin circularly polarised metasurfaces can be realised [312], [313], [314]. To further elucidate the principle of the PB phase, the Jones matrix analysis [315] is introduced, wherein EM waves are expressed in complex form.

$$\vec{E}(z,t) = \overrightarrow{E_0} \cdot e^{i(\omega t - kz)} \tag{4.1}$$

where ω is the angular frequency, k represents the wavenumber. In this case, the EM wave propagates along the z-axis, $\overrightarrow{E_0}$ represents the vector of the electric field in the x-y plane, which can be given without loss of generality

$$\overrightarrow{E_0} = E_x e^{i\phi_x}\hat{x} + E_y e^{i\phi_y}\hat{y} \tag{4.2}$$

where $(\hat{x}, \hat{y})$ are unit vectors along the x-axis and y-axis, E_x and E_y represents the amplitude of the electric field. ϕ_x and ϕ_y are the phases of the x-component and y-component of the electric field. The EM wave can be packaged in vector notation.

$$\vec{E}(z,t) = \begin{pmatrix} E_x e^{i\phi_x} \\ E_y e^{i\phi_y} \end{pmatrix} e^{i(\omega t - kz)} = E_0 e^{i\phi_x} \begin{pmatrix} cos\chi \\ sin\chi e^{i\phi} \end{pmatrix} e^{i(\omega t - kz)} \tag{4.3}$$

where E_0 is the real-valued amplitude, ${E_0}^2 = {E_x}^2 + {E_y}^2$ and $\phi = \phi_y - \phi_x$. The Jones vector is given by:

$$|j\rangle = \begin{pmatrix} cos\chi \\ sin\chi e^{i\phi} \end{pmatrix} \tag{4.4}$$

where χ can represent the polarisation angle of the electric field and ϕ is the phase difference between the x and y components. An arbitrarily polarised electromagnetic wave can be represented using the Jones vector [156]: linear polarisation is $|j\rangle = [cos\theta; sin\theta]$, left-hand circular polarisation (LHCP) is $|L\rangle = [1, i]/\sqrt{2}$, right-hand circular polarisation (RHCP) is $|R\rangle = [1, -i]/\sqrt{2}$.

Jones matrix, $\boldsymbol{J}$, consists of four complex numbers, which can represent the performance of a metasurface unit cell. It is given by:

$$\boldsymbol{J} = \begin{pmatrix} J_{xx} & J_{xy} \\ J_{yx} & J_{yy} \end{pmatrix} \tag{4.5}$$

where J_{xx} represents the case where an incident wave with an x-component results in the amplitude and phase of the outgoing wave with an x-component after interacting with the unit cell. In contrast, J_{xy} refers to the amplitude and phase of the outgoing y-component resulting from an incident x-component. Therefore, when LHCP is incident on a unit cell, the Jones matrix calculation can be given by:

$$E^{out} = \begin{bmatrix} e^{-i\varphi} & 0 \\ 0 & e^{-i\varphi} \end{bmatrix} \cdot \frac{\sqrt{2}}{2} \cdot \begin{bmatrix} 1 \\ i \end{bmatrix} \tag{4.6}$$

When the unit cell is rotated by an angle θ, the Jones matrix is multiplied by a rotation matrix.

$$\begin{aligned} E^{out} &= \begin{bmatrix} cos\theta & sin\theta \\ -sin\theta & cos\theta \end{bmatrix} \cdot \begin{bmatrix} e^{-i\varphi} & 0 \\ 0 & e^{-i\varphi} \end{bmatrix} \cdot \frac{\sqrt{2}}{2} \cdot \begin{bmatrix} 1 \\ i \end{bmatrix} \\ &= e^{-i\varphi} \cdot e^{-i\theta} \cdot \frac{\sqrt{2}}{2} \cdot \begin{bmatrix} 1 \\ i \end{bmatrix} \end{aligned} \tag{4.7}$$

This indicates that the transmitted wave preserves its circular polarisation, while an additional phase shift is imparted by the metasurface unit cell. The same applies to

RHCP. Therefore, PB metasurface unit cells can achieve phase modulation of circularly polarised waves through rotation.

4.1.2 Jones Matrix Calculation

Since HFSS simulation software provides results only for x- and y-polarised waves, the CP results must be obtained by combining the dual linear polarisation components through Jones matrix analysis. This approach allows the derivation of the LHCP and RHCP components. The simulation results of the dual linear polarisations can therefore be represented in the following Jones matrix, expressed as:

$$\boldsymbol{T} = \begin{bmatrix} T_{xx} & T_{xy} \\ T_{yx} & T_{yy} \end{bmatrix} \tag{4.8}$$

where T denotes the transmission coefficient, and the subscripts are the same as those in Equation (4.8). Under the LHCP incidence, $|L\rangle = [1, i]/\sqrt{2}$, the corresponding Jones matrix is expressed as:

$$\begin{bmatrix} T_{xx} & T_{xy} \\ T_{yx} & T_{yy} \end{bmatrix} \cdot \frac{\mathbf{1}}{\sqrt{\mathbf{2}}} \begin{bmatrix} \mathbf{1} \\ \boldsymbol{i} \end{bmatrix} = \boldsymbol{A} \cdot \frac{\mathbf{1}}{\sqrt{\mathbf{2}}} \cdot \begin{bmatrix} \mathbf{1} \\ \boldsymbol{i} \end{bmatrix} + \boldsymbol{B} \cdot \frac{\mathbf{1}}{\sqrt{\mathbf{2}}} \cdot \begin{bmatrix} \mathbf{1} \\ -\boldsymbol{i} \end{bmatrix} \tag{4.9}$$

After the LHCP incidence, both LHCP and RHCP components are obtained, where A and B represent the transmission coefficients of these two components, respectively. Based on the calculation, the transmission coefficients A and B can be expressed as follows:

$$\begin{aligned} \boldsymbol{A} &= \frac{\mathbf{1}}{\mathbf{2}}\left[T_{xx} - T_{yy} + i\left(T_{xy} + T_{yx}\right)\right] \\ \boldsymbol{B} &= \frac{\mathbf{1}}{\mathbf{2}}\left[T_{xx} + T_{yy} + i\left(T_{xy} - T_{yx}\right)\right] \end{aligned} \tag{4.10}$$

By inputting this equation into the simulation software, the transmission coefficients for the LHCP and RHCP components of the unit cell can be obtained. Similarly, for unit cells designed to convert linear polarisation into circular polarisation, the corresponding transmission coefficients can be calculated using the following equation, when an X-polarised wave is incident.

$$\begin{bmatrix} T_{xx} & T_{xy} \\ T_{yx} & T_{yy} \end{bmatrix} \cdot \begin{bmatrix} \mathbf{1} \\ \mathbf{0} \end{bmatrix} = \boldsymbol{A} \cdot \frac{\mathbf{1}}{\sqrt{\mathbf{2}}} \cdot \begin{bmatrix} \mathbf{1} \\ \boldsymbol{i} \end{bmatrix} + \boldsymbol{B} \cdot \frac{\mathbf{1}}{\sqrt{\mathbf{2}}} \cdot \begin{bmatrix} \mathbf{1} \\ -\boldsymbol{i} \end{bmatrix}$$
$$\boldsymbol{A} = \frac{\sqrt{\mathbf{2}}}{\mathbf{2}} \left[T_{xx} + i \cdot T_{yx}\right] \tag{4.11}$$
$$\boldsymbol{B} = \frac{\sqrt{\mathbf{2}}}{\mathbf{2}} \left[T_{xx} - i \cdot T_{yx}\right]$$

Thus, the transmission coefficients for various polarisations can be calculated.

4.2 Circularly-Polarised Multimaterial Metasurface Lens For High Gain Enhancement and 2D Beam-Scanning

The THz spectrum (0.1 - 10 THz) has been attracting increasing research attention. Recently, the THz frequency band from 95 GHz to 3 THz has been allocated for sixth-generation (6G) mobile communication experiments, aiming to integrate air-, space-, and ground-based connections [316], as illustrated in Fig. 4.2. THz waves provide broadband communication capability for inter-satellite links, with minimal atmospheric absorption in the vacuum environment. To achieve dynamic and reliable communication, the beam-steering technique [317] is highly anticipated to play a key role in future 6G networks.

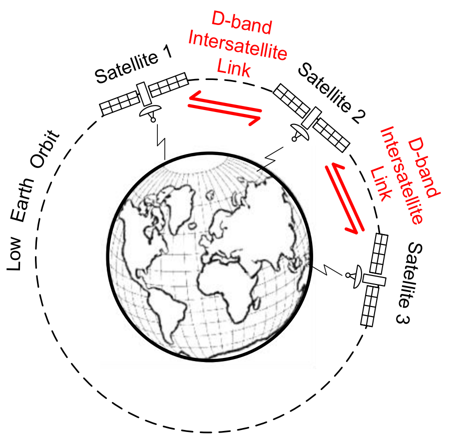

Fig. 4.2. Schematic of the D-band intersatellite THz communications

As the operating frequency increases, the minimum design feature of the metalens (ML) is approaching the fabrication limits of PCB technology, thereby posing significant challenges in the design of THz unit cells (UCs). The development of THz ML UCs with simplified geometries is therefore anticipated to alleviate fabrication constraints. According to the open literature, various THz ML UCs have been realised using 3D-printed dielectric posts[30], [318], Fabry–Perot-like resonators [319], [320], frequency-selective surfaces (FSSs) [321], [322], Huygens UCs [323], and transmitting–receiving (Tx–Rx) UCs [324], [325]. However, only a limited number of studies have proposed THz MLs for linear-to-circular polarisation (LP–CP) conversion. In [326], 3D printing was employed to design CP THz MLs, in which dielectric UCs incorporated CP polarisers to achieve LP-CP conversion. At lower frequencies, various LP-CP Tx-Rx UCs have been reported, including designs featuring a U-shaped slot [327], [328], an off-centre feeding point [329], [330], and CP antennas [331], [332], [333]. Statistically, the gap between the ground hole and the metal via in these designs is approximately 0.01 λ_0(where λ_0 denotes the central wavelength), which approaches the fabrication precision limits of standard PCB technology in the THz band.

This section presents a sub-THz wideband LP-CP ML for $\pm30°$ two-dimensional (2D) beam-scanning applications. A novel angle-multiplexed multifocal phase distribution (PD) calculation method is proposed to enable 2D beam steering with higher gain enhancement and without the need for additional optimisation. A coaxial-line-based UC is also introduced to achieve improved P-B phase performance. The first D-band conductive–dielectric multimaterial LP-CP ML was realised through additive manufacturing, reaching the highest operating frequency range attainable within the precision limits of current additive manufacturing technology. The proposed 26×26 LP-CP ML achieved a gain enhancement of 16.3 dB compared with the standard WR-06 waveguide probe. The simulated and measured 3-dB gain bandwidths are 19.6% and 16.3%, respectively.

4.2.1 Circularly-Polarised Metasurface Unit Cell with 3D Transmission Line

The proposed designs are fabricated using an additive manufacturing technique

[159], [334], [335]. The arbitrary thickness of the dielectric layer (ε_r = 2.7, tanδ = 0.04 at D-band) can be obtained. The accuracy reached through this method is approximately 36 μm for printing the conductive layer. The accuracy of the thickness of the dielectric layer is about 17 μm. The minimum width of the conductive layer is 100 μm, and the minimum diameter of the metallic via is 200 μm. The conventional Tx-Rx UC consists of a lower LP Rx patch and an upper CP Tx patch, and there is only one ground plane between the upper and lower patches. Metal vias and a ground hole work for connection, as shown in Fig. 4.3 (a) and (b). The conventional and proposed Tx-Rx UC are marked as UC1 and UC2. A three-dimensional coaxial line (CL) is introduced in the revised UC, and the size of the patches is optimised for impedance matching in the same frequency band. Fig. 4.3 (b) shows an exaggerated structure, and Fig. 4.3 (c) shows the detail of the proposed UC2; the actual size depends on the data. The coaxial line and the patches are made of the same material, and the different colours are only used to distinguish them.

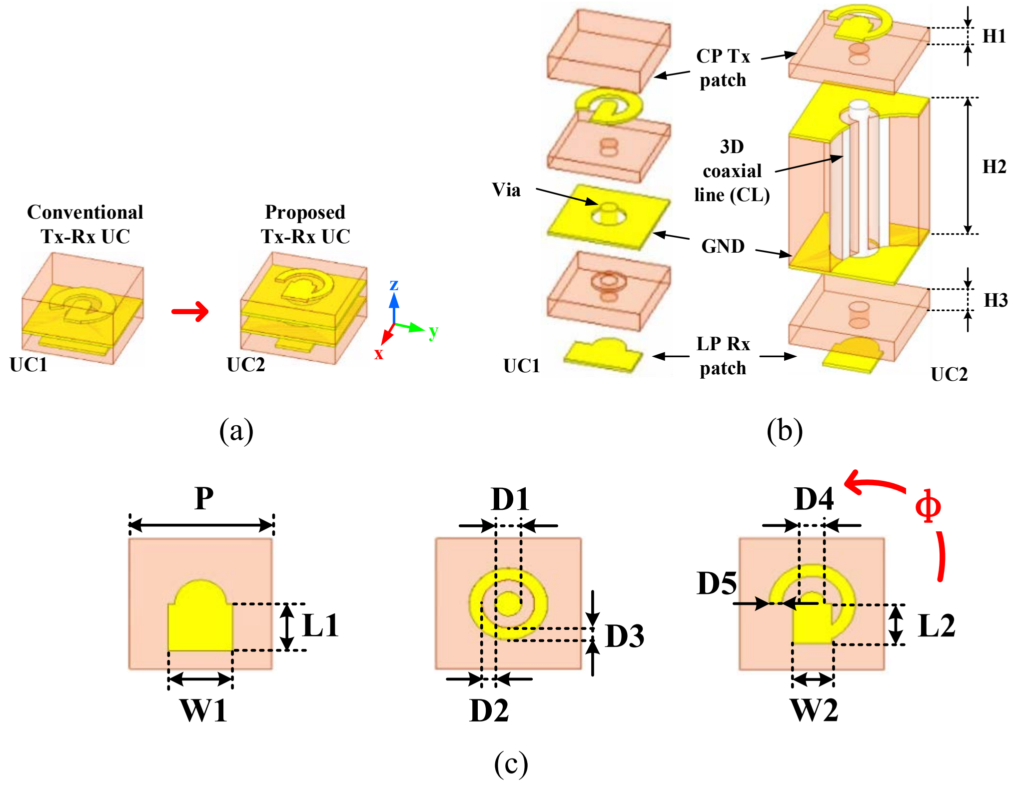

Fig. 4.3. Configuration of the conventional and proposed unit cell (UC): (a) CP Tx-Rx unit cell (UC). (b) Exploded diagrams. (c) Proposed UC2 details: H1 = 0.175, H2 = 0.2, H3 = 0.24, P = 1.1, L1 = 0.4, L2 = 0.33, W1 = 0.5, W2 = 0.3, D1=0.2, D2=0.1, D3=0.1, D4=0.2, D5=0.1. Units: mm. Φ is the rotation angle.

The "e"-shaped CP patch is employed to generate CP waves. Intuitively, rotating the CP patch can modulate the transmission phase with only a minor influence on the reflection coefficient. As shown in Figs. 4.4 (a) and (b), when the straight arm and the LP patch are oriented in the same direction ($\Phi = 0°$, $D2 = 0.05\ mm$), UC1 exhibits a broader -10 dB bandwidth, ranging from 110 GHz to 158 GHz. Conversely, when the two components are oriented oppositely ($\Phi = 180°$), the bandwidth narrows to 121 - 137 GHz, with only slight variations in the transmission coefficients. However, a gap (D2) of 0.05 mm is too narrow for practical fabrication and must be increased to at least 0.1 mm. As illustrated in Figs. 4.4 (c) and (d), this adjustment deteriorates both the transmission and reflection coefficients when $\Phi = 180°$, although UC1 still maintains a broad bandwidth at $\Phi = 0°$. The enlarged central gap adversely affects the reflection coefficients when applying the PB phase method. Moreover, the ground hole with via is often neglected at lower frequencies due to its small physical size. In Table 4.1, the "Gap" refers to the distance between the via and the ground hole, corresponding to the parameter D2 in Fig. 4.3 (c). The Tx–Rx unit cells [328], [336], [337] that employ only a single ground plane typically exhibit a small gap of approximately $0.01\lambda_0$. In contrast, the substrate-integrated cavity slot-fed unit cell [338] can realise the Pancharatnam–Berry (PB) phase while accommodating a larger gap. To alleviate the adverse effects of this large gap and to electrically connect the upper and lower patches, a coaxial line is introduced. Based on this approach, a new unit cell (UC2) is proposed.

TABLE 4.1
GEOMETRY COMPARISON BETWEEN VARIOUS TX-RX UNIT CELLS

Unit cell	Freq (GHz)	Via diameter (mm)	Ground hole diameter (mm)	D2 Gap (mm)	D2 Gap (λ_0)
[328]	10.5	0.4	1	0.3	0.01
[336]	10	0.5	1.4	0.45	0.01
[337]	20	0.56	0.88	0.16	0.01
[338]	28	0.3	1.3	0.5	0.04
Proposed	125	0.2	0.4	0.1	0.04

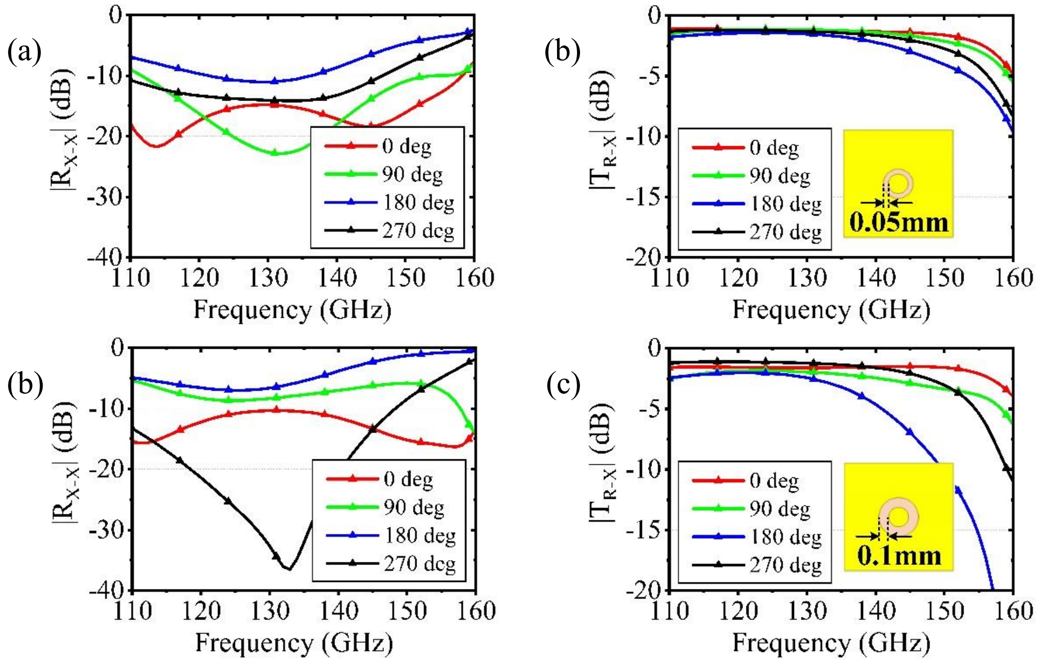

Fig. 4.4. Performance of the UC1 with different gaps for different rotation angles using the lossless substrate. (a) Reflection coefficients and (b) transmission coefficients when D2=0.05mm; (c) Reflection coefficients and (d) Transmission coefficients when D2=0.1mm. $|R_{X-X}|$ represents the reflection coefficient from X to X polarised waves. $|T_{R-X}|$ represents the transmission coefficient from X to RHCP waves.

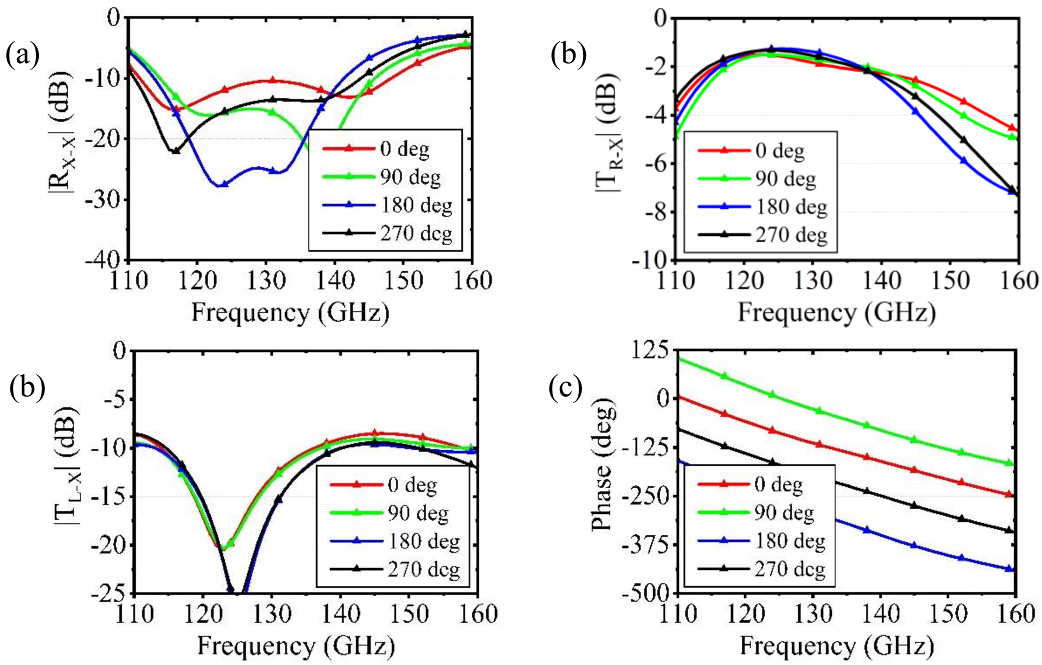

Fig. 4.5. P-B performance of the UC 2 with the coaxial line. (a) Reflection coefficients from X to X polarised waves; (b) transmission coefficients from X to RHCP waves; (c) Transmission coefficients from X to LHCP waves, (d) Transmission phase of $|T_{R-X}|$.

The simulated performance of the UC2 is given in Fig. 4.5. A wide -10 dB bandwidth is from 116.7 GHz to 142.4 GHz (19.8%) for any rotation angles. To prove the concept, the lossless substrate is used in the simulation. The peak transmission coefficient from X to RHCP polarised waves is -0.2 dB, and the normalised -1 dB bandwidth is from 116 GHz to 141.1 GHz (19.5%). The transmission coefficients from X to LHCP polarised waves are better than -10 dB over the operating frequency band. The transmission phase of $|T_{R-X}|$ varies with the rotation of the CP patch, which can provide a 360° phase cycle.

4.2.2 Angle-Multiplexed Multifocal Method

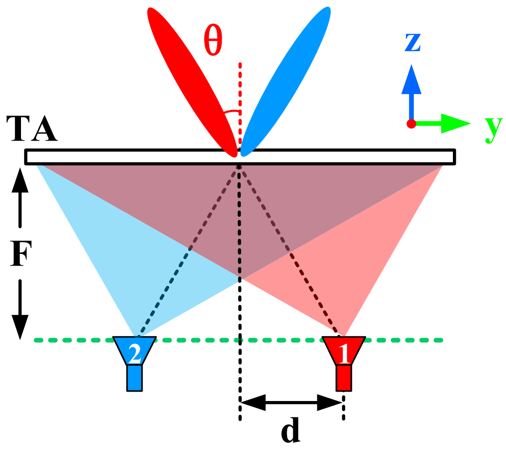

Fig. 4.6. Coordinate system of the proposed MLA. The light red represents the radiation coverage of Port 1.

The proposed CP UC is designed for a 26 × 26 ML. An ML with a focal plane is designed for beam-scanning applications. For comparison, the bifocal method [338], [339], [340] and the angle-multiplexed multifocal method are adopted to calculate the PD for one-dimensional (1D) beam-scanning. The related coordinate system is depicted in Fig. 4.6, θ is the tilted angle of the radiation beam, d represents the offset of Port 1 from the centre. The common bifocal PDs for Port 1 and Port 2 can be given by:

$$\Psi_1 = k_0(\sqrt{x^2 + (y-d)^2 + F^2} + y * sin\theta) \tag{4.12}$$

$$\Psi_2 = k_0(\sqrt{x^2 + (y + d)^2 + F^2} - y * sin\theta) \quad (4.13)$$

$$\Psi_{bifocal\_1} = (\Psi_1 + \Psi_2)/2 \quad (4.14)$$

where k_0 is the wave number in free space, and (x, y) is the position of the metasurface lens unit cell. The focal length is 12 mm, and the θ is set to 30°. Two single-focal PDs Ψ_1 and Ψ_2 are shown in Fig. 4.7 (a) and (b), respectively. The common bifocal PD is presented in Fig. 4.7 (c). The basic principle of the bifocal method is based on similar PDs for two focal points. When the following equation holds:

$$d = F * tan\theta \quad (4.15)$$

The centres of the two single-focal PDs are located in the centre of the ML, which can minimise the phase errors of the $\Psi_{bifocal\_1}$. On the other hand, the authors take an initial approach by adopting the angle-multiplexing technique adapted from OAM metasurface designs [341], [342].

$$\Psi_{bifocal\_2} = angle[exp(j\Psi_1) + \exp(j\Psi_2)] \quad (4.16)$$

The $angle[\cdot]$ is used to obtain the complex phase angle. The angle-multiplexed PD is shown in Fig. 4.7 (d). As shown in Fig. 4.7(e), the difference between the two phase distributions takes only two discrete values, 0° and 180°, indicating that $\Psi_{bifocal\_1}$ and $\Psi_{bifocal\_2}$ exhibit highly similar patterns. The angle-multiplexed multifocal method was first validated in a 1D application scenario, demonstrating that it can achieve equally accurate results without introducing additional computational complexity. The advantages of this approach become more pronounced in the subsequent subsection, where it is applied to a 2D scenario.

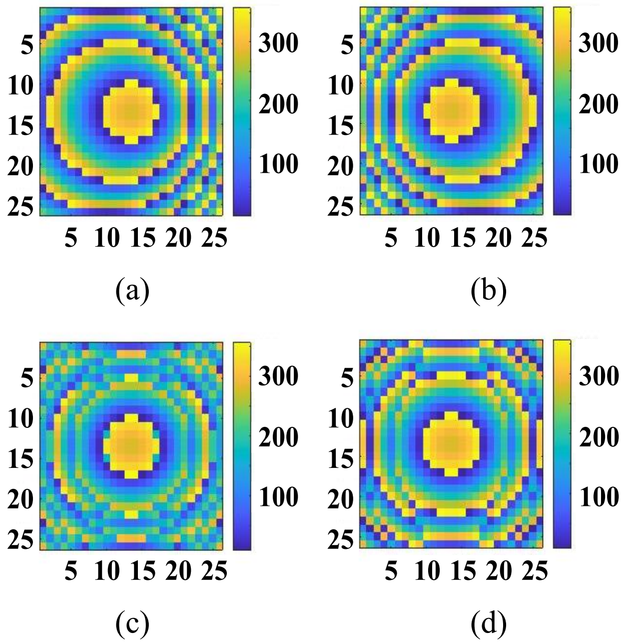

Fig. 4.7. Phase distributions (PDs) at 125 GHz. (a) PD fed by port 1 only for a single tilted beam. (b) PD fed by port 2 only for a single tilted beam. (c) Conventional bifocal PD, $\Psi_{bifocal\_1}$. (d) Angle-multiplexed bifocal PD, $\Psi_{bifocal\_2}$.

The theoretical analysis is as follows. The angle-multiplexed method is more theoretically suitable for multifocal metasurface design. For simplicity, the bifocal case is discussed below. The radiating field of the feed sources (Ports 1 and 2) can be given:

$$U_{pn} = cos^{q}(\theta_{pn}) \frac{\exp(-jk_0|\vec{r} - \overrightarrow{r_{pn}}|)}{|\vec{r} - \overrightarrow{r_{pn}}|} = E_{pn} exp(-jk_0 R_n) \ ; \quad n = 1, 2 \qquad (4.17)$$

Here, $cos^{q1}(\theta_{p1})$ represents the model of the radiation pattern of port n ($n = 1, 2$). $\vec{r}$ and $\overrightarrow{r_{pn}}$ are the position vectors of the phase centre of port n. E_{pn} is the illuminated amplitude to the metasurface. R_n is the spatial distance between port n and each pixel in the metasurface. The complex transmittance of the normal bifocal ($T_{bifocal\_1}$) and angle-multiplexed bifocal ($T_{bifocal\_2}$) PD in the metasurface is given:

$$T_{bifocal\_1} = A[exp(jk_0 R_1 + jk_0 y * sin\theta + jk_0 R_2 - jk_0 y * sin\theta)] \qquad (4.18)$$

$$T_{bifocal\_2} = A[exp(jk_0 R_1 + jk_0 y * sin\theta) + exp(jk_0 R_2 - jk_0 y * sin\theta)] \qquad (4.19)$$

A represents the amplitude of the complex transmittance. When the wave U_{p1} from Port 1 illuminates the angle-multiplexed bifocal metasurface. The generated wave is therefore given by:

$$\begin{aligned} U1 &= T_{bifocal\_1} \cdot U_{p1} \\ &= A\{ exp(jk_0R_1 + jk_0y * sin\theta + jk_0R_2 - jk_0y * sin\theta) \\ &\qquad \cdot E_{p1} \exp(-jk_0R_1) \\ &= A' exp(jy * sin\theta + jk_0(R_2 - R_1) - jk_0y * sin\theta) \\ &= A' exp(j\varphi_{PW} + j\varphi_{Residue}) \end{aligned} \tag{4.20}$$

$$\begin{aligned} U2 &= T_{bifocal\_2} \cdot U_{p1} \\ &= A\{ exp(jk_0R_1 + jk_0y * sin\theta) + exp(jk_0R_2 - jk_0y * sin\theta)\} \\ &\qquad \cdot E_{p1} \exp(-jk_0R_1) \\ &= A' exp(jy * sin\theta) + A' exp(jk_0(R_2 - R_1) - jk_0y * sin\theta) \\ &= A' ex\,p(j\varphi_{PW}) + A' ex\,p(j\varphi_{Residue}) \end{aligned} \tag{4.21}$$

The first term ($A' ex\,p(j\varphi_{PW})$) in Equation (4.21) represents a radiated planar wave (PW) beam with a tilted angle of θ. In the normal bifocal case, Equation (4.20), the PD generating a PW is contaminated by the $\varphi_{Residue}$. By comparison, the angle-multiplexed method can obtain a term to generate a pure PW. Although the residue is inevitable, its effect is alleviated in the angle-multiplexed case. As for the case of several focal points, the angle-multiplexed method is more suitable for 2D beam-scanning.

When designing for a 2D beam-scanning ML, the difference between the common and angle-multiplexed methods increases. Fig. 4.8 (a) shows eight PDs for a single tilted beam, and Fig. 4.8 (b) and (c) are the combination of these PDs using the common and angle-multiplex methods. These PDs can be calculated by:

$$\begin{aligned} \Psi_n = k_0(&\sqrt{(x - d * cos\varphi_n)^2 + (y - d * sin\varphi_n)^2 + F^2} \\ &- sin\theta * [x * \cos(\varphi_n + \pi) + y * \sin(\varphi_n + \pi)]) \end{aligned}$$

$$\varphi_n = (n-1)\,\frac{\pi}{4} \quad n=1, 2, 3, \dots, 8 \tag{4.22}$$

$$\Psi_{multi-focal\_1} = \frac{1}{8}\sum_{n=1}^{8} \Psi_n \tag{4.23}$$

$$\Psi_{multi-focal\_2} = angle[\sum_{n=1}^{8} exp(j\Psi_n)] \tag{4.24}$$

where the parameter φ_n represents the angle between the focal point and the X-axis. The $\varphi_n + \pi$ is the direction of the ML radiation beam. The simulated radiation patterns and gains versus frequency are shown in Fig. 4.9. The simulated results are based on a lossless material to show the improvement of the proposed method. The beams for the direction of (φ, θ) have been coloured: red for the plane of $\varphi = 0°$, and green for the plane of $\varphi = 90°$. The plane of $\varphi = 45°$ (black) is omitted for clarity. They are correlated with the radiation patterns. In Fig. 4.9 (b) and (c), the gains of four beams by using the common method are 21.6 dBic for the direction of $(\varphi = 0°, \theta = 0°)$, 19.8 dBic for $(\varphi = 0°, \theta = 30°)$, 19.1 dBic for $(\varphi = 90°, \theta = -30°)$, and 19.2 dBic for $(\varphi = 45°, \theta = -30°)$. By comparison, the gains by using the angle-multiplexed method are 24.8 dBic, 23.6 dBic, 23.8 dBic and 23.6 dBic. In Fig. 4.9 (d) and (e), compared with the common method, about 3-4 dB gain enhancement and 1.2 dB scan loss are achieved by using the angle-multiplexed method.

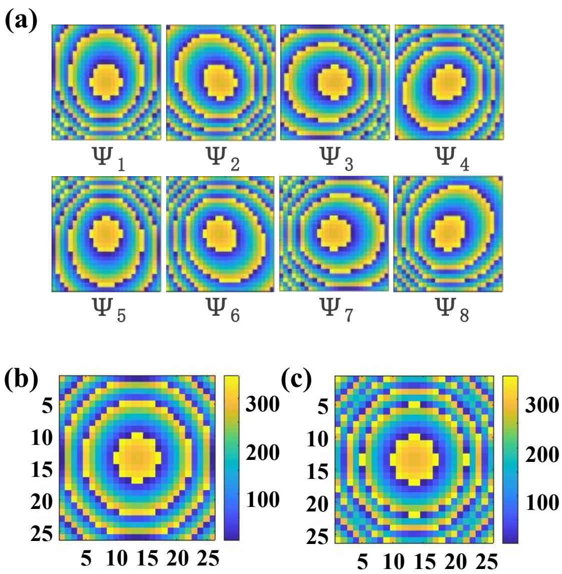

Fig. 4.8. Phase distributions (PDs) at 125 GHz. (a) Eight PDs for a single tilted beam. (b) Conventional bifocal PD, $\Psi_{multi-focal\_1}$. (c) Angle-multiplexed PD, $\Psi_{multi-focal\_2}$

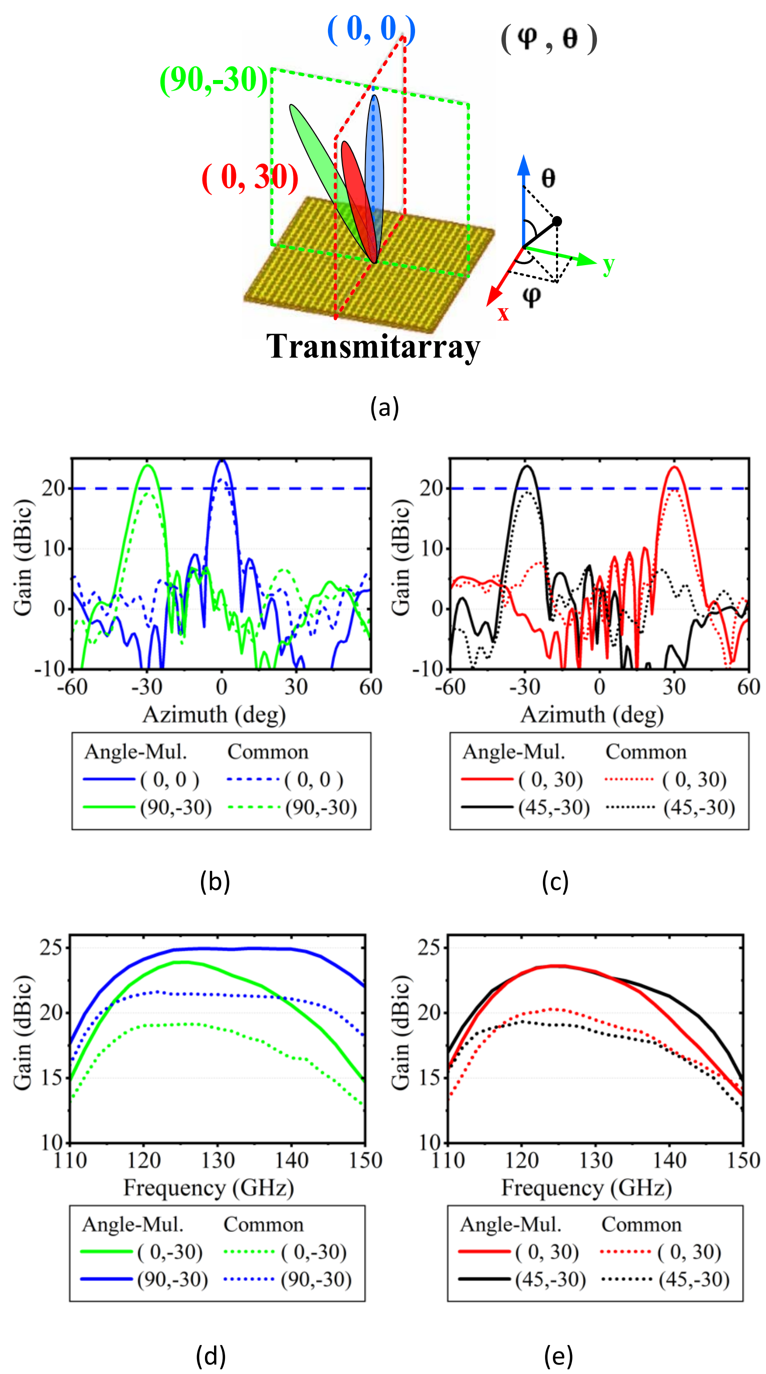

Fig. 4.9. Comparison between the angle-multiplexed and common method with a lossless material. (a) Schematic of three beams. (b) and (c) Radiation patterns at 125 GHz. (d) and (e) Gain versus frequency of four beams.

4.2.3 Measurement and Comparison

The prototype is shown in Fig. 4.10. The ML is fed by the standard WR-06 waveguide probe. The measured and simulated radiation patterns at 125 GHz are presented in Fig. 4.11. The beams' directions are −30°, −15°, 0°, 15°, and 30°. Seven beams have been marked from #1 to #7, and their related feed sources' position is plotted in Fig. 4.11 (d); the related coordinates of the seven points are (0,0), (3.5,0), (7,0), (2.47,2.47), (4.95,4.95), (0,3.5), and (0,7), with all dimensions expressed in millimetres (mm). The simulated gain of the ML reduces to 22.7 dBic with a scan loss of 1.2 dB, while the measured one is 19.6 dBic and 0.7 dB.

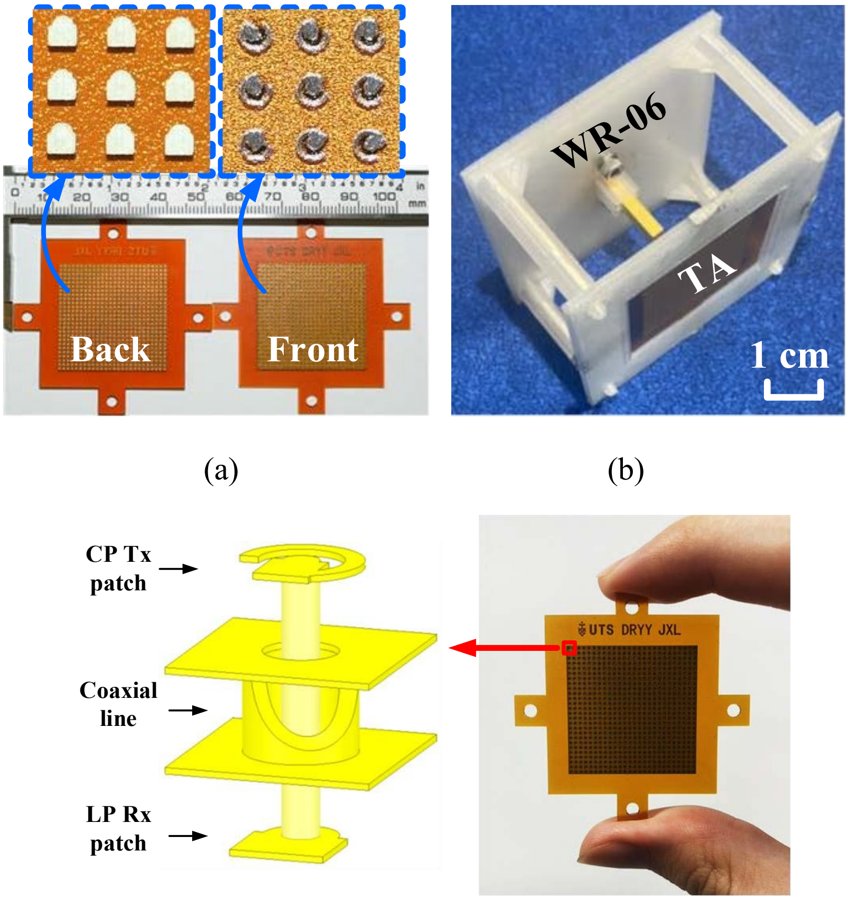

(a) (b)

(c) (d)

Fig. 4.10. (a) Back and front of the prototype and the zoom-in image. (b) Transmitarray antenna. (c) Additively manufactured ML UC with four metal layers without showing the dielectric materials. Invisible coaxial lines are 3D-printed for the connection between the Tx and Rx patches. (d) The photo of the proposed metasurface.

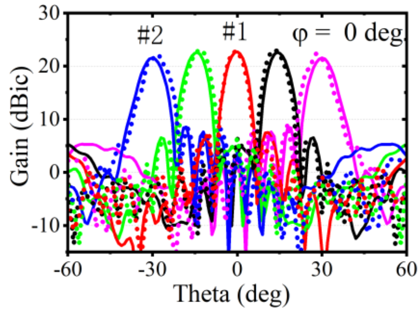

(a)

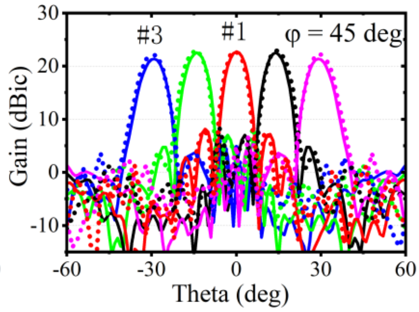

(b)

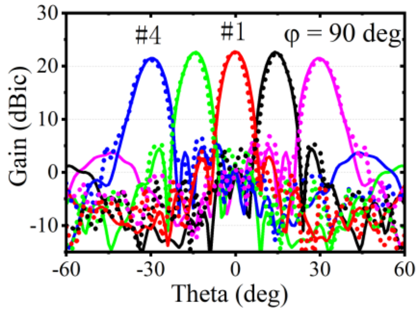

(c)

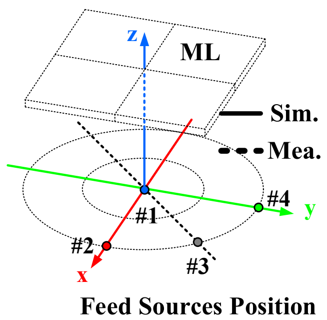

(d)

Fig. 4.11. Measured and simulated radiation patterns at 125 GHz in the plane of (a) $\varphi = 0°$, (b) $\varphi = 45°$, and (c) $\varphi = 90°$. θ is the elevation angle (measured from the z-axis), and φ is the azimuth angle (measured clockwise from the x-axis around the z-axis). (d) The position of four feed sources with marks under the ML. Solid line: simulated results. Dash line: measured results.

The simulated and measured gain and AR curves versus frequency for various beams are shown in Fig. 4.12. The simulated overlapped 3-dB gain bandwidth for beams #1-#7 is from 114 GHz to 138 GHz (19.6%), and the AR bandwidth is from 110 GHz to 145 GHz (27.4%). The measured overlapped 1-dB and 3-dB gain bandwidth, and the AR bandwidths are from 120.6 to 133.8 GHz (10.4%), from 116.2 to 136.8 GHz (16.3%) and 110 to 150 GHz (30.7%) for various beams. The average beam scan loss is about 1.7 dB. The performance comparison is given in Table 4.2.

The primary function of the beam-scanning metasurface is to enhance the gain and directivity of the feed sources. Furthermore, a higher feed source gain directly contributes to a higher gain of the metalens antenna (MLA). Therefore, to comprehensively demonstrate the performance of the proposed metalens (ML), its gain enhancement must be included in the evaluation. Compared with [343], the proposed ML achieves greater gain enhancement while maintaining a similar focal-to-diameter (F/D) ratio. Theoretically, a smaller F/D ratio yields stronger gain enhancement; however, the proposed ML demonstrates superior performance even when compared with [338]. Despite the higher material losses - accounting for an estimated 2-3 dB loss budget—the proposed MLA still achieves lower scan loss and higher gain enhancement than that reported in [323]. Currently, only a few designs for sub-THz CP MLAs have been reported, with [326] being one of the few examples, as the design and fabrication of sub-THz MLs remain highly challenging.

An increase in the feed source gain directly leads to an increase in the ML antenna gain. Therefore, the gain enhancement relative to the feed source is discussed here to evaluate the intrinsic performance of the ML. The proposed ML achieves a gain enhancement of 16.3 dB using the angle-multiplexed multifocal method, even when accounting for an estimated 2-3 dB material loss. This gain improvement is achieved partly at the expense of the gain bandwidth and beam coverage.

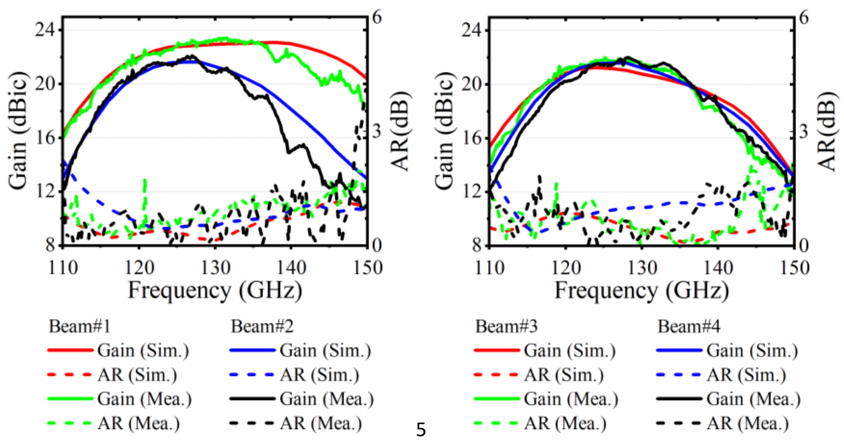

(a) (b)

Fig. 4.12. Measured and simulated gain and AR. (a) Beam #1 and Beam #2. (b) Beam #3 and Beam #4.

TABLE 4.2
PERFORMANCE COMPARISON WITH OTHER METASURFACE LENSES

Ref.	Freq (GHz)	Pol.	F/D	Gain (dBi)	Gain Enhancement (dB)	1dB Gain BW	3dB Gain BW	AR BW	Beam Coverage	Scan Loss (dB)
[343]	27	LP-CP	0.44	21.5	11.5	N.G.	33.3 %	40.7 %	$\pm 33°$ (1D)	2
[338]	26	CP	0.37	21.4	13.4	N.G.	20.0 %	20.0 %	$\pm 33°$ (2D)	1.2
[323]	200	LP	2.47	29	7	N.G.	19.1 %	N.A.	$\pm 48°$ (1D)	2.85
[326]	300	LP-CP	2	30	7	13.3 %	13.3 %	18.8 %	N.A.	N.A.
Proposed	125	LP-CP	0.42	22.8	16.3	10.4 %	16.3 %	30.7 %	$\pm 30°$ (2D)	1.7

N.G.: Not Given; N.A.: Not Applicable

A sub-THz CP MLA for 2D beam steering is realised using the angle-multiplexed multifocal method. The proposed MLA achieves high gain improvement, LP-CP conversion, and a wide 2D beam-steering range of $\pm 30°$ with a scan loss of only 1.7 dB in the planes of $\varphi = 0°$, $\varphi = 90°$, and $\varphi = 45°$. The prototype is fabricated using 3D multimaterial additive manufacturing. A coaxial line is employed to connect the Tx and Rx antenna patches, effectively mitigating the influence of the PB phase on the reflection coefficients. The angle-multiplexed approach further enhances the beam-steering performance. Overall, the proposed MLA represents a promising candidate for future inter-satellite communication applications.

4.3 Dual-Polarised Multimaterial Metasurface Lens for Beam-Scanning Applications

Metamaterial lenses (MLs) are believed to be an exciting technology for beam-shaping and possibly steering using elaborately designed phase-shift unit cells. Studies on metasurfaces have demonstrated their strong plasticity. They can be designed with the functions of transmittance enhancement [344], orbital angular momentum (OAM) [345], 1D beam-steering [346], and near-field focusing (NFF) [347]. However, these complex unit cells are difficult to achieve in THz bands due to fabrication challenges.

In this section, a multilayered ML is proposed for beam-steering applications. The ML consists of 22×22 phase-shifting unit cells, each comprising seven metal layers integrated within a single substrate. The 3D-printed ML was fabricated using a piezoelectric printing system [348], capable of simultaneously depositing conductive and dielectric materials. The designed ML unit cells achieve a full 360° phase shift by stacking circular patches, with the interlayer spacing flexibly adjusted to fine-tune the phase response. The proposed ML is excited by a standard WR-06 waveguide probe and demonstrates beam-steering capability through rotation of the waveguide along a predefined trajectory of $\pm 30°$.

4.3.1 Multilayered Metasurface Unit Cell

The proposed step-shaped ML in Fig. 4.13 (a) consists of 22×22 unit cells and operates at 120 GHz with a total dimension of $26.4\,mm \times 26.4\,mm$, and a focal length of $27\,mm$. Fig. 4.13 (b) shows a typical ML unit cell with a period of 1.2 mm. It consists of multiple circular patches arranged in multiple layers, with an interlayer spacing of $300\,\mu m$. The number of patches increases with the transmission phase delay, and the diameter of each patch can be adjusted to match the phase step of the desired transmission phase. The parameter H1 is fixed at 2 mm, corresponding to the maximum height (H2) of the dielectric material. By adjusting the substrate height, the transmission phase shift of the unit cell can be tuned. The dielectric constant and loss tangent of the material are 2.5 and 0.02, respectively. The schematic diagram of the beam-steering ML is shown in Fig. 4.13 (c), where α denotes the rotation (incident) angle of the feed point, and θ represents the main beam angle. The rotation centre of the feed point is located behind the ML, with a separation distance of dz = 2.5 mm.

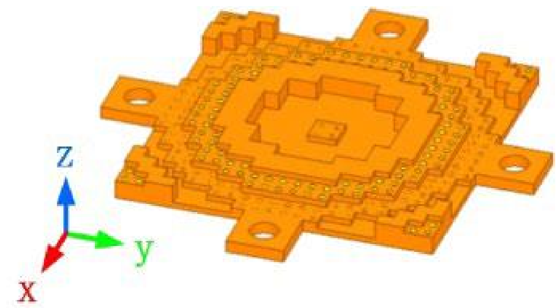

(a)

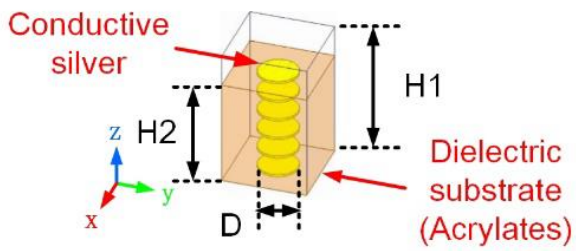

(b)

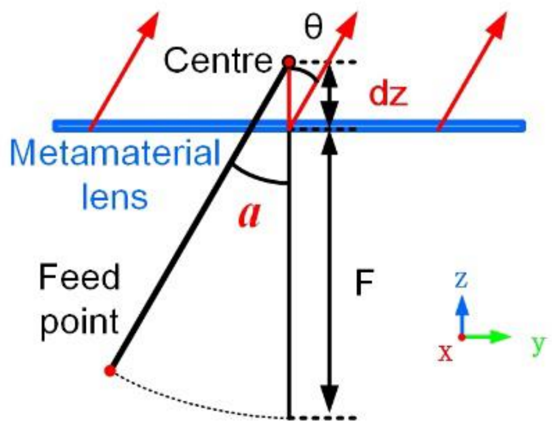

(c)

Fig. 4.13. (a) 3D model of the THz ML, (b) Proposed phase shift unit cell. (c) Schematic of the beam-steering setup.

Fig. 4.14 illustrates the transmission phase shift of the eight proposed ML unit cells. The thicknesses of the unit cells are categorised into four levels: 2.0 mm, 1.5 mm, 1.0 mm, and 0.5 mm. Each unit cell can be regarded as a composite structure consisting of an air layer and a dielectric layer. For unit cells with the same total thickness, the diameter of the circular patches can be adjusted to achieve increased phase delay. According to the design guideline, the minimum microstrip patch width should exceed 110 μm [349]. The proposed circular patches offer greater structural robustness and are less sensitive to fabrication errors during 3D printing. The minimum printable layer thicknesses are 0.3 μm for the conductive layer and 2.5 μm for the dielectric layer. The maximum substrate thickness that can be fabricated is 3 mm, with a fabrication tolerance of $\pm 5\%$. This tolerance may deteriorate when the printed substrate thickness approaches the upper fabrication limit.

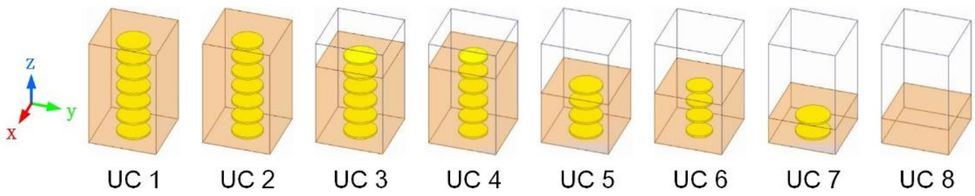

(a)

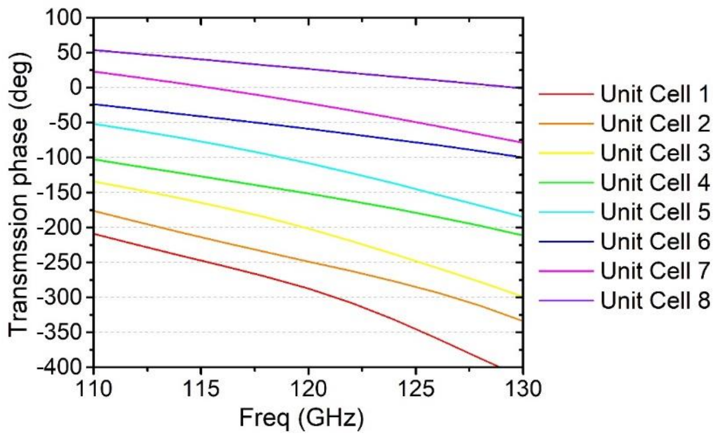

(b)

Fig. 4.14. (a) Simulation model of eight UCs. (b) The proposed phase shift unit cells (UCs) and their transmission phase response cover a full range of 360 degrees.

Additionally, the 3D printing dielectric inks—typically acrylate-based materials—

exhibit relatively high losses in the THz band. Reducing the thickness of the unit cells can effectively minimise dielectric losses and improve the transmission coefficient of the ML. The designed unit cells are positioned near the centre of the lens aperture by optimising the phase distribution of the ML, thereby enhancing the overall gain. The phase distribution of the proposed ML can be derived from Fermat's principle, as expressed below:

$$\varphi(x,y) = \frac{2\pi}{\lambda_0}\left(\sqrt{x^2 + y^2 + F^2} - F\right) + \varphi_0 \tag{4.25}$$

where the original focal length F is 21 mm, λ_0 is the wavelength at 120 GHz and φ_0 represents the initial phase. According to Equation (4.25), the feed source at the feed point in Fig. 4.13 (c) is regarded as an ideal point source and radiates a spherical wave from the phase centre of the feed source. However, the ideal phase centre is non-existent. Therefore, the optimisation of the focal length is needed, which is carried out by the full EM simulation tool - HFSS.

4.3.2 Optimisation

As shown in Fig. 4.15 (a), increasing the focal length (F) from 21 mm to 27 mm results in a significant gain improvement from 16.7 dBi to 21.6 dBi at 120 GHz. The optimised gain across the operating frequency band ranges from 19.1 dBi to 21.6 dBi. Compared with the gain of the WR-06 waveguide, a gain enhancement of approximately 12.5 - 15.7 dB is achieved. When the feed source is rotated by 30°, the radiation patterns at 120 GHz for different dz values are illustrated in Fig. 4.15 (b). It can be observed that the main beam direction of the ML increases with dz, reaching 30° when dz = 2.5 mm. Therefore, the proposed ML successfully achieves beam-steering performance while maintaining the same incident angle (α) and beam angle (θ).

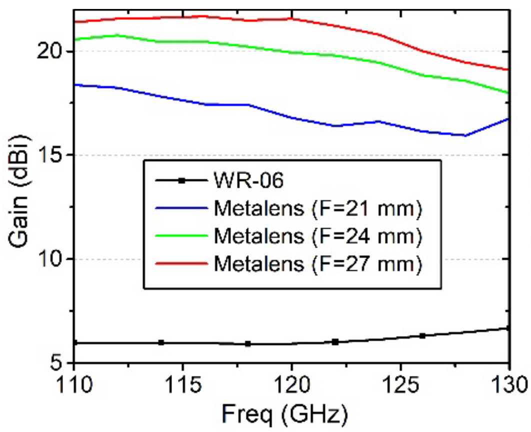

(a)

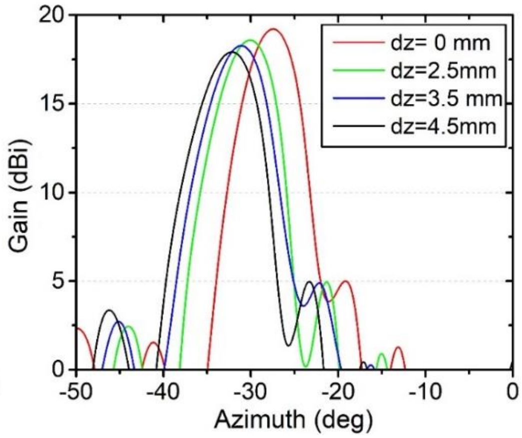

(b)

Fig. 4.15. (a) Gain of WR-06 waveguide and ML with different focal length F. (b) Radiation patterns at 120 GHz with different dz when $\alpha = 30°$.

4.3.3 Experimental Results

Fig. 4.16 (a) and (b) show the 3D printed 120 GHz ML prototype. A D-band (110 - 170 GHz) far-field scanning measurement setup is built to measure the radiation patterns of the ML at 120 GHz, as shown in Fig. 4.16 (c). The measured radiation patterns exhibit good agreement with the simulated results. The simulated results with different $\alpha\alpha$ are 21.5 dBi at 0°, 21.3 dBi at -10°, 20.6 dBi at -20° and 18.3 dBi at -30° in H-plane, while the measured ones are 20.6 dBi, 21.1 dBi, 20.0 dBi and 18.0 dBi. Because of the symmetry of the structure, only half of the scanning angle is measured.

The proposed ML achieves a gain enhancement of approximately 14.1 dB when fed by a standard WR-06 waveguide. By rotating the waveguide, the ML demonstrates excellent beam-steering performance within a $\pm 30°$ scanning range. These results confirm the potential of the proposed ML for beam-steering and multibeam applications. Furthermore, multibeam performance can be realised by exciting the ML with a waveguide array. Overall, the proposed ML represents a promising candidate for future THz beam-steering communication systems.

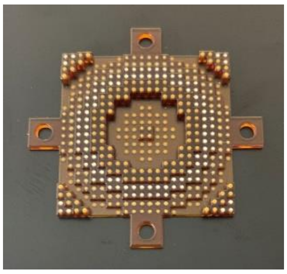

(a)

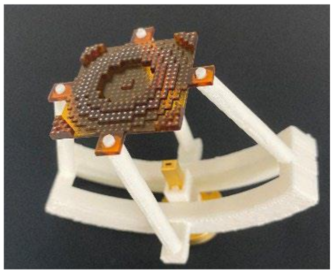

(b)

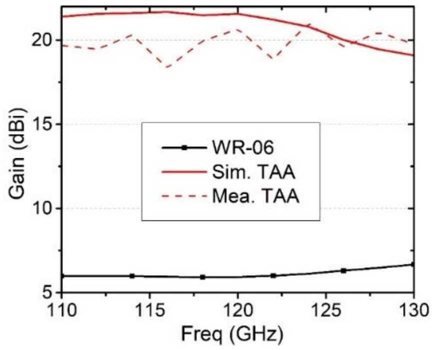

(c)

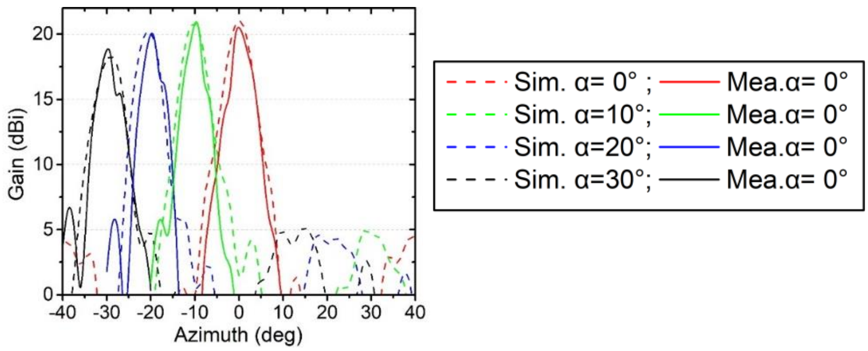

(d)

Fig. 4.16. (a) Top view of the ML. (b) ML with a WR-06 waveguide on a 1D scanning setup. (c) Simulated and measured gain versus frequency. (d) Simulated and measured radiation patterns at 120 GHz.

4.4 Other Multifunctional Unit Cells

This section investigates a range of multifunctional unit cell designs. Multifunctional THz metasurface unit cells offer several advantages, including flexible polarisation control, which enables the realisation of diverse polarisation states, such as linear, circular, and elliptical polarisations. This flexibility is essential for advanced applications, including polarisation multiplexing, THz full-aperture shared-aperture antennas, and compact multifunctional metasurfaces. Furthermore, integrating multiple functionalities into a single metasurface can significantly reduce system size and complexity, presenting a promising pathway toward miniaturised and high-performance THz systems. However, the realisation of these capabilities is accompanied by several technical challenges.

4.4.1 Multilayered Unit Cell

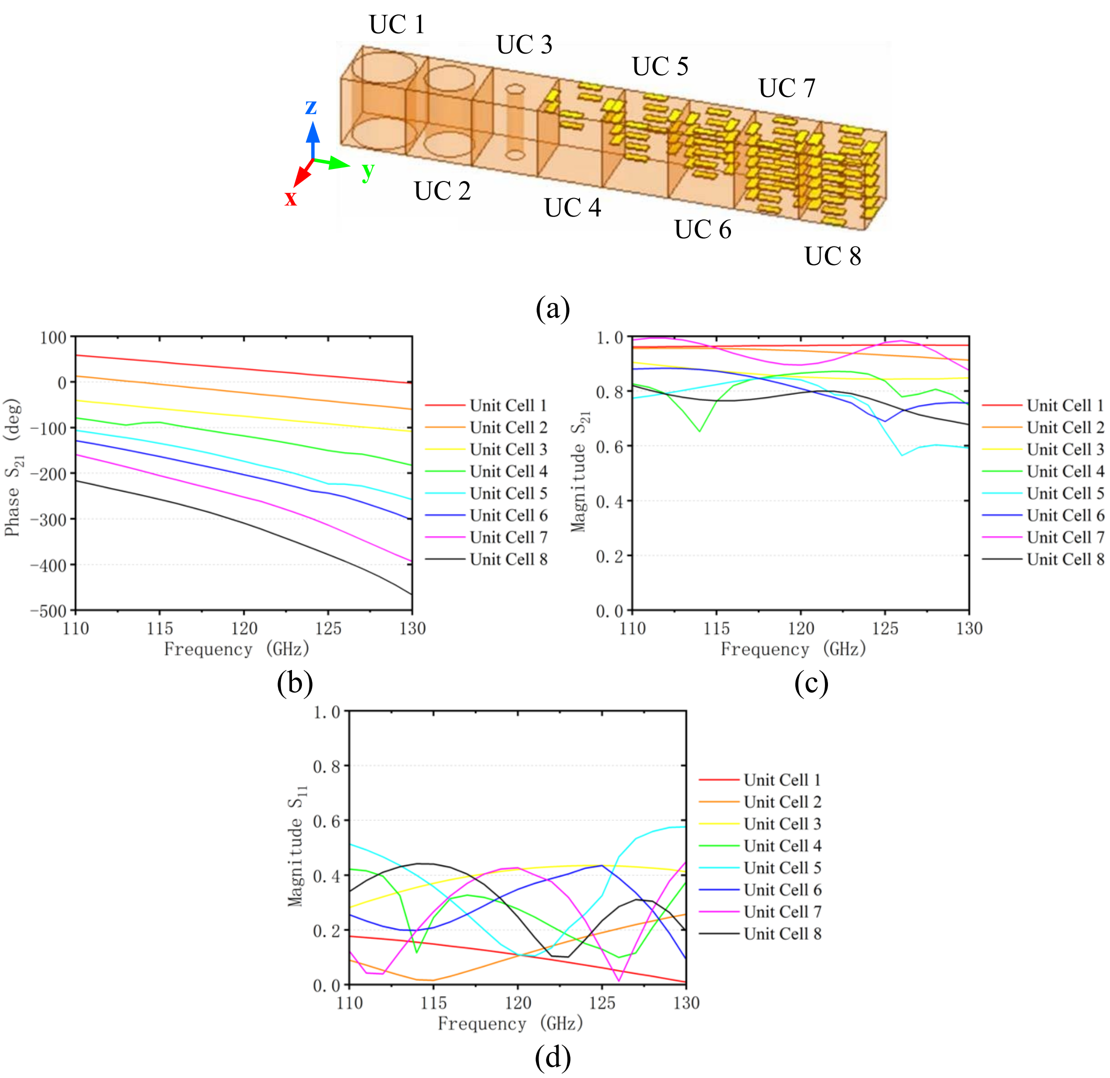

Fig. 4.17. (a) Eight unit cells designed for a 360° phase coverage. (b) Transmission phase of each unit cell (UC) spanning the full 360° range. (c) Simulated transmission coefficients of each UC. (d) Simulated reflection coefficients of each UC.

Fig. 4.17 presents eight unit cells designed to cover a full 360° phase cycle, with the phase delay capability increasing from left to right. The three unit cells on the left are dielectric-based, incorporating air holes to achieve variations in the transmission phase, while the five unit cells on the right are composed of multilayered metallic patches. Additive manufacturing electronics (AME) technology enables the realisation of multilayered structures without the substrate thickness limitations inherent in printed circuit board (PCB) fabrication, allowing for arbitrary layer numbers and thicknesses.

Based on the reflection coefficients, the operating frequency bandwidth of unit cell 8 (black line) extends from 110 GHz to 135 GHz. However, for unit cell 8, the magnitude of the transmission coefficient decreases to below 0.67 at 130 GHz, primarily due to the relatively high loss tangent of 0.015. If a lossless dielectric material were employed, the transmission coefficient could improve to approximately -1 dB. Furthermore, the dielectric material used in AME is relatively brittle, and the incorporation of air-hole structures renders the lens fragile and challenging to fabricate.

To leverage the design flexibility offered by AME technology, the multilayered unit cell illustrated in Fig. 4.18 was investigated. The unit cell comprises both an air region and a dielectric cube incorporating multilayered cross-shaped patches. It was initially expected that increasing the number of layers would effectively enhance the phase delay. However, in practice, the observed delay improvement was insignificant, and a substantial phase shift could only be achieved by modifying the patch geometry.

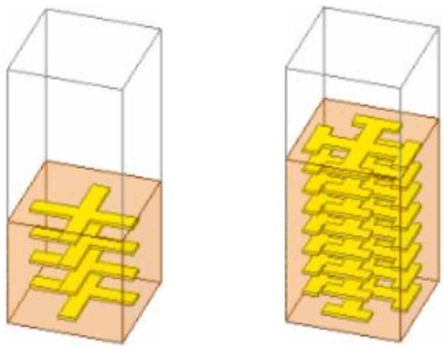

(a) (b)

Fig. 4.18. Multilayered unit cell. (a) Unit cell with fewer layers for minimal phase delay. (b) Unit cell with more layers for increased phase delay.

As illustrated in Fig. 4.19, a shared-aperture circularly polarised (CP) transmission design was proposed, in which the upper layer comprises CP unit cells operating at 300 GHz, while the lower layer employs CP unit cells operating at 150 GHz. Because the two frequencies differ by a factor of two, the unit cell dimensions were designed with a 2:1 ratio, allowing both lenses to theoretically share the same aperture. As shown in Fig. 4.20, when a left-handed circularly polarised (LHCP) wave is incident, the transmitted wave is predominantly right-handed circularly polarised (RHCP), and the transmission coefficient of the LHCP component remains below -10 dB. However, in practice, strong mutual coupling between the two layers severely degraded performance, preventing the successful realisation of dual-band functionality. As shown in Fig. 4.21, the dual-band CP unit cell performance at both high and low frequencies is adversely affected.

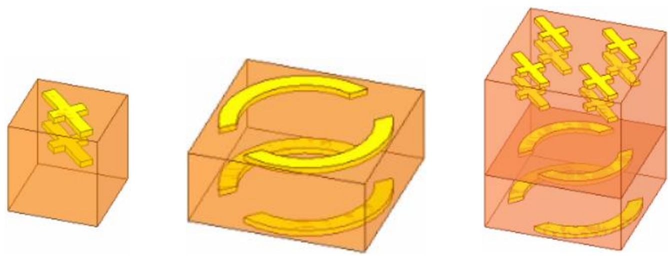

(a) (b) (c)

Fig. 4.19. Dual-band circularly polarised unit cells. (a) CP unit cell 1 operating at 300 GHz. (b) CP unit cell 2 operating at 150 GHz. (c) CP unit cell 3: the combination of the two CP unit cells.

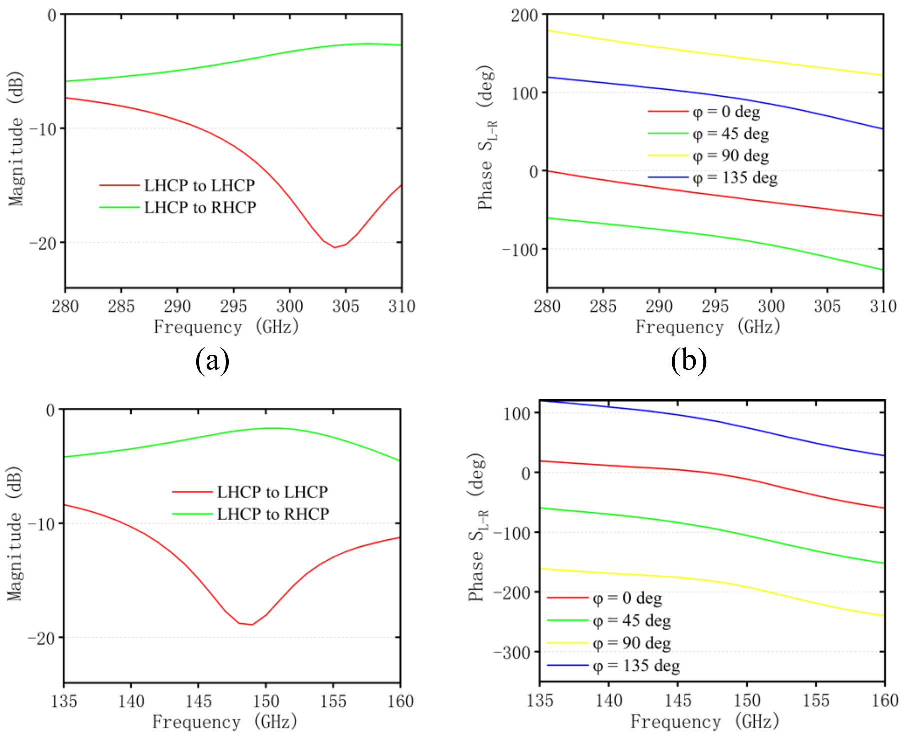

(c) (d)

Fig. 4.20. Simulated performance of the two CP unit cells: (a) Transmission coefficients and (b) transmission phase of unit cell 1 with varying rotation angles; (c) Transmission coefficients and (d) transmission phase of unit cell 2 with varying rotation angles.

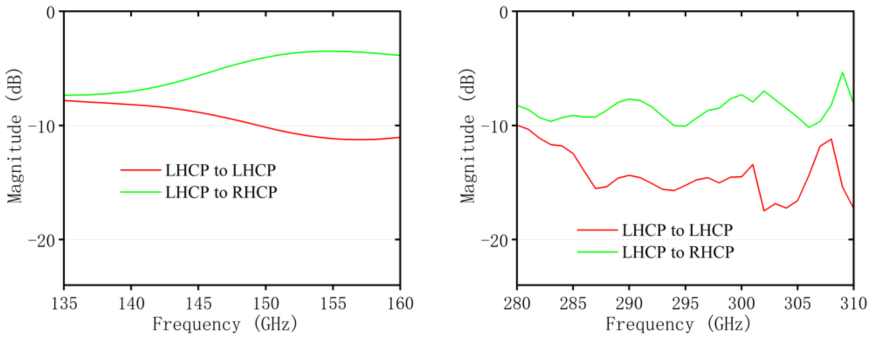

(a) (b)

Fig. 4.21. Simulated transmission coefficients of CP unit cell 3 at (a) the lower frequency band and (b) the higher frequency band.

4.4.2 Transmitting and Receiving Unit Cell

As shown in Fig. 4.22, the unit cell presented in [156] was optimised to operate at 128 GHz. This design adopts a typical Antenna-Circuit-Antenna (ACA) configuration, which belongs to the transmitting and receiving (Tx-Rx) type. Although the overall structural concept remains the same, the fabrication precision achievable through AME is insufficient to meet the design requirements at 128 GHz, as the slot spacing on the antenna patch is only 0.05 mm. Moreover, the operating bandwidth extends from 125 GHz to 130 GHz, but the transmission coefficient remains low (approximately -5 dB), primarily due to losses introduced by the meandering stripline.

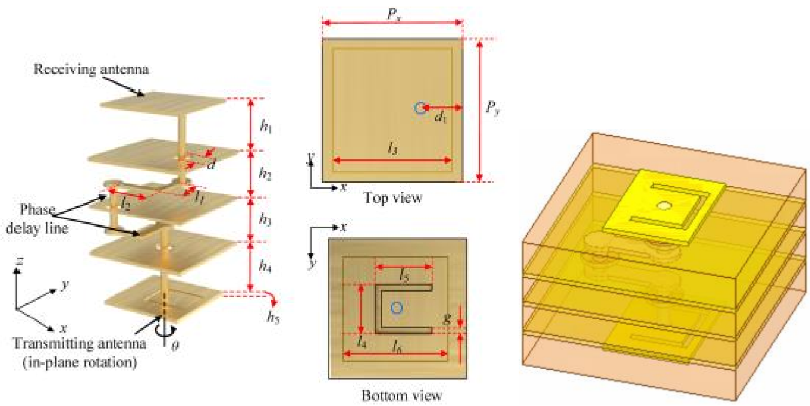

(a) (b)

Fig. 4.22. Antenna-Circuit-Antenna (ACA) structure. (a) Unit cell in [156]. (b) Modified unit cell in 128 GHz.

As illustrated in Fig. 4.23, the perpendicular stripline unit cell operates at 115 GHz. The upper and lower layers consist of rectangular patch antennas, while the intermediate section incorporates a winding stripline positioned between two perpendicular ground planes on the front and back surfaces. The antenna ground is electrically connected to the stripline ground. The winding configuration of the stripline extends the electromagnetic wave path, thereby increasing the phase delay. This perpendicular layout fully exploits the design freedom enabled by AME technology. Moreover, as sub-THz unit cells are too compact to accommodate horizontal striplines, the vertical configuration provides a practical and effective alternative.

However, fabrication precision remains the primary limitation of this unit cell design. The smallest feature size and spacing are both 0.1 mm, which approaches the threshold of current manufacturing capabilities and may lead to fabrication inaccuracies. Owing to this constraint, the antenna structures on the upper and lower layers cannot be overly complex, making narrowband patch antennas the only practical option. Consequently, this unit cell exhibits narrowband performance, and its operating bandwidth varies with changes in stripline length. Additionally, the dielectric material used in AME introduces considerable losses in the sub-THz band. As shown in Fig. 4.24 (a), the transmission coefficient exhibits notable variation as the stripline length increases. Meanwhile, the transmission phase gradually achieves full 360° coverage, as illustrated in Fig. 4.24 (b), although the overall transmission magnitude remains low.

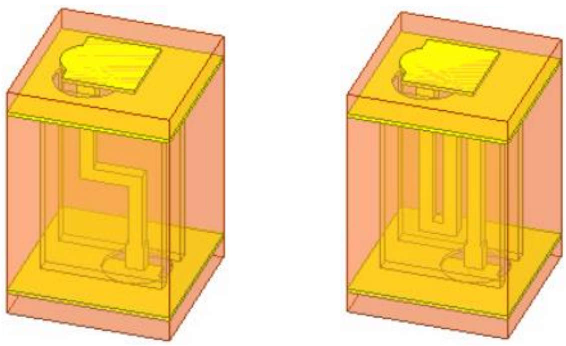

(a) (b)

Fig. 4.23. Perpendicular stripline unit cell. (a) Unit cell with the shortest stripline for minimal phase delay. (b) Unit cell with the longest stripline for increased phase delay.

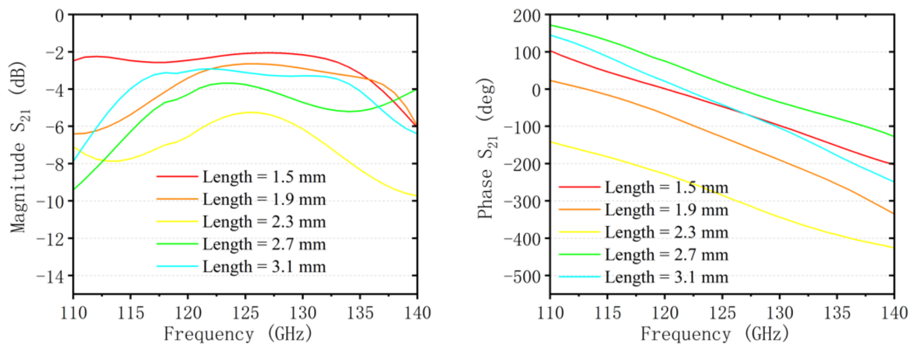

(a) (b)

Fig. 4.24. Simulated (a) transmission coefficients, and (b) transmission phases of perpendicular stripline unit cells with varying stripline lengths.

4.4.3 Fabry-Perot Unit Cell

Fig. 4.25 shows the Fabry-Perot (FP) unit cell operating at 150 GHz. Conventional FP unit cells typically use gratings as their top and bottom surfaces. In contrast, the proposed design incorporates open-ring structures, while phase modulation is achieved by varying the V-shaped metal patch in the middle layer, as illustrated in Fig. 4.25(a). The unit cell has a period of one-quarter wavelength, allowing four unit cells to be combined into a half-wavelength sub-array, as shown in Fig. 4.25(b). The open-ring configuration provides rotational capability, offering both phase and rotational degrees of freedom. This additional flexibility creates the potential to realise the functionalities proposed in [350], thereby overcoming the limitations of polarisation multiplexing. However, as shown in Fig. 4.25(c), the nano-bar-based design enables independent phase modulation for dual polarisations while also supporting unit cell rotation, achieving multi-polarisation functionality—a feature not present in the proposed unit cell. This limitation arises because phase modulation of linearly polarised waves is extremely challenging to achieve within the restricted dimensions of a terahertz metasurface unit cell.

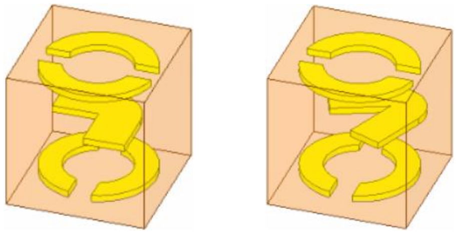

(a)

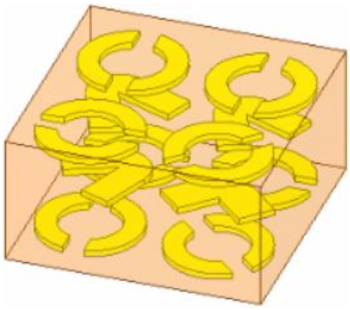

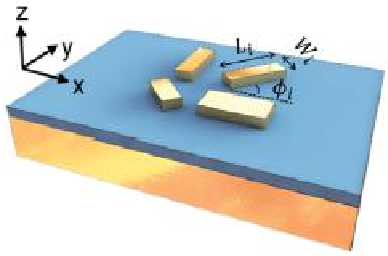

(b) (c)

Fig. 4.25. (a) FP unit cell at 150 GHz with varying phase delay. (b) Sub-array unit cell. (c) Polarisation-multiplexed metasurface unit cell (diagram in (c) is from [350]).

Fig. 4.26 (a) is the FP unit cell operating from 120 GHz to 160 GHz. By adjusting the opening size of the C-shaped elements, the dual-C-shaped structure enables phase modulation. Based on the calculated phase distribution, the metasurface can realise holographic imaging, wherein the electric field is spatially modulated to form a specific pattern - in this case, the letter “S”, as illustrated in Fig. 4.26(b). The metasurface is excited by a waveguide located beneath it. However, due to its relatively simple structure and the fact that the proposed FP unit cell differs from the conventional FP configuration only by incorporating the dual-C-shaped structure in the middle layer, this design does not introduce significant innovation. As shown in Fig. 4.27, the FP unit operates within the 120 - 160 GHz bandwidth; however, owing to the high material loss, the transmission coefficient is limited to approximately -2 dB.

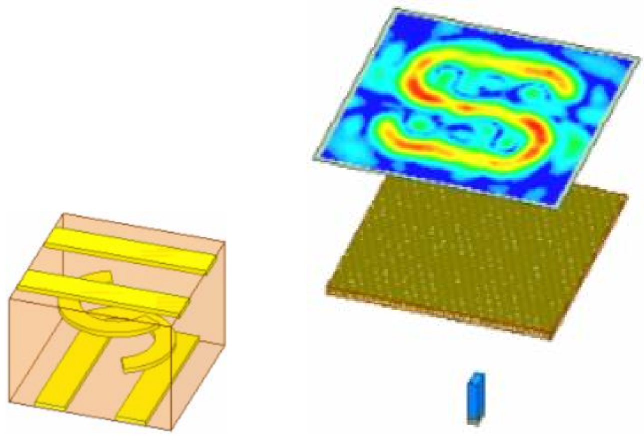

(a) (b)

Fig. 4.26. (a) FP unit cell. (b) FP metasurface for holographic imaging.

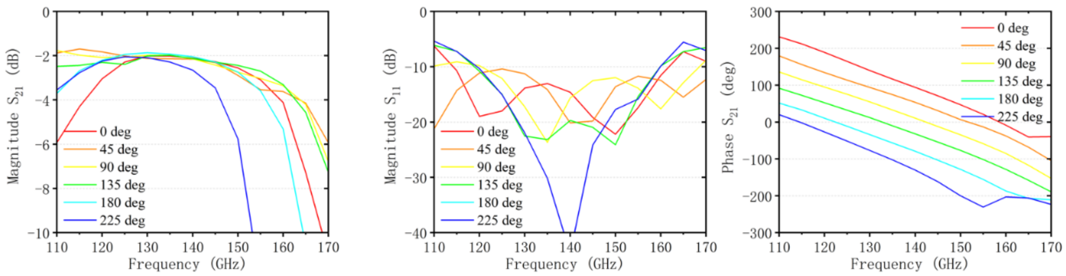

(a) (b) (c)

Fig. 4.27. Simulated (a) transmission coefficients, (b) reflection coefficients and (c) transmission phases.

4.5 Conclusion

In summary, a series of conductive and dielectric metasurface lenses operating in the D-band has been proposed, demonstrating that low-cost additive manufacturing technology can be effectively applied to design sub-THz devices. Although the loss tangent of the dielectric material reduces the gain of the metasurface lens antenna, this limitation can be partially mitigated by employing a larger-aperture lens, thereby achieving higher gain performance. However, due to the precision constraints of additive manufacturing, the geometric complexity of sub-THz designs remains limited, which in turn restricts the flexibility and functionality of the fabricated devices. Despite these challenges, the proposed metasurface lenses exhibit high gain enhancement and beam-scanning capabilities, making them promising candidates for next-generation sub-THz communication systems.

Chapter V Sub-THz Metasurface Sensor for Real-Time Skin Condition Monitoring

5.1 Introduction

Terahertz (THz) technology plays a pivotal role in biological imaging and sensing applications [351], [352]. THz radiation offers several unique features, including abundant spectral resources, short wavelengths, non-ionising properties [353], and strong sensitivity to water [354]. Previous studies [355] have reported that high-intensity THz radiation does not induce thermal effects or oxidative stress in human skin fibroblasts, indicating its relative safety under such conditions. THz technology holds great promise for medical imaging, genetic diagnostics, security screening, and manufacturing quality control [356]. THz waves have been proposed for their use in skin screening, such as burn injury assessment [357] and skin cancer imaging [358]. Recent studies have demonstrated that metamaterial stickers can deliver excellent screening performance in the sub-THz range (100–300 GHz) for fruit ripeness evaluation [359], underscoring the significant potential of sub-THz metamaterials and metasurfaces for non-invasive sensing applications.

Before introducing the skin condition monitoring system, a brief overview of relevant skin properties is provided. For electromagnetic (EM) waves, the dielectric constant of biological tissues is a key parameter for detection [360], as it closely correlates with water content. The fundamental principle of THz-based detection systems relies on the difference in water content between normal and cancerous tissues, leading to variations in dielectric properties [361], [362], [363]. Human skin has a multilayered structure, comprising the stratum corneum (SC), epidermis, and dermis, with typical thicknesses of $10-30\,\mu m$, $60-100\,\mu m$, and $1.2-2.8\,mm$, respectively [364], as illustrated in Fig. 5.1. Commonly studied abnormal skin tissues include melanoma (MM), basal cell carcinoma (BCC), and squamous cell carcinoma (SCC), with cancerous lesions typically 4 - 6 mm in diameter [365], [366] and primarily originating in the epidermis [367]. The THz skin cancer detection system operates in the frequency range of 0.1–3 THz [368], enabling the detection of skin features within a depth of 1 mm. Thus, THz imaging offers sufficient resolution to visualise abnormal skin tissue while achieving appropriate penetration depths without interference from deeper skin layers, making it highly suitable for non-invasive skin condition monitoring.

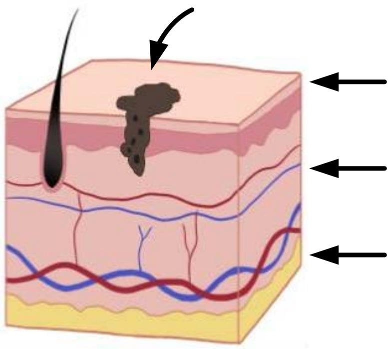

Fig. 5.1. Schematic of the skin.

Various EM wave-based methods have been developed for skin detection. Near-field detection probes, which achieve direct contact with the materials under test (MUTs), come in different forms, including microstrip lines [369], coaxial probes [370], [371], and waveguides [372], [373], [374]. These probes typically measure the reflection coefficient at a single resonant frequency [374]. Probe-based detection approaches require the establishment of extensive databases encompassing skin from different body parts across diverse individuals, alongside complex algorithms to define abnormal skin conditions—such as setting thresholds based on reflection coefficients. In contrast, imaging-based detection is more intuitive and effective, as it only necessitates identifying localised differences relative to the surrounding skin tissue. In [375], [376], a synthetic ultra-wideband imaging system operating from 12 to 110 GHz was proposed for ex vivo human skin imaging, where high-resolution time-domain pulses were reconstructed via inverse Fourier transform (IFT). These EM imaging systems are typically based on vector network analysers (VNAs). An alternative approach is terahertz time-domain spectroscopy (THz-TDS) [377], which directly captures time-domain THz pulses and reconstructs broadband spectra from 0.3 to 5 THz using Fast Fourier Transform (FFT). In vivo human skin characterisation has been reported using THz-TDS [378]. These imaging methods commonly employ focusing optics to detect single-pixel regions. While they require minimal amounts of MUTs, the reliance on raster scanning for image acquisition results in time-consuming procedures that hinder real-time or large-area clinical applications.

THz metasurface (MS) sensors [379], [380] have been proposed for ex vivo cancer cell detection [381], [382], [383]. Cells under test are cultivated on the surface of the MS resonator [384], and the dielectric constant of the cells affects the transmission, reflection or absorption of the MS, which then can be detected by the VNA or THz-TDS. Currently, most MS sensors require direct contact between the MUT and the resonator while demanding that the MUT be very thin [385], [386] and have a low loss [387]. This method can generate a strong resonance with a high Q factor and high sensitivity to changes in refractive index. However, high-loss MUTs can degrade the performance of these MS sensors, making the resonance less apparent and reducing the Q factor [388]. If MS sensors are to be used for in-vivo skin condition monitoring, the impact of the skin losses must be addressed, and only the reflection can be measured. The propagation path of the waves must be from air to the MS and then to the skin in the semi-infinite half-space. Therefore, traditional transmissive measurement setups [389], [390], [391], [392] are not suitable for in-vivo skin detection.

In this chapter, a real-time skin condition monitoring system based on a refractive-index-sensitive metasurface (MS) sensor is proposed, as illustrated in Fig. 5.2. Pork skin is considered a relatively good model for simulating human skin due to its similar anatomical and physiological properties [393], [394]. Therefore, porcine skin is employed as the experimental model in this chapter. The abnormal skin tissue refers to cancerous lesions, severe tissue damage (such as burns), and non-cancerous conditions, including mild inflammation, dehydration, and surface dryness. These abnormalities alter the local water content and dielectric properties of the skin, thereby affecting THz wave interactions and enabling their detection. The proposed MS sensor detects changes in the dielectric constant of high-loss MUTs by inducing shifts in the resonant frequency. Unlike conventional MS sensors, which suffer performance degradation in high-loss environments, the proposed design leverages interference theory [395], [396] to minimise loss effects while maintaining sensitivity to dielectric variations. Although MSs have been previously applied for imaging enhancement [397] and biomolecular detection [398], the proposed MS is specifically tailored to detect dielectric property changes in biological tissues. In practice, an MS sensor is applied to the skin surface. Abnormal tissue presence leads to measurable changes in the MS reflection coefficients, which are subsequently captured by a THz imager. This method enables a rapid, portable, and non-invasive approach to skin condition assessment and holds promise for future clinical applications in early skin disease screening.

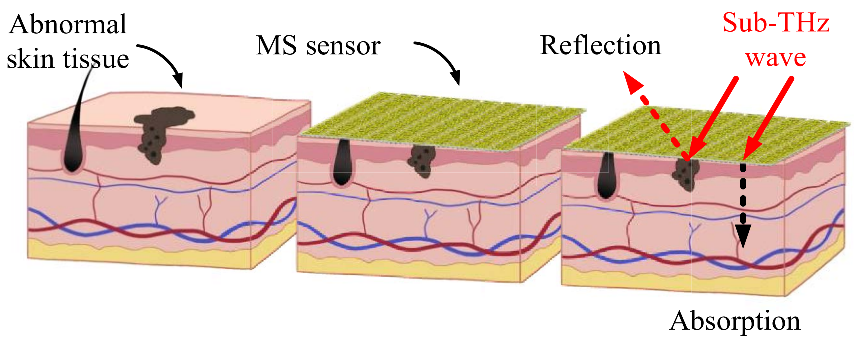

(a)

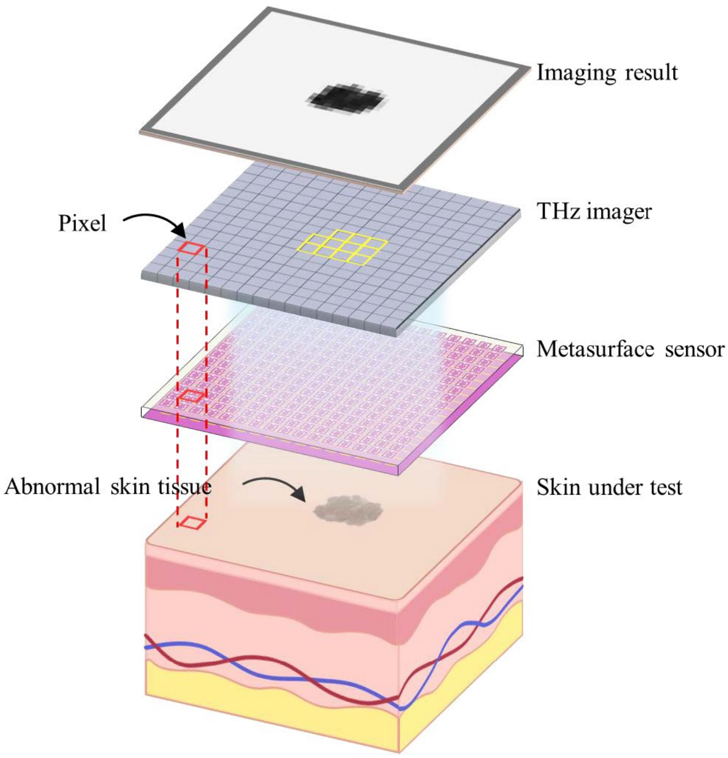

(b)

Fig. 5.2. Schematic of (a) the working principle of the MS sensor, and (b) the MS-

based real-time skin condition monitoring system.

5.2 Mathematical Model of the Skin

The Debye model and Cole-Cole model [399] have been widely used to describe the permittivity of biological tissues. The complex permittivity can be characterised by $\varepsilon_r^*(\omega) = \varepsilon_r'(\omega) - i\,\varepsilon_r''(\omega)$, the asterisk (*) in the superscript denotes the complex number. The Debye model leads to the equation:

$$\varepsilon_r^*(\omega) = \varepsilon_r(\infty) + \frac{\varepsilon_r(0) - \varepsilon_r(\infty)}{1 + i\omega\tau_0} \tag{5.1}$$

where $\varepsilon_r(0)$ is the static permittivity at the lower frequency, $\varepsilon_r(\infty)$ is the permittivity as the frequency approaches infinity, τ_0 is a characteristic constant called the relaxation time, ω is the angular frequency and equals 2π·frequency. These parameters are usually given in the reference papers. The Cole-Cole model can be given:

$$\varepsilon_r^*(\omega) - \varepsilon_r(\infty) = \frac{\varepsilon_r(0) - \varepsilon_r(\infty)}{1 + (i\omega\tau_0)^{1-\alpha}} \tag{5.2}$$

where involving a disposable constant α for more accurate fitting in the wide band. In the EM wave field, dielectric constant and loss tangent are commonly used, while refractive index, absorption coefficient and conductivity are prevalent in optics. Therefore, the relationships between the dielectric constant and the refractive index [400] are given:

$$\varepsilon_r^*(\omega) = n^*(\omega)^2 \tag{5.3}$$

$$n^*(\omega) = n(\omega) - ica(\omega)/2\omega \tag{5.4}$$

$$\sigma(\omega) = -\omega\varepsilon_0 \cdot imag(\varepsilon_r^*(\omega)) \tag{5.5}$$

$$tan\delta(\omega) = \varepsilon_r''(\omega)/\varepsilon_r'(\omega) \tag{5.6}$$

where $n(\omega)$ and $\alpha(\omega)$ are the real refractive index and the absorption coefficient, ε_0 and c refer to the vacuum permittivity and the speed of light, and $\sigma(\omega)$ is the conductivity. $imag(\cdot)$ represents the function for extracting the imaginary part. $tan\delta(\omega)$ is the loss tangent.

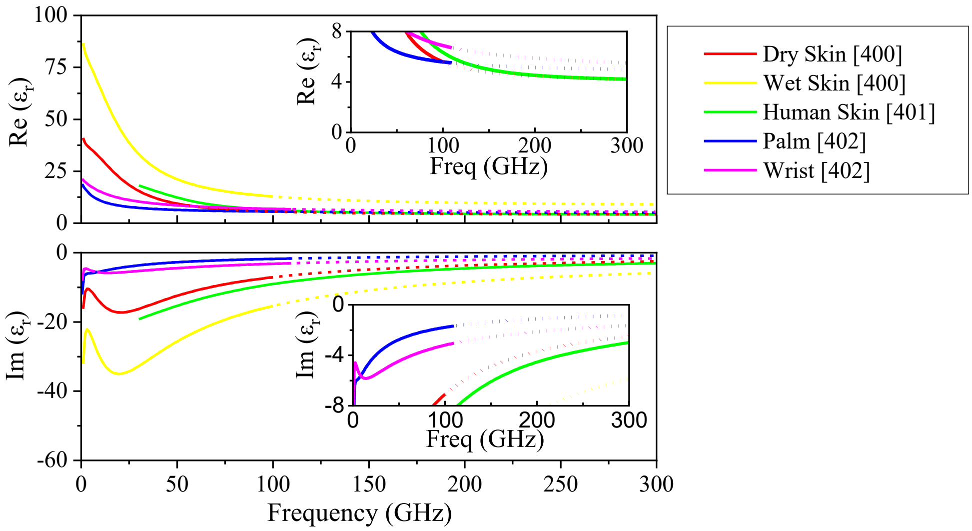

(a)

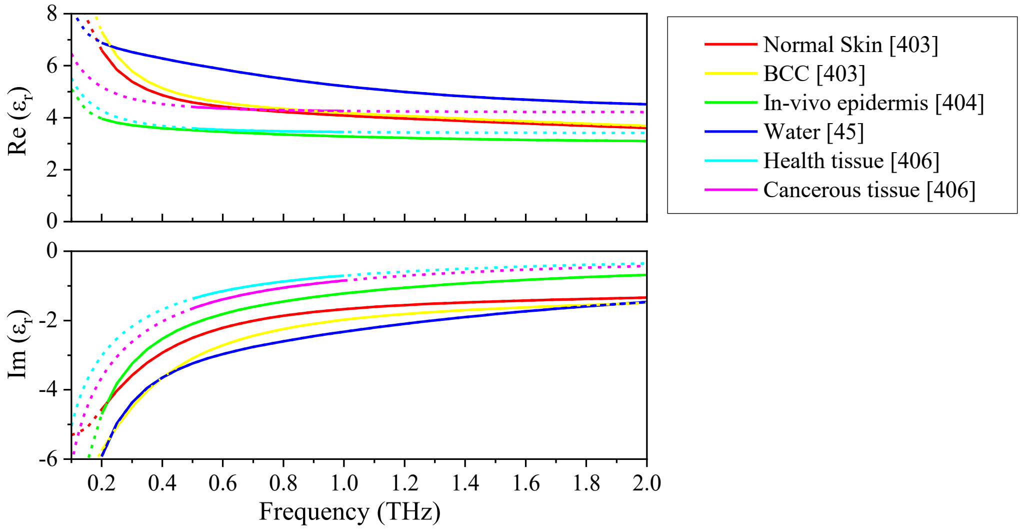

(b)

Fig. 5.3. The real and imaginary parts of the biological tissues' complex permittivity in reference papers. (a) GHz spectrum. (b) THz spectrum. Solid lines correspond to experimental measurements, whereas dashed lines represent values extrapolated or calculated using empirical models.

According to the Debye, Cole-Cole model and the above equations, the real and imaginary parts of the biological tissues' complex permittivity [400]-[406] are shown in Fig. 5.3. The solid line represents the data provided in the reference papers, while the dashed line represents the data predicted by the mathematical model. When comparing the zoom-in image in Fig. 5.3 (a) with Fig. 5.3 (b), the permittivity data from 100 to 300 GHz (0.1 to 0.3 THz) are contradictory between the GHz and THz spectra. This is potentially because of the edge effects of the Fast Fourier Transformation (FFT) in the THz-TDS. However, the predicted data from [406] in the THz spectrum is similar to that in the GHz spectrum, which means the data is likely to be accurate. Also, the data includes the permittivity of the cancerous tissue. Therefore, we adopted the data to carry out the simulation experiments. The extracted data in the D-band (110 to 170 GHz) are shown in Fig. 5.4.

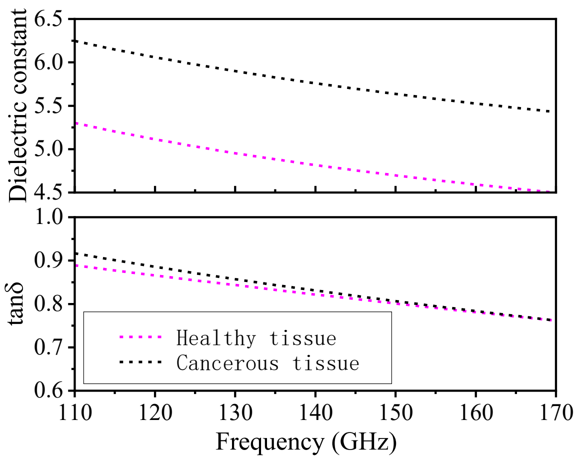

Fig. 5.4. Predicted dielectric constant and loss tangent in D-band [406]. Dashed lines represent values extrapolated or calculated using empirical models.

5.3 Metasurface Sensor Design

As shown in Fig. 5.5 (a), conventional metasurface (MS) sensors are typically designed with the MUT positioned along the transmission path of the incident EM wave, requiring the MUT to be only a few micrometres thick. Furthermore, these sensors perform optimally when the MUT exhibits low dielectric loss. However, for practical skin detection, it is necessary to place the MS directly onto the skin surface, resulting in the MUT occupying the wave propagation direction with an effectively infinite thickness, as shown in Fig. 5.5 (b). Additionally, biological tissues such as skin inherently have high dielectric losses, which severely degrade the performance of conventional MS designs. To overcome these limitations, we propose a novel MS sensor capable of operating under high-loss conditions, enabling effective skin condition monitoring.

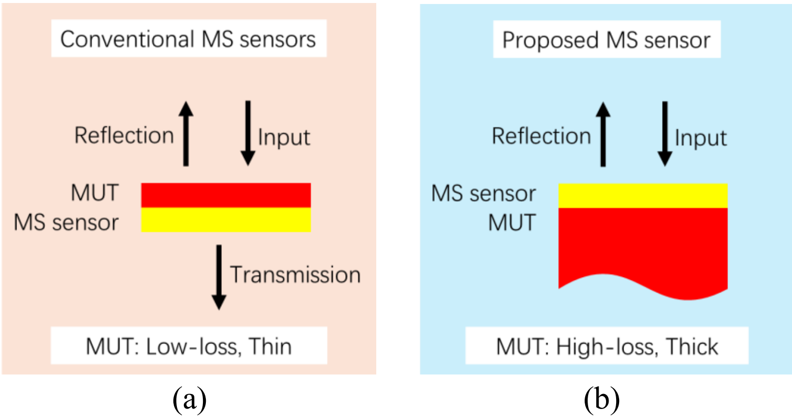

Fig. 5.5. Comparison between the conventional and proposed MS sensor with MUT. (a) Conventional MS sensor for ex vivo sensing. (b) Proposed MS sensor for in-vivo skin sensing.

5.3.1 Limitations of Conventional Metasurface Sensors in High-Loss Environments

Before introducing the proposed metasurface sensor, it is important to review the characteristics and limitations of conventional metasurface (MS) designs. Conventional MS sensors depend on LC resonance and dipole resonance [407], which typically require the material under test (MUT) to be thin, low-loss, and in direct contact with the resonant elements. The metasurface and the MUT together form the sensing unit cell, where changes in the dielectric constant of the MUT are translated into variations in the overall reflection coefficient for detection. The thickness and the loss tangent of the MUT can also affect the resonance behaviour of the system. As shown in Fig. 5.6 (a), a simple and conventional MS sensor consists of a low-loss substrate for impedance matching and a ground plane with a rectangular slot array for resonating when the electric field polarisation direction is perpendicular to the slot. With the increase of the loss tangent, the resonance point of the reflection is flattened in Fig. 5.6 (b). The widely accepted metrics for evaluating a sensor's performance include sensitivity (S) and quality factor (Q) [380]. They can be given:

$$\mathrm{S} = \Delta f/\Delta n \tag{5.7}$$

$$\mathrm{Q} = f/\mathrm{FWHM} \tag{5.8}$$

where Δf and Δn are the variations in the resonance frequency and refractive index, f represents the resonance frequency, and FWHM is the full width at half maximum. The increase in the loss tangent of the MUT leads to a reduction in the Q-factor of the sensor, thereby diminishing the prominence of the resonant frequency shift. As a result, sensing high-loss materials remains a significant challenge.

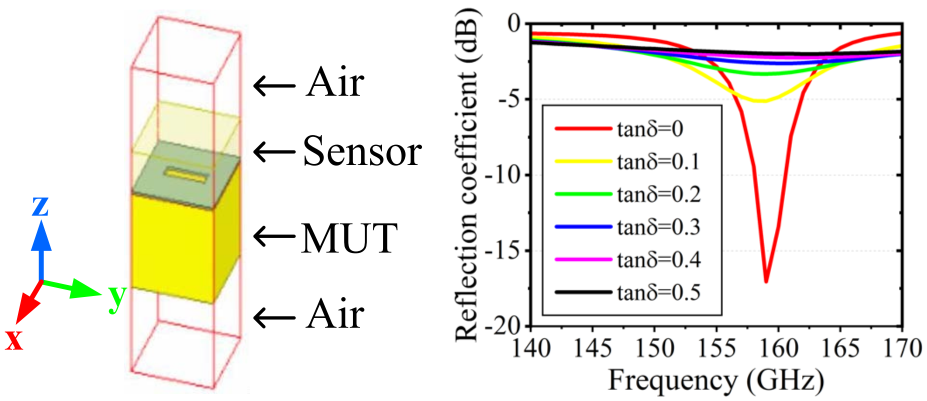

(a) (b)

Fig. 5.6. Challenge of measuring high-loss materials. (a) Conventional MS sensor with a rectangular slot. (b) Reflection coefficients with the increase of the MUT's loss tangent from 0 to 0.5.

5.3.2 Proposed MS Sensor for Skin Tissue Characterisation

The proposed MS in Fig. 5.7 consists of a split ring resonator (SRR) and a ground with a rectangular slot, which is fabricated using the cyclic olefin copolymer (COC) microfabrication techniques [408], [409]. The flexible COC MS has two gold (Au) layers with a thickness of $200nm$, and the total thickness is within $100\mu m$ — the ultrathin thickness results in a significant coupling effect between the two layers. The dielectric constant and the loss tangent of the COC are 2.34 and 0.0007. The skin is considered a half-infinite space.

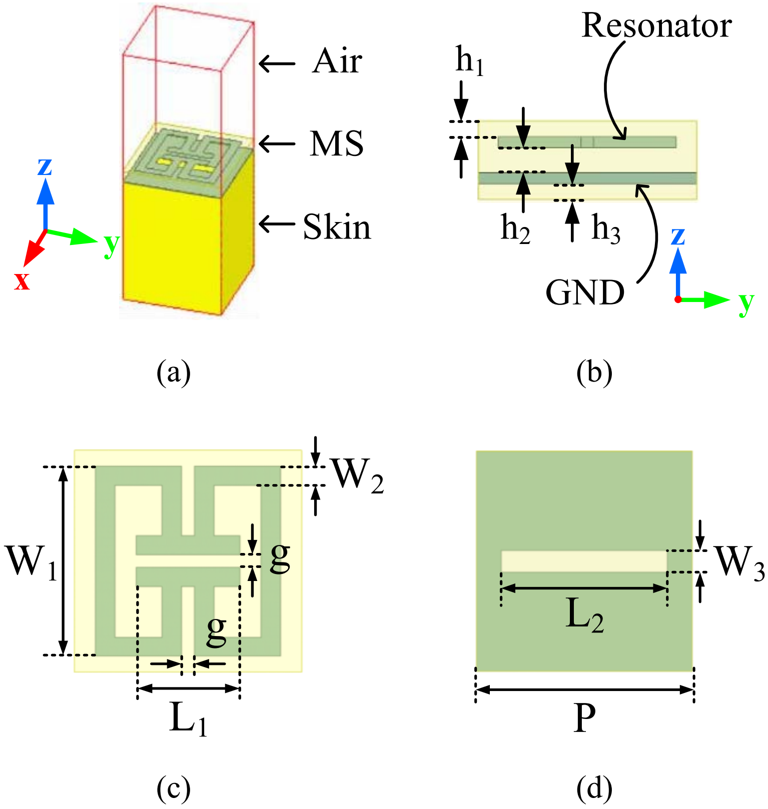

Fig. 5.7. Proposed COC MS sensor. (a) Oblique view in simulation. (b) Side view details. (c) Resonator details. (d) Ground plane (GND) details: $h_1 = 10\mu m$, $h_2 = 80\mu m$, $h_3 = 5\mu m$, $W_1 = 600\mu m$, $W_2 = 60\mu m$, $W_3 = 70\mu m$, $\mathrm{g} = 40\mu m$, $L_1 = 320\mu m$, $L_2 = 440\mu m$, $P = 700\mu m$, Conductor thickness= $200nm$.

Instead of the equivalent circuit theory, the interference theory [395], [396] is used to analyse the COC MS, as shown in Fig. 5.7 (a). The overall reflection and transmission of the MS are superpositions of the multiple reflections and transmissions between the resonator and the ground.

$$\begin{aligned} \mathrm{S}_{11}^{*} &= \mathrm{Sr}_{11}^{*} + \mathrm{Sr}_{21}^{*}\mathrm{Sg}_{11}^{*}\mathrm{Sr}_{12}^{*}e^{i\cdot 2\beta} + \mathrm{Sr}_{21}^{*}\mathrm{Sg}_{11}^{*2}\mathrm{Sr}_{22}^{*}\mathrm{Sr}_{12}^{*}e^{i\cdot 4\beta} + \cdots \\ &= \mathrm{Sr}_{11}^{*} + \mathrm{Sr}_{21}^{*}\mathrm{Sr}_{12}^{*}\mathrm{Sg}_{11}^{*}e^{i\cdot 2\beta}\sum_{n=0}^{\infty}\mathrm{Sg}_{11}^{*n}\mathrm{Sr}_{22}^{*n}e^{i\cdot 2n\beta} \end{aligned} \tag{5.9}$$

$$S_{11}^* = Sr_{11}^* + \frac{Sr_{21}^* Sr_{12}^* Sg_{11}^* e^{i\cdot 2\beta}}{1 - Sg_{11}^* Sr_{22}^* e^{i\cdot 2\beta}} \tag{5.10}$$

$$S_{21}^* = \frac{Sr_{21}^* Sg_{21}^* e^{i\cdot\beta}}{1 - Sg_{11}^* Sr_{22}^* e^{i\cdot 2\beta}} \tag{5.11}$$

where Sr_{ij}^* and Sg_{ij}^* represents the S parameters in the interface of the resonator and ground, and the subscript "$i\ j$" means the wave propagation from port j to port i, as shown in Fig. 5.8 (c), (e) and (g). The asterisk (*) in the superscript denotes the complex number, $S_{ij}^* = S_{ij}e^{i\Phi_{ij}}$. The magnitude of Sr_{11}^* and Sr_{22}^* are almost identical. The "Deembed setting" in the simulation is set to reach the resonator's and ground's surface. In Fig. 5.8 (c), the magnitude of the Sr_{11}^* is equal to that of the Sr_{22}^*. For the ease of parameter sweeping, the dielectric constant and loss tangent of the skin are set to fixed values, $\varepsilon_r = 5.8$, $tan\delta = 0.8$. In Fig. 5.8 (c) and (g), the effect of the dielectric constant on the reflection and transmission is tiny in magnitude but relatively significant in phase. The comparison in Fig. 5.9 shows that the magnitude and phase of the calculated S_{21} are close to those of simulated S_{21}, whereas the S_{11} partially aligns. This is because the mutual coupling effects between the resonator and ground can not be accounted for during the data extraction process, Sr^* and Sg^*. And the distance between the resonator and the ground is small, only $80\mu m$. However, the interference theory is enough to explain the principle of the proposed MS. The Sr_{ij}^* and Sg_{ij}^* are substituted into Equ. (5.10) and (5.11), and the calculated results in Fig. 5.10 (a) exhibit a trend of the resonance frequency shift. As for the S_{11}^* at 152 GHz, the calculation process of the superpositions is presented in Fig. 5.10 (b), which shows the addition calculation process of Equation (5.10) from the Sr_{11}^*at the bottom left to the S_{11}^* at the top right, the difference between various skin's dielectric constants is accumulated. The simulated results in Fig. 5.11 (a) demonstrate that the resonant frequency of the proposed MS will shift with the increase of the high-loss skin's dielectric constant, making the proposed MS suitable for high-loss materials detection applications. And the simulated S_{11} of the health and cancer tissue [406] with the proposed MS sensor are shown in Fig. 5.11 (b); the resonant frequency shift is apparent, which indicates that the proposed MS can be used for skin dielectric detection.

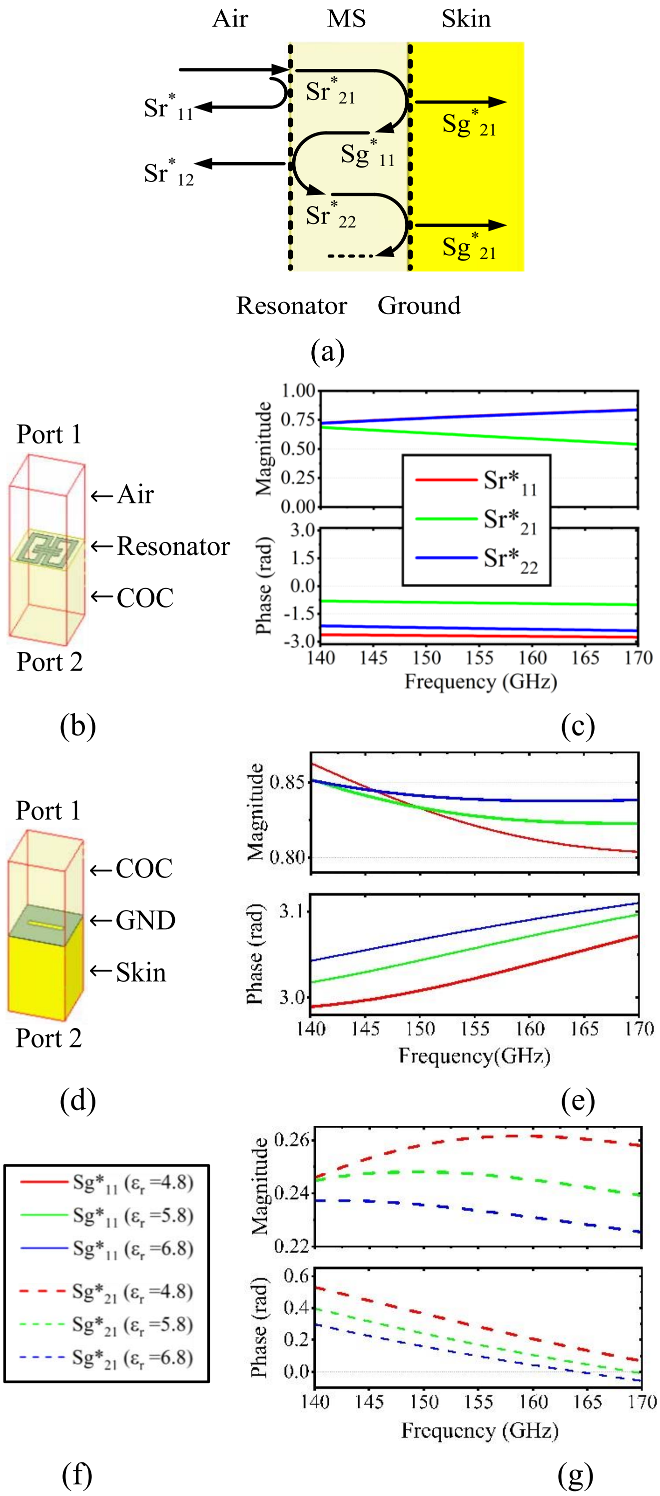

Fig. 5.8. (a) Schematic of the interference theory. (b) Simulation model of the resonator interface. (c) Magnitude and phase of the resonator interface. (d) Simulation model of the ground interface. (e) Magnitude and phase of the reflection in the ground interface with the increase of the skin's dielectric constant. (f) Legends of the figures (e) and (g). (g) Magnitude and phase of the transmission in the ground interface.

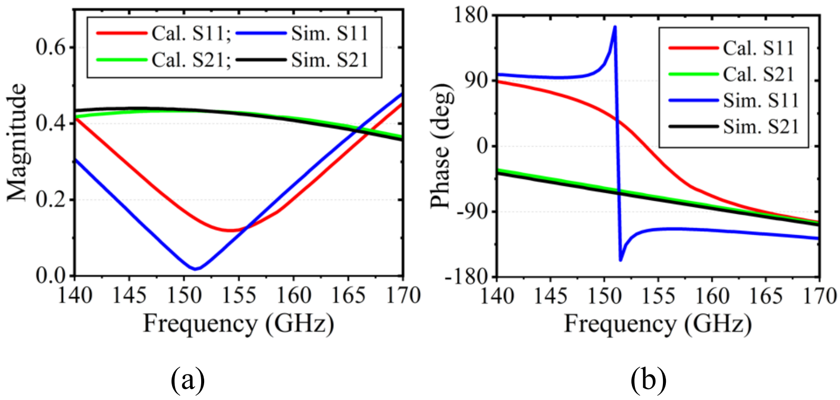

Fig. 5.9. Comparison between calculated and simulated results. (a) Magnitude. (b) Phase. Skin: $\varepsilon_r = 5.8$, $tan\delta = 0.8$

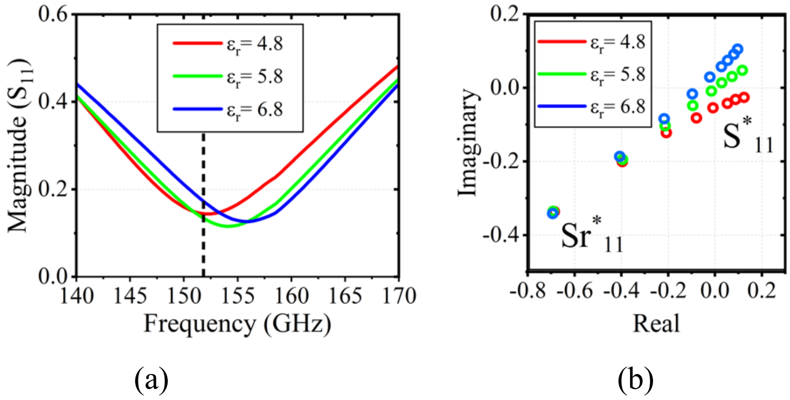

Fig. 5.10. (a) Calculated reflection coefficients S_{11} with the increase of the skin's dielectric constant. (b) S parameter calculation as the iterative number increases at 152 GHz in the complex plane (Skin: $tan\delta = 0.8$).

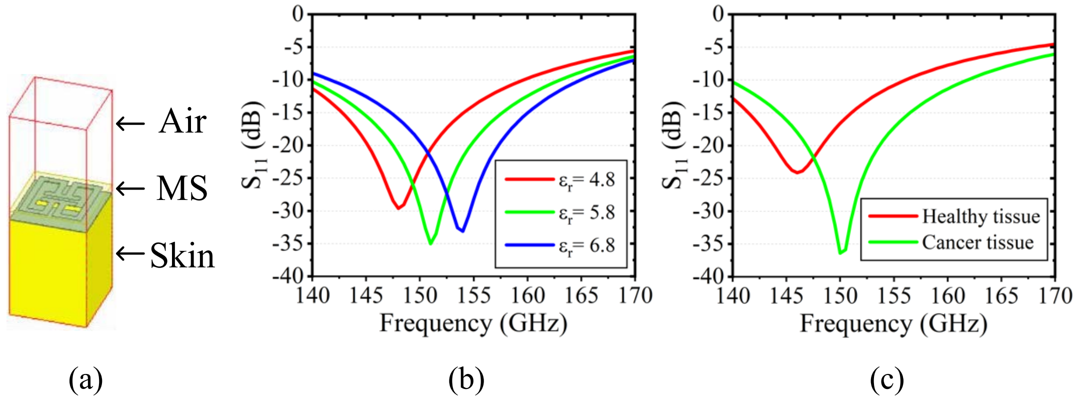

Fig. 5.11. (a) Simulation models and simulated reflection coefficients S_{11} with (b) various dielectric constants of the skin tissue (Skin: $tan\delta = 0.8$) and (c) the predicted dielectric constants and loss tangents in [406] (Healthy tissue: $\varepsilon_r = 4.5\sim4.8$, $tan\delta = 0.76\sim0.82$; Cancer tissue: $\varepsilon_r = 5.4\sim5.7$, $tan\delta = 0.76\sim0.83$).

Because the skin is soft and the MS is flexible, it is necessary to use a hard surface to flatten them for a better sensing effect. In Fig. 5.12 (a), the flattening sheet is characterised by $\varepsilon_r = 2.65$ and $tan\delta = 0.02$. Due to the limitation of the measurement setup, the incident angle (θ) to the MS cannot be 0°. Thus, When $h_F = 0.5\ mm$, reflection coefficients with various incident angles have been simulated and shown in Fig. 5.12 (b). The incident angle is set to 30° after this, and the skin is characterised by $\varepsilon_r = 4.8$ and $tan\delta = 0.8$. When adding the flattening sheet, the resonance frequency in Fig. 5.12 (c) shifts with the variation of its thickness. The reflection coefficient can still respond to the variety of skin tissue's dielectric constants in Fig. 5.12 (d). The frequency shift is partly restricted, but the amplitude variety still exists, which can be utilised for imaging experiments.

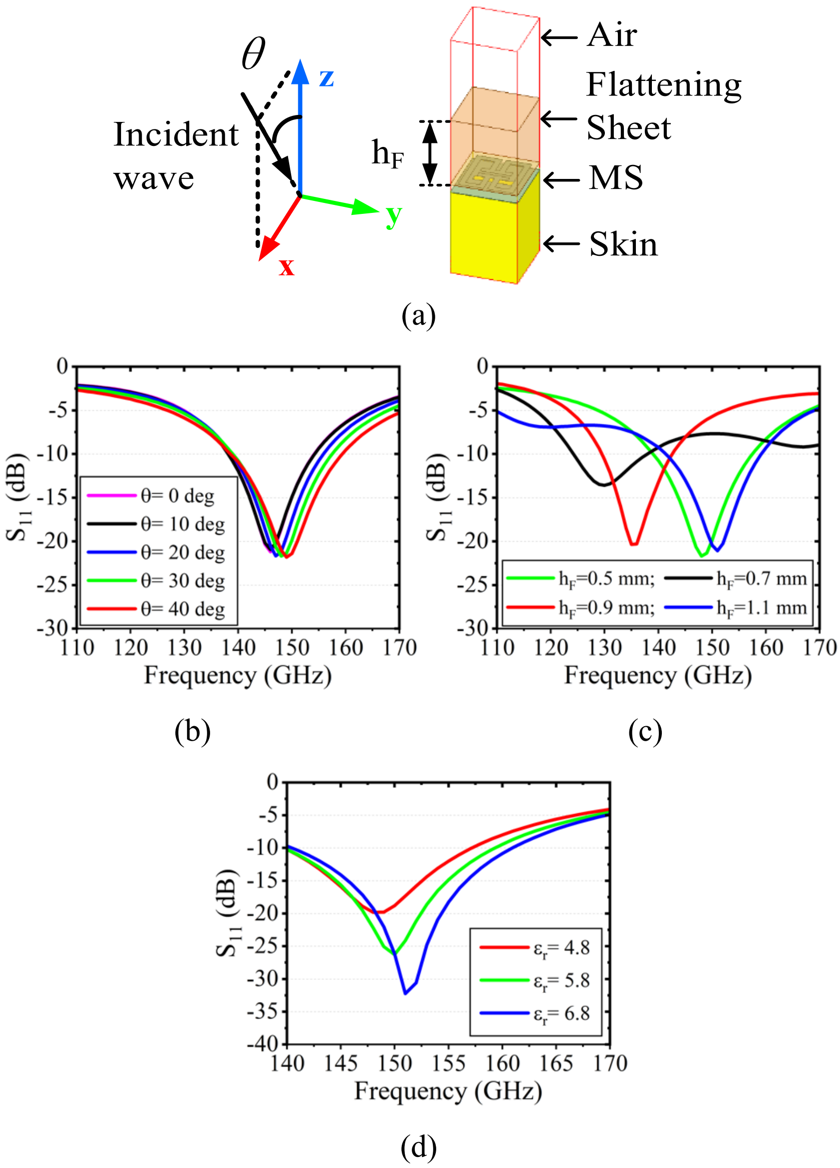

(a) (b) (c) (d)

Fig. 5.12. (a) Simulation models. Simulated reflection coefficients S_{11} with various (b) incident angles, (c) heights of the flattening sheet, and (d) dielectric constants of the skin (skin: $tan\delta = 0.8$).

5.4 Experiments and Comparisons

This section aims to validate the capability of the proposed MS sensor to detect variations in skin properties through imaging experiments. Pork skin is used as the skin under test. The experiment is conducted to characterise the functional roles and material properties of three key components shown in Fig. 5.12 (a): a flattening sheet, the proposed MS sensor, and the pork skin sample. Accordingly, the experimental procedure is organised into three parts: (1) optimisation of the flattening sheet parameters, (2) characterisation of the pork skin, and (3) measurement with the proposed MS sensor with the flattening sheet and pork skin.

5.4.1 Reflection Coefficients Measurement Setup

The measurement setup is shown in Fig. 5.13 (a). This system is capable of capturing the reflection coefficient resulting from planar wave incidence, allowing for direct comparison with simulation data. In principle, by comparing simulation and experimental results, the system is capable of characterising a wide range of materials. The sub-THz wave from the transmitting (Tx) side goes through a biconvex lens and a plano-convex lens to irradiate the material under test (MUT). The reflected wave then travels back through the same lens pair and is collected by the receiving (Rx) side. As shown in Fig. 5.13 (b) and (c), both the Tx and Rx sides comprise a VDI frequency extension module, a WR-06 waveguide twist to ensure TM-mode incidence, a pyramidal rectangular square horn and a large biconvex lens. The large biconvex lens is used to capture as much power as possible and to generate a distant focal point, thereby reducing multiple reflections between the two lenses.

As a first step, the dielectric constant of the flattening sheet is measured. The plano-convex lens from [410] in Fig. 5.13 (d) produces a plane wave, and the MUT is a curable polymeric dielectric substrate (PDS) using additive manufacturing [308] and is secured with adhesive tape on the other side of the fixture in Fig. 5.13 (e). The plano-convex lens and biconvex lens are made of COC using a fused deposition modelling (FDM) 3D printer, while the fixture is made of polylactic acid (PLA). The angles of incidence and reflection of the Tx and Rx sides are 30°. By replacing the MUT with air and metal, the reflection from the air and ground (GND) is measured by the VNA, marked as S^*_{21-air}, S^*_{21-GND}. The calibrated reflection coefficient of the MUT can be given:

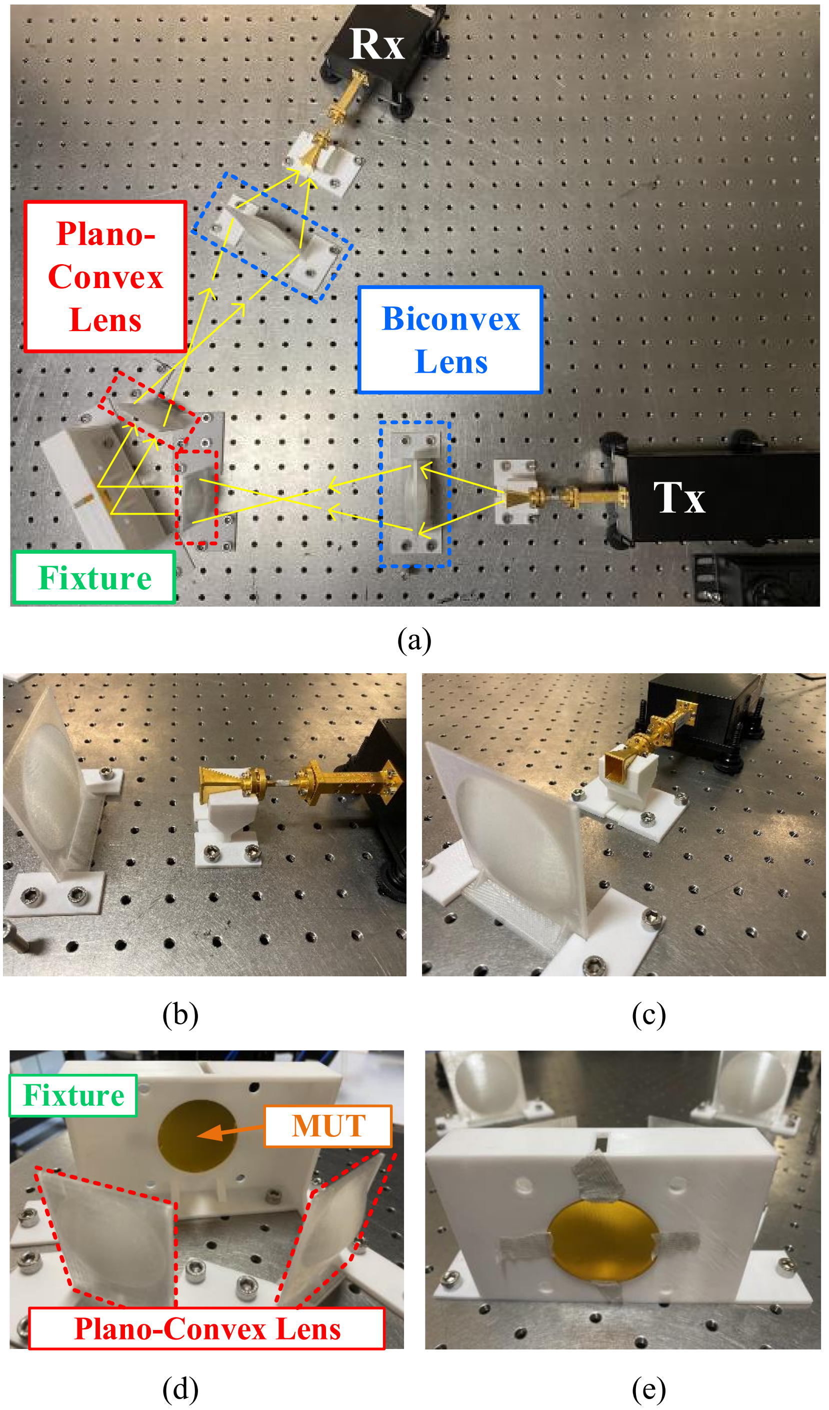

Fig. 5.13. (a) Reflection coefficient measurement setup with an incident angle of 30°. (b) Transmitting (Tx) side. (c) Receiving (Rx) side. (d) Fixture and material under test (MUT). (e) The other side of the fixture.

$$S^*_{11-MUT} = \frac{S^*_{21-MUT} - S^*_{21-Air}}{S^*_{21-GND} - S^*_{21-Air}} \tag{5.12}$$

where the asterisk (*) in the superscript denotes the complex number. S^*_{11-MUT} represents the complex reflection coefficient of the MUT and is the same as the reflection from FloquetPort1 to FloquetPort1 in the simulation. In Fig. 5.14, the measured and simulated results match well with each other, which verifies the simulation model and the permittivity of the PDS ($\varepsilon_r = 2.65$, $tan\delta = 0.02$). The PDS sheet is used to flatten the skin and MS.

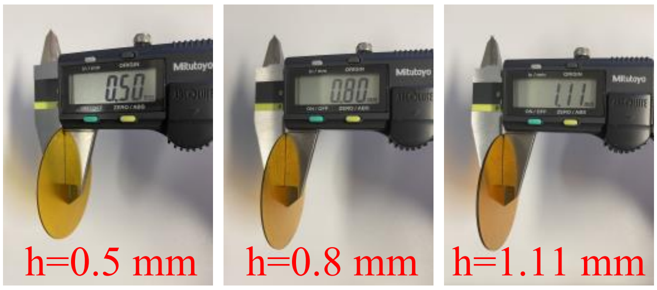

(a)

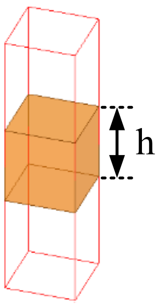

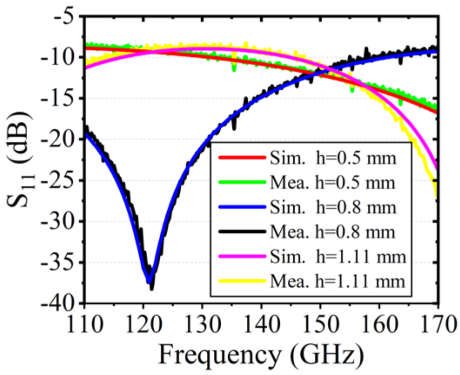

(b) (c)

Fig. 5.14. (a) MUTs in three thicknesses; $h = 0.5\,mm, 0.8\,mm$ and $1.11\,mm$. (b) Simulation model. (c) Comparison between measured and simulated results. (PDS: $\varepsilon_r = 2.65$, $tan\delta = 0.02$).

5.4.2 Skin Tissue Measurement

The approximate number of the dielectric constant and loss tangent of the skin can be obtained by comparing the simulated and measured reflection coefficient. As shown in Fig. 5.15 (a) and (b), the pork belly (PB) and hindquarter (HQ) skin samples are measured by using the reflection coefficients measurement setup. After purchase, the entire PB skin was covered with plastic wrap to retain moisture and prevent evaporation. In contrast, the HQ skin was exposed to air, resulting in relatively less moisture. In this way, skin samples with different dielectric constants are obtained. The PDS sheet is used to flatten the skin samples. The fixture will not deform due to its structural design. The thickness of the PBS sheet is adjusted to 0.97mm to ensure the resonance frequency falls within the D-band. By varying the dielectric constant and the loss tangent of the skin model in Fig. 5.15 (c), the measured and simulated results match each other in Fig. 5.15 (d). The accurate dielectric constant and the loss tangent of the skin samples should be a function of frequency. The parameters at each frequency point are slightly different. Therefore, there are slight differences between measurement and simulation. The comparison indicates the PB to be ($\varepsilon_r = 4.6$, $tan\delta = 0.7$). Then, HQ skin is used to represent abnormal skin, providing a skin under test with a different dielectric constant and loss compared to PB skin. The HQ is about ($\varepsilon_r = 2.9$, $tan\delta = 1.3$). The reflections of the PDS+PB and PDS+HQ across the D-band are tiny, approximately less than -10 dB.

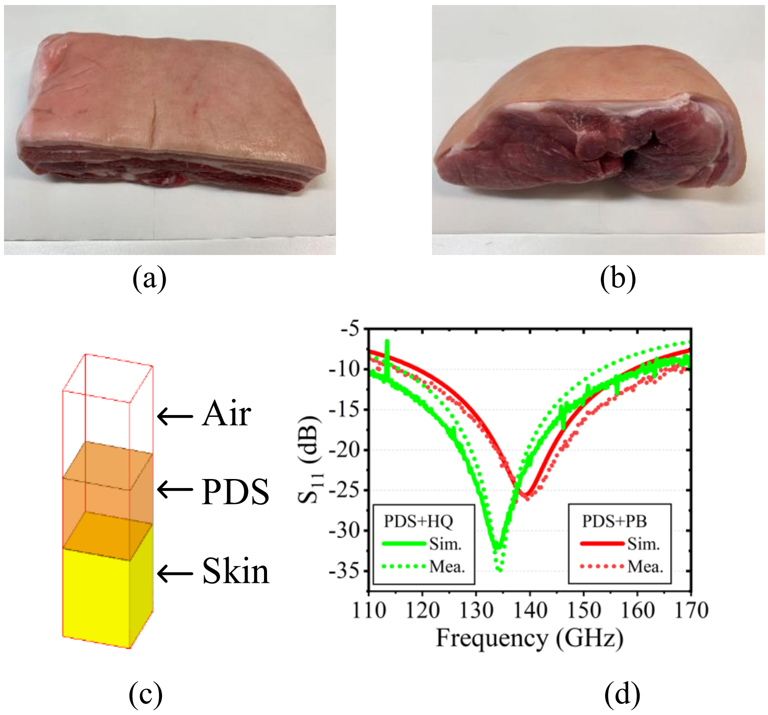

Fig. 5.15. The approximate values of the dielectric constant and loss tangent. (a) Pork belly (PB) skin sample. (b) Hindquarter (HQ) skin sample. (c) Simulation model. (d) Comparison between measured and simulated results. (PB: $\varepsilon_r = 4.6$, $tan\delta = 0.7$, HQ: $\varepsilon_r = 2.9$, $tan\delta = 1.3$).

5.4.3 Metasurface Sensor Measurement with Flattening Sheet and Skin Tissue

The PDS sheet is required to measure the MS, and the skin sample is pressed against both the PDS and MS to ensure there are no air gaps. Numerous experiments have been conducted to adjust the resonance frequency of the PDS+MS+Skin by changing the thickness of the PDS sheet. Finally, a 0.5 mm PDS sheet with four layers of transparent tape (T4) is used as the flattening sheet. According to the experiments, the transparent tape can finely adjust the resonance frequency, as shown in Fig. 5.16 (a). The resonance frequency in Fig. 5.16 (b) and (c) shifts to the left with the increase in the number of transparent tape layers. By using the 0.5 mm PDS sheet with four layers of transparent tape (T4), the resonance frequency of the T4+MS+PB/HQ is located at 140 GHz, which matches the operating frequency of the imaging system. The images of the fabricated MS are shown in Fig. 5.17 (a) and (b). The fabrication process [408], [409] starts by spin-coating and curing the $5\mu m$ COC layer on a silicon (Si) wafer. The gold layer is applied to the COC layer using deposition techniques. The slots and resonators are patterned using lift-off techniques. The COC layer covers the gold layer using polymer bonding techniques. The corresponding simulation model is shown in Fig. 5.17 (c) to visually display the position of the MS. Because the dielectric constant and loss tangent of the PB and HQ used in the simulation are not accurate, the error between the simulation and measurement is significant, so the simulated results are not presented here. In Fig. 5.17 (d), the reflection coefficient difference at 140 GHz between the PB and HQ becomes apparent when adding the proposed MS, and the dielectric constant decreases from about 4.6 to 2.9. The magnitude difference can be utilised for skin imaging detection. It is essential to realise the variation in the skin's permittivity, as it helps mimic the abnormal skin condition under the MS sensors.

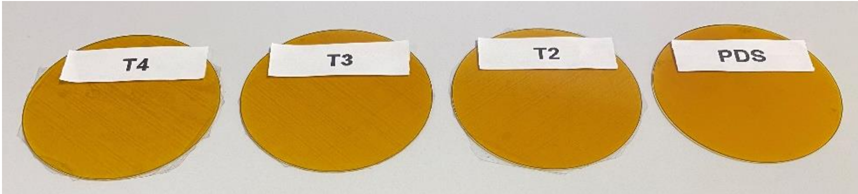

(a)

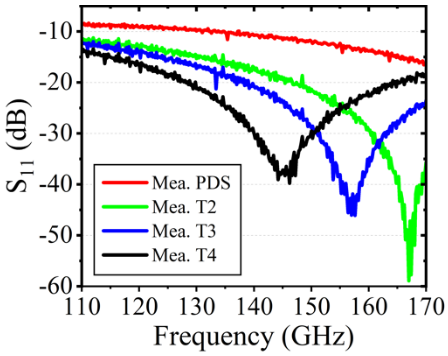

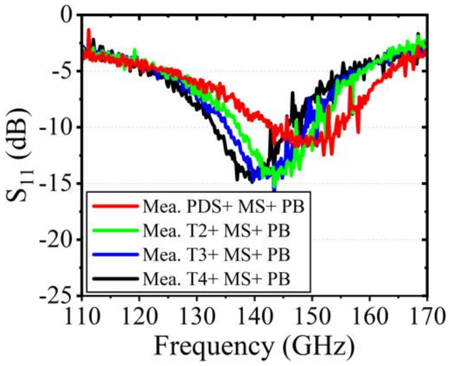

(b) (c)

Fig. 5.16. (a) Photo of the samples: PDS with a thickness of 0.5 mm. T2-4: 0.5 mm PDS with two to four layers of transparent tape. (b) Measured reflection coefficients of PDS, T2, T3 and T4. (c) Measured reflection coefficients for various conditions.

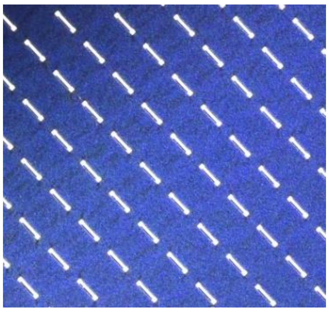

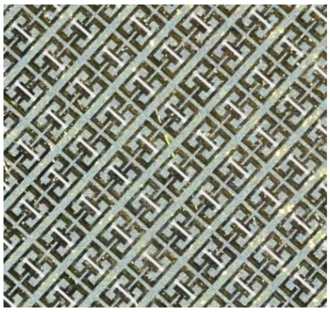

(a) (b)

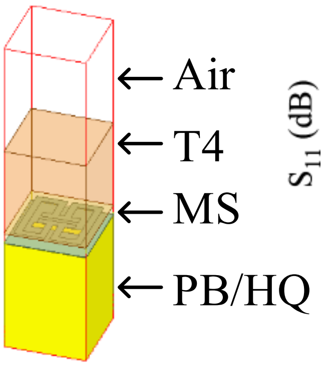

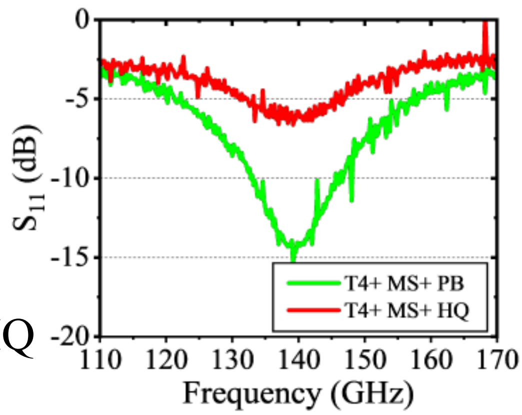

(c) (d)

Fig. 5.17. Fabricated metasurface; (a) Zoom-in view of the slots. (b) Zoom-in view of the resonators. (c) Schematic of the MS under test. (d) Measured reflection coefficients with different skin under test.

5.5 Real-Time Imaging on Skin Tissues

When the skin is pressed against a flattening board, the board occludes the skin, and the moisture from the skin's breathing cannot evaporate, causing it to accumulate and increase skin hydration. This is the occlusion effect [411]. The refractive index of the skin increases over time, while the extinction coefficient slightly decreases. There is a great change in the first 3 minutes of the occlusion, and the permittivity rises by 10% to 15% after 20 minutes. Due to the moisture variation, the occlusion effect will impact the detection of normal and cancerous skin, posing a challenge to the detection system's accuracy. Thus, a real-time imaging system is important for skin condition monitoring. Based on a sub-THz camera, a reflection real-time imaging setup is used for skin imaging, as shown in Fig. 5.18. The transmitting (Tx) feed source generates a continuous wave at a single frequency of 140 GHz. The biconvex and fixture come from the reflection coefficient measurement setup in Fig. 5.13. The plano-convex lens has a larger aperture size of 90 mm diameter to generate a plane wave with an incident angle of $30°$ to the fixture, and the imaging lens operating at 140 GHz generates a mirror image on the camera. The THz camera is manufactured by TeraSense Group, Inc., which has 1024 pixels (32×32 array) with values ranging from 0 to 255; the size of its pixels is $1.5\ mm$.

The skin imaging experiment process is presented in Fig. 5.19. A notch with a dimension of 4.6 mm ×4.6 mm is cut in the PB skin using a scalpel. Then, a piece of HQ skin is cut out and placed into the notch of the PB skin. The hybrid skin is obtained, which can mimic an abnormal skin with different dielectric constants. Finally, the hybrid skin is pressed against the proposed MS sensor and the PDS sheet with four layers of transparent tape, the situation of T4+MS+skin. The imaging result at 140 GHz is shown in Fig. 5.19 (d). The reflection coefficient of the T4+MS+HQ at 140 GHz is higher than that of the T4+MS+PB, as shown in Fig. 5.17 (c). Therefore, a hot spot is presented, and its size is about 2 to 3 pixels, which matches the size of the cut-out HQ skin. The imaging was performed in the x–y axes 2D imaging plane, where each pixel corresponds to a spatial size of approximately 1.5 mm. As illustrated in Fig. 3.21 (c), the focusing effect becomes more pronounced when the feed source is a waveguide probe, resulting in a focal spot diameter of approximately 3 - 4.5 mm, corresponding to 2–3 pixels, indicating an approximate imaging resolution of around 3 – 4.5 mm. To allow sufficient space for the incident wave to illuminate the metasurface, the focal ratio of the lens cannot be too small. Since a smaller focal ratio generally leads to higher imaging resolution, the relatively larger focal ratio in this design results in lower resolution. Therefore, the system is suitable for detecting the presence or absence of abnormal skin regions, rather than resolving detailed contours of the affected area. The image quality can be further refined if each component of the imaging system can be improved further.

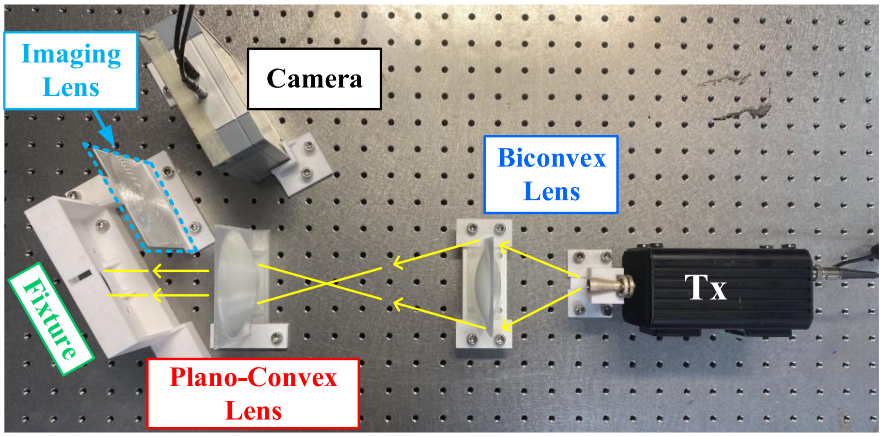

(a)

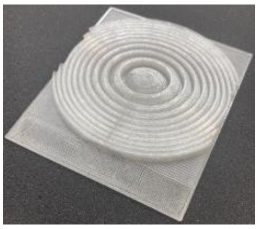

(b)

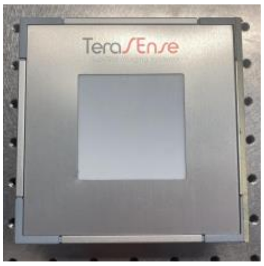

(c)

Fig. 5.18. Reflection real-time imaging setup. (a) Overall structure. (b) Imaging lens. (c) THz camera.

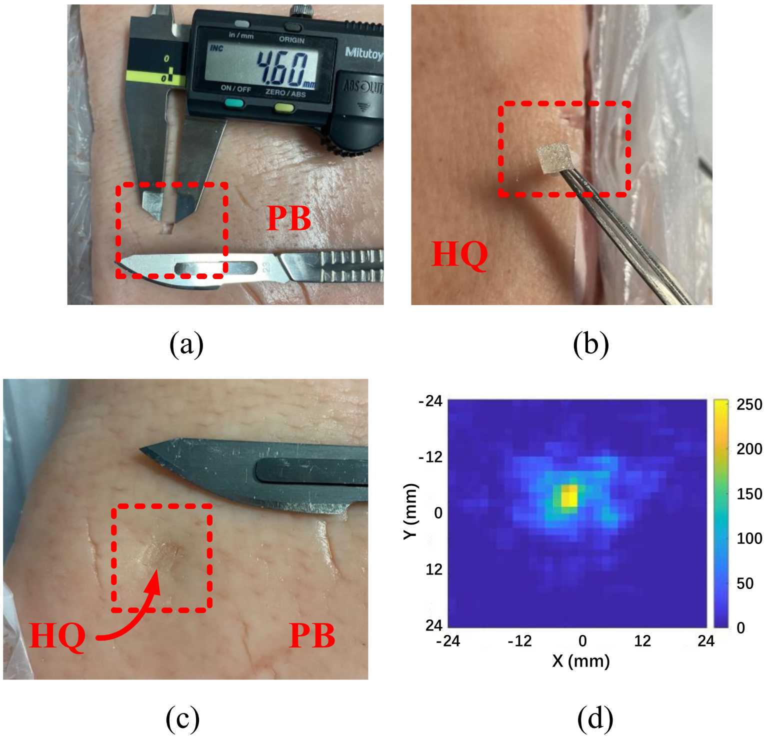

Fig. 5.19. Experiment process: (a) A notch with a dimension of $4.6\ mm\ \times 4.6\ mm$ is cut in the PB skin. (b) A piece of HQ skin is obtained by cutting it out. (c) The cut-out HQ skin is placed into the notch of the PB skin. (d) Imaging result of the hybrid skin.

5.6 Discussion

The imaging results presented in this experiment were obtained directly from the built-in software of the THz camera [412], with minimal additional signal processing. To improve the imaging quality, several approaches can be considered, such as applying algorithms for filtering, denoising, and machine learning - based image enhancement [413]. Alternatively, higher-resolution THz cameras are needed. Conventional THz cameras [414] typically capture only amplitude signals, so further research is required to develop corresponding imaging algorithms. Another direction is to optimise the optical path of the imaging system using ray-tracing theory [415] to refine the design and surface profile of the imaging lens.

The objective of this approach is to achieve a relatively low-cost, portable, and rapid imaging system. Compared with raster-scanning-based imaging [416], its inherent spatial resolution is lower, making multiple-spot imaging more challenging. Therefore, this system is mainly intended for identifying the presence or absence of abnormal skin regions.

Regarding the metasurface sensor, the proposed metasurface is specifically designed for the imaging system and thus exhibits a narrow bandwidth and relatively weak reflection signals. In the future, electromagnetically induced transparency (EIT)-based metasurfaces [381] could potentially be explored to enhance performance. Moreover, further optimisation of the structural design is necessary. The current metasurface requires high-precision fabrication processes that are unsuitable for mass production. Future work should aim to adapt the structure for PCB-compatible fabrication, enabling low-cost metasurface sensors.

5.7 Conclusion

In this work, a metasurface sensor for skin condition monitoring has been proposed and analysed. To address the challenges posed by lossy biological tissues, a dual-layer MS design based on interference theory was introduced. Simulations demonstrate a clear resonant frequency shift in response to changes in the dielectric constant of the skin under test. To enable practical measurement, a flattening sheet was employed to convert the frequency shift into a detectable variation in reflection amplitude, enabling real-time detection through a lens-based imaging system. The feasibility of this approach was verified through experiments using pork skin. With further customisation for human skin and cancerous tissues, the proposed system holds the potential for rapid skin cancer detection. Moreover, by reducing the size of the THz illumination region, a portable and practical detection device may be developed. Overall, the proposed MS sensor offers potential applications in skin moisture assessment and early cancer diagnosis.

Chapter VI Conclusion and Future Work

6.1 Conclusion

Sub-terahertz (sub-THz) technologies represent a promising frontier in both communication and biomedical applications, the key characteristics of which have been discussed in the preceding chapters. In this thesis, a range of metasurface designs has been proposed and investigated to explore and demonstrate the application potential of sub-THz technologies in communication and biomedical contexts.

Chapter I first introduces the properties of THz waves. Based on these characteristics, the promising applications of sub-THz waves—particularly in communication and biomedical fields—are discussed. To build a solid foundation for subsequent research, this chapter also explores a range of fundamental considerations that are essential for implementing THz technologies. These include evaluating the suitability of various antenna types for THz operation, analysing the characteristics of human skin relevant to THz interaction, assessing the safety of THz exposure, and reviewing the available measurement systems and their limitations.

Based on these insights, it is concluded that THz research for communication and skin detection is both theoretically grounded and practically feasible under current experimental conditions.

Chapter II presents a comprehensive literature review on metasurfaces and skin cancer detection techniques. It discusses metasurface lens unit cells designed for phase modulation, sensor unit cells developed for permittivity sensing, and a range of existing methods employed in skin cancer detection. The relevant content entitled “3D Terahertz Antenna Measurement: A Comparison Between Solid-State Electronics and Photomixing Approaches” has been accepted in **IEEE Antennas and Propagation Magazine.**

Chapter III focuses on the design of all-dielectric metalenses. Two beam-scanning metalenses and one imaging metalens are proposed, with the primary contribution focusing on the calculation and design of phase distributions. The effectiveness of these metalenses is demonstrated through their applicability in both communication and imaging systems. The relevant content entitled “A 3-D Printed 140 GHz Multifocal Dielectric Transmitarray Antenna for 2-D Mechanical Beam Scanning” has been accepted in **IEEE Antennas and Wireless Propagation Letters**. The relevant content entitled “A 3D Printing 120 GHz Lens Antenna for Terahertz one-dimensional (1D) Beam-Scanning Applications” has been accepted in the **2022 International Symposium on Antennas and Propagation (ISAP)**.

Chapter IV proposes the conductive and dielectric metasurface lens designs, including multilayered metasurface, circularly-polarised metasurface and various metasurface unit cells. Different from conventional circularly-polarised metasurface unit cells, a 3D printed coaxial line is introduced to maintain the Pancharatnam−Berry (PB) phase performance and the angle-multiplexed multifocal method is proposed to achieve multifocal phase distribution of high gain beam scanning. A stepped metalens based on the AME fabrication technique is proposed for beam-scanning applications. The relevant content entitled “An Angle-Multiplexed Multifocal Method for D-Band two-dimensional (2D) Beam-Scanning Transmitarray Leveraging 3D Transmission Line Component” has been accepted in **IEEE Antennas and Wireless Propagation Letters**. The relevant content entitled “A 3D Printed Terahertz Metamaterial Lens for Beam-Steering Applications” has been accepted for the **2023 IEEE/MTT-S International Microwave Symposium (IMS).**

Chapter V Chapter 5 combines key technologies from the previous chapters—namely, all-dielectric metalens design, AME-based fabrication, and metal-dielectric metasurface sensor—to implement a real-time skin monitoring system. The system leverages a metasurface sensor capable of capturing reflection variations that arise from different skin tissues under test, providing a foundation for distinguishing tissue types based on electromagnetic responses. Meanwhile, an all-dielectric metalens is employed to achieve real-time mirror imaging, enabling intuitive visualisation of the detected signals. This work not only validates the feasibility of combining metasurface sensing and imaging in biomedical applications but also lays the groundwork for the future development of compact, real-time, and non-invasive diagnostic tools in the sub-terahertz band.

6.2 Future Work

Although this thesis has demonstrated the feasibility of metasurface-based devices for sub-terahertz communication and biomedical sensing applications, there remain several avenues for further investigation and development. The current work primarily focuses on proof-of-concept designs and preliminary experimental validations. To transition these technologies toward practical applications, future research should address challenges related to device performance, integration, and system-level implementation.

Currently, the all-dielectric metalens design primarily exploits the shortened wavelength in dielectric materials and the refraction effects at the air-dielectric interface to achieve basic phase modulation. However, its full potential has yet to be explored. By introducing total internal reflection (TIR) within the dielectric structure, it is possible to unlock a wider range of functionalities. This may enable the development of advanced optical components such as high-efficiency focusing lenses, imaging lenses, beam-steering lenses, and even diffraction-free lenses. Future work could investigate how to engineer internal light paths using TIR-based geometries, allowing for more compact, versatile, and functionally rich metalens systems.

For metasurfaces composed of metal and dielectric materials, future designs can benefit from the integration of more advanced microstrip circuit theories to realise more complex structures and diversified functionalities. By embedding transmission line models, impedance matching networks, or resonant unit cells, it is possible to achieve greater control over electromagnetic wave propagation. Additionally, introducing external components such as ferrite may enable the realisation of nonreciprocal metasurfaces, which break time-reversal symmetry and can lead to one-way wave transmission or isolation functionalities. These approaches will significantly broaden the applicability of hybrid metasurfaces in advanced communication and sensing systems.

For future development of the skin condition monitoring system, several key improvements are needed to enhance sensing precision and accuracy. More sensitive metasurface sensors should be introduced to detect finer differences in tissue properties. In addition, imaging metalenses with wider fields of view is necessary to capture larger areas of skin. A uniform and stable plane-wave source is also essential to ensure a quiet zone performance across the imaging region. Furthermore, the integration of artificial intelligence algorithms could be employed to enhance image reconstruction, optimise signal processing, and reduce noise in the data received by terahertz cameras. In future work, the proposed metasurface-based skin condition monitoring system holds strong potential to be further developed into a non-invasive THz skin cancer diagnostic platform, featuring real-time detection, compactness for portability and wide deployment, reusability, and low cost.

References

[1] W. Wang, Y. J. Tan, T. C. Tan, A. Kumar, P. Pitchappa, P. Szriftgiser, G. Ducournau, R. Singh, "On-chip topological beamformer for multi-link terahertz 6G to XG wireless," in *Nature*, vol. 632, no. 8025, pp. 522-527, Aug. 2024.

[2] Y. Yang, H. Liu, M. Yang, B. Cui, W. Zhang, "Dielectric sphere-coupled THz super-resolution imaging," in *Applied Physics Letters*, vol. 113, no. 3, Jul. 2018.

[3] H. Feng, D. An, H. Tu, W. Bu, W. Wang, Y. Zhang, H. Zhang, X. Meng, W. Wei, B. Gao, S. Wu, "A passive video-rate terahertz human body imager with real-time calibration for security applications," in *Applied Physics B*, vol. 126, no. 8, pp. 143, Aug. 2020.

[4] S. Shi, S. Yuan, J. Zhou, P. Jiang, "Terahertz technology and its applications in head and neck diseases," in *IScience*, vol. 26, no. 7, Jul. 2023.

[5] A. S. Kucheryavenko, I. N. Dolganova, A. A. Zhokhov, V. M. Masalov, G. R. Musina, V. V. Tuchin, N. V. Chernomyrdin, A. A. Gavdush, D. R. Il'enkova, S. V. Garnov, K. I. Zaytsev, "Terahertz-wave scattering in tissues: examining the limits of the applicability of effective-medium theory," in *Physical Review Applied*, vol. 20, no. 5, pp. 054050, Nov. 2023.

[6] L. Wei, L. Yu, H. Jiaoqi, H. Guorong, Z. Yang, F. Weiling, "Application of terahertz spectroscopy in biomolecule detection," in *Frontiers in Laboratory Medicine*, vol. 2, no. 4, pp. 127-133, Dec. 2018.

[7] M. Exter, C. Fattinger, D. Grischkowsky, "Terahertz time-domain spectroscopy of water vapor," in *Optics Letters*, vol. 14, no. 20, pp. 1128-1130, Oct. 1989.

[8] J. F. Federici, B. Schulkin, F. Huang, D. Gary, R. Barat, F. Oliveira, D. Zimdars, "THz imaging and sensing for security applications—explosives, weapons and drugs," in *Semiconductor Science and Technology*, vol. 20, no. 7, pp. S266, Jun. 2005.

[9] A. Nagarajan, R. Singh, "Terahertz brain–computer interfaces," in *Nature Reviews Bioengineering*, vol. 3, no. 3, pp. 185-186, Mar. 2025.

[10] J. Accardo, M. A. Chaudhry, "Radiation exposure and privacy concerns surrounding full-body scanners in airports," in *Journal of Radiation Research and Applied Sciences*, vol. 7, no. 2, pp. 198-200, Apr. 2014.

[11] B. Ji, Y. Han, S. Liu, F. Tao, G. Zhang, Z. Fu, C. Li, "Several key technologies for 6G: Challenges and opportunities," in *IEEE Communications Standards Magazine*, vol. 5, no. 2, pp. 44-51, Jun. 2021.

[12] A. Shafie, N. Yang, C. Han, J. M. Jornet, M. Juntti, T. Kürner, "Terahertz communications for 6G and beyond wireless networks: Challenges, key advancements, and opportunities," in *IEEE Network*, vol. 37, no. 3, pp. 162-169, Sep. 2022.

[13] W. Jiang et al., "Terahertz communications and sensing for 6G and beyond: A comprehensive review," in *IEEE Communications Surveys & Tutorials*, vol. 26, no. 4, pp. 2326-2381, Fourth quarter 2024.

[14] Y. He, Y. Chen, L. Zhang, S. -W. Wong and Z. N. Chen, "An overview of terahertz antennas," in *China Communications*, vol. 17, no. 7, pp. 124-165, Jul. 2020.

[15] M. de Kok, A. B. Smolders and U. Johannsen, "A review of design and integration technologies for D-band antennas," in *IEEE Open Journal of Antennas and Propagation*, vol. 2, pp. 746-758, 2021.

[16] R. Pant, L. Malviya, "THz antennas design developments challenges and applications: A review," in *International Journal of Communication Systems*, vol. 36, no. 8, pp. 5474, May 2023.

[17] A. Simsek et al., "A 146.7 GHz transceiver with 5 GBaud data transmission using a low-cost series-fed patch antenna array through wirebonding integration," *2020 IEEE Radio and Wireless Symposium (RWS)*, San Antonio, TX, USA, 2020, pp. 68-71.

[18] M. Frank, F. Lurz, R. Weigel and A. Koelpin, "122 GHz low-cost substrate integrated waveguide based leaky-wave antenna design," *2019 IEEE Radio and Wireless Symposium (RWS)*, Orlando, FL, USA, 2019, pp. 1-4.

[19] B. Aqlan, M. Himdi, L. Le Coq and H. Vettikalladi, "Sub-THz circularly polarized horn antenna using wire electrical discharge machining for 6G wireless

communications," in *IEEE Access*, vol. 8, pp. 117245-117252, 2020.

[20] D. Dancila, V. Valenta, A. -C. Bunea, D. Neculoiu, H. Schumacher and A. Rydberg, "Differential microstrip patch antenna as feeder of a hyper-hemispherical lens for F-band MIMO radars," *2016 Global Symposium on Millimeter Waves (GSMM) & ESA Workshop on Millimetre-Wave Technology and Applications*, Espoo, Finland, 2016, pp. 1-4.

[21] N. M. Burford, M. O. El-Shenawee, "Review of terahertz photoconductive antenna technology," in *Optical Engineering*, vol. 56, no. 1, pp. 010901, Jan. 2017.

[22] K. Medrar et al., "H-band substrate-integrated discrete-lens antenna for high data rate communication systems," in *IEEE Transactions on Antennas and Propagation*, vol. 69, no. 7, pp. 3677-3688, Jul. 2021.

[23] Z.-W. Miao, Z.-C. Hao, G. Q. Luo, L. Gao, J. Wang, X. Wang, and W. Hong, "140 GHz high-gain LTCC-integrated transmit-array antenna using a wideband SIW aperture-coupling phase delay structure," in *IEEE Transactions on Antennas and Propagation*, vol. 66, no. 1, pp. 182-190, Jan. 2018.

[24] G. E. Becker, S. H. Autler, "Water vapor absorption of electromagnetic radiation in the centimeter wave-length range," in *Physical Review*, vol. 70, no. 5-6, pp. 300, Sep. 1946.

[25] D. M. Slocum, E. J. Slingerland, R. H. Giles, T. M. Goyette, "Atmospheric absorption of terahertz radiation and water vapor continuum effects," in *Journal of Quantitative Spectroscopy and Radiative Transfer*, vol. 127, pp. 49-63, Sep. 2013.

[26] X. Wang, L. Kong, F. Kong, F. Qiu, M. Xia, S. Arnon, G. Chen, "Millimeter wave communication: A comprehensive survey," in *IEEE Communications Surveys & Tutorials*, vol. 20, no. 3, pp. 1616-1653, Jun. 2018.

[27] D. Zheng, G. B. Wu, Z. H. Jiang, W. Hong, C. H. Chan, K. Wu, "Enabling beam-scanning antenna technologies for terahertz wireless systems: A review," in *Fundamental Research*, vol. 5, no. 2, pp. 556-570, Mar. 2025.

[28] H. Xu, H. Aliakbarian, E. Van der Westhuizen, R. Wolhuter and G. A. E. Vandenbosch, "An architectural scheme for real-time multiple users beam tracking systems," in *IEEE Systems Journal*, vol. 11, no. 4, pp. 2905-2916, Dec. 2017.

[29] S. Kosulnikov, X. Wang and S. A. Tretyakov, "Discrete-impedance metasurfaces for wireless communications in D-band," in *IEEE Transactions on Antennas and Propagation*, vol. 72, no. 1, pp. 591-599, Jan. 2024.

[30] J. Lai, X. Lv and Y. Yang, "A 3-D printed 140 GHz multifocal dielectric transmitarray antenna for 2-D mechanical beam scanning," in *IEEE Antennas and Wireless Propagation Letters*, vol. 23, no. 4, pp. 1366-1370, Apr. 2024.

[31] J. Lai, X. Lv, M. M. Rahman, M. A. I. Oni, S. Dey and Y. Yang, "An angle-multiplexed multifocal method for D-band 2-D beam-scanning transmitarray leveraging 3-D transmission line component," in *IEEE Antennas and Wireless Propagation Letters*, vol. 24, no. 3, pp. 731-735, Mar. 2025.

[32] H. Ge, Z. Sun, Y. Jiang, X. Wu, Z. Jia, G. Cui, Y. Zhang, "Recent advances in THz detection of water," in *International Journal of Molecular Sciences*, vol. 24, no. 13, pp. 10936, Jun. 2023.

[33] A. Mirbeik-Sabzevari and N. Tavassolian, "Characterization and validation of the slim-form open-ended coaxial probe for the dielectric characterization of biological tissues at millimeter-wave frequencies," in *IEEE Microwave and Wireless Components Letters*, vol. 28, no. 1, pp. 85-87, Jan. 2018.

[34] J. L. Schepps, K. R. Foster, "The UHF and microwave dielectric properties of normal and tumour tissues: variation in dielectric properties with tissue water content," in *Physics in Medicine & Biology*, vol. 25, no. 6, pp. 1149, Nov. 1980.

[35] I. L. Mulay, R. Roy, B. E. Knox, N. H. Suhr, W. E. Delaney, "Trace-metal analysis of cancerous and non-cancerous human tissues," in *Journal of the National Cancer Institute*, vol. 47, no. 1, pp. 1-3, Jul. 1971.

[36] M. Lazebnik, D. Popovic, L. McCartney, et al, "A large-scale study of the ultrawideband microwave dielectric properties of normal, benign and malignant breast tissues obtained from cancer surgeries," in *Physics in Medicine & Biology*, vol. 50, no. 20, pp.6093, Oct. 2007.

[37] Y. Xie, B. Guo, L. Xu, J. Li and P. Stoica, "Multistatic adaptive microwave imaging for early breast cancer detection," in *IEEE Transactions on Biomedical Engineering*, vol. 53, no. 8, pp. 1647-1657, Aug. 2006.

[38] A. Zamani, S. A. Rezaeieh, A. M. Abbosh, "Lung cancer detection using frequency‐domain microwave imaging," in *Electronics Letters*, vol. 51, no. 10, pp. 740, May 2015.

[39] S. Kharkovsky, M. T. Ghasr, M. A. Abou-Khousa and R. Zoughi, "Near-field microwave and mm-wave noninvasive diagnosis of human skin," *2009 IEEE International Workshop on Medical Measurements and Applications*, Cetraro, Italy, 2009, pp. 5-7.

[40] B. You, C. Y. Chen, C. P. Yu, P. H. Wang, J. Y. Lu, "Frequency-dependent skin penetration depth of terahertz radiation determined by water sorption–desorption," in *Optics Express*, vol. 26, no. 18, pp. 22709-22721, Aug. 2018.

[41] V. P. Wallace, A. J. Fitzgerald, S. Shankar, N. Flanagan, R. Pye, J. Cluff, D. D. Arnone, "Terahertz pulsed imaging of basal cell carcinoma ex vivo and in vivo," in *British Journal of Dermatology*, vol. 151, no. 2, pp. 424-432, Aug. 2004.

[42] R. M. Woodward, V. P. Wallace, R. J. Pye, B. E. Cole, D. D. Arnone, E. H. Linfield, M. Pepper, "Terahertz pulse imaging of ex vivo basal cell carcinoma," in *Journal of Investigative Dermatology*, vol. 120, no. 1, pp. 72-78, Jan. 2003.

[43] American Cancer Society, "Cancer facts and figures 2018." [Online]. Available: https://www.cancer.org/content/dam/cancer-org/research/cancer-facts-and-statistics/annual-cancer-facts-and-figures/2021/cancer-facts-and-figures-2021.pdf

[44] M. Zhadobov, N. Chahat, R. Sauleau, et al., "Millimeter-wave interactions with the human body: State of knowledge and recent advances," in *International Journal of Microwave and Wireless Technologies*, vol. 3, no. 2, pp. 237-247, Apr. 2011.

[45] P. J. Caspers, G. W. Lucassen, H. A. Bruining, G. J. Puppels, "Automated depth‐scanning confocal Raman microspectrometer for rapid in vivo determination of water concentration profiles in human skin," in *Journal of Raman Spectroscopy*, vol. 31, no. 8‐9, pp. 813-818, Aug. 2000.

[46] Y. Feldman, A. Puzenko, P. B. Ishai, A. Caduff, I. Davidovich, F. Sakran, A. J. Agranat, "The electromagnetic response of human skin in the millimetre and submillimetre wave range," in *Physics in Medicine & Biology*, vol. 54, no. 11, pp. 3341, May 2009.

[47] V. Suntzeff, C. Carruthers, "The water content in the epidermis of mice undergoing carcinogenesis by methylcholanthrene," in *Cancer Research*, vol. 6, no. 10, pp. 574-577, Oct. 1946.

[48] K. Chand, P. Mehta, D. G. Beetner, R. Zoughi and W. V. Stoecker, "Microwave reflectometry as a novel diagnostic method for detection of skin cancers," *2005 IEEE Instrumentation and Measurement Technology Conference Proceedings*, Ottawa, ON, Canada, 2005, pp. 1425-1428.

[49] J. P. Grant, N. M. Spyrou, "Complex permittivity differences between normal and pathological tissues: Mechanisms and medical significance," in *Journal of Bioelectricity*, vol. 4, no. 2, pp. 419-458, Jan. 1985.

[50] V. Madan, J. T. Lear, R. M. Szeimies, "Non-melanoma skin cancer," in *The Lancet*, vol. 375, no. 9715, pp. 673-685, Feb. 2010.

[51] A. I. Rubin, E. H. Chen, D. Ratner, "Basal-cell carcinoma," in *New England Journal of Medicine*, vol. 353, no. 21, pp. 2262-2269, Nov. 2005.

[52] M. Alam, D. Ratner, "Cutaneous squamous-cell carcinoma," in *New England Journal of Medicine*, vol. 344, no. 13, pp. 975-983, Mar. 2001.

[53] A. Mirbeik-Sabzevari, N. Tavassolian, "Tumor detection using millimeter-wave technology: Differentiating between benign lesions and cancer tissues," in *IEEE Microwave Magazine*, vol. 20, no. 8, pp. 30-43, Jul. 2019.

[54] H. P. Schwan, "Electrical properties of tissues and cell suspensions: mechanisms and models," *Proceedings of 16th Annual International Conference of the IEEE Engineering in Medicine and Biology Society*, Baltimore, MD, USA, 1994, pp. A70-A71 vol.1.

[55] K. S. Cole, "Membranes, ions and impulses: a chapter of classical biophysics," in *Univ of California Press*, 1972.

[56] S. Gabriel, et al. “The dielectric properties of biological tissues: III. parametric models for the dielectric spectrum of tissues.” in *Physics in Medicine and Biology*, vol. 41, Nov. 1996, pp. 2271–2293.

[57] C. M. Alabaster, "Permittivity of human skin in millimetre wave band," in *Electronics Letters*, vol. 39, no. 21, pp. 1521-1522, Oct. 2003.

[58] H. Hwang, J. Yim, J. W. Cho, C. Cheon and Y. Kwon, "110 GHz broadband measurement of permittivity on human epidermis using 1 mm coaxial probe," *IEEE MTT-S International Microwave Symposium Digest*, 2003, Philadelphia, PA, USA, 2003, pp. 399-402 vol.1.

[59] S. I. Alekseev, M. C. Ziskin, "Human skin permittivity determined by millimeter wave reflection measurements, " in *Bioelectromagnetics*, vol. 28, no. 5, pp. 331-339, Jul. 2007.

[60] M. Lazebnik, M. Okoniewski, J. H. Booske and S. C. Hagness, "Highly accurate Debye models for normal and malignant breast tissue dielectric properties at microwave frequencies," in *IEEE Microwave and Wireless Components Letters*, vol. 17, no. 12, pp. 822-824, Dec. 2007.

[61] K. S. Cole, R. H. Cole, "Dispersion and absorption in dielectrics I. Alternating current characteristics," in *The Journal of Chemical Physics*, vol. 9, no. 4, pp. 341-351, Apr. 1941.

[62] O. P. Cherkasova, D. S. Serdyukov, A. S. Ratushnyak, E. F. Nemova, E. N. Kozlov, Y. V. Shidlovskii, K. I. Zaytsev, V. V. Tuchin, "Effects of terahertz radiation on living cells: A review," in *Optics and Spectroscopy*, vol. 128, no. 6, pp. 855-866, Jun. 2020.

[63] A. I. Nikitkina, P. Y. Bikmulina, E. R. Gafarova, N. V. Kosheleva, Y. M. Efremov, E. A. Bezrukov, D. V. Butnaru, I. N. Dolganova, N. V. Chernomyrdin, O. P. Cherkasova, A. A. Gavdush, "Terahertz radiation and the skin: a review," in *Journal of Biomedical Optics*, vol. 26, no. 4, pp. 043005, Apr. 2021.

[64] M. Wang, G. Yang, W. Li and Q. Wu, "An overview of cancer treatment by terahertz radiation," *2013 IEEE MTT-S International Microwave Workshop Series on RF and Wireless Technologies for Biomedical and Healthcare Applications (IMWS-BIO)*, Singapore, 2013, pp. 1-3

[65] G. J. Wilmink, B. D. Rivest, C. C. Roth, B. L. Ibey, J. A. Payne, L. X. Cundin, J. E. Grundt, X. Peralta, D. G. Mixon, W. P. Roach, "In vitro investigation of the biological effects associated with human dermal fibroblasts exposed to 2.52 THz radiation," in *Lasers in Surgery and Medicine*, vol. 43, no. 2, pp. 152-163, Feb.

2011.

[66] B. S. Alexandrov, V. Gelev, A. R. Bishop, A. Usheva, K. Ø. Rasmussen, "DNA breathing dynamics in the presence of a terahertz field," in *Physics Letters A*, vol. 374, no. 10, pp. 1214-1217, Feb. 2010.

[67] A. G. Markelz, D. M. Mittleman, "Perspective on terahertz applications in bioscience and biotechnology," in *ACS Photonics*, vol. 9, no. 4, pp. 1117-1126, Apr. 2022.

[68] M. N. Dione, S. Shang, Q. Zhang, S. Zhao, X. Lu, "Non-thermal effects of terahertz radiation on gene expression: Systematic review and meta-analysis," in *Genes*, vol. 15, no. 8, pp. 1045, Aug. 2024.

[69] "IEEE standard for safety levels with respect to human exposure to electric, magnetic, and electromagnetic fields, 0 Hz to 300 GHz - Corrigenda 2," in *IEEE Std C95.1-2019/Cor2-2020 (Corrigenda to IEEE Std C95.1-2019)*, vol., no., pp.1-15, 21 Oct. 2020.

[70] Virginia Diodes, Inc., “Product overview – VNAX vector network analyzer extension modules,” VNAX Product Manual, Oct 31, 2024. [Online]. Available: https://www.vadiodes.com/images/Products/VNA/Product_Manual/VDI-707.1-VNAx-Product-Manual.pdf

[71] L. V. Titova, A. K. Ayesheshim, A. Golubov, R. Rodriguez-Juarez, R. Woycicki, F. A. Hegmann, O. Kovalchuk, "Intense THz pulses down-regulate genes associated with skin cancer and psoriasis: A new therapeutic avenue?," in *Scientific Reports*, vol. 3, no. 1, pp. 2363, Aug. 2013.

[72] T. M. Rünger, "How different wavelengths of the ultraviolet spectrum contribute to skin carcinogenesis: the role of cellular damage responses," in *Journal of Investigative Dermatology*, vol. 127, no. 9, pp. 2103-2105, Sep. 2007.

[73] I. R. R. Barani, L. A. Bronckers and A. C. F. Reniers, "Integrated-antenna over-the-air testing for millimeter-wave applications: An overview of systems and uncertainty [measurements corner]," in *IEEE Antennas and Propagation Magazine*, vol. 64, no. 5, pp. 97-110, Oct. 2022.

[74] Z. -W. Miao, Z. -C. Hao, Y. Wang, B. -B. Jin, J. B. Wu and W. Hong, "A 400-GHz

high-gain quartz-based single layered folded reflectarray antenna for terahertz applications," in *IEEE Transactions on Terahertz Science and Technology*, vol. 9, no. 1, pp. 78-88, Jan. 2019.

[75] J. Yu, H. Yu, T. Chen, J. Wang, Y. Yao and X. Chen, "Application of compact antenna test range in terahertz antenna measurement," *2020 Cross Strait Radio Science & Wireless Technology Conference (CSRSWTC)*, Fuzhou, China, 2020, pp. 1-3.

[76] P. Wu, K. Liu and Z. Yu, "220 GHz high-gain substrate integrated antennas with low fabrication cost based on higher order mode and PCB technology," in *IEEE Transactions on Antennas and Propagation*, vol. 71, no. 1, pp. 18-28, Jan. 2023.

[77] G. -B. Wu, K. F. Chan, S. -W. Qu and C. H. Chan, "A 2-D beam-scanning Bessel launcher for terahertz applications," in *IEEE Transactions on Antennas and Propagation*, vol. 68, no. 8, pp. 5893-5903, Aug. 2020.

[78] L. Boehm, F. Boegelsack, M. Hitzler and C. Waldschmidt, "The challenges of measuring integrated antennas at millimeter-wave frequencies [measurements corner]," in *IEEE Antennas and Propagation Magazine*, vol. 59, no. 4, pp. 84-92, Aug. 2017.

[79] G. Breed, "The mathematics of mixers: basic principles. " [Online]. Avaiable: https://highfrequencyelectronics.com/Jan11/HFE0111_Tutorial.pdf.

[80] C. Nickolas, "The basics of mixers." DigiKey, Dec. 20 2011. [Online]. Avaiable: https://www.digikey.com/en/articles/the-basics-of-mixers

[81] J. Neu, C A. Schmuttenmaer, "Tutorial: An introduction to terahertz time domain spectroscopy (THz-TDS)," in *Journal of Applied Physics*, vol. 124, no.23, pp. 231101, Dec. 2018.

[82] A. Andreone, L. Angrisani, G. Cavallo, A. Liccardo, et al, "THz measurement systems," in *New Trends and Developments in Metrology*, pp. 21-48, Dec. 2016.

[83] R. Peretti et al., "THz-TDS time-trace analysis for the extraction of material and metamaterial parameters," in *IEEE Transactions on Terahertz Science and Technology*, vol. 9, no. 2, pp. 136-149, Mar. 2019.

[84] T. Umezawa et al., "80-GHz signal detection in high speed UTC-PD using EO

sampling THz probe," *2017 42nd International Conference on Infrared, Millimeter, and Terahertz Waves (IRMMW-THz)*, Cancun, Mexico, 2017, pp. 1-2.

[85] T. Umezawa et al., "Bias-free operational UTC-PD above 110 GHz and its application to high baud rate fixed-fiber communication and W-band photonic wireless communication," in *Journal of Lightwave Technology*, vol. 34, no. 13, pp. 3138-3147, Jul. 2016.

[86] T. Nagatsuma, H. Ito, and T. Ishibashi, "High-power RF photodiodes and their applications," in *Laser & Photonics Reviews*, vol. 3, no. 1–2, pp. 123–137, Feb. 2009.

[87] I. S. Gregory et al., "Optimization of photomixers and antennas for continuous-wave terahertz emission," in *IEEE Journal of Quantum Electronics*, vol. 41, no. 5, pp. 717-728, May 2005.

[88] S. Hisatake, G. Kitahara, K. Ajito, Y. Fukada, N. Yoshimoto and T. Nagatsuma, "Phase-sensitive terahertz self-heterodyne system based on photodiode and low-temperature-grown GaAs photoconductor at 1.55 μm ," in *IEEE Sensors Journal*, vol. 13, no. 1, pp. 31-36, Jan. 2013.

[89] D. J. Lee, N. W. Kang, J. H. Choi, et al, "Recent advances in the design of electro-optic sensors for minimally destructive microwave field probing," in *Sensors*, vol. 11, no. 1, pp. 806-824, Jan. 2011.

[90] S. Hisatake, "Near-field measurement and far-field characterization of antennas in microwave, millimeter-wave and THz wave band based on photonics," *2022 International Symposium on Antennas and Propagation (ISAP)*, Sydney, Australia, 2022, pp. 351-352.

[91] D. J. Lee, J. Y. Kwon, N. W. Kang, "Field analysis of electro-optic probes for minimally invasive microwave sampling," in *Optics Express*, vol. 22, no.3, pp. 2897-2909, Feb. 2014.

[92] S. Hisatake, T. Nagatsuma, "Nonpolarimetric technique for homodyne-type electrooptic field detection," in *Applied Physics Express*, vol. 5, no. 1, pp.012701, Dec. 2011.

[93] Y. Tanaka et al., "Photonics-based near-field measurement and far-field

characterization for 300-GHz band antenna testing," in *IEEE Open Journal of Antennas and Propagation*, vol. 3, pp. 24-31, 2022.

[94] S. Hisatake, H. H. N. Pham, T. Nagatsuma, "Visualization of the spatial–temporal evolution of continuous electromagnetic waves in the terahertz range based on photonics technology," in *Optica*, vol. 1, no. 6, pp. 365-371, Dec. 2014.

[95] Z. Zheng, Y. Zhang, L. Shi, L. Wu and J. -F. Mao, "An overview of probe-based millimeter-wave/terahertz far-field antenna measurement setups [Measurements corner]," in *IEEE Antennas and Propagation Magazine*, vol. 63, no. 2, pp. 63-118, Apr. 2021.

[96] A. Fung et al., "Two-port vector network analyzer measurements up to 508 GHz," in *IEEE Transactions on Instrumentation and Measurement*, vol. 57, no. 6, pp. 1166-1170, June 2008.

[97] D. Koller, S. Durant, C. Rowland, E. Bryerton and J. Hesler, "Initial measurements with WM164 (1.1–1.5THz) VNA extenders," *2016 41st International Conference on Infrared, Millimeter, and Terahertz waves (IRMMW-THz)*, Copenhagen, Denmark, 2016, pp. 1-2.

[98] E. Vassos, J. Churm, A. Feresidis, "Ultra-low-loss tunable piezoelectric-actuated metasurfaces achieving 360° or 180° dynamic phase shift at millimeter-waves," in *Scientific Reports*, vol. 10, no. 1, pp. 15679, Sep. 2020.

[99] J. Yi et al., "Frequency-tunable and magnitude-tunable microwave metasurface absorbers enabled by shape memory polymers," in *IEEE Transactions on Antennas and Propagation*, vol. 70, no. 8, pp. 6804-6812, Aug. 2022.

[100] H. L. Zhu, S. W. Cheung, K. L. Chung and T. I. Yuk, "Linear-to-circular polarization conversion using metasurface," in *IEEE Transactions on Antennas and Propagation*, vol. 61, no. 9, pp. 4615-4623, Sep. 2013.

[101] M. Borgese and F. Costa, "A simple equivalent circuit approach for anisotropic frequency-selective surfaces and metasurfaces," in *IEEE Transactions on Antennas and Propagation*, vol. 68, no. 10, pp. 7088-7098, Oct. 2020

[102] H. -X. Xu, T. Cai, Y. -Q. Zhuang, Q. Peng, G. -M. Wang and J. -G. Liang, "Dual-mode transmissive metasurface and its applications in multibeam

transmitarray," in *IEEE Transactions on Antennas and Propagation*, vol. 65, no. 4, pp. 1797-1806, Apr. 2017.

[103] T. Cai, G. -M. Wang, X. -L. Fu, J. -G. Liang and Y. -Q. Zhuang, "High-efficiency metasurface with polarization-dependent transmission and reflection properties for both reflectarray and transmitarray," in *IEEE Transactions on Antennas and Propagation*, vol. 66, no. 6, pp. 3219-3224, Jun. 2018.

[104] Q. -W. Lin and H. Wong, "A low-profile and wideband lens antenna based on high-refractive-index metasurface," in *IEEE Transactions on Antennas and Propagation*, vol. 66, no. 11, pp. 5764-5772, Nov. 2018

[105] S. Li, Z. N. Chen, T. Li, F. H. Lin and X. Yin, "Characterization of metasurface lens antenna for sub-6 GHz dual-polarization full-dimension massive MIMO and multibeam systems," in *IEEE Transactions on Antennas and Propagation*, vol. 68, no. 3, pp. 1366-1377, Mar. 2020

[106] F. Liu, D. H. Kwon and S. Tretyakov, "Reflectarrays and metasurface reflectors as diffraction gratings: A tutorial," in *IEEE Antennas and Propagation Magazine*, vol. 65, no. 3, pp. 21-32, Jun. 2023

[107] J. Budhu and A. Grbic, "Perfectly reflecting metasurface reflectarrays: mutual coupling modeling between unique elements through homogenization," in *IEEE Transactions on Antennas and Propagation*, vol. 69, no. 1, pp. 122-134, Jan. 2021

[108] A. Li, S. Kim, Y. Luo, Y. Li, J. Long and D. F. Sievenpiper, "High-power transistor-based tunable and switchable metasurface absorber," in *IEEE Transactions on Microwave Theory and Techniques*, vol. 65, no. 8, pp. 2810-2818, Aug. 2017

[109] B. Tang, Z. Li, E. Palacios, Z. Liu, S. Butun and K. Aydin, "Chiral-selective plasmonic metasurface absorbers operating at visible frequencies," in *IEEE Photonics Technology Letters*, vol. 29, no. 3, pp. 295-298, Feb. 2017

[110] Y. -T. Zhao, J. J. Zhang and B. Wu, "Low profile reflective polarization conversion metasurface with high frequency selectivity," in *IEEE Transactions on Antennas and Propagation*, vol. 70, no. 11, pp. 10614-10622, Nov. 2022

[111] M. Mavridou and A. P. Feresidis, "Dynamically reconfigurable high

impedance and frequency selective metasurfaces using piezoelectric actuators," in *IEEE Transactions on Antennas and Propagation*, vol. 64, no. 12, pp. 5190-5197, Dec. 2016

[112] A. Alipour, A. Farmani and A. Mir, "High sensitivity and tunable nanoscale sensor based on plasmon-induced transparency in plasmonic metasurface," in *IEEE Sensors Journal*, vol. 18, no. 17, pp. 7047-7054, Sep. 2018

[113] Q. Zhang, Z. Kou, J. Yang, Y. Li, Z. Yin and G. Deng, "Highly sensitive and robust metasurface-inspired microfluidic sensor for oil detection," in *IEEE Sensors Journal*, vol. 24, no. 24, pp. 40847-40854, Dec. 2024

[114] L. Yin et al., "Amplitude and phase independently adjustable transmitarray aperture and its applications to high gain and low sidelobe antenna," in *IEEE Transactions on Antennas and Propagation*, vol. 70, no. 6, pp. 4498-4506, Jun. 2022

[115] Z. Xu, S. Xu, Y. Shen, S. Xue and S. Hu, "Gain enhancement of dual-polarized 2-D multibeam antenna with transmitarray," in *IEEE Transactions on Antennas and Propagation*, vol. 72, no. 10, pp. 7574-7583, Oct. 2024

[116] Á. F. Vaquero et al., "Design of low-profile transmitarray antennas with wide mechanical beam steering at millimeter waves," in *IEEE Transactions on Antennas and Propagation*, vol. 71, no. 4, pp. 3713-3718, Apr. 2023

[117] S. Liu, Z. Ma, J. Pei, Q. Jiao, L. Yang, W. Zhang, H. Li, Y. Li, Y. Zou, X. Tan, "A review of anomalous refractive and reflective metasurfaces," in *Nanotechnology and Precision Engineering (NPE)*, vol. 5, no. 2, Jun. 2022.

[118] L. Li, P. Zhang, F. Cheng, M. Chang and T. J. Cui, "An optically transparent near-field focusing metasurface," in *IEEE Transactions on Microwave Theory and Techniques*, vol. 69, no. 4, pp. 2015-2027, Apr. 2021

[119] X. Bai, F. Kong, Y. Sun, G. Wang, J. Qian, X. Li, A. Cao, C. He, X. Liang, R. Jin, W. Zhu, "High‐efficiency transmissive programmable metasurface for multimode OAM generation," in *Advanced Optical Materials*, vol. 8, no. 17, pp. 2000570, Sep. 2020.

[120] L. Huang, S. Zhang, T. Zentgraf, “Metasurface holography: from fundamentals

to applications," in *Nanophotonics*, vol. 7, no. 6, pp. 1169-1190, 2018.

[121] PCBWay, "PCB capabilities - we offer a wide range of PCB capabilities to fit all of your PCB needs," [Online]. Available: https://www.pcbway.com/capabilities.html

[122] A. Mirbeik-Sabzevari and N. Tavassolian, "Ultrawideband, stable normal and cancer skin tissue phantoms for millimeter-wave skin cancer imaging," in *IEEE Transactions on Biomedical Engineering*, vol. 66, no. 1, pp. 176-186, Jan. 2019.

[123] H. Yi, S. W. Qu, K. -B. Ng, C. H. Chan and X. Bai, "3-D Printed millimeter-wave and terahertz lenses with fixed and frequency scanned beam," in *IEEE Transactions on Antennas and Propagation*, vol. 64, no. 2, pp. 442-449, Feb. 2016

[124] C. Fan, W. Yang, W. Che, S. He, Q. Xue, "A wideband and low-profile discrete dielectric lens using 3-D printing technology," in *IEEE Transactions on Antennas and Propagation*, vol. 66, no. 10, pp. 5160-5169, Aug. 2018.

[125] G. B. Wu, Y. S. Zeng, K. F. Chan, S. W. Qu, C. H. Chan, "High-gain circularly polarized lens antenna for terahertz applications," in *IEEE Antennas and Wireless Propagation Letters*, vol. 18, no. 5, pp. 921-925, Mar. 2019.

[126] F. Wei, J. W. Hao, L. Xu, X. Shi, "A circularly polarized 3-D printed dielectric transmitarray antenna at millimeter-wave band," in *IEEE Antennas and Wireless Propagation Letters*, vol. 20, no. 7, pp. 1264-1268, May 2021.

[127] J. Zhu, Y. Yang, D. McGloin, S. Liao, Q. Xue, "3-D printed all-dielectric dual-band broadband reflectarray with a large frequency ratio," in *IEEE Transactions on Antennas and Propagation*, vol. 69, no. 10, pp. 7035-7040, May 2021.

[128] A. Massaccesi, G. Dassano, P. Pirinoli, "Beam scanning capabilities of a 3D-printed perforated dielectric transmitarray," in *Electronics*, vol. 8, no. 4, pp. 379, Mar. 2019.

[129] G. -B. Wu et al., "3-D-printed terahertz metalenses for next-generation communication and imaging applications," in *Proceedings of the IEEE*, vol. 112, no. 8, pp. 1033-1050, Aug. 2024

[130] J. Zhu, Y. Yang, D. McGloin, S. Liao, Q. Xue, "Sub-terahertz 3-D printed all-dielectric low-cost low-profile lens-integrated polarization beam splitter," in *IEEE*

Transactions on Terahertz Science and Technology, vol. 11, no. 4, pp. 433-442, Mar. 2021.

[131] G. B. Wu, K. F. Chan, C. H. Chan, "3-D printed terahertz lens to generate higher order Bessel beams carrying OAM," in *IEEE Transactions on Antennas and Propagation*, vol. 69, no. 6, pp. 3399-3408, Oct. 2020.

[132] K. K. K. Ho, G. -B. Wu, B. -J. Chen, K. F. Chan and C. H. Chan, "Spot focusing coma correction by linearly polarized dual-transmitarray antenna in the terahertz region," in *IEEE Transactions on Terahertz Science and Technology*, vol. 13, no. 5, pp. 493-502, Sep. 2023.

[133] N. K. Grady, J. E. Heyes, D. R. Chowdhury, Y. Zeng, M. T. Reiten, A. K. Azad, A. J. Taylor, D. A. Dalvit, H. T. Chen, "Terahertz metamaterials for linear polarization conversion and anomalous refraction," in *Science*, vol. 340, no. 6138, pp. 1304-1307, Jun. 2013.

[134] J. Zhao et al., "A high aperture efficiency and wideband transmitarray antenna using novel double C-shaped elements," in *IEEE Antennas and Wireless Propagation* Letters, vol. 23, no. 12, pp. 4024-4028, Dec. 2024

[135] K. Duan, K. Chen, T. Jiang, J. Zhao and Y. Feng, "Noninterleaved bidirectional metasurface for spatial energy allocation," in *IEEE Transactions on Antennas and Propagation*, vol. 72, no. 8, pp. 6423-6436, Aug. 2024

[136] L. Yin, C. Jin, Q. Lv, B. Zhang, K. Cao, P. Zhang, Z. Xue, "Amplitude and phase independently adjustable transmitarray aperture and its applications to high gain and low sidelobe antenna," in *IEEE Transactions on Antennas and Propagation*, vol. 70, no. 6, pp. 4498-4506, Jan. 2022.

[137] L. Song, T. Zhang, P. Y. Qin, J. Du, Y. J. Guo, "Sub-THz broadband transmitting metasurfaces with enhanced frequency-scanning capability," in *IEEE Transactions on Terahertz Science and Technology*, vol. 14, no. 1, pp. 82-90, Sep. 2023.

[138] K. Medrar, L. Marnat, L. Dussopt, C. Belem-Goncalves, G. Ducournau, C. Luxey, F. Gianesello, "H-band substrate-integrated discrete-lens antenna for high data rate communication systems," in *IEEE Transactions on Antennas and*

Propagation, vol. 69, no. 7, pp. 3677-3688, Dec. 2020.

[139] S. M. A. M. H. Abadi and N. Behdad, "Design of wideband, FSS-based multibeam antennas using the effective medium approach," in *IEEE Transactions on Antennas and Propagation*, vol. 62, no. 11, pp. 5557-5564, Nov. 2014.

[140] P. Mei, S. Zhang and G. F. Pedersen, "A dual-polarized and high-gain X-/Ka-Band shared-aperture antenna with high aperture reuse efficiency," in *IEEE Transactions on Antennas and Propagation*, vol. 69, no. 3, pp. 1334-1344, Mar. 2021.

[141] Y. -H. Yu, Z. -Y. Zong, W. Wu, Q. Chen and D. -G. Fang, "Dual-polarized linear array with overlapping handover of subarray to produce continuous beam scanning for transmitarray antenna," in *IEEE Transactions on Antennas and Propagation*, vol. 69, no. 2, pp. 859-868, Feb. 2021.

[142] P. -Y. Qin, L. Z. Song and Y. J. Guo, "Beam steering conformal transmitarray employing ultra-thin triple-layer slot elements," in *IEEE Transactions on Antennas and Propagation*, vol. 67, no. 8, pp. 5390-5398, Aug. 2019.

[143] H. Li, G. Wang, J. Liang, X. Gao, H. Hou and X. Jia, "Single-layer focusing gradient metasurface for ultrathin planar lens antenna application," in *IEEE Transactions on Antennas and Propagation*, vol. 65, no. 3, pp. 1452-1457, Mar. 2017.

[144] Y. Hu et al., "A digital multibeam array with wide scanning angle and enhanced beam gain for millimeter-wave massive MIMO applications," in *IEEE Transactions on Antennas and Propagation*, vol. 66, no. 11, pp. 5827-5837, Nov. 2018.

[145] W. An, S. Xu, F. Yang and M. Li, "A double-layer transmitarray antenna using Malta crosses with vias," in *IEEE Transactions on Antennas and Propagation*, vol. 64, no. 3, pp. 1120-1125, Mar. 2016.

[146] P. -Y. Feng, S. -W. Qu and S. Yang, "Phased transmitarray antennas for 1-D beam scanning," in *IEEE Antennas and Wireless Propagation Letters*, vol. 18, no. 2, pp. 358-362, Feb. 2019.

[147] W. Saleh, Y. Letestu, R. Sauleau and E. M. Cruz, "High-gain transmitarray

antenna for backhauling at D-band," *2021 15th European Conference on Antennas and Propagation (EuCAP)*, Dusseldorf, Germany, 2021, pp. 1-4.

[148] S. Wang et al., "Compact Dual-Band Independently Modulated Huygens' Metasurface for Full-Space EM Wave Manipulation," in *IEEE Transactions on Microwave Theory and Techniques*, vol. 71, no. 12, pp. 5160-5170, Dec. 2023

[149] X. Wang, P. Y. Qin, A. Tuyen Le, H. Zhang, R. Jin and Y. J. Guo, "Beam Scanning Transmitarray Employing Reconfigurable Dual-Layer Huygens Element," in *IEEE Transactions on Antennas and Propagation*, vol. 70, no. 9, pp. 7491-7500, Sep. 2022

[150] C. Pfeiffer, A. Grbic, "Metamaterial Huygens' surfaces: tailoring wave fronts with reflectionless sheets," in *Physical Review Letters*, vol. 110, no. 19, pp. 197401, May 2013.

[151] M. Chen, M. Kim, A. M. Wong, G. V. Eleftheriades, "Huygens' metasurfaces from microwaves to optics: a review," in *Nanophotonics*, vol. 7, no. 6, pp. 1207-1231, Jun. 2018.

[152] Q. Lou, C. Xue, Z. N. Chen, "High-efficiency metalens antenna using Huygens' metasurface with glide symmetric I-shape metal strips," in *IEEE Transactions on Antennas and Propagation*, vol. 69, no. 11, pp. 7394-7403, Jun. 2021.

[153] S. Sakurai, J. G. N. Rahmeier, T. Tomura, J. Hirokawa and S. Gupta, "Millimeter-wave huygens' transmit arrays based on coupled metallic resonators," in *IEEE Transactions on Antennas and Propagation*, vol. 69, no. 5, pp. 2686-2696, May 2021.

[154] R. Zhao, Z. Zhu, G. Dong, T. Lv, Y. Li, C. Guan, J. Shi, H. Zhang, "High-efficiency Huygens' metasurface for terahertz wave manipulation," in *Optics Letters*, vol. 44, no. 14, pp. 3482-3485, Jul. 2019.

[155] X. Wang, P. Y. Qin, L. Z. Song, R. Jin, Y. J. Guo, "Tightly coupled Huygens element-based conformal transmitarray for E-band airborne communication systems," in *IEEE Transactions on Antennas and Propagation*, vol. 71, no. 3, pp. 2467-2475, Feb. 2023.

[156] J. Zhu, M. Li, J. Lai, Y. Yang, "Multimaterial additively manufactured

transmissive spin‐decoupled polarization‐maintaining metasurfaces," in *Laser & Photonics Reviews*, vol. 17, no. 12, pp. 2300433, Dec. 2023.

[157] Z. Zhai, F. Lin, Y. Yang and H. Sun, "Additively manufactured wideband low-profile bidirectional 2-D beam-scanning antenna using double folded transmitarrays with curved polarizers," in *IEEE Transactions on Antennas and Propagation*, vol. 72, no. 1, pp. 476-486, Jan. 2024.

[158] B. -J. Xiang and K. -M. Luk, "A wideband low-profile folded transmitarray antenna based on magnetoelectric dipole elements," in *IEEE Transactions on Antennas and Propagation*, vol. 71, no. 11, pp. 8659-8667, Nov. 2023.

[159] J. Zhu, Y. Yang, F. Wang, J. Lai, M. Li, "3D printed spin‐decoupled transmissive metasurfaces based on versatile broadband cross‐polarization rotation meta‐atom," in *Advanced Optical Materials*, vol. 11, no. 4, pp. 2202416, Feb. 2023.

[160] H. Lei et al., "A low-profile risley-prism-based 2-D beam-scanning circularly polarized folded transmitarray antenna at Ku-band," in *IEEE Transactions on Antennas and Propagation*, vol. 71, no. 7, pp. 6173-6178, Jul. 2023.

[161] H. Lei, Y. Liu, Y. Jia, Z. Yue and X. Wang, "A low-profile dual-band dual-circularly polarized folded transmitarray antenna with independent beam control," in *IEEE Transactions on Antennas and Propagation*, vol. 70, no. 5, pp. 3852-3857, May 2022.

[162] Z. -W. Miao et al., "140 GHz high-gain LTCC-integrated transmit-array antenna using a wideband SIW aperture-coupling phase delay structure," in *IEEE Transactions on Antennas and Propagation*, vol. 66, no. 1, pp. 182-190, Jan. 2018.

[163] B. Xi, Y. Xiao, H. Dong, M. Xiang, F. Yang and Z. Chen, "Low-profile wideband 1-bit reconfigurable transmitarray with 2-D beam-scanning capacity," in *IEEE Transactions on Antennas and Propagation*, vol. 71, no. 4, pp. 3228-3237, Apr. 2023.

[164] L. Li, L. Ma, H. Sun, S. Hu, M. Wu, Z. Qi, and W. Wu, “Equivalent circuit models of a bifunctional optical metasurface for beam splitting and refractive index sensing,” in *ACS Photonics*, vol. 10, no. 8, pp. 2746–2754, Jun. 2023.

[165] J. F. O'Hara, W. Withayachumnankul, I. Al-Naib, "A review on thin-film sensing with terahertz waves," in *Journal of Infrared, Millimeter, and Terahertz Waves*, vol. 33, pp. 245-291, Mar. 2012.

[166] M. Beruete, I. Jáuregui‐López, "Terahertz sensing based on metasurfaces," in *Advanced Optical Materials*, vol. 8, no. 3, pp. 1900721, Feb. 2020.

[167] J. Bae and T. Nozokido, "Highly sensitive sensing of refractive index using surface lattice resonance in capacitive metal meshes at millimeter wave frequencies," in *IEEE Sensors Journal*, vol. 23, no. 21, pp. 25927-25937, Nov. 2023.

[168] S. Shen, X. Liu, Y. Shen, J. Qu, E. Pickwell‐MacPherson, X. Wei, Y. Sun, "Recent advances in the development of materials for terahertz metamaterial sensing," in *Advanced Optical Materials*, vol. 10, no. 1, pp. 2101008-2101009, Jan. 2022.

[169] F. Y. Meng, Q. Wu, D. Erni, K. Wu, J. C. Lee, "Polarization-independent metamaterial analog of electromagnetically induced transparency for a refractive-index-based sensor," in *IEEE Transactions on Microwave Theory and Techniques*, vol. 60, no. 10, pp. 3013-3022, Aug. 2012.

[170] J. Li, J. Shao, Y. H. Wang, M. J. Zhu, J. Q. Li, Z. G. Dong, "Toroidal dipolar response by a dielectric microtube metamaterial in the terahertz regime," in *Optics Express*, vol. 23, no. 22, pp. 29138-29144, Nov. 2015.

[171] A. Hamouleh-Alipour, A. Mir, A. Farmani, "Analytical modeling and design of a graphene metasurface sensor for thermo-optical detection of terahertz plasmons," in *IEEE Sensors Journal*, vol. 21, no. 4, pp. 4525-4532, Nov. 2020.

[172] Y. Wang, D. Zhu, Z. Cui, L. Yue, X. Zhang, L. Hou, K. Zhang, H. Hu, "Properties and sensing performance of all-dielectric metasurface THz absorbers," in *IEEE Transactions on Terahertz Science and Technology*, vol. 10, no. 6, pp. 599-605, Jul. 2020.

[173] X. Y. Yin, N. Yang, Q. Wang, X. Yan, J. X. Jiang, L. Wang, "High FOM refractive index sensor based on quasi-bound states in the continuum of tri-prism metasurface," in *IEEE Sensors Journal*, vol. 23, no. 7, pp. 7683-7689, Mar. 2023.

[174] E. Shokati, S. Asgari and N. Granpayeh, "Dual-band polarization-sensitive graphene chiral metasurface and its application as a refractive index sensor," in *IEEE Sensors Journal*, vol. 19, no. 21, pp. 9991-9996, Nov. 2019.

[175] A. S. Saadeldin, M. F. O. Hameed, E. M. A. Elkaramany and S. S. A. Obayya, "Highly sensitive terahertz metamaterial sensor," in *IEEE Sensors Journal*, vol. 19, no. 18, pp. 7993-7999, 15 Sep. 2019.

[176] L. Cong, S. Tan, R. Yahiaoui, F. Yan, W. Zhang, R. Singh, "Experimental demonstration of ultrasensitive sensing with terahertz metamaterial absorbers: A comparison with the metasurfaces, " in *Applied Physics Letters*, vol.106, no. 3, Jan. 2015.

[177] S. J. Park, S. W. Jun, A. R. Kim, Y. H. Ahn, "Terahertz metamaterial sensing on polystyrene microbeads: Shape dependence, " in *Optical Materials Express*, vol. 5, no. 10, pp. 2150-2155, Oct. 2015.

[178] A. K. Azad, A. J. Taylor, E. Smirnova, J. F. O'Hara, "Characterization and analysis of terahertz metamaterials based on rectangular split-ring resonators," in *Applied Physics Letters*, vol. 92, no. 1, Jan. 2008.

[179] Y. Zhong, L. Du, Q. Liu, L. Zhu, B. Zhang, "Metasurface-enhanced ATR sensor for aqueous solution in the terahertz range," in *Optics Communications*, vol. 465, pp. 125508, Jun. 2020.

[180] S. Ramani, M. T. Reiten, P. L. Colestock, A. J. Taylor, A. K. Azad, J. F. O'Hara, "Electromagnetic response of finite terahertz metafilm arrays excited on total internal reflection boundaries," in *IEEE Transactions on Terahertz Science and Technology*, vol. 3, no. 6, pp. 709-720, Nov. 2013.

[181] U. Fano, "Effects of configuration interaction on intensities and phase shifts," in *Physical Review*, vol. 124, no. 6, pp. 1866, Dec. 1961.

[182] S. E. Harris, "Electromagnetically induced transparency," in *Physics Today*, vol. 50, no. 7, pp. 36-42, Jul. 1997.

[183] Z. Xu, Y. Wang, S. Liu, J. Ma, S. Fang and H. Wu, "Metamaterials with analogous electromagnetically induced transparency and related sensor designs—a review," in *IEEE Sensors Journal*, vol. 23, no. 7, pp. 6378-6396, Apr. 2023.

[184] F. Bagci, B. Akaoglu, "A polarization independent electromagnetically induced transparency-like metamaterial with large group delay and delay-bandwidth product," in *Journal of Applied Physics*, vol. 123, no. 17, May 2018.

[185] R. Zhou, C. Wang, Y. Huang, K. Huang, Y. Wang, W. Xu, L. Xie, Y. Ying, "Label-free terahertz microfluidic biosensor for sensitive DNA detection using graphene-metasurface hybrid structures," in *Biosensors and Bioelectronics*, vol. 188, pp. 113336, Sep. 2021.

[186] M. Iwanaga, "All-dielectric metasurface fluorescence biosensors for high-sensitivity antibody/antigen detection," in *ACS nano*, vol. 14, no. 12, pp. 17458-17467, Nov. 2020.

[187] X. Yan, M. Yang, Z. Zhang, L. Liang, D. Wei, M. Wang, M. Zhang, T. Wang, L. Liu, J. Xie, J. Yao, "The terahertz electromagnetically induced transparency-like metamaterials for sensitive biosensors in the detection of cancer cells," in *Biosensors and Bioelectronics*, vol. 126, no. 1, pp. 485-492, Feb. 2019.

[188] J. Maleki, D. Fathi, "Refractive index sensor based on Fano-magnetic toroidal quadrupole resonance enabled by bound state in the continuum in all-dielectric metasurface," in *Scientific Reports*, vol. 14, no. 1, pp. 4110, Feb. 2024.

[189] X. Liu, G. Liu and J. Qin, "Feasibility of using terahertz toroidal metasurface sensor for detection and quantification of chlorothalonil in water," in *IEEE Sensors Journal*, vol. 23, no. 24, pp. 30360-30367, Dec. 2023.

[190] S. K. Patel, J. Parmar, R. B. Zakaria, S. A., T. K. Nguyen and V. Dhasarathan, "Sensitivity analysis of metasurface array-based refractive index biosensors," in *IEEE Sensors Journal*, vol. 21, no. 2, pp. 1470-1477, Jan. 2021.

[191] C. Zhang, T. Xue, J. Zhang, L. Liu, J. Xie, G. Wang, J. Yao, W. Zhu, X. Ye, "Terahertz toroidal metasurface biosensor for sensitive distinction of lung cancer cells," in *Nanophotonics*, vol. 11, no. 1, pp. 101-109, Dec. 2021.

[192] Z. Vafapour, W. Troy and A. Rashidi, "Colon cancer detection by designing and analytical evaluation of a water-based THz metamaterial perfect absorber," in *IEEE Sensors Journal*, vol. 21, no. 17, pp. 19307-19313, Sep. 2021.

[193] J. Zhang, N. Mu, L. Liu, J. Xie, H. Feng, J. Yao, T. Chen, W. Zhu, "Highly

sensitive detection of malignant glioma cells using metamaterial-inspired THz biosensor based on electromagnetically induced transparency," in *Biosensors and Bioelectronics*, vol. 185, pp. 113241, Aug. 2021.

[194] M. Y. Azab, M. F. O. Hameed, A. M. Nasr and S. S. A. Obayya, "Highly sensitive metamaterial biosensor for cancer early detection," in *IEEE Sensors Journal*, vol. 21, no. 6, pp. 7748-7755, Mar. 2021.

[195] M. Yang, L. Liang, Z. Zhang, Y. Xin, D. Wei, X. Song, H. Zhang, Y. Lu, M. Wang, M. Zhang, T. Wang, "Electromagnetically induced transparency-like metamaterials for detection of lung cancer cells," in *Optics Express*, vol. 27, no. 14, pp. 19520-19529, Jul. 2019.

[196] Y. Yang, I. I. Kravchenko, D. P. Briggs, J. Valentine, "All-dielectric metasurface analogue of electromagnetically induced transparency," in *Nature Communications*, vol. 5, no. 1, pp. 5753, Dec. 2014.

[197] S. Nourinovin, M. M. Rahman, M. Naftaly, M. P. Philpott, Q. H. Abbasi and A. Alomainy, "Highly sensitive terahertz metasurface based on electromagnetically induced transparency-like resonance in detection of skin cancer cells," in *IEEE Transactions on Biomedical Engineering*, vol. 71, no. 7, pp. 2180-2188, Jul. 2024.

[198] L. Cong, M. Manjappa, N. Xu, I. Al‐Naib, W. Zhang, R. Singh, "Fano resonances in terahertz metasurfaces: a figure of merit optimization," in *Advanced Optical Materials*, vol. 3, no. 11, pp. 1537-1543, Nov. 2015.

[199] A. Keshavarz and Z. Vafapour, "Water-based terahertz metamaterial for skin cancer detection application," in *IEEE Sensors Journal*, vol. 19, no. 4, pp. 1519-1524, Feb. 2019.

[200] N. R. Abbasi, H. M. Shaw, D. S. Rigel, et al, "Early diagnosis of cutaneous melanoma: revisiting the ABCD criteria, " in *JAMA*, vol. 292, no. 22, pp.2771-2776, 2004.

[201] S. M. Goldsmith, A. R. Solomon, "A series of melanomas smaller than 4 mm and implications for the ABCDE rule, " in *Journal of the European Academy of Dermatology and Venereology*, vol. 21, no. 7, pp. 929-934, 2007.

[202] M. F. Healsmith, J. F. Bourke, J. E. Osborne, R. A. Graham‐Brown, "An evaluation of the revised seven‐point checklist for the early diagnosis of cutaneous malignant melanoma," in *British Journal of Dermatology*, vol. 130, no. 1, pp. 48-50, Jan. 1994.

[203] M. Keefe, D. C. Dick, R. A. Wakeel, "A study of the value of the seven‐point checklist in distinguishing benign pigmented lesions from melanoma," in *Clinical and Experimental Dermatology*, vol. 15, no. 3, pp. 167-171, May 1990.

[204] K. Sellheyer, W. F. Bergfeld, "A retrospective biopsy study of the clinical diagnostic accuracy of common skin diseases by different specialties compared with dermatology," in *Journal of the American Academy of Dermatology*, vol. 52, no. 5, pp. 823-830, May 2005.

[205] A. Masood, A. A. Al-Jumaily, "Computer aided diagnostic support system for skin cancer: A review of techniques and algorithms," in *International Journal of Biomedical Imaging*, vol. 2013, no. 1, pp. 323268-323260, 2013.

[206] A. Gerger, R. Hofmann‐Wellenhof, H. Samonigg, J. Smolle, "In vivo confocal laser scanning microscopy in the diagnosis of melanocytic skin tumours," in *British Journal of Dermatology*, vol. 160, no. 3, pp. 475-481, Mar. 2009.

[207] A. Lorber, M. Wiltgen, R. Hofmann‐Wellenhof, S. Koller, W. Weger, V. Ahlgrimm‐Siess, J. Smolle, A. Gerger, "Correlation of image analysis features and visual morphology in melanocytic skin tumours using in vivo confocal laser scanning microscopy," in *Skin Research and Technology*, vol. 15, no. 2, pp. 237-241, May 2009.

[208] M. Mogensen, L. Thrane, T. M. Jørgensen, P. E. Andersen, G. B. Jemec, "OCT imaging of skin cancer and other dermatological diseases," in *Journal of Biophotonics*, vol. 2, no. 6‐7, pp. 442-451, Jul. 2009.

[209] J. Welzel, "Optical coherence tomography in dermatology: a review," in *Skin Research and Technology: Review article*, vol. 7, no. 1, pp. 1-9, Feb. 2001.

[210] M. C. Pierce, J. Strasswimmer, B. H. Park, B. Cense, J. F. De Boer, "Advances in optical coherence tomography imaging for dermatology," in *Journal of Investigative Dermatology*, vol. 123, no. 3, pp. 458-463, Sep. 2004.

[211] L. Serrone, F. M. Solivetti, M. F. Thorel, L. Eibenschutz, P. Donati, C. Catricala, "High frequency ultrasound in the preoperative staging of primary melanoma: a statistical analysis," in *Melanoma Research*, vol. 12, no. 3, pp. 287-290, Jun. 2002.

[212] A. Blum, M. H. Schmid-Wendtner, V. Mauss-Kiefer, J. Y. Eberle, C. Kuchelmeister, D. Dill-Müller, "Ultrasound mapping of lymph node and subcutaneous metastases in patients with cutaneous melanoma: results of a prospective multicenter study," in *Dermatology*, vol. 212, no. 1, pp. 47-52, Nov. 2005.

[213] I. Ono, F. Kaneko, "Magnetic resonance imaging for diagnosing skin tumors," in *Clinics in Dermatology*, vol. 13, no. 4, pp. 393-399, Jul. 1995.

[214] S. el Gammal, R. Hartwig, S. Aygen, T. Bauermann, C. el Gammal, P. Altmeyer, "Improved resolution of magnetic resonance microscopy in examination of skin tumors," in *Journal of Investigative Dermatology*, vol. 106, no. 6, pp. 1287-1292, Jun. 1996.

[215] A. Mirbeik, R. Ashinoff, T. Jong, A. Aued, N. Tavassolian, "Real-time high-resolution millimeter-wave imaging for in-vivo skin cancer diagnosis," in Scientific Reports, vol. 12, no. 1, pp. 4971, Mar. 2022.

[216] A. Mirbeik-Sabzevari, R. Ashinoff and N. Tavassolian, "Ultra-wideband millimeter-wave dielectric characteristics of freshly excised normal and malignant human skin tissues," in *IEEE Transactions on Biomedical Engineering*, vol. 65, no. 6, pp. 1320-1329, Jun. 2018

[217] F. Kazemi, F. Mohanna, J. Ahmadi-Shokouh, "Detection of biological abnormalities using a near-field microwave microscope," in *International Journal of Microwave and Wireless Technologies*, vol. 10, no. 8, pp. 933-941, Oct. 2018.

[218] A. Taeb, S. Gigoyan, S. Safavi-Naeini, "Millimetre-wave waveguide reflectometers for early detection of skin cancer," in *IET Microwaves, Antennas & Propagation*, vol. 7, no. 14, pp. 1182-1186, Nov. 2013.

[219] F. Töpfer, S. Dudorov, J. Oberhammer, "Millimeter-wave near-field probe designed for high-resolution skin cancer diagnosis," in *IEEE Transactions on*

Microwave Theory and Techniques, vol. 63, no. 6, pp. 2050-2059, May 2015.

[220] P. Mehta, K. Chand, D. Narayanswamy, D. G. Beetner, R. Zoughi, W. V. Stoecker, "Microwave reflectometry as a novel diagnostic tool for detection of skin cancers," in *IEEE Transactions on Instrumentation and Measurement*, vol. 55, no. 4, pp. 1309-1316, Jul. 2006.

[221] D. Popovic, M. Okoniewski, "Effects of mechanical flaws in open-ended coaxial probes for dielectric spectroscopy," in *IEEE Microwave And Wireless Components Letters*, vol. 12, no. 10, pp. 401-403, Oct. 2002.

[222] G. Mansutti, A. T. Mobashsher, K. Bialkowski, B. Mohammed, A. Abbosh, "Millimeter-wave substrate integrated waveguide probe for skin cancer detection," in *IEEE Transactions on Biomedical Engineering*, vol. 67, no. 9, pp. 2462-2472, Dec. 2019.

[223] A. Mirbeik-Sabzevari, S. Li, E. Garay, H. -T. Nguyen, H. Wang and N. Tavassolian, "Synthetic ultra-high-resolution millimeter-wave imaging for skin cancer detection," in *IEEE Transactions on Biomedical Engineering*, vol. 66, no. 1, pp. 61-71, Jan. 2019

[224] A. Mirbeik-Sabzevari, E. Oppelaar, R. Ashinoff and N. Tavassolian, "High-contrast, low-cost, 3-D visualization of skin cancer using ultra-high-resolution millimeter-wave imaging," in *IEEE Transactions on Medical Imaging*, vol. 38, no. 9, pp. 2188-2197, Sep. 2019.

[225] D. M. Sheen, D. L. McMakin and T. E. Hall, "Three-dimensional millimeter-wave imaging for concealed weapon detection," in *IEEE Transactions on Microwave Theory and Techniques*, vol. 49, no. 9, pp. 1581-1592, Sep. 2001.

[226] Xu Li, S. K. Davis, S. C. Hagness, D. W. van der Weide and B. D. Van Veen, "Microwave imaging via space-time beamforming: experimental investigation of tumor detection in multilayer breast phantoms," in *IEEE Transactions on Microwave Theory and Techniques*, vol. 52, no. 8, pp. 1856-1865, Aug. 2004.

[227] X. Yang, X. Zhao, K. Yang, Y. Liu, Y. Liu, W. Fu, Y. Luo, "Biomedical applications of terahertz spectroscopy and imaging," in *Trends in Biotechnology*, vol. 34, no. 10, pp. 810-824, Oct. 2016.

[228] L. Wei, L. Yu, H. Jiaoqi, H. Guorong, Z. Yang, F. Weiling, "Application of terahertz spectroscopy in biomolecule detection," in *Frontiers in Laboratory Medicine*, vol. 2, no. 4, pp. 127-133, Dec. 2018.

[229] Z. D. Taylor, R. S. Singh, M. O. Culjat, J. Y. Suen, W. S. Grundfest, H. Lee, E. R. Brown, "Reflective terahertz imaging of porcine skin burns," in *Optics Letters*, vol. 33, no. 11, pp. 1258-1260, May 2008.

[230] D. Hou, X. Li, J. Cai, Y. Ma, X. Kang, P. Huang, G. Zhang, "Terahertz spectroscopic investigation of human gastric normal and tumor tissues," in *Physics in Medicine & Biology*, vol. 59, no. 18, pp. 5423, Aug. 2014.

[231] B. C. Q. Truong, H. D. Tuan, A. J. Fitzgerald, V. P. Wallace and H. T. Nguyen, "A dielectric model of human breast tissue in terahertz regime," in *IEEE Transactions on Biomedical Engineering*, vol. 62, no. 2, pp. 699-707, Feb. 2015.

[232] G. G. Hernandez-Cardoso, S. C. Rojas-Landeros, M. Alfaro-Gomez, A. I. Hernandez-Serrano, I. Salas-Gutierrez, E. Lemus-Bedolla, A. R. Castillo-Guzman, H. L. Lopez-Lemus, E. Castro-Camus, "Terahertz imaging for early screening of diabetic foot syndrome: A proof of concept," in *Scientific Reports*, vol. 7, no. 1, pp. 42124, Feb. 2017.

[233] V. P. Wallace, A. J. Fitzgerald, S. Shankar, N. Flanagan, R. Pye, J. Cluff, D. D. Arnone, "Terahertz pulsed imaging of basal cell carcinoma ex vivo and in vivo," in *British Journal of Dermatology*, vol. 151, no. 2, pp. 424-432, Aug. 2004.

[234] E. Pickwell, B. E. Cole, A. J. Fitzgerald, M. Pepper, V. P. Wallace, "In vivo study of human skin using pulsed terahertz radiation," in *Physics in Medicine & Biology*, vol. 49, no. 9, pp. 1595, Apr. 2004.

[235] B. E. Cole, R. M. Woodward, D. A. Crawley, et al, "Terahertz imaging and spectroscopy of human skin in vivo, " in *Commercial and Biomedical Applications of Ultra-short Pulse Lasers; Laser Plasma Generation and Diagnostics. International Society for Optics and Photonics*, vol. 4276, pp. 1-10, 2001.

[236] A. Nahata, A. S. Weling, T. F. Heinz, "A wideband coherent terahertz spectroscopy system using optical rectification and electro - optic sampling," in *Applied Physics Letters*, vol. 69, no. 16, pp. 2321-2323, Oct. 1996.

[237] R. M. Woodward, B. E. Cole, V. P. Wallace, R. J. Pye, D. D. Arnone, E. H. Linfield, M. Pepper, "Terahertz pulse imaging in reflection geometry of human skin cancer and skin tissue," in *Physics in Medicine & Biology*, vol. 47, no. 21, pp. 3853-3850, Oct. 2002.

[238] V. P. Wallace, A. J. Fitzgerald, E. Pickwell, R. J. Pye, P. F. Taday, N. Flanagan, T. Ha, "Terahertz pulsed spectroscopy of human basal cell carcinoma," in *Applied Spectroscopy*, vol. 60, no. 10, pp. 1127-1133, Oct. 2006.

[239] C. S. Joseph, A. N. Yaroslavsky, V. A. Neel, T. M. Goyette, R. H. Giles, "Continuous wave terahertz transmission imaging of nonmelanoma skin cancers," in *Lasers in Surgery and Medicine*, vol. 43, no. 6, pp. 457-462, Aug. 2011.

[240] M. El-Shenawee, N. Vohra, T. Bowman, K. Bailey, "Cancer detection in excised breast tumors using terahertz imaging and spectroscopy," in Biomedical Spectroscopy and Imaging, vol. 8, no. 1-2, pp. 1-9, Feb. 2019.

[241] Y. X. Zheng, B. J. Xiang, Y. M. Pan and S. Y. Zheng, "Compact cylinder Luneburg-lens antennas based on 3-D-printing technology," in *IEEE Transactions on Antennas and Propagation*, vol. 71, no. 3, pp. 2311-2320, Mar. 2023

[242] Y. -H. Lou, Y. -X. Zhu, G. -F. Fan, W. Lei, W. -Z. Lu and X. -C. Wang, "Design of Ku-band flat luneburg lens using ceramic 3-D printing," in *IEEE Antennas and Wireless Propagation Letters*, vol. 20, no. 2, pp. 234-238, Feb. 2021

[243] Y. Guo, F. Meng, K. Ma, J. Ma and Y. Luo, "A terahertz wide-angle beam-steering 3D-printed dual-polarized GRIN lens with planar focal surface," in *IEEE Transactions on Terahertz Science and Technology*, vol. 15, no. 3, pp. 519-525, May 2025.

[244] M. K. T. Al-Nuaimi and W. Hong, "Discrete dielectric reflectarray and lens for e-band with different feed," in *IEEE Antennas and Wireless Propagation Letters*, vol. 13, pp. 947-950, 2014.

[245] S. A. Matos et al., "3-D-printed transmit-array antenna for broadband backhaul 5G links at V-band," in *IEEE Antennas and Wireless Propagation Letters*, vol. 19, no. 6, pp. 977-981, June 2020.

[246] J. Zhu, Y. Yang, D. McGloin, S. Liao and Q. Xue, "3-D printed all-dielectric dual-band broadband reflectarray with a large frequency ratio," in *IEEE Transactions on Antennas and Propagation*, vol. 69, no. 10, pp. 7035-7040, Oct.

2021

[247] M. Liang, W. -R. Ng, K. Chang, K. Gbele, M. E. Gehm and H. Xin, "A 3-D Luneburg lens antenna fabricated by polymer jetting rapid prototyping," in *IEEE Transactions on Antennas and Propagation*, vol. 62, no. 4, pp. 1799-1807, Apr. 2014

[248] F. Wei, J. -W. Hao, L. Xu and X. Shi, "A circularly polarized 3-D printed dielectric transmitarray antenna at millimeter-wave band," in *IEEE Antennas and Wireless Propagation Letters*, vol. 20, no. 7, pp. 1264-1268, Jul. 2021.

[249] G. -B. Wu, K. F. Chan, S. -W. Qu and C. H. Chan, "A 2-D beam-scanning Bessel launcher for terahertz applications," in *IEEE Transactions on Antennas and Propagation*, vol. 68, no. 8, pp. 5893-5903, Aug. 2020.

[250] G. -B. Wu, K. F. Chan and C. H. Chan, "3-D printed terahertz lens to generate higher order Bessel beams carrying OAM," in *IEEE Transactions on Antennas and Propagation*, vol. 69, no. 6, pp. 3399-3408, June 2021.

[251] A. Massaccesi et al., "3D-printable dielectric transmitarray with enhanced bandwidth at millimeter-waves," in *IEEE Access*, vol. 6, pp. 46407-46418, 2018.

[252] Y. Cai, P. Mei, X. Q. Lin and S. Zhang, "A generalized method for gain bandwidth enhancement of transmitarray antennas considering oblique incidences," in *IEEE Transactions on Circuits and Systems II: Express Briefs*, vol. 71, no. 1, pp. 121-125, Jan. 2024

[253] P. Mei, G. F. Pedersen and S. Zhang, "Performance improvement of mechanically beam-steerable transmitarray antennas by using offset unifocal phase symmetry," in *IEEE Transactions on Antennas and Propagation*, vol. 71, no. 1, pp. 1129-1134, Jan. 2023.

[254] P. Nayeri, F. Yang and A. Z. Elsherbeni, "Bifocal design and aperture phase optimisations of reflectarray antennas for wide-angle beam scanning performance," in *IEEE Transactions on Antennas and Propagation*, vol. 61, no. 9, pp. 4588-4597, Sep. 2013.

[255] L. Peebles, "A dielectric bifocal lens for multibeam antenna applications," in *IEEE Transactions on Antennas and Propagation*, vol. 36, no. 5, pp. 599-606, May 1988.

[256] W. Shao and Q. Chen, "2-D beam-steerable generalized Mikaelian lens with unique flat-shape characteristic," in *IEEE Antennas and Wireless Propagation Letters*, vol. 20, no. 10, pp. 2033-2037, Oct. 2021.

[257] L. -Z. Song, P. Y. Qin, S. -L. Chen and Y. J. Guo, "An elliptical cylindrical shaped transmitarray for wide-angle multibeam applications," in *IEEE Transactions on Antennas and Propagation*, vol. 69, no. 10, pp. 7023-7028, Oct. 2021.

[258] L. -Z. Song, M. Ansari, P. -Y. Qin, S. Maci, J. Du and Y. J. Guo, "Two-dimensional wide-angle multibeam flat GRIN lens with a high aperture efficiency," in *IEEE Transactions on Antennas and Propagation*, vol. 71, no. 10, pp. 8018-8029, Oct. 2023

[259] L. -Z. Song, T. Zhang, J. -X. Lai, Y. Yang and J. Du, "A 180-GHz to 220-GHz wideband transmitarray with wide-angle beam steering for intersatellite communications," in *IEEE Transactions on Antennas and Propagation*, vol. 72, no. 1, pp. 950-955, Jan. 2024.

[260] P. Nayeri, F. Yang and A. Z. Elsherbeni, "Design of multifocal transmitarray antennas for beamforming applications," *2013 IEEE Antennas and Propagation Society International Symposium (APSURSI)*, Orlando, FL, USA, 2013, pp. 1672-1673.

[261] A. Massaccesi, G. Dassano, P. Pirinoli, "Beam scanning capabilities of a 3D-printed perforated dielectric transmitarray," in *Electronics*, vol. 8, no. 4, pp. 379, Mar. 2019.

[262] J. Chen, S. X. Huang, K. F. Chan, G. B. Wu, C. H. Chan, "3D-printed aberration-free terahertz metalens for ultra-broadband achromatic super-resolution wide-angle imaging with high numerical aperture," in *Nature Communications*, vol. 16, no. 1, pp. 363, Jan. 2025.

[263] W. T. Chen, A. Y. Zhu, V. Sanjeev, M. Khorasaninejad, Z. Shi, E. Lee, F. Capasso, "A broadband achromatic metalens for focusing and imaging in the visible," in *Nature Nanotechnology*, vol. 13, no. 3, pp. 220-226, Mar. 2018.

[264] W. Shao, Q. Chen, "Single-pixel scanning near-field imaging with subwavelength resolution using sharp focusing Mikaelian lens," in *IEEE Transactions on Microwave Theory and Techniques*, vol. 71, no. 2, pp. 795-804, Sep. 2022.

[265] J. C. Zhang, G. B. Wu, M. K. Chen, X. Liu, K. F. Chan, D. P. Tsai, C. H. Chan, "A 6G meta-device for 3D varifocal," in *Science Advances*, vol. 9, no. 4, pp. 8478, Jan. 2023.

[266] G. B. Wu, K. F. Chan, S. W. Qu, C. H. Chan, "A 2-D beam-scanning Bessel

launcher for terahertz applications," in *IEEE Transactions on Antennas and Propagation*, vol. 68, no. 8, pp. 5893-5903, Apr. 2020.

[267] K. K. Ho, G. B. Wu, B. J. Chen, K. F. Chan, C. H. Chan, "Spot focusing coma correction by linearly polarized dual-transmitarray antenna in the terahertz region," in *IEEE Transactions on Terahertz Science and Technology*, vol. 13, no. 5, pp. 493-502, Jul. 2023.

[268] Z. Wang, X. Ding, K. Zhang, B. Ratni, S. N. Burokur, X. Gu, Q. Wu, "Huygens metasurface holograms with the modulation of focal energy distribution," in *Advanced Optical Materials*, vol. 6, no. 12, pp. 1800121, Jun. 2018.

[269] C. Guan, Z. Wang, X. Ding, K. Zhang, B. Ratni, S. N. Burokur, M. Jin, Q. Wu, "Coding Huygens' metasurface for enhanced quality holographic imaging," in *Optics Express*, vol. 27, no. 5, pp. 7108-7119, Feb. 2019.

[270] Y. Bao, L. Wen, Q. Chen, C. W. Qiu, B. Li, "Toward the capacity limit of 2D planar Jones matrix with a single-layer metasurface," in *Science Advances*, vol. 7, no. 25, pp. 0365, Jun. 2021.

[271] B. Xiong, Y. Liu, Y. Xu, L. Deng, C. W. Chen, J. N. Wang, R. Peng, Y. Lai, Y. Liu, M. Wang, "Breaking the limitation of polarization multiplexing in optical metasurfaces with engineered noise," in *Science*, vol. 379, no. 6629, pp. 294-299, Jan. 2023.

[272] N. Gagnon and A. Petosa, "Using Rotatable Planar Phase Shifting Surfaces to Steer a High-Gain Beam," in *IEEE Transactions on Antennas and Propagation*, vol. 61, no. 6, pp. 3086-3092, June 2013.

[273] K. Sato and Y. Monnai, "Two-Dimensional Terahertz Beam Steering Based on Trajectory Deflection of Leaky-Mode," in *IEEE Transactions on Terahertz Science and Technology*, vol. 11, no. 6, pp. 676-683, Nov. 2021.

[274] Y. Hu et al., "A digital multibeam array with wide scanning angle and enhanced beam gain for millimeter-wave massive MIMO applications," in *IEEE Transactions on Antennas and Propagation*, vol. 66, no. 11, pp. 5827-5837, Nov. 2018.

[275] A. Dreher, N. Niklasch, F. Klefenz and A. Schroth, "Antenna and receiver system with digital beamforming for satellite navigation and communications," in *IEEE Transactions on Microwave Theory and Techniques*, vol. 51, no. 7, pp. 1815-1821, Jul. 2003.

[276] H. Yi, S. W. Qu, K. Ng, C. H. Chan and X. Bai, "3-D printed millimeter- wave

and terahertz lenses with fixed and frequency scanned beam," in *IEEE Transactions on Antennas and Propagation*, vol. 64, no. 2, pp. 442-449, Feb. 2016.

[277] X. Chen, et. al., “A 140GHz transceiver with integrated antenna, inherent-low-loss duplexing and adaptive self-interference cancellation for FMCW monostatic radar”, in *International Solid-State Circuits Conference (ISSCC)*, vol. 65, pp. 80-82, Feb. 2022.

[278] E. Mavrona, J. Graf, E. Hack, P. Zolliker, "Optimized 3D printing of THz waveguides with cyclic olefin copolymer," in *Optical Materials Express*, vol. 11, no. 8, pp. 2495-2504, Jul. 2021.

[279] C. Fan, W. Yang, W. Che, S. He, Q. Xue, "A wideband and low-profile discrete dielectric lens using 3-D printing technology," in *IEEE Transactions on Antennas and Propagation*, vol. 66, no. 10, pp. 5160-5169, Aug. 2018.

[280] E. R. F. Almajali and D. A. McNamara, "Angle of incidence effects in reflectarray antenna design: making gain increases possible by including incidence angle effects," in *IEEE Antennas and Propagation Magazine*, vol. 58, no. 5, pp. 52-64, Oct. 2016.

[281] X. Liu et al., "Ultrabroadband all-dielectric transmitarray designing based on genetic algorithm optimization and 3-D print technology," in *IEEE Transactions on Antennas and Propagation*, vol. 69, no. 4, pp. 2003-2012, Apr. 2021.

[282] W. -s. Yu, L. Peng, Y. -f. Liu, Q. X. Zhao, X. Jiang and S. M. Li, "An ultrawideband and high-aperture-efficiency all-dielectric lens antenna," in *IEEE Antennas and Wireless Propagation Letters*, vol. 20, no. 12, pp. 2442-2446, Dec. 2021.

[283] A. Yu, F. Yang, A. Z. Elsherbeni, J. Huang, and Y. Rahmat–Samii, "Aperture efficiency analysis of reflectarray antennas," in *Microwave and Optical Technology Letters*, vol. 52, no. 2, pp. 364–372, 2010.

[284] "IEEE Standard for Definitions of Terms for Antennas," in IEEE Std 145-2013 (Revision of IEEE Std 145-1993), vol., no., pp.1-50, Mar. 2014.

[285] M. Żebrowski, "Illumination and Spillover Efficiency Calculations for Rectangular Reflectarray Antennas," in *High Frequency Design*, vol. 1, pp. 28-38, Dec. 2012.

[286] K. Ryu, J. G. Rhee, K. M. Park, J. Kim, "Concept and design of modular Fresnel lenses for concentration solar PV system," in *Solar Energy*, vol. 80, no. 12, pp. 1580-1587, Dec. 2006.

[287] G. -B. Wu, Y. -S. Zeng, K. F. Chan, S. -W. Qu and C. H. Chan, "3-D printed

circularly polarized modified Fresnel lens operating at terahertz frequencies," in *IEEE Transactions on Antennas and Propagation*, vol. 67, no. 7, pp. 4429-4437, Jul. 2019.

[288] M. Li, M. A. Al-Joumayly and N. Behdad, "Broadband true-time-delay microwave lenses based on miniaturized element frequency selective surfaces," in *IEEE Transactions on Antennas and Propagation*, vol. 61, no. 3, pp. 1166-1179, Mar. 2013.

[289] Y. Yang et al., "A review of multimaterial additively manufactured electronics and 4-D printing/origami shape-memory devices: Design, fabrication, and implementation," in *Proceedings of the IEEE*, vol. 112, no. 8, pp. 954-999, Aug. 2024.

[290] B. Zhang and H. Zirath, "Metallic 3-D printed rectangular waveguides for millimeter-wave applications," in *IEEE Transactions on Components, Packaging and Manufacturing Technology*, vol. 6, no. 5, pp. 796-804, May 2016.

[291] G. -L. Huang, C. -Z. Han, W. Xu, T. Yuan and X. Zhang, "A compact 16-way high-power combiner implemented via 3-D metal printing technique for advanced radio-frequency electronics system applications," in *IEEE Transactions on Industrial Electronics*, vol. 66, no. 6, pp. 4767-4776, Jun. 2019.

[292] A. Massaccesi et al., "3D-printable dielectric transmitarray with enhanced bandwidth at millimeter-waves," in *IEEE Access*, vol. 6, pp. 46407-46418, 2018.

[293] G. Shao, R. Hai, C. Sun, "3D printing customized optical lens in minutes," in *Advanced Optical Materials*, vol. 8, no. 4, pp. 19011646, Feb. 2020.

[294] M. Li, J. Cai, L. Deng, X. Li, F. Iacopi, Y. Yang, "Additively manufactured conductive and dielectric 3D metasurfaces for independent manipulation of broadband orbital angular momentum," in *Materials & Design*, vol. 249, pp. 113500, Jan. 2025.

[295] J. Kwon, Y. Takeda, R. Shiwaku, S. Tokito, K. Cho, S. Jung, "Three-dimensional monolithic integration in flexible printed organic transistors," in *Nature Communications*, vol. 10, no. 1, pp. 54-55, Jan. 2019.

[296] F. Cai, Y. -H. Chang, K. Wang, C. Zhang, B. Wang and J. Papapolymerou, "Low-loss 3-D multilayer transmission lines and interconnects fabricated by

additive manufacturing technologies," in *IEEE Transactions on Microwave Theory and Techniques*, vol. 64, no. 10, pp. 3208-3216, Oct. 2016.

[297] F. Cai, Y. -h. Chang, K. Wang, W. T. Khan, S. Pavlidis and J. Papapolymerou, "High resolution aerosol jet printing of D-band printed transmission lines on flexible LCP substrate," *2014 IEEE MTT-S International Microwave Symposium (IMS2014)*, Tampa, FL, USA, 2014, pp. 1-3.

[298] Nano Dimension, "DragonFly IV | A new era in 3D electronics printing," https://www.nano-di.com/dragonfly-iv.

[299] M. Li, Y. Yang, F. Iacopi, M. Yamada and J. Nulman, "Compact multi-layer bandpass filter using low-temperature additive manufacturing solution," in *IEEE Transactions on Electron Devices*, vol. 68, no. 7, pp. 3163-3169, Jul 2021.

[300] M. Li, J. Cai, L. Deng, X. Li, F. Iacopi, Y. Yang, "Additively manufactured conductive and dielectric 3D metasurfaces for independent manipulation of broadband orbital angular momentum," in *Materials & Design*, vol. 249, pp. 113500, Jan. 2025.

[301] J. Zhu and Y. Yang, "3-D printed transmission-reflection-integrated metasurface for spin-decoupled full-space quadruplex channels independent phase modulation," in *IEEE Transactions on Microwave Theory and Techniques*, vol. 72, no. 8, pp. 4790-4800, Aug. 2024.

[302] J. Zhu et al., "Additively manufactured millimeter-wave dual-band single-polarization shared aperture fresnel zone plate metalens antenna," in *IEEE Transactions on Antennas and Propagation*, vol. 69, no. 10, pp. 6261-6272, Oct. 2021.

[303] M. Li, Y. Yang, Y. Zhang, F. Iacopi, S. Ram and J. Nulman, "A fully integrated conductive and dielectric additive manufacturing technology for microwave circuits and antennas," *50th European Microwave Conference (EuMC)*, Utrecht, Netherlands, 2021, pp. 392-395.

[304] J. Zhu, Y. Yang, N. Hu, S. Liao, J. Nulman, "Additively manufactured multi-material ultrathin metasurfaces for broadband circular polarization decoupled beams and orbital angular momentum generation," in *ACS Applied Materials &*

Interfaces, vol. 13, no. 49, pp. 59460-59470, Dec. 2021.

[305] M. R. Akram, M. Q. Mehmood, X. Bai, R. Jin, M. Premaratne, W. Zhu, "High efficiency ultrathin transmissive metasurfaces," in *Advanced Optical Materials*, vol. 7, no. 11, pp. 1801628, Jun. 2019.

[306] S. Gao and H. Wong, "A wideband dual-circularly polarized transmitarray antenna based on magnetoelectric dipole elements and source," in *IEEE Transactions on Antennas and Propagation*, vol. 73, no. 6, pp. 3537-3546, Jun. 2025.

[307] B. -J. Xiang and K. -M. Luk, "A Wideband Low-Profile Folded Transmitarray Antenna Based on Magnetoelectric Dipole Elements," in *IEEE Transactions on Antennas and Propagation*, vol. 71, no. 11, pp. 8659-8667, Nov. 2023.

[308] J. Zhu, Y. Yang, J. Lai and M. Li, "3-D printed noninterleaved reflective metasurfaces supporting dual-band spin-decoupled quadruplex channel independent beam-shaping with controllable energy distribution," in *IEEE Transactions on Microwave Theory and Techniques*, vol. 72, no. 2, pp. 1196-1205, Feb. 2024.

[309] L. Wu, J. Tao, G. Zheng, "Controlling phase of arbitrary polarizations using both the geometric phase and the propagation phase," in *Physical Review B*, vol. 97, no. 24, pp. 245426, Jun. 2018.

[310] Q. Song, A. Baroni, R. Sawant, P. Ni, V. Brandli, S. Chenot, S. Vézian, B. Damilano, P. de Mierry, S. Khadir, P. Ferrand, "Ptychography retrieval of fully polarized holograms from geometric-phase metasurfaces," in *Nature Communications*, vol. 11, no. 1, pp. 2651, May 2020.

[311] Y. Qiu, S. Tang, T. Cai, H. Xu, F. Ding, "Fundamentals and applications of spin-decoupled Pancharatnam—Berry metasurfaces," in *Frontiers of Optoelectronics*, vol. 14, no. 2, pp. 134-147, Jun. 2021.

[312] X. Ding, F. Monticone, K. Zhang, L. Zhang, D. Gao, S. N. Burokur, A. De Lustrac, Q. Wu, C. W. Qiu, A. Alù, "Ultrathin Pancharatnam ‐ Berry metasurface with maximal cross ‐ polarization efficiency," in *Advanced Materials*, vol. 27, no. 7, pp. 1195-1200, Feb. 2015.

[313] W. Luo, S. Sun, H. X. Xu, Q. He, L. Zhou, "Transmissive ultrathin Pancharatnam-Berry metasurfaces with nearly 100% efficiency," in *Physical Review Applied*, vol. 7, no. 4, pp. 044033, Apr. 2017.

[314] R. Mao, G. Wang, T. Cai, K. Liu, D. Wang, B. Wu, "Ultra-thin and high-efficiency full-space Pancharatnam-Berry metasurface," in *Optics Express*, vol. 28, no. 21, pp. 31216-31225, Oct. 2020.

[315] N. A. Rubin, Z. Shi, F. Capasso, "Polarization in diffractive optics and metasurfaces," in *Advances in Optics and Photonics*, vol. 13, no. 4, pp. 836-970, Jan. 2022.

[316] B. Ji; Y. Han; S. Liu; F. Tao; G. Zhang; Z. Fu, "Several key technologies for 6G: challenges and opportunities," in *IEEE Communications Standards Magazine*, vol. 5, no. 2, pp. 44-51, Jun. 2021.

[317] J. Y. Dai et al., "Wireless communication based on information metasurfaces," in *IEEE Transactions on Microwave Theory and Techniques*, vol. 69, no. 3, pp. 1493-1510, Mar. 2021.

[318] G. -B. Wu, K. F. Chan and C. H. Chan, "3-D printed terahertz lens to generate higher order Bessel beams carrying OAM," in *IEEE Transactions on Antennas and Propagation*, vol. 69, no. 6, pp. 3399-3408, Jun. 2021.

[319] L. Song, T. Zhang, P. -Y. Qin, J. Du and Y. J. Guo, "Sub-THz broadband transmitting metasurfaces with enhanced frequency-scanning capability," in *IEEE Transactions on Terahertz Science and Technology*, vol. 14, no. 1, pp. 82-90, Jan. 2024.

[320] O. Koutsos, F. F. Manzillo, M. Caillet, R. Sauleau and A. Clemente, "Experimental demonstration of a 43-dBi gain transmitarray in PCB technology for backhauling in the 300-GHz band," in *IEEE Transactions on Terahertz Science and Technology*, vol. 13, no. 5, pp. 485-492, Sep. 2023.

[321] W. Saleh, Y. Letestu, R. Sauleau and E. M. Cruz, "Design and measurements of a high-performance wideband transmitarray antenna for D-band communications," in *IEEE Antennas and Wireless Propagation Letters*, vol. 20, no. 9, pp. 1765-1769, Sep. 2021.

[322] D. Seo, H. Kim, S. Oh, J. Kim and J. Oh, "Ultrathin high-gain D-band transmitarray based on a spatial filter topology utilizing bonding layer effect," in *IEEE Antennas and Wireless Propagation Letters*, vol. 21, no. 10, pp. 1945-1949, Oct. 2022.

[323] L. -Z. Song, T. Zhang, J. -X. Lai, Y. Yang and J. Du, "A 180-GHz to 220-GHz wideband transmitarray with wide-angle beam steering for intersatellite communications," in *IEEE Transactions on Antennas and Propagation*, vol. 72, no. 1, pp. 950-955, Jan. 2024.

[324] Z. -W. Miao Z. -C. Hao; G. Q. Luo; L. Gao; J. Wang; X. Wang, "140 GHz high-gain LTCC-integrated transmit-array antenna using a wideband SIW aperture-coupling phase delay structure," in *IEEE Transactions on Antennas and Propagation*, vol. 66, no. 1, pp. 182-190, Jan. 2018.

[325] F. Foglia Manzillo, A. Clemente and J. L. González-Jiménez, "High-gain D-band transmitarrays in standard PCB technology for beyond-5G communications," in *IEEE Transactions on Antennas and Propagation*, vol. 68, no. 1, pp. 587-592, Jan. 2020.

[326] G. B. Wu, Y. -S. Zeng, K. F. Chan, S. -W. Qu and C. H. Chan, "High-gain circularly polarized lens antenna for terahertz applications," in *IEEE Antennas and Wireless Propagation Letters*, vol. 18, no. 5, pp. 921-925, May 2019.

[327] F. Diaby, A. Clemente, K. T. Pham, R. Sauleau and L. Dussopt, "Circularly polarized transmitarray antennas at Ka-band," in *IEEE Antennas and Wireless Propagation Letters*, vol. 17, no. 7, pp. 1204-1208, Jul. 2018.

[328] J. Wang, X. Zhang, J. Ding, H. Zhang, W. Chen and C. Chen, "Characteristic mode inspired broadband circularly polarised folded transmitarray antenna," in *IEEE Transactions on Antennas and Propagation*, vol. 71, no. 9, pp. 7632-7637, Sep. 2023.

[329] H. Kaouach, "Design and characterisation of circularly polarized discrete lens antennas in 60-GHz band," in *IEEE Antennas and Wireless Propagation Letters*, vol. 15, pp. 1200-1203, 2016.

[330] C. Yang, G.-B. Wu, D. Zheng, K. F. Chan and C. H. Chan, "An ultralow-profile

folded transmitarray antenna based on a multifunctional metasurface with both-sided wavefront control," in *IEEE Transactions on Antennas and Propagation*, vol. 71, no. 10, pp. 7804-7812, Oct. 2023.

[331] X. Dai, G. -B. Wu and K. -M. Luk, "A wideband circularly polarized transmitarray antenna for millimeter-wave applications," in *IEEE Transactions on Antennas and Propagation*, vol. 71, no. 2, pp. 1889-1894, Feb. 2023.

[332] L. Xiang, F. Wu, Z. -W. Miao, Z. H. Jiang, C. Yu and W. Hong, "A wideband circularly polarised magnetoelectric dipole transmitarray antenna based on element rotation techniques," in *IEEE Transactions on Antennas and Propagation*, vol. 71, no. 8, pp. 6953-6958, Aug. 2023.

[333] H. Lei, Y. Liu, Y. Jia, Y. Zhong and Z. -X. Liu, "A low-profile 2-D beam-scanning circularly polarized antenna combining reflectarray and transmitarray," in *IEEE Antennas and Wireless Propagation Letters*, vol. 23, no. 12, pp. 4558-4562, Dec. 2024.

[334] J. Zhu, Y. Yang, J. Lai, J. Nulman, "Additively manufactured polarisation insensitive broadband transmissive metasurfaces for arbitrary polarization conversion and wavefront shaping," in *Advanced Optical Materials*, vol. 10, no. 21, pp. 2200928, Nov. 2022.

[335] X. Lv, Y. Yang, Z. Luo and J. S. Tyo, "Multimaterial 3-D-Printed FSSs for Ultrawide and Dual Passbands in the K-Ka Spectra," in *IEEE Transactions on Microwave Theory and Techniques*, vol. 73, no. 1, pp. 75-86, Jan. 2025

[336] J. Yang et al., "Folded transmitarray antenna with circular polarisation based on metasurface," in *IEEE Transactions on Antennas and Propagation*, vol. 69, no. 2, pp. 806-814, Feb. 2021.

[337] B. Zheng, Y. Fan and Y. J. Cheng, "Wideband high-efficiency circularly polarised transmitarray with linearly polarised feed," in *IEEE Antennas and Wireless Propagation Letters*, vol. 22, no. 6, pp. 1451-1455, Jun. 2023.

[338] J. Hu, H. Wong and L. Ge, "A circularly-polarized multi-beam magneto-electric dipole transmitarray with linearly-polarised feeds for millimeter-wave applications," in *IEEE Transactions on Antennas and Propagation*, vol. 70, no. 7,

pp. 6012-6017, Jul. 2022.

[339] P. Nayeri, F. Yang and A. Z. Elsherbeni, "Bifocal design and aperture phase optimisations of reflectarray antennas for wide-angle beam scanning performance," in *IEEE Transactions on Antennas and Propagation*, vol. 61, no. 9, pp. 4588-4597, Sep. 2013.

[340] X. Tong; Z. H. Jiang; H. Chen; F. Wu; J. Cao; R. Sauleau, "A dual-CP multibeam transmit-array antenna based on anisotropic impedance surfaces and hybrid phase compensation," in *IEEE Antennas and Wireless Propagation Letters*, vol. 22, no. 5, pp. 1144-1148, May 2023

[341] L. Wang, Y. Yang, L. Deng, W. Hong, C. Zhang, S. Li, "Terahertz angle‐multiplexed metasurface for multi‐dimensional multiplexing of spatial and frequency domains," in *Advanced Theory and Simulations*, vol. 3, no. 10, pp. 2000115, Oct 2020.

[342] Y. Li, X. Li, L. Chen, M. Pu, J. Jin, M. Hong, X. Luo, "Orbital angular momentum multiplexing and demultiplexing by a single metasurface," in *Advanced Optical Materials*, vol. 5, no. 2, pp. 1600502, Jan 2017.

[343] Z. H. Jiang, Y. Zhang, J. Xu, Y. Yu and W. Hong, "Integrated broadband circularly polarised multi-beam antennas using Berry-phase transmit-arrays for Ka-band applications," in *IEEE Transactions on Antennas and Propagation*, vol. 68, no. 2, pp. 859-872, Feb. 2020.

[344] Y. Kato and A. Sanada, "Extraordinary transmission by double-sided hyperbolic metasurfaces with Γ-point degeneration at millimeter-wave bands," in *IEEE Transactions on Microwave Theory and Techniques*, vol. 67, no. 8, pp. 3297-3305, Aug. 2019.

[345] Y. Wang et al., "Broadband high-efficiency ultrathin metasurfaces with simultaneous independent control of transmission and reflection amplitudes and phases," in *IEEE Transactions on Microwave Theory and Techniques*, vol. 70, no. 1, pp. 254-263, Jan. 2022.

[346] S. Zheng, C. Li, S. Wu, H. Li, G. Yang and G. Fang, "Terahertz transmissive metasurface for realizing beam steering by frequency scanning," in *Journal of*

Lightwave Technology, vol. 39, no. 17, pp. 5502-5507, Sep. 2021.

[347] L. Li, P. Zhang, F. Cheng, M. Chang and T. J. Cui, "An optically transparent near-field focusing metasurface," in *IEEE Transactions on Microwave Theory and Techniques*, vol. 69, no. 4, pp. 2015-2027, Apr. 2021.

[348] DragonFly LDM Lights-Out Digital Manufacturing System.Accessed: Apr. 10, 2021. [Online]. Available: https://www.nano-di.com/amedragonfly-ldm

[349] M. Li, Y. Yang, F. Iacopi, J. Nulman and S. Chappel-Ram, "3D-printed low-profile single-substrate multi-metal layer antennas and array with bandwidth enhancement," in *IEEE Access*, vol. 8, pp. 217370-217379, 2020.

[350] B. Xiong, Y. Liu, Y. Xu, L. Deng, C. W. Chen, J. N. Wang, R. Peng, Y. Lai, Y. Liu, M. Wang, "Breaking the limitation of polarization multiplexing in optical metasurfaces with engineered noise," in *Science*, vol. 379, no. 6629, pp. 294-299, Jan. 2023.

[351] U. Welp, K. Kadowaki, R. Kleiner, "Superconducting emitters of THz radiation," in *Nature Photonics*, vol. 7, no. 9, pp. 702-710, Sep. 2013.

[352] J. Wang, M. Ando, H. Nagata, S. Yoshida, K. Sakai, T. Kiwa, "Multifunctional terahertz microscopy for biochemical and chemical imaging and sensing," in *Biosensors and Bioelectronics*, vol. 220, pp. 114901, Jan. 2023.

[353] A. Nagarajan, R. Singh, "Terahertz brain–computer interfaces, " in *Nature Reviews Bioengineering*, pp. 1-2, Jan. 2025.

[354] P. Y. Han, G. C. Cho, X. C. Zhang, "Time-domain transillumination of biological tissues with terahertz pulses," in *Optics Letters*, vol. 25, no. 4, pp. 242-244, Feb. 2000.

[355] D. S. Sitnikov, I. V. Ilina, V. A. Revkova, S. A. Rodionov, S. A. Gurova, R. O. Shatalova, A. V. Kovalev, A. V. Ovchinnikov, O. V. Chefonov, M. A. Konoplyannikov, V. A. Kalsin, "Effects of high intensity non-ionizing terahertz radiation on human skin fibroblasts," in *Biomedical Optics Express*, vol. 12, no. 11, pp. 7122-7138, Oct. 2021.

[356] B. Ferguson, X. C. Zhang, "Materials for terahertz science and technology," in *Nature Materials*, vol. 1, no. 1, pp. 26-33, Sep. 2002.

[357] O. B. Osman, Z. B. Harris, J. W. Zhou, M. E. Khani, A. J. Singer, M. H. Arbab, "In vivo assessment and monitoring of burn wounds using a handheld terahertz hyperspectral scanner," in *Advanced Photonics Research*, vol. 3, no. 5, pp. 2100095, May 2022.

[358] R. M. Woodward, B. E. Cole, V. P. Wallace, R. J. Pye, D. D. Arnone, E. H. Linfield, M. Pepper, "Terahertz pulse imaging in reflection geometry of human skin cancer and skin tissue," in *Physics in Medicine & Biology*, vol. 47, no. 21, pp. 3853, Oct. 2002.

[359] S. Karmakar, A. Kludze, R. Chandra, Y. Ghasempour, "Sub-terahertz metamaterial stickers for non-invasive fruit ripeness sensing," in *Nature Food*, vol. 6, no. 1, pp. 97-10, Jan. 2025.

[360] S. Birkballe, M. R. Jensen, S. Nørregaard, F. Gottrup, T. Karlsmark, "Can tissue dielectric constant measurement aid in differentiating lymphoedema from lipoedema in women with swollen legs?," in *British Journal of Dermatology*, vol. 170, no. 1, pp. 96-10, Jan. 2014.

[361] V. P. Wallace, A. J. Fitzgerald, E. Pickwell, R. J. Pye, P. F. Taday, N. Flanagan, T. Ha, “Terahertz pulsed spectroscopy of human basal cell carcinoma,” in *Applied Spectroscopy*, vol. 60, no.10, pp. 1127-1133, Oct. 2006.

[362] S. Nourinovin, M. M. Rahman, S. J. Park, H. Hamid, M. P. Philpott and A. Alomainy, "Terahertz dielectric characterization of three-dimensional organotypic treated basal cell carcinoma and corresponding double Debye model," in *IEEE Transactions on Terahertz Science and Technology*, vol. 13, no. 3, pp. 246-253, May 2023.

[363] M. Tros, L. Zheng, J. Hunger, M. Bonn, D. Bonn, G. J. Smits, S. Woutersen, "Picosecond orientational dynamics of water in living cells," in *Nature Communications*, vol. 8, no. 1, pp. 904, Oct. 2017.

[364] M. Zhadobov, N. Chahat, R. Sauleau, C. Le Quement, Y. Le Drean, “Millimeter-wave interactions with the human body: State of knowledge and recent advances,” in *International Journal of Microwave and Wireless Technologies*, vol. 3, no. 2, pp. 237-247, Apr. 2011.

[365] N.R. Abbasi, H. M. Shaw, D. S. Rigel, R. J. Friedman, W. H. McCarthy, I. Osman, A. W. Kopf, D. Polsky, “Early diagnosis of cutaneous melanoma: Revisiting the ABCD criteria,” in *JAMA*, vol. 292, no. 22, pp. 2771-2776, Dec. 2004.

[366] S. M. Goldsmith, A. R. Solomon, "A series of melanomas smaller than 4 mm and implications for the ABCDE rule," in *Journal of the European Academy of Dermatology and Venereology*, vol. 21, no. 7, pp. 929-934, Aug. 2007.

[367] A. Mirbeik-Sabzevari, N. Tavassolian, "Tumor detection using millimeter-wave technology: Differentiating between benign lesions and cancer tissues," in *IEEE Microwave Magazine*, vol. 20, no. 8, pp. 30-43, Jul. 2019.

[368] V. P. Wallace, A. J. Fitzgerald, S. Shankar, N. Flanagan, R. Pye, J. Cluff, D. D. Arnone, "Terahertz pulsed imaging of basal cell carcinoma ex vivo and in vivo," in *British Journal of Dermatology*, vol. 151, no. 2, pp. 424-432, Aug. 2004.

[369] F. Kazemi, F. Mohanna, J. Ahmadi-Shokouh, "Detection of biological abnormalities using a near-field microwave microscope," in *International Journal of Microwave and Wireless Technologies*, vol. 10, no. 8, pp. 933-941, Oct. 2018.

[370] S. A. R. Naqvi, A. T. Mobashsher, B. Mohammed, D. Foong and A. Abbosh, "Benign and malignant skin lesions: Dielectric characterization, modelling and analysis in frequency band 1 to 14 GHz," in *IEEE Transactions on Biomedical Engineering*, vol. 70, no. 2, pp. 628-639, Feb. 2023.

[371] P. Mehta, K. Chand, D. Narayanswamy, D. G. Beetner, R. Zoughi and W. V. Stoecker, "Microwave reflectometry as a novel diagnostic tool for detection of skin cancers," in *IEEE Transactions on Instrumentation and Measurement*, vol. 55, no. 4, pp. 1309-1316, Aug. 2006.

[372] A. Taeb, S. Gigoyan, S. Safavi‐Naeini, “Millimetre‐wave waveguide reflectometers for early detection of skin cancer,” in *IET Microwaves, Antennas & Propagation*, vol. 7, no. 17, pp. 1182-1186, Nov. 2013.

[373] G. Mansutti, A. T. Mobashsher, K. Bialkowski, B. Mohammed and A. Abbosh, "Millimeter-wave substrate integrated waveguide probe for skin cancer detection,"

in *IEEE Transactions on Biomedical Engineering*, vol. 67, no. 9, pp. 2462-2472, Sep. 2020

[374] F. Töpfer, S. Dudorov, J. Oberhammer, "Millimeter-wave near-field probe designed for high-resolution skin cancer diagnosis," in *IEEE Transactions on Microwave Theory and Techniques*, vol. 63, no. 6, pp. 2050-2059, May 2015.

[375] A. Mirbeik-Sabzevari, S. Li, E. Garay, H. T. Nguyen, H. Wang and N. Tavassolian, "Synthetic Ultra-high-resolution millimeter-wave imaging for skin cancer detection," in *IEEE Transactions on Biomedical Engineering*, vol. 66, no. 1, pp. 61-71, Jan. 2019.

[376] A. Mirbeik-Sabzevari, E. Oppelaar, R. Ashinoff and N. Tavassolian, "High-contrast, low-cost, 3-D visualization of skin cancer using ultra-high-resolution millimeter-wave imaging," in *IEEE Transactions on Medical Imaging*, vol. 38, no. 9, pp. 2188-2197, Sep. 2019.

[377] M. Koch, D. M. Mittleman, J. Ornik, E. Castro-Camus, "Terahertz time-domain spectroscopy," in *Nature Reviews Methods Primers*, vol. 3, no. 1, pp. 48, Jun. 2023.

[378] E. Pickwell, B. E. Cole, A. J. Fitzgerald, M. Pepper, V. P. Wallace, "In vivo study of human skin using pulsed terahertz radiation," in *Physics in Medicine & Biology*, vol. 49, no. 9, pp. 1595-1609, Apr. 2004.

[379] Y. M. Bahk, K. H. Kim, K. J. Ahn, H. R. Park, "Recent developments in terahertz nanosensors," in *Advanced Photonics Research*, vol. 5, no. 1, pp. 2300211, Jan. 2024.

[380] S. Shen, X. Liu, Y. Shen, J. Qu, E. Pickwell‐MacPherson, X. Wei, Y. Sun, "Recent advances in the development of materials for terahertz metamaterial sensing," in *Advanced Optical Materials*, vol. 10, no. 1, pp. 2101008, Jan. 2022.

[381] M. Yang, L. Liang, Z. Zhang, Y. Xin, D. Wei, X. Song, H. Zhang, Y. Lu, M. Wang, M. Zhang, T. Wang, "Electromagnetically induced transparency-like metamaterials for detection of lung cancer cells," in *Optics Express*, vol. 27, no. 14, pp. 19520-19529, Jul. 2019.

[382] Z. Vafapour, W. Troy, A. Rashidi, "Colon cancer detection by designing and analytical evaluation of a water-based THz metamaterial perfect absorber," in *IEEE Sensors Journal*, vol. 21, no. 17, pp. 19307-19313, Jun. 2021.

[383] X. Yan, M. Yang, Z. Zhang, L. Liang, D. Wei, M. Wang, M. Zhang, T. Wang, L. Liu, J. Xie, J. Yao, "The terahertz electromagnetically induced transparency-like metamaterials for sensitive biosensors in the detection of cancer cells," in *Biosensors and Bioelectronics*, vol. 126, pp. 485-492, Feb. 2019.

[384] S. W. Jun, Y. H. Ahn, "Terahertz thermal curve analysis for label-free identification of pathogens," in *Nature Communications*, vol. 13, no. 1, pp. 3470, Jun. 2022.

[385] Y. Yang, D. Xu, W. Zhang, "High-sensitivity and label-free identification of a transgenic genome using a terahertz meta-biosensor," in *Optics Express*, vol. 26, no. 24, pp. 31589-31598, Nov. 2018.

[386] R. Zhou, C. Wang, Y. Huang, K. Huang, Y. Wang, W. Xu, L. Xie, Y. Ying, "Label-free terahertz microfluidic biosensor for sensitive DNA detection using graphene-metasurface hybrid structures," in *Biosensors and Bioelectronics*, vol. 188, pp. 113336, Sep. 2021.

[387] J. Zhang, N. Mu, L. Liu, J. Xie, H. Feng, J. Yao, T. Chen, W. Zhu, “Highly sensitive detection of malignant glioma cells using metamaterial-inspired THz biosensor based on electromagnetically induced transparency,” in *Biosensors and Bioelectronics*, vol. 185, pp. 113241, Aug. 2021.

[388] S. Nourinovin, M. M. Rahman, M. Naftaly, M. P. Philpott, Q. H. Abbasi and A. Alomainy, "Highly sensitive terahertz metasurface based on electromagnetically induced transparency-like resonance in detection of skin cancer cells," in *IEEE Transactions on Biomedical Engineering*, vol. 71, no. 7, pp. 2180-2188, Jul. 2024

[389] F. Y. Meng, Q. Wu, D. Erni, K. Wu, J. C. Lee, "Polarization-independent metamaterial analog of electromagnetically induced transparency for a refractive-index-based sensor," in *IEEE Transactions on Microwave Theory and Techniques*, vol. 60, no. 10, pp. 3013-3022, Oct. 2012.

[390] Y. Yang, I. I. Kravchenko, D. P. Briggs, J. Valentine, "All-dielectric metasurface analogue of electromagnetically induced transparency," in *Nature Communications*, vol. 5, no. 1, pp. 5753, Dec. 2014.

[391] J. Hu, F. Safir, K. Chang, S. Dagli, H. B. Balch, J. M. Abendroth, J. Dixon, P. Moradifar, V. Dolia, M. K. Sahoo, B. A. Pinsky, "Rapid genetic screening with high quality factor metasurfaces," in *Nature Communications*, vol. 14, no. 1, pp. 4486, Jul. 2023.

[392] J. Chen, S. X. Huang, K. F. Chan, G. B. Wu, C. H. Chan, "3D-printed aberration-free terahertz metalens for ultra-broadband achromatic super-resolution wide-angle imaging with high numerical aperture," in *Nature Communications*, vol. 16, no. 1, pp. 363, Jan. 2025.

[393] B. You, C. Y. Chen, C. P. Yu, P. H. Wang, J. Y. Lu, "Frequency-dependent skin penetration depth of terahertz radiation determined by water sorption–desorption," in *Optics Express*, vol. 26, no. 18, pp. 22709-22721, Aug. 2018.

[394] S. F. Bernatchez, P. J. Parks, D. M. Grussing, S. L. Matalas, G. S. Nelson, "Histological characterization of a delayed wound healing model in pig," in *Wound Repair and Regeneration*, vol. 6, no. 3, pp. 223-233, May 1998.

[395] H. T. Chen, "Interference theory of metamaterial perfect absorbers," in *Optics Express*, vol. 20, no. 7, pp. 7165-7172, Mar. 2012.

[396] T. Hao, W. Zheng, W. He and K. Lin, "Air-ground impedance matching by depositing metasurfaces for enhanced GPR detection," in *IEEE Transactions on Geoscience and Remote Sensing*, vol. 58, no. 6, pp. 4061-4075, Jun. 2020.

[397] D. Conteduca, I. Barth, G. Pitruzzello, C. P. Reardon, E. R. Martins, T. F. Krauss, "Dielectric nanohole array metasurface for high-resolution near-field sensing and imaging," in *Nature Communications*, vol. 12, no. 1, pp. 3293, Jun. 2021.

[398] F. Yesilkoy, E. R. Arvelo, Y. Jahani, M. Liu, A. Tittl, V. Cevher, Y. Kivshar, H. Altug, "Ultrasensitive hyperspectral imaging and biodetection enabled by dielectric metasurfaces," in *Nature Photonics*, vol. 13, no. 6, pp. 390-396, Jun. 2019.

[399] K. S. Cole, R. H. Cole, “Dispersion and absorption in dielectrics I. Alternating current characteristics,” in *The Journal of Chemical Physics*, vol. 9, no. 4, pp. 341-351, Apr. 1941.

[400] S. Gabriel, R. W. Lau, C. Gabriel, “The dielectric properties of biological tissues: III. in Parametric models for the dielectric spectrum of tissues,” in *Physics in Medicine & Biology*, vol. 41, no. 11, pp. 2271-2278, Nov. 1996.

[401] O. P. Gandhi and A. Riazi, “Absorption of millimeter waves by human beings and its biological implications,” in *IEEE Transactions on Microwave Theory and Techniques*, vol. 34, no. 2, pp. 228-235, Feb. 1986.

[402] H. Hwang, J. Yim, J. W. Cho, C. Cheon and Y. Kwon, “110 GHz broadband measurement of permittivity on human epidermis using 1 mm coaxial probe,” *IEEE MTT-S International Microwave Symposium Digest*, 2003, Philadelphia, PA, USA, 2003, pp. 399-402 vol.1.

[403] E. Pickwell, A. J. Fitzgerald, B. E. Cole, P. F. Taday, R. J. Pye, T. Ha, M. Pepper, V. P. Wallace, “Simulating the response of terahertz radiation to basal cell carcinoma using ex vivo spectroscopy measurements,” in *Journal of Biomedical Optics*, vol. 10, no. 6, pp. 064021-064021, Dec. 2005.

[404] E. Pickwell, B. E. Cole, A. J. Fitzgerald, M. Pepper, V. P. Wallace, “In vivo study of human skin using pulsed terahertz radiation,” in *Physics in Medicine & Biology*, vol. 49, no. 9, pp. 1595-1609, Apr. 2004.

[405] E. Pickwell, B. E. Cole, A. J. Fitzgerald, V. P. Wallace, M. Pepper, “Simulation of terahertz pulse propagation in biological systems,” in *Applied Physics Letters*, vol. 84, no. 12, pp. 2190-2192, Mar. 2004.

[406] Z. S. Tabatabaeian, “Developing THz metasurface with array rectangular slot with high Q-factor for early skin cancer detection,” in *Optik*, vol. 264, no. 1, pp. 169400, Aug. 2022.

[407] R. Sun, W. Li, T. Meng, G. Zhao, "Design and optimization of terahertz metamaterial sensor with high sensing performance," in *Optics Communications*, vol. 494, pp. 127051, Sep. 2021.

[408] R. T. Ako, A. Upadhyay, W. Withayachumnankul, M. Bhaskaran, S. Sriram, “Dielectrics for terahertz metasurfaces: Material selection and fabrication techniques,” in *Advanced Optical Materials*, vol. 8, no. 3, pp. 1900750, Feb. 2020.

[409] X. Lv, R. T. Ako, M. Bhaskaran, S. Sriram, C. Fumeaux, W. Withayachumnankul, “Frequency-selective-surface-based mechanically reconfigurable terahertz bandpass filter,” in *IEEE Transactions on Terahertz Science and Technology*, vol. 12, no. 3, pp. 257-266, Feb. 2022.

[410] E. Hajisaeid, A. F. Dericioglu and A. Akyurtlu, “All 3-D printed free-space setup for microwave dielectric characterization of materials,” in *IEEE Transactions on Instrumentation and Measurement*, vol. 67, no. 8, pp. 1877-1886, Aug. 2018

[411] Q. Sun, E. P. Parrott, Y. He, E. Pickwell‐MacPherson, “In vivo THz imaging of human skin: Accounting for occlusion effects,” in *Journal of Biophotonics*, vol. 11, no. 2, pp. 201700111, Feb. 2018.

[412] TeraSense Group, Inc., “Software and manuals for TERA-256/1024/4096.” [Online]. Available: https://terasense.com/software/tera/

[413] M. Trigka, E. Dritsas, "A comprehensive survey of deep learning approaches in image processing," in *Sensors*, vol. 25, no. 2, pp. 531, Jan. 2025.

[414] H. Zhang et al., "Terahertz Sensing, Communication, and Networking: A Survey," in *IEEE Transactions on Network Science and Engineering*, Early Access.

[415] J. Y. Youm, J. M. Yang, "Analytic ray tracing model and MATLAB code for GRIN rod lens imaging probe design," in *Optics Express*, vol. 33, no. 13, pp. 28679-28696, Jun. 2025.

[416] X. You, R. T. Ako, S. Sriram, W. Withayachumnankul, "3D terahertz confocal imaging with chromatic metasurface," in *Laser & Photonics Reviews*, vol. 19, no. 7, pp. 2401011, Apr. 2025.

Publications

Journal papers:

[1] **J. Lai** and Y. Yang, "3D terahertz antenna measurement: A comparison between solid-state electronics and photomixing approaches," in *IEEE Antennas and Propagation Magazine*, vol. 66, no. 4, pp. 37-50, Aug. 2024.

[2] **J. Lai**, X. Lv and Y. Yang, "A 3-D printed 140 GHz multifocal dielectric transmitarray antenna for 2-D mechanical beam scanning," in *IEEE Antennas and Wireless Propagation Letters*, vol. 23, no. 4, pp. 1366-1370, Apr. 2024.

[3] **J. Lai**, X. Lv, M. M. Rahman, M. A. I. Oni, S. Dey and Y. Yang, "An angle-multiplexed multifocal method for D-band 2-D beam-scanning transmitarray leveraging 3-D transmission line component," in *IEEE Antennas and Wireless Propagation Letters*, vol. 24, no. 3, pp. 731-735, Mar. 2025.

[4] J. Zhu, Y. Yang, **J. Lai**, J. Nulman, "Additively manufactured polarization insensitive broadband transmissive metasurfaces for arbitrary polarization conversion and wavefront shaping," in *Advanced Optical Materials*, vol. 10, no. 21, pp. 2200928-2200921, Nov. 2022.

[5] J. Zhu, Y. Yang, F. Wang, **J. Lai**, M. Li, "3D printed spin‐decoupled transmissive metasurfaces based on versatile broadband cross‐polarization rotation meta‐atom," in *Advanced Optical Materials*, vol. 11, no. 4, pp. 2202416, Feb. 2023.

[6] J. Zhu, M. Li, **J. Lai**, Y. Yang, "Multimaterial additively manufactured transmissive spin‐decoupled polarization‐maintaining metasurfaces," in *Laser & Photonics Reviews*, vol. 17, no. 12, pp. 2300433, Dec. 2023.

[7] J. Zhu, Y. Yang, **J. Lai** and M. Li, "3-D printed noninterleaved reflective metasurfaces supporting dual-band spin-decoupled quadruplex channel independent beam-shaping with controllable energy distribution," in *IEEE Transactions on Microwave Theory and Techniques*, vol. 72, no. 2, pp. 1196-1205, Feb. 2024

[8] L. -Z. Song, T. Zhang, **J. Lai**, Y. Yang and J. Du, "A 180-GHz to 220-GHz wideband transmitarray with wide-angle beam steering for intersatellite communications," in *IEEE Transactions on Antennas and Propagation*, vol. 72, no. 1, pp. 950-955, Jan. 2024

[9] Z. Yin, H. Zhu, X. Lv, **J. Lai** and Y. Yang, "3-D-printed ultracompact butler matrix for wideband millimeter-wave beamforming," in *IEEE Transactions on Microwave Theory and Techniques*, vol. 73, no. 9, pp. 5953-5965, Sep. 2025

Conference papers:

[1] **J. Lai**, Y. Sun, Z. Luo and Y. Yang, "3D printed lens antenna for contactless heartbeat and respiration detection using mm-wave radar sensing," 2*022 IEEE MTT-S International Microwave Biomedical Conference (IMBioC)*, Suzhou, China, 2022, pp. 180-182

[2] **J. Lai** and Y. Yang, "A 3D printing 120 GHz lens antenna for terahertz 1D beam-scanning applications," *2022 International Symposium on Antennas and Propagation (ISAP)*, Sydney, Australia, 2022, pp. 75-76.

[3] **J. Lai** and Y. Yang, "A 3D printed terahertz metamaterial lens for beam-steering applications," *2023 IEEE/MTT-S International Microwave Symposium - IMS 2023*, San Diego, CA, USA, 2023, pp. 692-695.

[4] **J. Lai**, J. Zhu and Y. Yang, "3D printed polarisation insensitive wideband metasurfaces for dynamic polarization conversion and beam shaping," *2023 IEEE International Symposium on Antennas and Propagation and USNC-URSI Radio*

Science Meeting (USNC-URSI), Portland, OR, USA, 2023, pp. 793-794

[5] **J. Lai** and Y. Yang, "3D printed quasi-Fresnel lens with oblique incidence for sub-terahertz near-field imaging," *2025 6th Australian Microwave Symposium (AMS)*, Gold Coast, Australia, 2025, pp. 1-2.

[6] Z. Yin, J. Cai, J. Zhu, **J. Lai** and Y. Yang, "A 3D printed beam-shaping transmissive metasurface for antenna-in-package applications," *2023 IEEE International Symposium on Radio-Frequency Integration Technology (RFIT)*, Cairns, Australia, 2023, pp. 26-28

[7] M. Esfandiari, X. Lv, S. Chamani, **J. Lai** and Y. Yang, "Dielectric target imaging with thz chipless RFID technology," *2025 6th Australian Microwave Symposium (AMS)*, Gold Coast, Australia, 2025, pp. 1-2

[8] M. Esfandiari, X. Lv, S. Chamani, **J. Lai** and Y. Yang, "Millimeter-wave curved cylindrical waveguide sensor for early detection of melanoma," *2025 6th Australian Microwave Symposium (AMS)*, Gold Coast, Australia, 2025, pp. 1-2